Epitaxy of crystalline oxides for functional materials integration on silicon

Gang Niu

▶ **To cite this version:**

HAL Id: tel-00601689

https://theses.hal.science/tel-00601689v2

Submitted on 20 Jun 2011

ÉCOLE CENTRALE DE LYON

THÈSE

Présentée publiquement en vue de l'obtention du grade de

DOCTEUR DE L' ÉCOLE CENTRALE DE LYON

Discipline: Dispositifs de l'Électronique Intégrée

Par

Gang NIU

Epitaxy of crystalline oxides for functional materials integration on silicon

Thèse préparée à l'INL – Ecole Centrale de Lyon
Sous la direction de Guy Hollinger

Soutenance le 20/10/2010 devant la commission d'examen composée par

M. Christian BRYLINSKI	Professeur, LMI-Lyon 1, Lyon	Rapporteur
M. Emmanuel DEFAY	C. I., LETI-CEA, Grenoble	Rapporteur
Mme. Pascale ROY	D. R., SOLEIL-CNRS, Paris	Examinateur
M. Wilfrid PRELLIER	D. R., CRISMAT-CNRS, Caen	Examinateur
M. Guillaume SAINT-GIRONS	C. R., INL-CNRS, Ecully	Co-encadrant
M. Bertrand VILQUIN	MCF, INL-ECL, Ecully	Co-encadrant
M. Guy HOLLINGER	D. R., INL-CNRS, Ecully	Directeur

Content

General Introduction

For several decades, silicon-based Metal Oxide Semiconductor field - effect transistor (MOSFETs) dominates modern electronics and forms the cornerstone of our new Information Age. The continuous dimensional scaling of MOSFETs enables simultaneously better performance and lower cost chips, which allows the sustaining prosperity of semiconductor industry since the 1970s. However, the scaling also makes the SiO_2, which performs incredible electrical properties and has been the unique "oxide" in semiconductor industry over 40 years, turn out to be necessarily replaced. The year of 2007 marks a milestone of silicon-based MOSFETs: the SiO_2 gate dielectric has been replaced by hafnium-base high-k oxides in the 45nm microprocessor technology produced by leading manufacturers. At the beginning of 2010, 32nm technology microprocessor was released using the same hafnium-base oxides dielectrics, and identifying other suitable high k oxides dielectrics becomes a key issue for future 22nm and sub-22nm technologies.

Meanwhile, oxides are indeed an exciting class of electronic materials. In addition to dielectricity, they exhibit a wide range of electronic, magnetic and optical properties: high temperature superconductivity, ferroelectricity, piezoelectricity, ferromagneticity, multiferrocity, colossal magnetoresistance and non-linear optical effects. Therefore integration of oxides (particularly in epitaxial form) with silicon could not only provide an alternative to silica as gate dielectric, but also open a pathway to integrate the above mentioned functionalities on the same Si basewafer, which could lead to the design and fabrication of numerous novel devices such as FeFET (Ferroelectric Field Emission Transistor), MEMS (Micro- Electro- Mechanical systems) and FeRAM (Ferroelectric Random Access Memory). Moreover, crystalline oxides/silicon system could also be used as templates to integrate semiconductors such as III-V, Ge and Si itself with silicon to bridge the gap between semiconductor devices (lasers, solar cells …) and mainstream Si-based MOSFETs technologies. Indeed, the ability to synthesize and control oxides/Si heterostructures is becoming a key issue in the micro- and optoelectronic fields. Molecular Beam Epitaxy (MBE) technique, which allows a precise control of the interface, composition and thickness of growing structures at the atomic level, is a suitable method to study the epitaxial growth of

oxide/Si heterostructures.

In this context, the main objectives of this thesis are (i) to develop a strategy for the epitaxial growth of crystalline oxide layers and heterostructures on silicon, and (ii) to demonstrate that this strategy is suitable for the monolithic integration, on silicon, of novel functionalities based on oxide properties. We have focused our efforts on two key systems, namely $SrTiO_3$/Si (001) and Gd_2O_3/Si (111). Bulk $SrTiO_3$ is used as substrate for a wide range of so-called functional oxides having the perovskite ABO_3 crystal structure while Gd_2O_3 is considered as one of the most promising crystalline candidates to replace silica as gate oxide in advanced CMOS technologies.

This thesis follows the thesises of G. Delhaye, C. Mercking and L. Beccera, carried out at INL. The work was performed within the framework of the program "5 Ecoles Centrales" between China Scholarship Council (CSC) and Institut des Nanotechnologies de Lyon (INL, Ecole Centrale de Lyon). The work has been supported by series of ANR projects: MINOS, IMOX, BOTOX, and by the INL technology platform NANOLYON.

This manuscript consists of four chapters. In chapter I, the detail of the scientific background is presented, as well as the key points of the study. The motivations for developing an epitaxial strategy for oxides on Si are explained, and the researches in this domain in the past years are reviewed.

Chapter II focuses on the description of the experimental methods employed during this thesis. The oxide-dedicated MBE equipment is presented, as well as the techniques of structural and electrical characterizations.

Chapter III will be dedicated to the epitaxial growth and optimization of two oxides/Si systems: $SrTiO_3$/Si (001) and Gd_2O_3/Si (111). The preparation of Si surface will be firstly detailed, particularly the Sr-passivation technique of Si (001) surface for growth of $SrTiO_3$. For $SrTiO_3$/Si (001), we succeeded in finding the epitaxy widow, including the growth temperature and oxygen partial pressure. Then the relaxation process of STO films grown in optimal condition is studied. To further optimize the quality of STO films, several strategies have been performed: 1) definition of novel Si surface passivation method; 2) two-step

growth; 3) multi-step recrystallization growth. The quality of the STO is enhanced finally to a substrate-like level. For Gd_2O_3/Si (111), we optimized the growth condition (growth temperature and oxygen partial pressure) and growth procedure. A pheudomorphic monocrystalline Gd_2O_3 thin film is obtained.

The integration of diverse functionalinities with silicon using oxides/Si template depicted above will be presented in chapter IV. The electrical characterization results of Gd_2O_3 will be showed and discussed. The quality of the films as-deposited and with PDA will be compared in terms of EOTs, leakage current and charges. $BaTiO_3$, Pb(Mg, Nb)-$PbTiO_3$, Pb (Zr, Ti)O_3 and (La, Sr)MnO_3 are deposited on $SrTiO_3$/Si(001) template and demonstrate good piezoelectric, ferroelectric, ferromagnetic properties respectively. Germanium, as an example of semiconductor, is grown on silicon using $BaTiO_3$/$SrTiO_3$/Si (001) and Gd_2O_3/Si (111) respectively. And the quality of Ge epilayer is exhaustively analyzed. The good results on these heterostructures indicate that the oxides/silicon system is well controlled and could be applied to the heterogeneous integration.

Chapter I: Epitaxial crystalline oxides on silicon for future micro- and optoelectronic systems

I.1) Whither microelectronic industry?

I.1.1) History and context

In modern science history, three brilliant scientists will not be forgotten: William Shockley, John Bardeen, and Walter Brattain, who, in December 1947, created solid state transistor that revolutionized electronic technology and laid the foundation of the microelectronic industry.

Later, two other significant milestones were made: Jack Kilby's Integrated Circuit (IC) in 1958 followed quickly by Robert Noyce's planar integrated circuit in1959. In June 1963, Frank Wanlass at Fairchild Semiconductor originated and published the idea of complementary-MOS (CMOS) and it is in March 1971 that Intel developed the first microprocessor "4004", which opened the way to the integration of higher and higher density devices on a single chip, thus providing always faster and cheaper systems. Since then, microelectronics transforms continuously and radically human lives through miniaturization, automation, computation and robotization and achieves an unparalleled prosperity. Now electronics accounted for some 30% of overall industrial investment while in 1960 this figure was less than 5%.

Much of the power of the electronic industry comes from the versatility of semiconductor devices based on silicon. CMOS technologies make it possible to integrate digital and increasingly analogue circuitry in ever-smaller silicon chips. This dimension shrinking trend is well described by an empiric law: Moore's law. This law is named after Intel co-founder Gordon E. Moore, who introduced the concept in a 1965 paper: the number of transistors that can be placed inexpensively on an integrated circuit will be doubled approximately every two years, which was later modified to 18 months.[1]

Such scaling of transistors dimensions indeed led to tremendous improvements in circuit speed and computer performance. However, at the same time, it has also led to the exponential growth in the static power consumption of transistors due to quantum mechanical tunneling through the ever-thinner SiO_2 gate dielectric, which has been a key to the performance of MOSFETs. To solve this problem, one solution is to identify and develop alternative gate dielectrics and metal gate electrodes. The breakthrough came in 2007: Intel release its 45nm Penryn microprocessor using high-k (hafnium based) dielectric oxide and

metal gate technology. And in Jan. 2010, Intel demonstrated its 32nm node technology. However, even with such numerous novel techniques, the miniaturization will not be limitless. According to Intel, the end of Moore's law would come between 2013 and 2018 with 16 nanometer manufacturing processes and 5 nanometer gates, where each molecule can be individually positioned. Hence, a critical question emerges: Whither microelectronics industry?
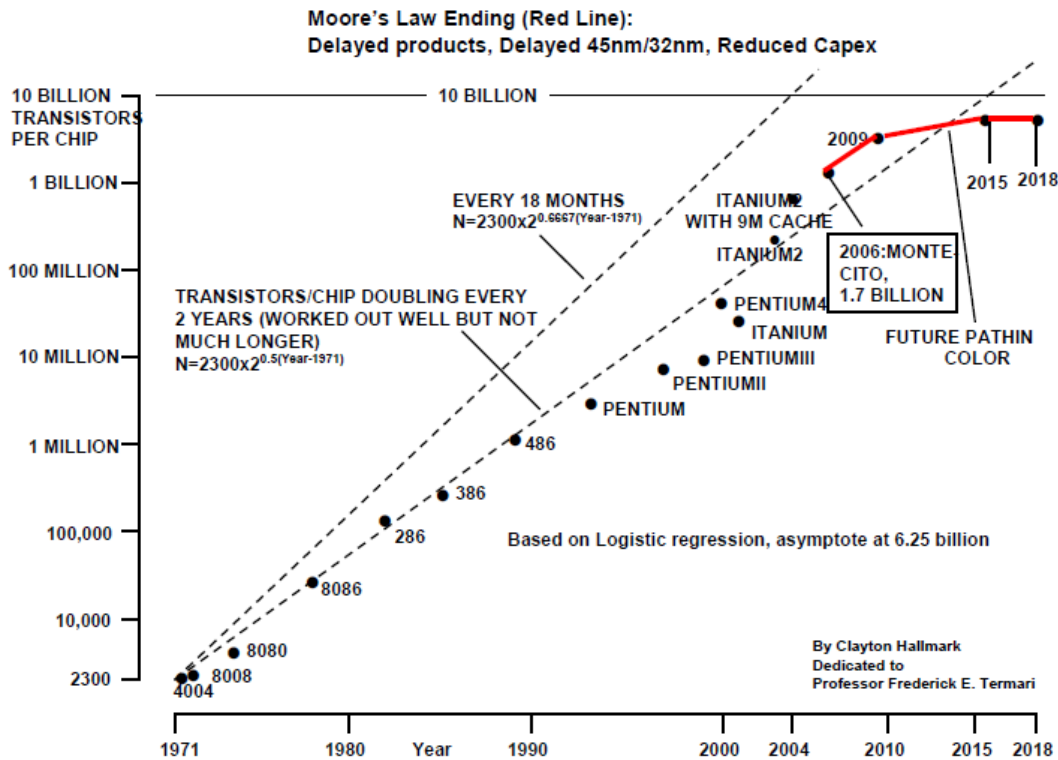
Figure I.1 Moore's law and its end

I.1.2) Future evolution of microelectronics industry

According to the European Nanoelectronics Initiative Advisory Council (ENIAC)[2], the research domain of silicon-based micro-/nano-electronics industry could be commonly classified into three categories (Figure I.2):

1) **More Moore (Advanced CMOS)**, to follow the continuous miniaturization of the transistors. Three leads are currently followed in this category. The first one consists in an improved exploitation of high dielectric constant oxide insulators (high-k oxides) combined with suitable metal gate (adequate work function), in order to reduce the leakage through the gate stack while maintaining a convenient capacity. The second strategy consists in increasing the charge carrier mobility μ in the conduction channel, which requires using alternative high

mobility materials such as Ge/III-V, strained silicon or SiGe alloys. The third lead consists in identifying novel architectures of CMOS devices, such as double or triple gates. But this method encounters many difficulties in fabrication techniques such as auto-alignment between different gates and access resistance.
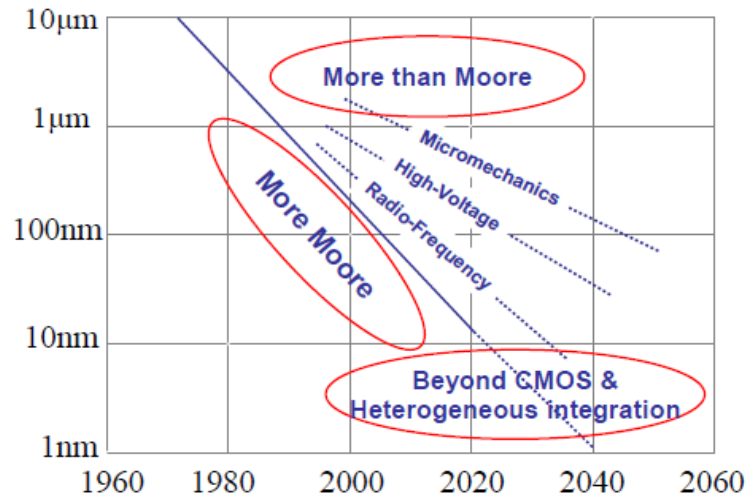
Figure I.2 The future of microelectronics by ENIAC

2) **More than Moore** (complementary to CMOS, non-digital functions). Nowadays classical CMOS technology turns out to be intrinsically limited. Non-digital functions such as radio frequency, analogue circuitry, high voltage switches, mains-operated circuitry such as electronic lighting and battery chargers, and the motion sensors and actuators all require a mixture of technologies, each optimized to the specific need. 'More than Moore' is required to meet such challenges to enable implementation of new functionalities, such as mechanics, optics, acoustics, etc.

3) **Beyond CMOS**. Topics to be investigated range from new materials (organic or inorganic) to new principles of operation (by replacing electron by magnetic excitation or by spin), to new architectures (e.g. 3 dimensional). Prominent examples for "Beyond CMOS" options are new materials for interconnects and transistors like carbo-nano-tubes or nano-wires, switches based on the electronic properties of organic molecules, resistive change polymers for memories, and new computing and memory architectures to fully exploit the properties of these new devices.

The future of nanoelectronics will involve a combination of 'More Moore' and 'More than Moore' with new '**Heterogeneous Integration'** technologies, particularly exploitation of

'system-on-chip' devices – involving designing complete electronic systems from mobile phones to engine controls on a single chip – or 'system-in-package', combining several discrete subsystems using different optimized process technologies in a single package.

In this thesis, our research belongs to 'Heterogeneous Integration' including 2 domains discussed above: 'More Moore', 'More than Moore', which will be described in detail in next section of Chapter I.

I.2) Monolithic integration of various materials on Si

I.2.1) High-k oxides

As will be discussed in the following, future advanced CMOS need high-k oxides[3, 4], which possess higher dielectric permittivity with respect to traditional SiO_2. The dielectric permittivity of SiO_2 is 3.9. An oxide is typically labeled "high-k" when its permittivity exceeds 10, which is for example the case of Al_2O_3[5, 6]. Intensively studied binary oxides such as Gd_2O_3, HfO_2, La_2O_3[7] have a k value around 20. For the perovskite oxides such as $SrTiO_3$ and $BaTiO_3$, the permittivity can exceed 300[8, 9].

I.2.1.1) Scaling and the replacement of SiO_2

Generally, the capacity of a MOS capacitor can be expressed as:

$$C = \varepsilon_0 \varepsilon_r \frac{S}{t_{ox}} = \varepsilon_0 \varepsilon_{SiO_2} \frac{S}{t_{SiO_2}}$$
<div align="right">Equation I-1</div>

where ε_r is the relative permittivity of the gate oxide (dielectric constant), ε_0 is the permittivity of vacuum ($=8.85 \times 10^{-3}$ *fF/μm*), S is the gate electrode area, and t_{ox} is the gate oxide physical thickness. When replacing SiO_2 by an high-k oxide, the Equivalent Oxide Thickness (EOT) is defined by:

$$C_{SiO2} = C_{High-\kappa} \quad \Leftrightarrow \quad \frac{\kappa_{SiO2}}{t_{SiO2}} = \frac{\kappa_{High-\kappa}}{t_{High-\kappa}} \quad \Leftrightarrow \quad t_{SiO2} = EOT = \frac{3,9 \times t_{High-\kappa}}{\kappa_{High-\kappa}}$$
<div align="right">Equation I-2</div>

which means that with a high dielectric constant (ε) a thick gate dielectric layer gives an appropriate capacitance value equal to that of an equivalent thin silicon dioxide film. The EOT is always larger than t_{high-k}. Then, the advantage of employing high-k materials is the reduction of the leakage current caused by tunneling effect, as illustrated in Figure I. 3.
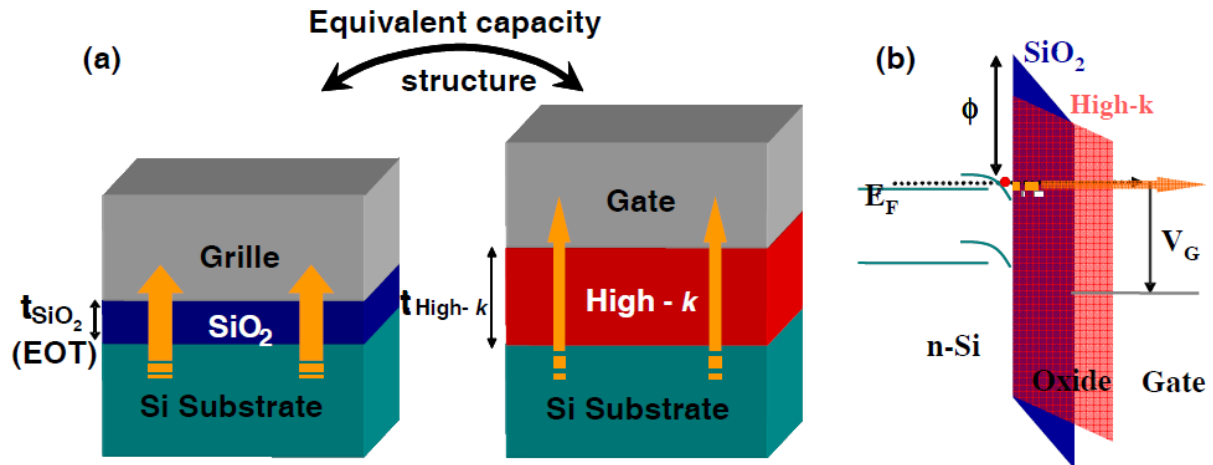
Figure I. 3 (a) Schema of the equivalent capacity structure. High-k oxide layer presents a thicker nature than SiO₂ insulator. (b) This difference in terms of thickness allows limiting the leakage current through gate by tunnel effect.

I.2.1.2) Criteria of high-k oxides selection

The dielectric constant is not the only parameter to be taken into account when choosing an alternative gate insulator. The materials must meet a set of other criteria. Bandgap is another critical point to be considered. A large band offset leads to low leakage current in the MOS device. It has to be noted that the permittivity influences bandgap. Robertson *et al.*[10, 11] reported that a higher k will result in a smaller value of bandgap, as shown in Figure I 4(a). In addition, the sufficient large conduction and valence band offsets with respect to Si (>1eV) are also required. For example, $SrTiO_3$ (k>300) is eliminated from the candidates for SiO_2 alternative due to its nearly zero conduction band offsets with respect to Si. Figure I. 4(b) indicates the band offsets of high-k candidates compared to that of silicon.
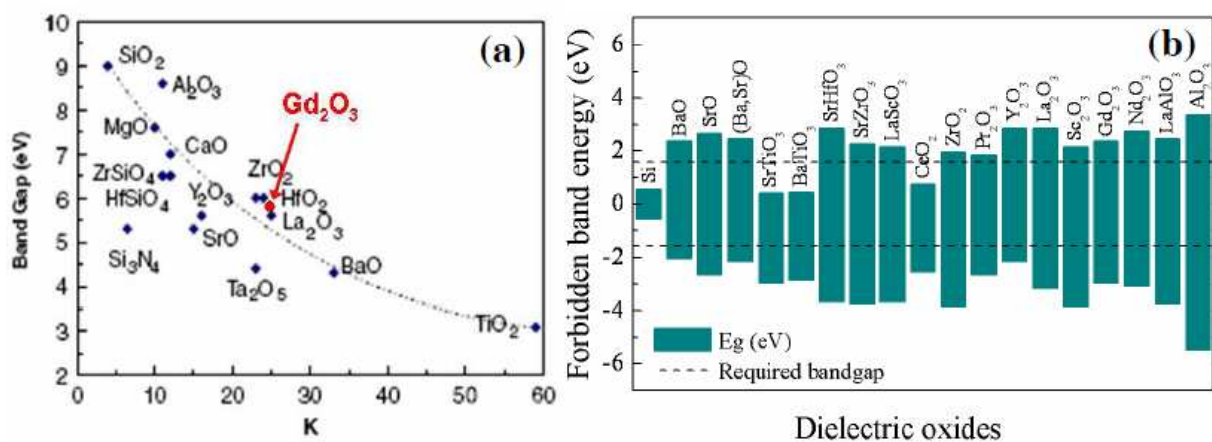
Figure I 4 (a) Relationship between the bandgap of oxides and their dielectric constants. (b) Band offset calculations for a number of potential high-k gate dielectric materials.

For the thin gate dielectrics, the thermodynamic stability on silicon also plays a key role since a high temperature (1050°C) annealing process is typically employed in standard CMOS process for dopants activation. Hubbard and Schlom[12, 13] published a comprehensive study on the thermal stability of binary oxide with respect to silicon at 1000K, as shown in Figure I. 5. Almost all the binary oxides are thermodynamically unstable at 1000K on silicon. It is the same case for the direct integration of the majority of ternary or higher multi-component-oxides. They react with Si under equilibrium conditions to form an undesirable interfacial layer (silicate or silicide), which will deteriorate electrical properties.
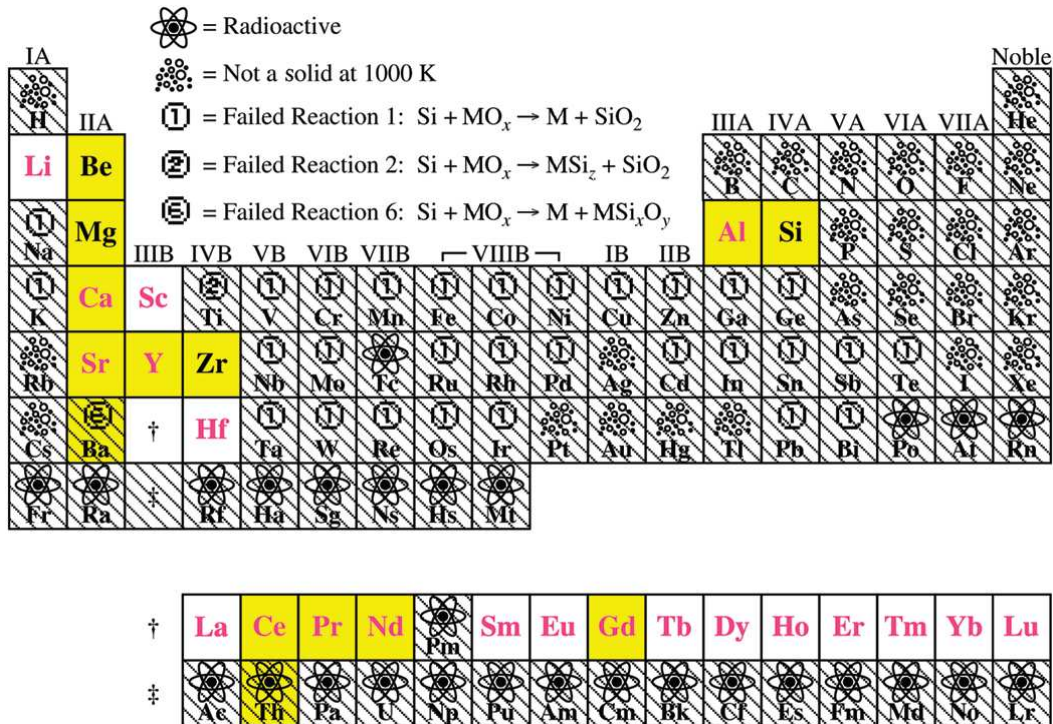
Figure I. 5 Thermodynamically stability of the oxides of elements in contact with Si at 1000K[13].

In most cases, interface quality plays a dominating role in determining overall electrical properties. Compared to relatively ideal SiO_2/Si interface, (D_{it}, interface defects density $\sim 2 \times 10^{10}$ cm^{-2}), most high-k dielectrics candidates show $D_{it} \sim 10^{11} \sim 10^{12}$ cm^{-2} and an additional substantial flatband voltage shift V_{FB} of about 300mV [4]. In addition, several oxides such as ZrO_2 and HfO_2 have high oxygen diffusivities[14], which lead the formation of SiO_x in the interface. Although sometimes this SiO_x/silicate interfacial layer could improve the performances such as D_{it}, mobility and leakage current[15], it will severely compromise the

capacitance gain from any high-k layers in the gate stack. The total capacity C_{total} of the double-oxide-layers system can be expressed by:

$$\frac{1}{C_{total}} = \frac{1}{C_{ox}} + \frac{1}{C_{int}}$$
<div align="right">Equation I-3</div>

where C_{ox} is the capacity of high-k oxides layer and C_{int} that of the interfacial layer.

The EOT of the system can be thereby expressed by:

$$EOT_{double-layer} = \left(\frac{t_{int}}{\kappa_{int}} \times \kappa_{SiO_2} \right) + \left(\frac{t_{High-\kappa}}{\kappa_{High-\kappa}} \times \kappa_{SiO_2} \right)$$
<div align="right">Equation I-4</div>

where t_{int} and k_{int} represent respectively the thickness and permittivity of the interfacial layer and t_{High-k} and k_{High-k} represent those of high-k oxides layer.

Another factor must be considered is the film morphology, i.e., amorphous, crystalline or polycrystalline. Polycrystalline gate dielectrics may be problematic because grain boundaries act as high-leakage paths. Moreover, grain size and orientation changes throughout a polycrystalline film can cause significant variations of the dielectric constant, leading to irreproducible properties [16]. Currently Hf-based oxides insulator used in Intel 32nm technology is amorphous. However, due to a tendency to crystallize under high temperature process and a relative high concentration of electronic defects in amorphous films limit their application for the future nodes[17]. The crystalline gate dielectrics are thus considered as very promising for the future nodes due to their epitaxial nature that allows circumventing the recrystallization issue encountered with amorphous oxides, which leads to a tremendous augmentation of the leakage current. In addition, using epitaxial growth techniques allows subtly monitoring the oxide stoichiometry[18].

Last but not least, the high-k dielectrics should not be hygroscopic (i.e. they must be stable in contact to air or water). Oxides such SrO and La_2O_3 are eliminated by this criterion[19].

I.2.1.3) The choice of crystalline gadolinium oxide

As discussed above, a set of different criteria must be satisfied by the suitable high-k gate dielectrics. An additional criterion has to be considered for a crystalline oxide, namely the lattice mismatch with respect to Si. It is defined by:

$$\frac{\Delta a}{a} = \frac{a_C - a_S}{a_S}$$
Equation I-5

with a_c the lattice parameter of epitaxial layer and a_s that of Si (a_{Si}=5.431Å).

Crystallographic Structure	Composition	Lattice parameter (Å)	Bandgap (eV)	Offsets (eV) CB - VB	Dielectric constant
Diamond	**Si**	**5.431**	**1.1**	**/**	**/**
NaCl	**BaO**	**5.534 (+1.8%)**	**4.4**	**1.8 - 1.5**	**34**
	SrO	**5.14 (-5.3%)**	**5.3**	**2.0 - 2.2**	**15**
	(Ba$_{0.72}$Sr$_{0.28}$)O	**5.431 (0%)**	**4.6**	**1.8 - 1.5**	**25**
Fluorite	**CeO$_2$**	**5.411(-0.36%)**	**3.3**	**0.2 - 2.0**	**17**
	ZrO$_2$	**5.148 (-5.2%)**	**5.8**	**1.4 - 3.3**	**22**
Perovskite	**SrTiO$_3$**	**3.905** $a\sqrt{2}$ =**5.52(+1.7%)**	**3.3**	**-0.14 - 2.4**	**300**
	BaTiO$_3$	**4.01** $a\sqrt{2}$ = **5.67 (+4%)**	**2**	**-0.1 - 2.3**	**2200**
	LaAlO$_3$	**3.81** $a\sqrt{2}$ =**5.39 (-0.7%)**	**6.2**	**1.8 - 3.2**	**25**
	SrHfO$_3$	**4.069** $a\sqrt{2}$ =**5.75 (+5.9%)**	**6.5**	**2.3 - 3.1**	**19**
	LaScO$_3$	**4.069** $a\sqrt{2}$ = **5.84 (+7.5%)**	**5.9**	**1.6 - 3.1**	**24**
Bixbyite	**Pr$_2$O$_3$**	**11.152** **a/2 = 5.57 (+2.7%)**	**3.9**	**1.3 - 2.1**	**15**
	Y$_2$O$_3$	**10.604** **a/2 = 5.302 (-2.4%)**	**6**	**2.3 - 1.6**	**11**
	Gd$_2$O$_3$	**10.813** **a/2 = 5.407 (+0.5%)**	**5.3**	**1.8 - 2.4**	**24**
	Nd$_2$O$_3$	**11.08** **a/2 = 5.54 (+2%)**	**5.8**	**2.2 - 2.5**	**12**
	La$_2$O$_3$	**11.32** **a/2 = 5.66 (+4.2%)**	**5.5**	**2.3 - 2.6**	**25**
Spinel	**γ-Al$_2$O$_3$**	**7.91** **2a/3 = 5.27 (-2.9%)**	**8.8**	**2.8 - 4.9**	**10**

Figure I. 6 Table presenting the parameters of potential high-k gate dielectrics candidates for future CMOS technology [20,21]

Figure I. 6 displays all the lattice parameters of potential high-k gate dielectrics candidates. If one considers that the lattice mismatch must be less than 3%, following candidates can be considered: BaO, (Ba, Sr)O, CeO$_2$, SrTiO$_3$, LaAlO$_3$, Pr$_2$O$_3$, Y$_2$O$_3$, Gd$_2$O$_3$,

Nd_2O_3 and γ-Al_2O_3. Considering that future 22nm and sub-22nm technologies require gate dielectrics with its k value at least around 20, Y_2O_3, Nd_2O_3 and γ-Al_2O_3 are eliminated. BaO, (Ba, Sr)O, CeO_2, $SrTiO_3$ and Pr_2O_3 are failed to satisfy the criteria of band offsets with silicon. Crystalline $LaAlO_3$ is also eliminated because its epitaxial growth temperature on Si is too high (>700°C) to realize an abrupt interface[22]. Finally the lanthanide oxide Gd_2O_3 appears to be the most promising candidate. It covers all the requirements of the next generation of CMOS technology: a high dielectric permittivity, a wide bandgap, large band offsets with respect to silicon, thermodynamically stability on Si and a slight lattice mismatch with silicon. Even though it is bi-domain when epitaxial grown on Si (001), good EOT results have been reported[23] and Gd_2O_3/Si(111) also shows excellent crystallographic and electric properties[24], both crystallographic and electrical ones.

In fact, amorphous $LaAlO_3$ on Si with a coherent interface is also considered as a promising candidate. This is the subject of Sylvain Pelloquin, PhD student at INL. In the present thesis, we will focus on the crystalline oxide Gd_2O_3.

I.2.2) Functional perovskite oxides

I.2.2.1) Introduction

Strontium Titanate ($SrTiO_3$), that we discussed in last section, is only one member of the large family of the transition metal perovskite oxides, whose structure is shown in Figure I. 7, with the A cations at the edges, the B cations in the body-center positions, and the oxygen anions sitting at the face-centered positions, forming an octahedron.
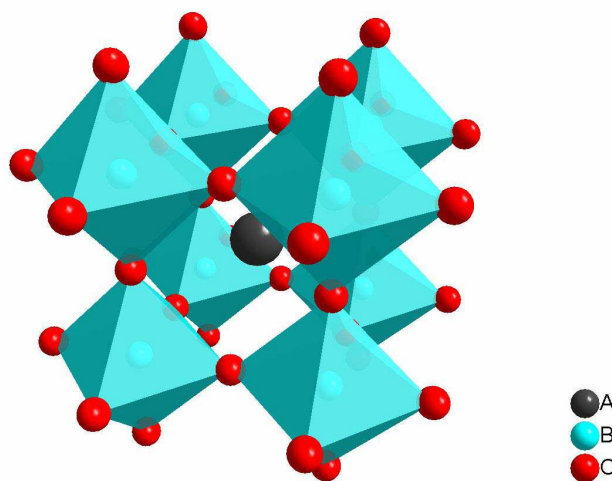
Figure I. 7 Schematic diagram of the ABO₃ perovskite structure with B0₆ octahedron.

Transition metal perovskites (the *B* site is occupied by a *3d*-transition metal element in the ABO_3 formula) have been widely and intensively studied in recent years since they exhibit a broad range of physical properties such as superconductivity, ferroelectricity, piezoelectricity, and (ferro)magnetism, as well as dielectricity as mentioned above[25]. Figure I. 8 shows different properties of ABO_3 perovskites with different B-cations.

Diverse functional devices are based on these perovskite oxides and normally epitaxially grown on $SrTiO_3$ substrates, due to their structure similarity and small variation of lattice constants. Future "More than Moore" and "Hetergeneous integration" technologies demand more functionalities integrated on the same silicon platform, which could be realized if we could integrate a "substrate-like" $SrTiO_3$ film on Si. With a good quality $SrTiO_3$ film on Si, the ferroelectricity, piezoelectricity, ferromagnetism can be easily combined on silicon platform. In addition, $SrTiO_3$ demonstrates ferroelectricity itself when strained on Si[26].
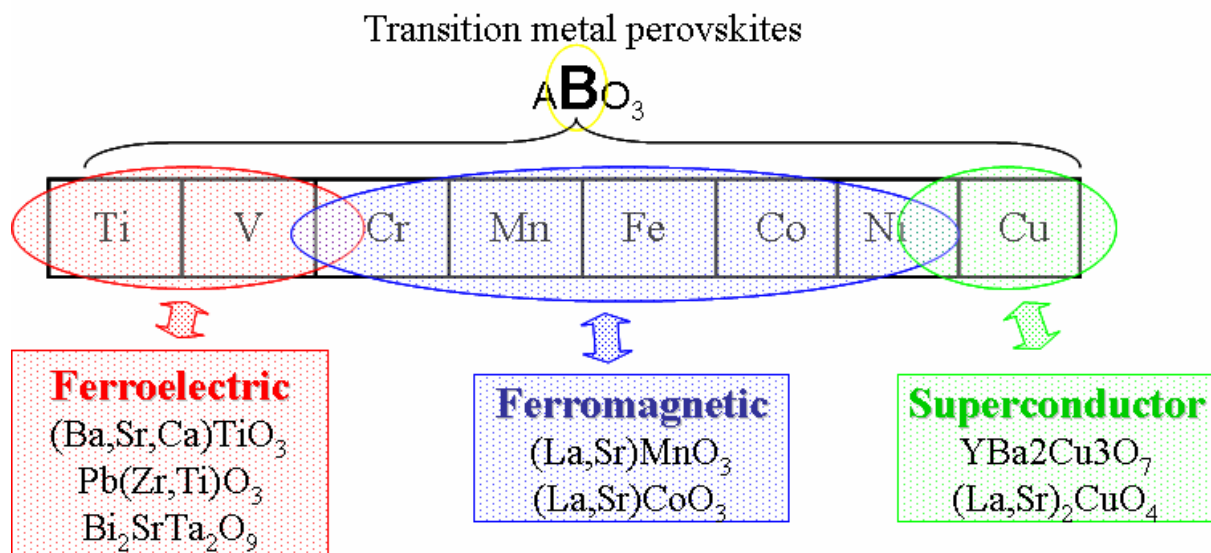
Figure I. 8 The evolution of the properties of 3d-transition metal perovskites with different B-cations.

I.2.2.2) Piezoelectricity

Piezoelectricity is defined by the ability of some materials to generate charge under applied stress. It was firstly discovered in 1880 by J. Curie and P. Curie in Rochelle salt crystals (sodium potassium tartrate tetrahydrate)[27].
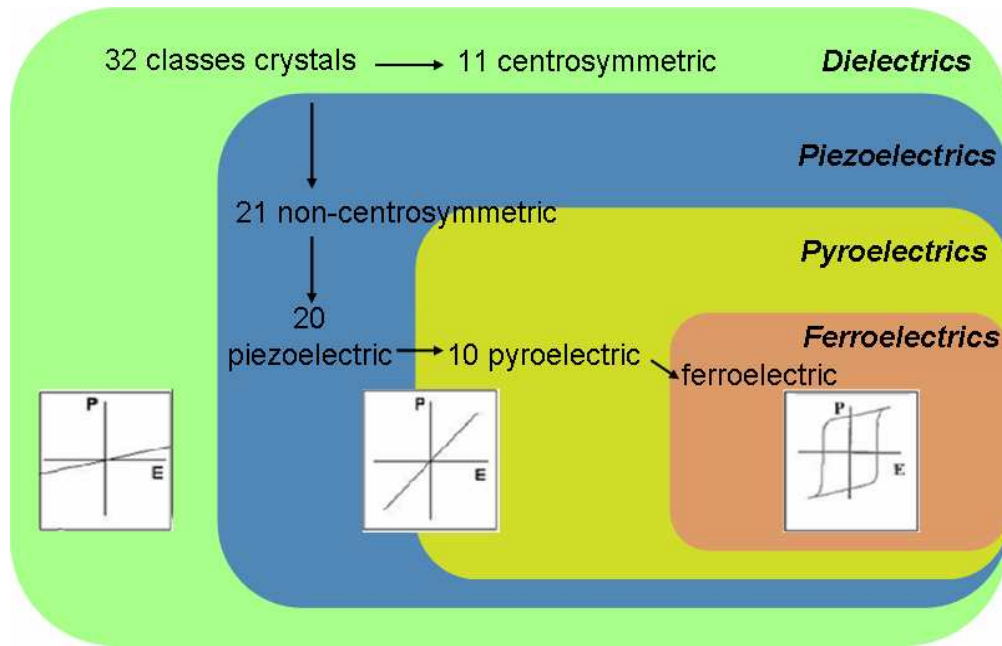
Figure I. 9 Schematic diagram of the relationship between crystals of different classes; insets shows their P (polarization)-E (electrical field) curves.

As shown in Figure I. 9, in the 32 classes crystals grouped by symmetry, 11 classes show a center of symmetry (termed centrosymmetric). Such crystals cannot develop polar properties. The remaining 21 classes are noncentrosymmetric, and the absence of a center of symmetry makes the presence of polar axis (the direction of dipole moment) possible. Among those classes, 20 exhibit piezoelectric effect, which is defined as a linear dependence of strain with an external electric field. When stress is applied to a piezoelectric material, an electric polarization is induced. This is called direct piezoelectric effect, which can be expressed by:

$$P_i = d_{ij}^{direct} X_j \quad \text{(i=1,2,3; j=1,2,…,6)} \hspace{3cm} \text{Equation I-6}$$

where P is the stress-induced polarization (in unit of C/cm), d is the piezoelectric tensor, and X is the applied stress[28]. The units of the direct piezoelectric coefficient are μC/N. Inversely the converse piezoelectric effect, describes the changes in dimensions of a piezoelectric material in response to an applied electric field E:

$$x_j = d_{ij}^{converse} E_i \hspace{5cm} \text{Equation I-7}$$

where x is the strain and E is the applied electric field (V/cm). The units of converse piezoelectric coefficients are pm/V. The coefficients connecting the field and strain in the converse effect are the same as those connecting the stress and the polarization in the direct effect. In general, the piezoelectric coefficient measured in the same direction as the electric field is called longitudinal piezoelectric coefficient, whereas the one measured perpendicular

to the field is the transverse coefficient and the others the shear coefficients (in tetragonal materials). In the piezoelectric film, the piezoelectric coefficient in directions perpendicular (d_{33}) is one of the major interests and themes in the studies.

I.2.2.3) Ferroelectricity

Some years later after the discovery of piezoelectricity, it was found that certain piezoelectric materials possess dielectric hysteretic behavior[29,30]. These type materials were classified as ferroelectric. As explained in I.2.2.2 (Figure I. 9), 20 of the 32 classes of crystals show piezoelectricity. From these 20 piezoelectric classes, 10 have a unique polar axis and as a result they can be spontaneously polarized. Since the phenomenon of polarization is temperature dependent, they are called pyroelectrics. When the polarization of a pyroelectric material can be reversed upon application of an appropriate electric field, the material is called ferroelectric.

The unique characteristic for ferroelectric materials is the existence of a spontaneous internal polarization even in absence of an external electric field. Moreover, the spontaneous polarization can be switched by applying an external electric field. Above a critical temperature (called Curie temperature, T_C), spontaneous polarization disappears and ferroelectric materials undergo a structural phase transition from a ferroelectric phase to paraelectric phase. Taking the prototypical ferroelectric perovskite $BaTiO_3$ for example, it shows various crystalline phases under different temperature, as shown in Figure I.10: cubic and non-polar above its Curie temperature (120°C), <100> polarized tetragonal at room temperature, <110> polarized orthorhombic under 5°C, and <111> polarized rhombohedral below 90°C.
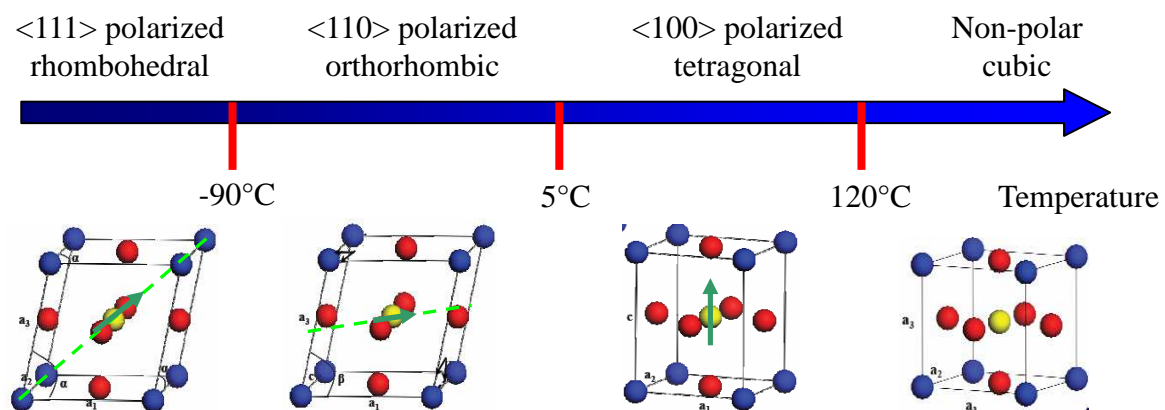
Figure I.10 Various crystalline phases of BaTiO₃

Figure I.11 shows the crystal structures of $BaTiO_3$ in their cubic and tetragonal phase[31]. As shown schematically in the figure, when $BaTiO_3$ is cooled down through the Curie temperature, it undergoes a phase transition which changes its structure. During the transition from the paraelectric phase to the ferroelectric phase the structure becomes tetragonal from cubic (Figure I. 11(b) and (c)). The Ba and Ti sub-lattices shift upward/downward relatively to the negatively charged oxygens, generating a charge separation in the unit cell, which results in a dipole moment and leads to presence of polarization.
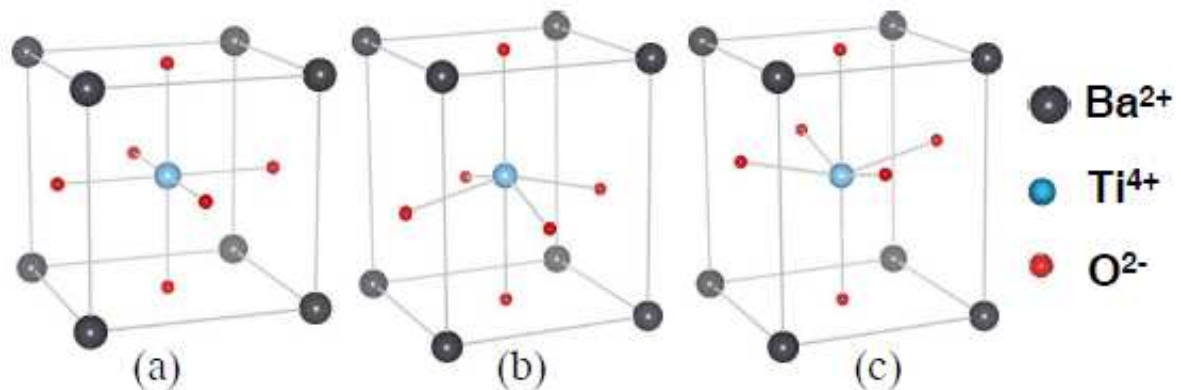
Figure I.11 Crystal structures of $BaTiO_3$: (a) cubic paraelectric phase; (b) ferroelectric phase with polarization vector pointing upwards and (c) downwards.

In addition, this shift breaks the cubic symmetry into a tetragonal phase and results six symmetry-related and crystallographically- equivalent variants, as illustrated in Figure I. 12(a). During the transition from the paraelectric phase to ferroelectric phase the polarization can arise along any of these six directions. Regions of crystal in which the polarization is oriented uniformly are called ferroelectric (polar) domains. The interface between two domains is called domain wall. The width of the domain walls of ferroelectric materials was found to be very small, only a few nm or less[32], which is particularly of interest for memory applications. In a tetragonal ferroelectric phase, they are named as *c* or 180° domain walls in case the domains with opposite polarization directions and *a* or 90° domain walls if the domains' polarization direction is perpendicular, as shown in Figure I. 12 (b).[29,33] In a rhombohedral phase, the angles between domain walls are 71°, 109°, 180°. 180° domains can be reversed with a minimal structural strain but switching of 71°, 90° and 109° domains requires significant structural deformation.
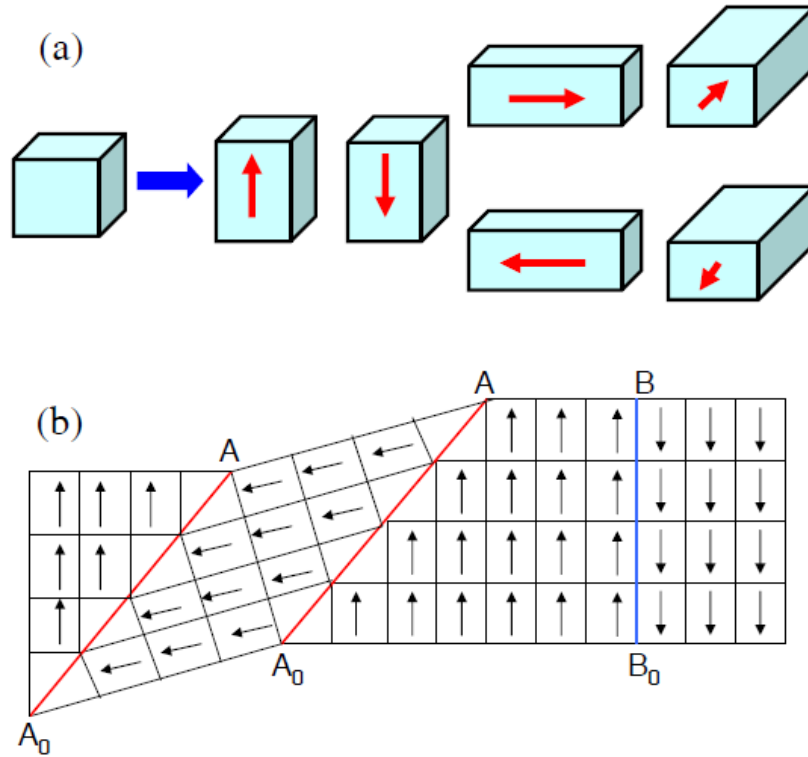
Figure I. 12 (a) six possible polarization directions of BaTiO$_3$ at room temperature; (b) schematic of domain walls: the segments AA$_0$ are 90° domain walls and the segment BB$_0$ is 180° domain wall.

An important characteristic of ferroelectric materials is the demonstration of the ferroelectric hysteresis loop when an external electric field applied on them, as depicted in Figure I. 13. The net polarization of an initially unpolarized ferroelectric material is small. Thus at first the response of polarization to an external field applied is linear, as described by following equation for all the dielectrics:

$$P_i = \chi_{ij} E_j \hspace{4cm} \text{Equation I-8}$$

where *P* is polarization vector, *E* is applied electric field and χ is the dielectric susceptibility. As the field increases, the polarization of the domains with polarization direction opposite to the field starts to switch to the direction of the field leading to a non-linear measurement of charge intensity. The switching continues until all the domains are align with the electric field direction (saturation) and the result of the P measurement returns to be linear. By decreasing the field, P decreases linearly according to the equation mentioned above and when the field returns to zero, the polarization remains a positive value which is called the remnant polarization P$_R$. When a negative electric field of sufficient strength is reached (coercive field E$_C$), the nucleation of reversed polarization domains starts. This process can be repeated.
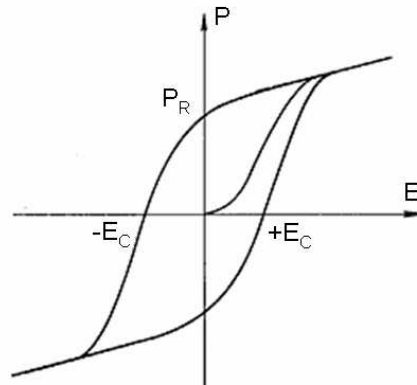
Figure I. 13 Typical ferroelectric hysteresis loop; P_R is the remnant polarization and E_C is the coercive field[33].

As a ferroelectric material is also piezoelectric, it is possible to determine its piezoelectric coefficients. According to converse piezoelectric effect, the strain is linearly proportional to the applied electric field when the piezoelectric coefficient is constant. However, polarization switching in a piezoelectric subjected to an electric field leads electromechanical hysteresis, as shown in Figure I.14(a). Figure I.14(b) demonstrates an ideal case of the piezoelectric response and polarization switch under a bipolar electric field: when the polarization direction changes, the sign of the strain changes and when it is stable the strain is linear with the field. The piezoelectric coefficients can be calculated from the slope of linear regions in the loop. In real crystals the strain versus applied field shows a characteristic butterfly shape[33] (Figure I.14(c)), given by the fact that different polarization orientations are present in the crystal, making the curve smoother in accordance with the change in polarization.
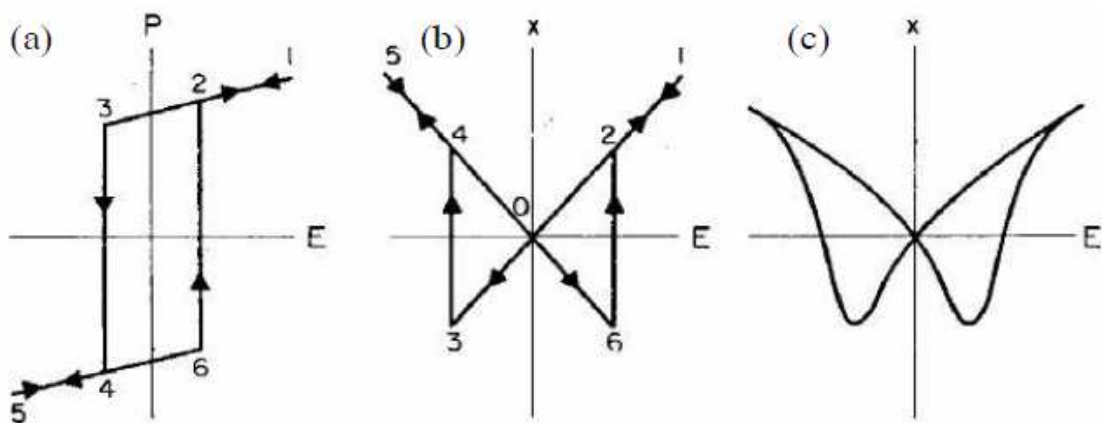
Fig. I 14 Schematic description of the converse piezoelectric effect. (a) Polarization hysteresis loop; (b) theoretical electromechanical hysteresis, piezoelectric coefficient is determined by the slope of the straight lines; (c) actual butterfly loop[31]. x denotes the uniaxial strain.

I.2.2.3) Ferromagnetism

The strongly correlated nature of electrons in transition metal perovskite and the unpaired electrons in the open 3d shells lead to local magnetic moments and complex magnetic properties. For instance, if the *B* site of perovskite ABO_3 is occupied by Mn or Co (as in as (La, Sr)MnO$_3$), the oxide displays ferromagnetism. Ferromagnetic material is one class of magnetic materials. Similarly to the definition of ferroelectricity, ferromagnetic materials historically refer to materials exhibiting spontaneous magnetization. However, recently different classes of spontaneous magnetization are identified leading to a more precise distinguish between ferromagnetic, ferrimagnetic and antiferromagnetic. In particular, in a ferromagnetic material all of its magnetic ions add a positive contribution to the net magnetization. In the case of antiferromagnetic material, magnetic moments of the aligned and anti-aligned ions balance completely so as to have zero net magnetization, despite the magnetic ordering. And in a ferrimagnetic material the anti-aligned ions also exist but the moments are unequal, i.e. the spontaneous magnetization remains. Figure I. 15 shows the ordering of the magnetic dipole in magnetic materials.
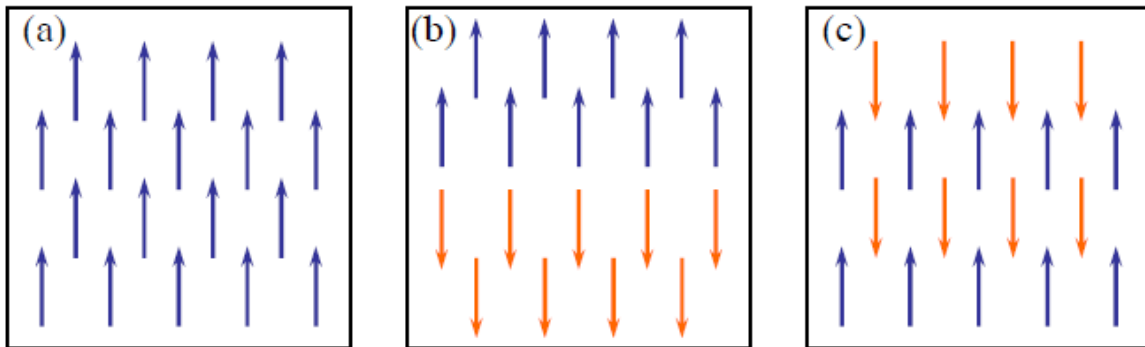
Figure I. 15 Ordering of the magnetic dipole in magnetic materials: (a) ferromagnetic; (b) antiferromagnetic; (c) ferrimagnetic.

In the ferromagnetic and in all magnetic materials, the macrosopic magnetization M is the sum of the magnetic dipole moments of ions per unit volume. The magnetic field can be also represented by magnetic induction B (in unit of Wb/m^2). Following equation shows the relationship between B, H and M (magnetization intensity):

$$B = M + \mu_0 H = \mu H = \mu_0 (1 + \chi) H \qquad\qquad \text{Equation I-9}$$

where μ permeability, μ_0 permeability in vacuum, H is the applied magnetic field and χ =I/H, which is magnetic susceptibility. Similar to ferroelectric materials, ferromagnetic materials possess domains, domain walls and Curie temperature. Furthermore, the response of B to H exhibits a hysteresis loop. We do not discuss in detail here.

In recent years the discovery of Colossal Magnetoresistance (CMR)[34,35] attracts intense research efforts on ferromagnetic material. An external magnetic field could cause the gigantic decrease of the resistivity around the T_C of the perovskite manganites CMR materials[35].

I.2.3) Germanium and III-V semiconductors
I.2.3.1) Introduction

As a member of the semiconductor family, although being the mainstream material in the industry, silicon does not possess the most excellent properties with respect to germanium and III-V materials in terms of mobility and gap type (silicon and Ge are indirect gap semiconductors while III-Vs are direct gap), etc., as shown in Figure I. 16. The integration of Ge and III-V on silicon with a monolithic platform has been a long term dream for the semiconductor industry. The initial motivation of this concept is a simple notion that the best physical properties of Ge or III-V semiconductors and devices (modulators, heteroepitaxial injection lasers, photodetectors, waveguide, solar cell could be married with the characteristics of the silicon manufacturing processes[36]. Recently, the interest in such heterogeneous technology is renewed by the requirements of the new high mobility tunnel to in the future CMOS with enhance performance. However, direct epitaxy of high quality Ge and III-V semiconductors on silicon has been hindered by materials incompatibilities (i.e. lattice mismatch, thermal mismatch and heterovalent interface) and practical processing constraints. Based on several results reported in the early 2000's[37,38,39], crystalline oxide/Si could serve as a template to bridge the gap between Ge or III-V semiconductors and silicon. Due to the strong crystallographic and chemical heterogeneity between III-V or IV-IV semiconductors and oxides, the elevated lattice mismatch between these materials is fully accommodated by a network of dislocations, confined at the heterointerface, and formed at the very early stages of the growth. As a consequence, the semiconductor grows with its bulk lattice parameter on the oxide surface and does not contain any threading defect related to any plastic relaxation mechanism, as explained in detail in one of our studies at INL[40].

	Ge	Si	GaAs	InSb	InP
Forbidden band width E_g (eV)	0.66	1.12	1.42	0.17	1.35
Electronic affinity χ (eV)	4.05	4.0	4.07	4.59	4.38
Hole mobility μ_t (cm²/Vs)	**1900**	**450**	400	1250	150
Electron mobility μ_e (cm²/Vs)	**3900**	**1500**	**8500**	**80000**	**4600**
Lattice constant (nm)	0.565	0.543	0.565	0.648	0.587
Dielectric constant	16.0	11.9	13.1	17.7	12.4
Fusion point T_f (°C)	937	1412	1240	527	1060

Figure I. 16 Characteristics of future alternative tunnel semiconductors and the comparisons with Si (according to ref.41)

I.2.3.2) High mobility channels for CMOS

The significant success of silicon-based microelectronic industry owes to the unique properties of the SiO_2-Si (SiO_2 as native oxide of silicon) system, particularly in terms of interface state density D_{it} and thermodynamic stability. These performances are worse for other semiconductors (Ge, GaAs, GaN). However, the introduction of high-k oxides to replace silica as the insulate layer makes it possible to reconsider the use of high mobility Ge and III-V channel materials as long as suitable surface passivation technique is identified to obtain good interface quality between oxide and semiconductor.

Among the main semiconductors shown in Figure I.16, Ge exhibits the highest hole mobility and it has actually been demonstrated that compressively-strained Ge *p*-MOSFETs provide 10 times or higher hole mobility against Si *p*-MOSFETs[42]. It is confirmed that the electron mobility of III-V materials is quite high. In addition, the lattice parameter of Ge equals that of GaAs. It is thus possible to consider a stack for future MOS, where a GOI substrate or Ge directly grown on Si substrate is used, and where GaAs is locally epitaxially grown on Ge, as illustrated in Figure I. 17[43]. Such a strategy has been studied in the framework of the European project Duallogic.
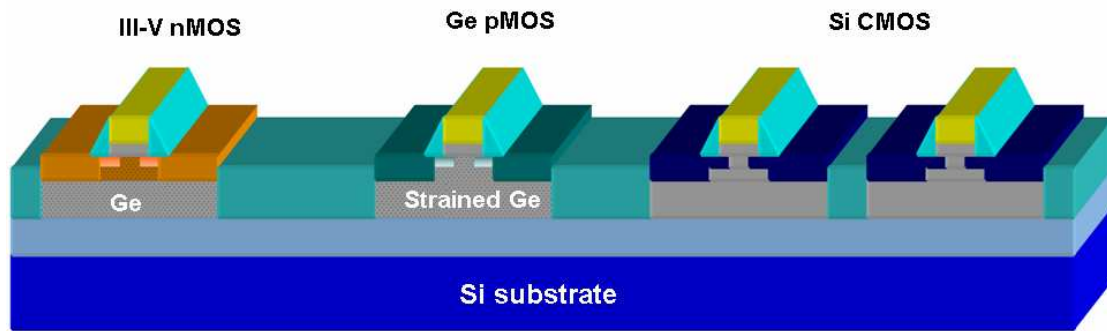
Figure I. 17 Perspective of co-integration of Ge pMOS and III-V nMOS on the same Si substrate

In order to develop a high speed and low power CMOS technology, there still remains a number of challenges to overcome[44]:

(1) <u>Engineering high electronic quality Ge films on Si in order to ensure volume production at low cost</u>. Ge layers directly grown on Si present an elevated density of threading dislocations due to an elevated lattice mismatch. Several epitaxial strategies have been developed to reduce this dislocation density and produce so-called Ge/Si virtual substrates[45]. However, Germanium-on-insulator (GOI) structures consisting in thin Ge layers on an insulator/Si template appear as highly desirable to obtain better electrostatic control of the gate, reduced junction capacitance and lower substrate coupling in radio frequency[46]. Many methods have been proposed to develop GOI layers[47], such as Ge condensation technique, liquid phase epitaxy and Smart cut[TM] technology etc.

(2) <u>Engineering high quality III-V films on Si substrate</u>. While III-V materials could be directly epitaxied on Si with methods such as selective epitaxy[48] or metamorphic growth[49], a better solution is using GeSi[50,51] or GOI substrates[52,53].

(3) <u>Developping adequate Ge and III-V surface passivation methodology and identify appropriate high-k gate dielectrics</u> to combine oxide scaling below 1 nm with good electrical quality of the interfaces. Direct deposition of high-k oxides on Ge has showed limited electrical quality (high interface state density D_{it} and prominent leakage current) even when the interface is abrupt, as exhibited by the attempts of depositing different dielectrics on Ge such as HfO_2[54], ZrO_2[55], Al_2O_3[56], $LaAlO_3$[57]. Thus the passivation of the Ge surface in order to obtain a good electrical characteristics interface between high-k oxides and Ge is a critical issue for the Ge MOS technology. Several strategies of Ge surface passivation are identified such as nitridation[58,59] (GeON), Si-passivation[60], sulfur passivation[61], fluorine treatment[62] and ozone oxidation[63], etc. Among them, nitridation is widely used and develops the electrical qualities of Ge MOS with a minimum

$D_{it}=1.8\times10^{-11}$ cm^{-2}eV^{-1})[56], as shown in Figure I.18.
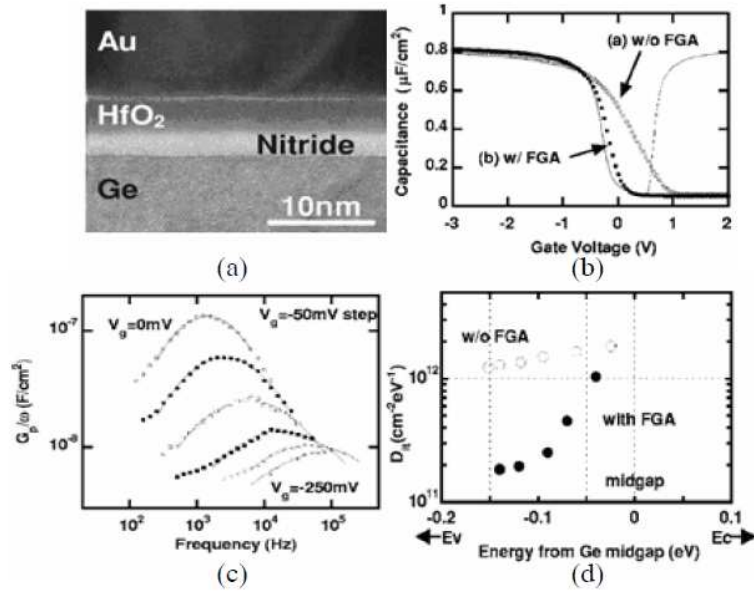
Figure I. 18 (a) XTEM images of the Au/HfO$_2$ /Ge nitride/Ge MIS structure with HfO$_2$ film;.(b)C-V characteristics of the MIS structure;(c) Measured frequency dependence of Gp/ω for various gate voltages of the MIS structure, where Gp is equivalent parallel conductance and ω is the angular frequency;(d) D$_{it}$ distribution as a function of the energy from the midgap of Ge without and with Forming Gas Annealing(FGA).

I.2.4) Summary

In this thesis, crystalline gadolinium oxide is studied as one of the most promising high-k gate insulator candidates for the future advanced CMOS technology thanks to its excellent properties. Furthermore, even though SrTiO$_3$ turns out not a viable high-k gate dielectric due to its too small electron injection barrier in the structures prepared so far[64], SrTiO$_3$/Si(001) system is investigated now as an alternative oxide for high-capacitance trench structures for memory applications. Moreover, it also opens a path to integrate numerous functional oxides on Si due to their isotype structure- perovskite with SrTiO$_3$. Thereby, the SrTiO$_3$/Si(001) is also studied in this thesis. Based on the STO/Si(001) and Gd$_2$O$_3$/Si(111) templates, we can integrate various functionalities such as piezo- (ferro-)electricity (BaTiO$_3$, Pb(Zr,Ti)O$_3$, Pb(Mg, Nb)O$_3$-PbTiO$_3$), ferromagnetism ((La,Sr)MnO$_3$), and optoelectronic (germanium) on the same silicon substrate.

I.3) State of arts of the systems studied in this thesis

I.3.1) Gadolinium oxide on silicon (Gd$_2$O$_3$/Si)

Gadolinium oxide (Gd_2O_3), which belongs to the family of rare-earth (RE) metal oxides (lanthanide oxides) possesses a cubic bixbyite Mn_2O_3 (II) structure in which the unit cell includes eight unit cells of an incomplete and distorted fluorite structure. Its lattice constant is 10.814Å, which is almost equal to 2 times of that of silicon (5.431 Å)[23]. Bulk Gd_2O_3 presents a dielectric constant of 24[65], a bandgap of 5.3eV[23], conduction and valence band offsets with respect to Si of 1.8eV and 2.4eV respectively[66].

Thanks to their relatively high dielectric constants (as shown in Figure I.6) and stability on Si even at high temperatures[12], binary bixbyite lanthanide oxides such as La_2O_3[67,68], Y_2O_3[69,70], Pr_2O_3[71,72], CeO_2[73,74], become interesting candidates for alternative dielectric and have been intensively studied. However, compared to Gd_2O_3, some of their intrinsic problems such as band offsets with Si (Figure I. 6) or strong hygroscopic nature (moisture absorption)[75,76] restrict their application. The study of Gd_2O_3 on Si was started by J. Kwo *et al.* at Bell Laboratory in early 2000's[77,78] and the group of Osten (Hannover Univ.) intensively studies the system Gd_2O_3/Si since 2006. Similarly to Pr_2O_3[79], Gd_2O_3 was found to grow with two orthogonal in-plane orientations on Si(001)[22, 24,80], as shown in Figure I.19.

(a)   (b)   (c)
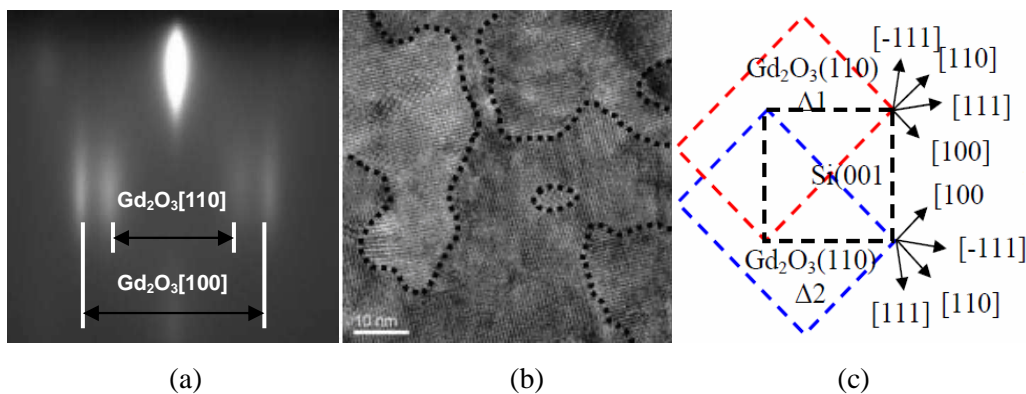
Figure I. 19 (a) RHEED pattern of Gd_2O_3 on Si(001) along Si[110] azimuth; (b) TEM plane view of Gd_2O_3 on Si(001) with the dotted lines showing domain boundaries; (c) A schema illustrating two Gd_2O_3 orientations on Si(001).

The epitaxial relationship between Gd_2O_3 and Si(001) for these two domains was found to be [-110] Gd_2O_3(110)//[110] Si(001) and [100] Gd_2O_3(110)//[110] Si(001). Even though first transistor based on this system have been presented in 2006[81] and some good electrical properties results have been obtained[82], it is found that such bi-domain structure significantly increases the leakage current compared to single domain epi-Gd_2O_3 layers[83]. Better results are obtained for Gd_2O_3 on Si (111) with a mono-domain pseudomorphic growth[76,84]. Osten group has studied the impact of oxygen supply[85], interface[86], top electrode[87] and post deposition

annealing[88] on the structural and electrical properties of the Gd_2O_3/Si system. Due to the highly perfect crystallinity of Gd_2O_3 on Si(111) and its potential application to the realization of Si nanostructures embedded in oxide[89], Gd_2O_3/Si(111) attracts a wide range of basic studies.

I.3.2) Strontium titanate and perovskite functional oxides on Silicon

One of the main difficulties for the monolithic growth of crystalline oxides on silicon is related to the contradiction between providing sufficient oxidants to form the desired phase of the oxide while avoiding the formation of amorphous silica or silicate at interface. R. A. McKee *et al.* suggested for the first time the possibility of growing a perovskite $BaTiO_3$ on Si by investigating the heterostructure $BaTiO_3$/BaO/$BaSi_2$/Si(001)[90], the $BaSi_2$ reconstruction acting as a "passivation layer" to avoid the formation of SiO_2 at the oxide/Si interface. This group has also achieved the first epitaxy a crystalline and commensurate STO film on Si, by employing a silicide ($SrSi_2$) layer to prevent the formation of amorphous interfacial SiO_2 layer[91,92]. Since then, several group such as PennState Univ., Motolora, IBM Zurich, and INL have investigated the $SrTiO_3$/Si(001) system. In order to prevent the oxidation of the silicon surface, particularly at the initial nucleation stage, an interface layer of alkaline earth oxide ($Ba_{0.72}Sr_{0.28}O$ or SrO) is indispensable before the deposition of perovskites. The group of PennState have systematically studied the transition from alkaline oxide (Ba,Sr)O or SrO to perovskite structure[93] and it is pointed out that SrO is the best choice as a buffer layer to obtain the best lattice matched perovskite layer due a topotactic reaction during the transformation. Whereas $Ba_{0.72}Sr_{0.28}O$ represents the best solid solution mixture to create best lattice matched alkaline oxide on silicon. In essence the realization of the SrO template comprises two step: 1) coverage of the Si surface by Sr and 2) oxidation of the Sr to form a SrO template. Motorola extensively studied the Sr/Ba coverage on silicon[94,95,96] and developed a Sr mediated deoxidation method to clean and passivate Si surface, which becomes the standard procedure to overcome the thermodynamic instability between STO and Si. Theoretical works pointed out that a Sr-rich layer would help the epitaxial growth of STO and improve the electronic properties of the interface[97,98,99,100,101]

Using such SrO templates, 2D monocrystalline STO layers can be grown on Si, on condition that a number of growth conditions are used: 1) the STO growth temperature must be sufficiently high to ensure a crystalline growth, while avoiding the oxidation of silicon by

the oxidant; 2) the oxygen partial pressure must be sufficiently high to ensure a complete oxidization of the metals while avoiding oxidization of silicon. Many reports of the epitaxy of STO on Si fall into a regime of high temperature and excess oxygen leading to an amorphous SiO_2 layer[102,103]. Different strategies are identified to meet the paradoxical requirements at the same time. X. Hu *et al.*[104] studied the influence of growth temperature to the interface under a low oxygen partial pressure ($10^{-8} \sim 10^{-7}$ Torr range). H. Li *et al.*[94,105,106] developed a stepped growth method in which an amorphous 1~3 monolayer(ML) STO layer was initially deposited at low temperature and under low oxygen partial pressure then recrystallized at high temperature without oxygen. By repeating this process until 5~10ML STO, the growth continued at high temperature and high oxygen partial pressure.

Codeposition and layer-by-layer deposition methods were also compared [92,107,108]. Since Sr and Ti have different oxidation behaviors (Figure I. 20) and it is found that presence of Sr promotes titanium oxidation[101], the codeposition method is better for the full oxidation of STO under the same growth condition. IBM Zurich reported the epitaxy of STO on Si with an abrupt interface using (Ba,Sr)O template, in which the influence of the oxygen partial pressure at the early stage of the growth was investigated[109,110]. Due to the critical role of the STO/Si heterointerface to achieve a perfect epitaxial STO layer on silicon, it is intensively studied both experimentally[105,111,112,113,114,115] and theoretically[116,117,118]. Once a coherent STO/Si interface is obtained, the strain relaxation of the grown STO film becomes another research focus[119,120].
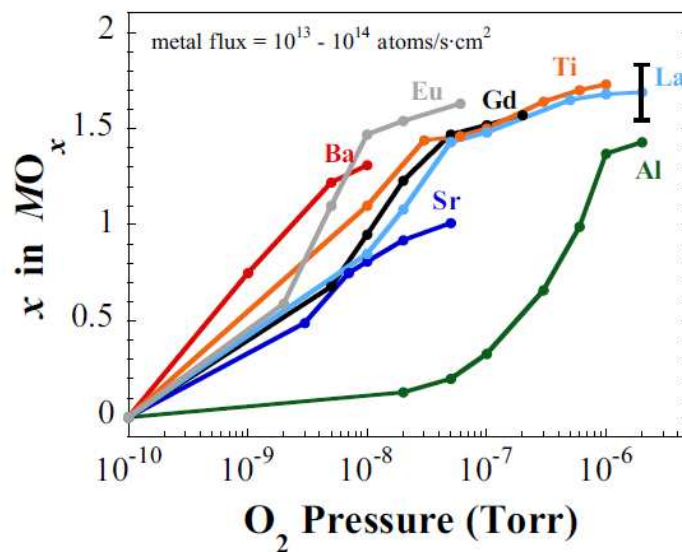
Figure I. 20 Composite graph showing the oxidation behavior of different metal species.

Since lots of high quality perovskite oxides films can be obtained on STO bulk substrate,

the STO/Si(001) heterostructure appears ideally suitable for the integration of functional perovskite oxides on Si. Barium Titanate ($BaTiO_3$, BTO) is widely studied as a typical piezo-(ferro-)electric material and the BTO/Si(001) system was realized by different deposition methods such as Molecular Beam Epitaxy[94,121,122,123], Pulse Laser Deposition[124] and Radio Frequency Sputtering[125,126]. Because there has been a significant efforts on the epitaxial growth of BTO on STO substrate[127,128,129,130], the experience could be easily transplanted to the BTO/STO/Si system. Lead zirconate titanate ($Pb(Zr,Ti)O_3$, PZT), which is a solid solution of $PbZrO_3$ and $PbTiO_3$, is the most commonly used piezoelectric material for various sensors and actuators[131]. T. Maruyama *et al.* has attempted to grow PZT layer on silicon with the heterostructure $SrRuO_3$/$BaTiO_3$/ZrO_2/Si by a reactive evaporation method[132]. Some groups reported epitaxial growth of PZT on STO/Si template using off-axis radio-frequency magnetron sputtering method[133,134]. Lead magnesium niobate with lead titanate ($Pb(Mg_{1/3}Nb_{2/3})O_3$-$PbTiO_3$, PMN-PT) belongs to relaxor ferroelectrics which have been considered as the next generation piezoelectric material recent years. Between PMN-PT 70/30 and PMN-PT 65/35 compositions, there exists a morphotropic phase boundary (MPB) of the system, and compositions near the MPB exhibit excellent dielectric and piezoelectric properties, which make them suitable for micro-sensor and micro-actuator applications[135]. They exhibit very high-dielectric permittivity[136] and a large piezoelectric response[137] when correctly biased. Some attempts have been performed to deposit PMN-PT on $SrTiO_3$ or $SrRuO_3$ substrate[134, 138]. Lanthanum Strontium Manganate ((La,Sr)MnO_3, LSMO) has broad potential magnetic application on magnetic memories, magnetic-field sensors, hard disk read heads, infrared devices, and micro-wave active components due to its CMR effect. Furthermore, owing to its high electrical conductivity and lattice matching with other isotype perovskite materials such as PZT and BTO, it can be used as bottom electrode in ferroelectric heterostructures. Direct deposition of LSMO on silicon is difficult. Thus various buffer layers such as $YBa_2Cu_3O_7$/YSZ [139] (Yttria-Stabilised-Zirconia), BTO/CeO_2/YSZ [140, 141, 142], STO/CeO_2/YSZ[143], BTO/YSZ[144] have been introduced to realized the integration of LSMO and Si. However, considering the accommodation of both lattice and thermal expansion coefficient mismatches of those complex stacks, the STO/Si template is a better choice and only very a few works have been reported on LSMO/STO/Si heterostructure[145,146].

I.3.3) Germanium on oxides/Si templates

The success of epitaxy of high quality crystalline oxides on silicon opens a new way to

integrate semiconductors on Si. For instance, Osten group succeeded in growing $Si/Gd_2O_3/Si$ nanostructures[87,147,148]. Several oxides/Si systems such as $SrHfO_3/Si$ (001)[149], PrO_2/Si (111)[150], $SrTiO_3/Si$ (001)[151,152,153], $(La_xY_{1-x})_2O_3/Si(111)$[154] and Gd_2O_3/Si (111)[155] have been reported to be used as a template to integrate Ge or III-V semiconductors, as shown in Figure I.21. It is found that Ge (or III-V) grows on oxides initially with a Volmer-Weber 3D growth mode and then coalescence occurs to form a 2D complete film. The elevated lattice mismatch between Ge (or III-V) and oxides is fully accommodated by a network of dislocations, confined at the heterointerface, and formed at the very early stages of the growth. As a consequence, the semiconductor grows with its bulk lattice parameter on the oxide surface and does not contain any threading defect related to any plastic relaxation mechanism[156]. Schroeder *et al.* have extensively studied the $Ge/Pr_2O_3/Si$ (111) system[149]. Simple geometric considerations indicate that two Ge domains should be formed on the Pr_2O_3 (111) surface. They have shown that electrostatic effects at the heterointerface select one of these two domains, leading to a single domain Ge growth[157]. In the end, this group has recently evidenced that microtwins were formed in Ge epilayers grown on Pr_2O_3/Si (111) templates, due to the fact that these layers result from the coalescence of initially three-dimensional Ge islands[158].
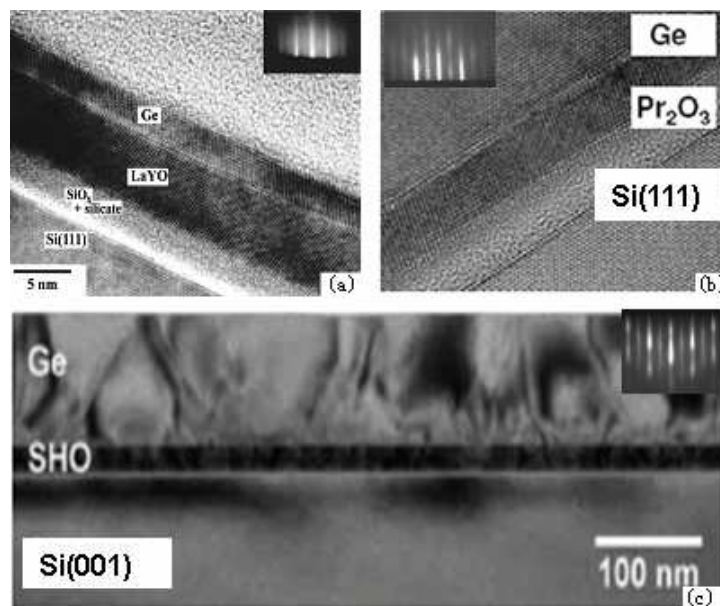
Figure I.21 Integration of Ge on Si using different oxides buffer layers (a)LaYO; (b)Pr_2O_3; (c)$SrHfO_3$.

I.3.3) State of art and strategy at INL

For several years, INL has explored the integration of oxides on silicon and has acquired high international level expertise in this domain. The key technology of epitaxy of different oxides on silicon has been mastered: SrO, Al_2O_3, Gd_2O_3, $LaAlO_3$, $LaAlO_3/Al_2O_3/Si$,

LaAlO$_3$/SrTiO$_3$/Si, Gd$_2$O$_3$/Al$_2$O$_3$/Si.[24,159,160,161] The system (Sr,Ba)TiO$_3$/Si is studied but need further developing to obtain a perfect crystalline "substrate-like" STO on Si with a commensurate registry.

In a short-term view, the objectives of epitaxial growth oxides on silicon could be summarized as follows:

(1) To identify a suitable alternative high-k dielectric for future 22nm and sub-22nm CMOS technology;

(2) Integration of diverse functional oxides on Si by using crystalline oxides/Si templates to meet the demand of future "Heterogeneous integration" technology;

(3) Integration Ge and III-V semiconductors (including 2D layer and new structures such as nanowire) on Si with crystalline oxides buffer layers.

In a long-term view, based on the realized heterostructures, we can not only foresee the possibility of fabricating various functional devices or high mobility CMOS, but also of a monolithic integration on silicon, as shown in Figure I.22
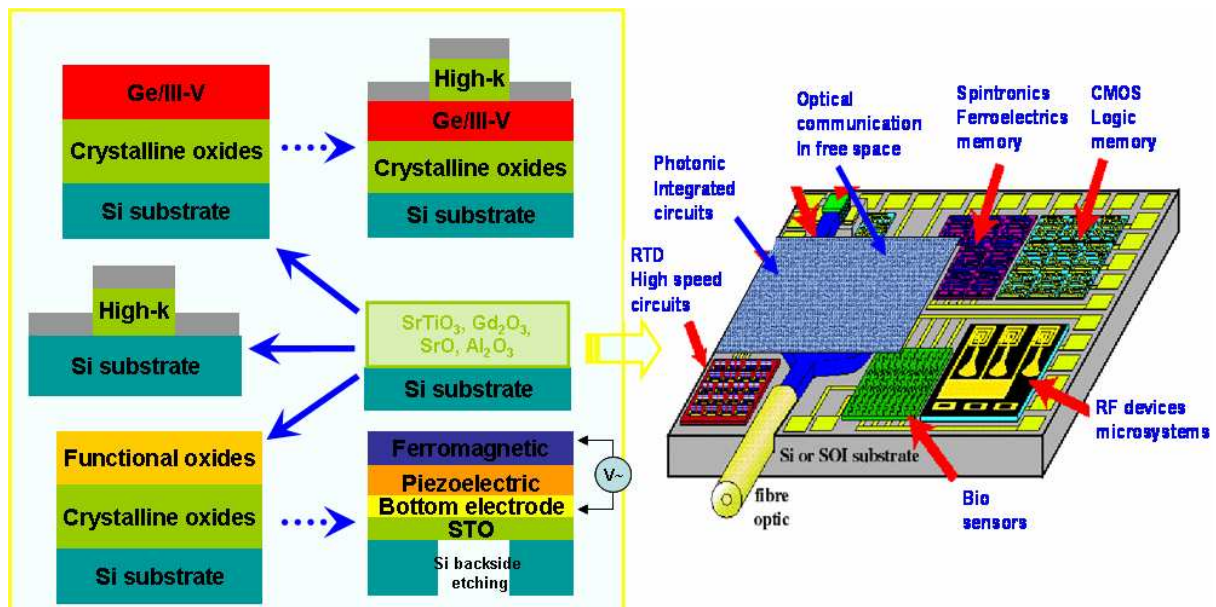
Figure I. 22 Strategy and perspectives of monolithic integration in INL

I.4) Motivations and goals of this thesis

As stated in I.1), this thesis is in the context of "More Moore", "More than Moore" and "Heterogeneous Integration". The objectives can be classified as follows:

(1) The investigation of Gd$_2$O$_3$/Si system as a dielectric alternative for future sub-22nm CMOS. The study will focus on the impact of different growth or post deposition

conditions such as oxidant type, growth temperature and annealing to its electrical properties.

(2) Development of fundamental issues related to the epitaxy of STO on Si using Molecular Beam Epitaxy. The interface structure, crystallographic quality and surface morphology will all be considered to find a optimize growth strategy which leads to a "substrate-like" STO film on Si.

(3) Exploration of integration of diverse functionalities on silicon. Attention will be paid on the integration of dielectric, piezoelectric, ferroelectric, ferromagnetic materials and germanium on Si using STO or Gd_2O_3 as buffer layers. A number of epitaxy related issues will be investigated and their properties characteristics will also be demonstrated.

I.5) Reference

[1] G. E. Moore, "*Cramming more components onto integrated circuits*", Electron. **38**, 8, (1965)

[2] http://www.cordis.lu/ist/eniac

[3] M. Houssa, in *High-k Dielectrics*, M. Houssa, editor, p3-13, Institute of Physics Publishing, Bristol, (2004)

[4] G. D. Wilk, R. M. Wallace and J. M. Anthony, "*High-k gate dielectrics: Current status and materials properties considerations*" Applied Physics Reviews, **89**, 5243 (2001)

[5] Y. C. Yeo, T. J. King, C. Hu, "*Direct tunneling leakage current and scalability of alternative gate dielectrics*" Appl. Phys. Lett. **81**, 11, 2091 (2002)

[6] Y. Hwang, K. Heo, C. H. Chang, M. K. Joo and M. Ree, "*Synchrotron X-ray reflectivity study of high dielectric constant alumina thin films prepared by atomic layer deposition*", Thin Solid Films **510**, 159 (2006)

[7] H. Wu, Y. Zhao, M.H. White, "*Quantum mechanical modeling of MOSFET gate leakage for high-k gate dielectrics*", Solid-State Electronics **50**, 1164 (2006)

[8] R. C. Neville, B. Hoeneisen and C. A. Mead, "*Permittivity of strontium titanate*", J. Appl. Phys. **43**, 2124 (1972)

[9] M. Zgonik, P. Bernasconi, M. Duelli, R. Schlesser, P. Gunter, M. H. Garrett, D, Rytz, Y. Zhu and X. Wu, "*Dielectric, elastic, piezoelectric, electro-optic, and elasto-optic tensors of BaTiO₃ crystals*", Phys. Rev. B **50**, 5941 (1994)

[10] J. Robertson and C. W. Chen, "*Schottky barrier heights of tantalum oxide, barium*

strontium titanate, lead titanate, and strontium bismuth tantalate" Appl. Phys. Lett. **74**, 1168 (1999)

[11] J. Robertson, "*Band offsets of wide-band-gap oxides and implications for future electronic devices*", J. Vac. Sci. Technol. B **18,** 1785 (2000)

[12] H. Hubbard, D.G. Schlom, "*Thermodynamic stability of binary oxides in contact with silicon*", J. Mater. Res. **11**, 11, 2757 (1996)

[13] D.G. Schlom, J.H. Haeni, "*A thermodynamic approach to selecting alternative gate dielectrics*", MRS Bulletin **27**, 3, 198 (2002)

[14] A. Kumar, D. Rajdev, and D. L. Douglass, "*Effect of Oxide Defect Structure on the Electrical Properties of ZrO$_2$*", J. Am. Chem. Soc. **55**, 439 (1972)

[15] J.P. Locquet, C. Marchiori, M. Sousa, J. Fompeyrine, J.W. Seo, "*High-K dielectrics for the gate stack*", J. Appl. Phys. **100**, 051610 (2006)

[16] M. Houssa, V. V. Afanas'ev, A. Stesmans, and M. M. Heyns, "*Variation in the fixed charge density of SiO$_x$/ZrO$_2$ gate dielectric stacks during postdeposition oxidation*", Appl. Phys. Lett. **77**, 1885 (2000).

[17] J. Robertson, "*High dielectric constant oxides*" J. Appl. Phys. **28**, 265 (2004)

[18] H. J. Osten, A. Laha, M. Czernohorsky, E. Bugiel, R. Dargis and A. Fissel, "*Introducing crystalline rare-earth oxides into Si technologies*", Phys. Status Solidi, **205**, 695 (2008)

[19] J. H. Jun, H. J. Kim, D.J. Choi, "*Effect of hydration on the properties of lanthanum oxide and lanthanum aluminate thin films*", Ceramics International **34**, 957 (2008)

[20] D.P. Norton, "*Synthesis and properties of epitaxial electronic oxide thin-film materials*", Mat. Sci. Eng. R **43**, 139, (2004)

[21] Thesis of C. Merckling, "*Croissance epitaxiale d'oxydes high-k sur silicium pour CMOS avancé: LaAlO$_3$, Gd$_2$O$_3$, and γ - Al$_2$O$_3$*", France, (2007)

[22] C. Merckling, G. Delhaye, M. El-Kazzi, S. Gaillard, Y. Rozier, L. Rapenne, B. Chenevier, O. Marty, G. Saint-Girons, M. Gendry, Y. Robach, G. Hollinger, "Epitaxial growth of LaAlO$_3$ on Si (001) using interface engineering", Microelectron. Reliab. **47**, 540 (2007)

[23] Q. Q. Sun, A. Laha, S. J. Ding, D.W. Zhang, H.J. Osten, A. Fissel, "*Effective Passivation of Intrinsic Dangling Bonds at the Interface of Single Crystalline Gd$_2$O$_3$ and Si(100)*", Appl. Phys. Lett. **92**, 152908, (2008)

[24] A. Laha, H.-J. Osten, and A. Fissel, "*Impact of Si substrate orientations on electrical properties of crystalline Gd$_2$O$_3$ thin films for high-K application*", Appl. Phys. Lett. **89**,

143514 (2006)

[25] R. E. Newnham, "*Electroceramics*", Rep. Prog. Phys. **52**, 123 (1989).

[26] P. M. Warusawithana, C. Cen, C. R. Sleasman, C. J. Woicik, Y. Li, L. F. Kourkoutis, J. A. Klug, H. Li, P. Ryan, L. P. Wang, M. Bedzyk, D. A. Muller, L. Q. Chen, J. Levy and D. G. Schlom, "*A ferroelectric oxide made directly on silicon*", Science, **324**, 367 (2009)

[27] P. J. Curie and P. Curie, "*Development by pressure of polar electricity in hemihedral crystals with inclined faces*", Bull. Soc. Min. de France **3**, 90, (1880).

[28] K. Lefki and G. J. M. Dormans, "*Measurement of piezoelectric coefficients of ferroelectric thin films*", J. Appl. Phys. **76**, 1764 (1994).

[29] Jaffe, Cook, and Jaffe. "*Piezoelectric Ceramics*," Academic Press Inc., London, (1971)

[30] Lines, M. E., and Glass, A. M. "*Principles and Applications of Ferroelectric and Related Materials*", Clarendon Press, Oxford, (1977).

[31] K. Momma and F. Izumi, "*VESTA: a three-dimensional visualization system for electronic and structural analysis*", J. Appl. Crystallogr., **41**, 653 (2008)

[32] F. Jona and G. Shirane, "*Ferroelectric crystals*", Clarendon Press (1962)

[33] D. Damjanovic, "*Ferroelectric, dielectric and piezoelectric properties of ferroelectric thin films and ceramics*", Rep. Progr. Phys. **61**, 1267 (1998)

[34] R. M. Kusters, J. Singleton, D. A. Keen, R. McGreevy, and W. Hayes, "*Magnetoresistance measurements on the magnetic semiconductor $Nd_{0.5}Pb_{0.5}MnO_3$*", Physica B **155**, 362 (1989)

[35] S. Jin, T. Tiefel, M. McCormack, R. Fastnacht, R. Ramesh, and L. Chen, "*Thousandfold Change in Resistivity in Magnetoresistive La-Ca-Mn-O Films*", Science **264**, 413 (1994)

[36] S. F. Yoon, "*III-V/Si integration: potential and outlook for integrated low power micro and nanosystems*" Proceedings of the 2009 international conference on Compilers, architecture, and synthesis for embedded systems, France (2009)

[37] Q.X. Zhao, O. Zsebök, U. SoKdervall, M. Karlsteen, M. Willander, X.Q. Liu, Y.D. Chen, W. Lu, S.C. Shen，"*GaAs film deposited on SrTiO3 substrate by molecular beam epitaxy*"，J. Crys. Growth, **208**, 117 (2000)

[38] K. Eisenbeiser, R. Emrick, R. Droopad, Z. Yu, J. Finder, S. Rockwell, J. Holmes, C. Overgaard, and W. Ooms, "*GaAs MESFETs fabricated on Si substrates using a SrTiO3 buffer layer*", IEEE Electron Device Lett., **23**, 300, (2002)

[39] H. Fujioka, J. Ohta, H. Katada, T. Ikeda, Y. Noguchi and M. Oshima, "*Epitaxial growth of semi- conductors on $SrTiO_3$ substrates*", J. Crys. Growth, **229**, 137 (2001)

[40] G. Saint-Girons, J. Cheng, P. Regreny, L. Largeau, G. Patriarche and G. Hollinger, "*Accommodation at the interface of highly dissimilar semiconductor/oxide epitaxial systems*", Phys. Rev. B **80**, 155308 (2009)

[41] Y. Kamata, "*High-κ / Ge MOSFETs for future nanoelectronics*", Materials Today **11**, 30, (2008)

[42] T. Tezuka; S. Nakaharai, Y. Moriyama, N. Sugiyama and S. Takagi, "*High-mobility strained SiGe-on-insulator pMOSFETs with Ge-rich surface channels fabricated by local condensation technique*" IEEE Electron. Device Lett. **26**, 243 (2005)

[43] M. Heyns, M. Meuris, M. Caymax, "*Ge and III/V as enabling materials for future CMOS technologies*", ECS Transactions **3**, 7, 511, (2006)

[44] A. Dimoulas, M. Houssa, A. Ritemour, J. Fompeyrine, W. Tsai, J.W. Seo, Y. Panayiotatos, P. Tsipas, D.P. Brunco, M. Caymax, J.-P. Locquet, C. Dieker, "*Current challenges in Ge MOS technology*", ECS Transactions **3**, 2, 371, (2006)

[45] Q. Li, Y.-B. Jiang, H. Xu, S. Hersee and S. M. Han, "*Heteroepitaxy of high-quality Ge on Si by nanoscale Ge seeds grown through a thin layer of SiO_2*", Appl. Phys. Lett., **85**, 11, 1928, (2004)

[46] B. Vincent , J. F. Damlencourt , Y. Morand , A. Pouydebasque, C. LeRoyer, L. Clavelier, N. Dechoux, P. Rivallin, T. Nguyen, S. Cristoloveanu, Y. Campidelli, D. Rouchon, M. Mermoux, S. eleonibus, D.Bensahel and T. Billon, "*The Ge condensation technique: A solution for planar SOI/GeOI co-integration for advanced CMOS technologies?*", Mater. Sci. Semicond. Process. **11**, 205, (2008)

[47] T. Akatsu, C. Deguet, L. Sanchez, F. Allibert, D. Rouchon, T. Signamarcheix, C. Richtarch, A. Boussagol, V. Loup, F. Mazen, J-M. Hartmann, Y. Campidelli, L. Clavelier, F. Letertre, N. Kernevez and C. Mazure, "*Germanium-on-insulator (GeOI) substrates-A novel engineered substrate for future high performance devices*", Mater. Sci. Semicond. Process. **9**, 444, (2006)

[48] Z. Zhao, K. Yadavalli, Z. Hao and K. Wang, "*Direct integration of III–V compound semiconductor nanostructures on silicon by selective epitaxy*", Nanotech. **20**, 035304 (2009)

[49] M.K. Hudait, G. Dewey, S. Datta, J.M. Fastenau, J. Kavalieros, W.K. Liu, D. Lubyshev, R. Pillarisetty, W. Rachmady, M. Radosavljevic, T. Rakshit, R. Chau, "*Heterogeneous Integration of Enhancement Mode In0.7Ga0.3As Quantum Well Transistor on Silicon Substrate using Thin (<2 μm) Composite Buffer Architecture for High-Speed and Low-voltage (0.5V) Logic Applications*", IEEE, IEDM, 625, (2007)

[50] V. K. Yang, M. E. Groenert, G. Taraschi, C. W. Leitz, A. J. Pitera, M. T. Currie, Z. Cheng, E. A. Fitzgerald, "*Monolithic integration of III-V optical interconnects on Si using SiGe virtual substrates*", J. Mater. Sci. Mater. Electron. **13**, 377 (2002)

[51] M. E. Groenert, C. W. Leitz, A. J. Pitera, V. Yang, H. Lee, R. J. Ram and E. A. Fitzgerald, "*Monolithic integration of room-temperature cw GaAs/AlGaAs lasers on Si substrates via relaxed graded GeSi buffer layers*", J. Appl. Phys. **93**, 362 (2003)

[52] H. Tanoto, S. F. Yoon, W. K. Loke, E. A. Fitzgerald, C. Dohrman, B. Narayanan, *et al.* "*Growth of GaAs on vicinal Ge surface using low-temperature migration-enhanced epitaxy*", J. Vac. Sci. Technol. B **24**, 152, (2006)

[53] C. L. Andre, J. A. Carlin, J. J. Boeckl, D. M.Wilt, M.A. Smith, A. J. Pitera, M. L. Lee, E. A. Fitzgerald, S. A.Ringel, "*Investigations of high-performance GaAs solar cells grown on Ge-Si$_{1-x}$Ge$_x$-Si substrates*", IEEE Trans. Electron. Devices, **52**, 1055 (2005)

[54] E. P. Gusev, H. Shang, M. Copel, M. Grilbeyuk, C. D'Emic, P. Kozlowski, T. Zabel, "*Microstructure and thermal stability of HfO$_2$ gate dielectric deposited on Ge(100)*", App. Phys. Lett., **85**, 2334, (2004)

[55] C. O. Chui, S. Ramanathan, B. B. Triplet, P. C. McIntyre, K. C. Saraswat, "*Ge MOS capacitors incorporating ultrathin High-K gate dielectric*", IEEE Elec. Dev. Lett., **23**, 473, (2002)

[56] S. Iwauchi, T. Tanaka, "*Interface properties of Al$_2$O$_3$-Ge structure and characteristics of Al$_2$O$_3$-Ge MOS transistors*", Jpn. J. Appl. Phys., **10**, 260, (1971)

[57] D. S. Yu, K. C. Chiang, C. F. Cheng, A. Chin, C. Zhu, M. F. Li, D-L. Kwong, "*Fully silicided NiSi:Hf-LaAlO$_3$/SC-GOI n-MOSFETs with high electron mobility*", IEEE Elec. Dev. Lett., **25**, 559, (2004)

[58] T. Maeda, M. Nishizawa, Y. Morita, "*Role of germanium nitride interfacial layers in HfO$_2$/ germanium nitride/germanium metal-insulator-semiconductor structures*", Appl. Phys. Lett., **90**, 072911, (2007)

[59] Y. Oshima, M. Shandalov, Y. Sun, P. Pianetta, P. C. McIntyre, "*Hafnium oxide/germanium oxynitride gate stacks on germanium: capacitance scaling and interface state denstity*", Appl. Phys. Lett., **94**, 183102, (2009)

[60] N. Taoka, M. Harada, Y. Yamashita, T. Yamamoto, N. Sugiyama, Shin-ichi Takagi, "*Effects of Si passivation on Ge metal-insulator-semiconductor interface properties and inversion hole mobility*", Appl. Phys. Lett. **92**, 113511, (2008)

[61] M. M. Frank, S. J. Koester, M. Copel, J. A. Ott, V. K. Paruchuri, H. Shang, "*Hafnium oxide gate dielectrics on sulfur-passivated germanium*", Appl. Phys. Lett., **89**, 112905, (2006)

[62] R. Xie, W. He, M. Yu, and C. Zhu, "*Effects of fluorine incorporation and forming gas annealing on high-k gated germanium metal–oxide–semiconductor with GeO$_2$ surface passivation*", Appl. Phys. Lett., 93, 073504, (2008)

63 D. Kuzum, T. Krishnamohan, A.J. Pethe, A.K. Okyay, Y. Oshima, S. Yun J.P. McVittie, P.A. Pianetta, P.C. McIntyre, K.C. Saraswat, "*Ge-Interface Engineering With Ozone Oxidation for Low Interface-State Density*", IEEE Elec. Dev. Lett. **4**, 328, (2008)

[64] S. A. Chambers, Y. Liang, Z. Yu, R. Droopad, and J. Ramdani, "*Band offset and structure of SrTiO$_3$/Si(001) heterojunctions*"J. Vac. Sci. Technol. A, **19**, 934 (2001).

[65] M. Czernohorsky, E. Bugiel, H. J. Osten, A. Fissel and O. Kirfel, "*Impact of oxygen supply during growth on the electrical properties of crystalline Gd$_2$O$_3$ thin films on Si(001)*", Appl. Phys. Lett. **88**, 152905 (2006)

[66] D. Landheer, J. A. Gupta, G. I. Sproule, J. P. McCaffrey, M. J. Graham, K.-C. Yang, Z. -H. Lu, and W. N. Lennard, "*Characterization of Gd$_2$O$_3$ films deposited on Si(100) by Electron Beam Evaporation*", J. Electrochem. Soc. **148**, G29 (2001)

[67] S. Schamm, P.-E.Coulon, S. Miao, S. N. Volkos, L. H. Lu, L. Lamagna, C. Wiemer, D. Tsoutsou, G. Scarel, and M. Fanciulli, "*ALD-Grown Rare Earth Oxides for Advanced Gate Stacks*", ECS Trans. **13**, 77 (2008)

[68] K. Tachi, H. Iwai, T. Hattori, N. Sugii, K. Tsutsui, P. Ahemt, and K. Kakushima, "*Effect of Oxygen for Ultra-Thin La2O3 Film Deposition*", ECS Trans. **3**, 425 (2006)

[69] M. H. Cho, D. H. Ko, Y. K. Choi, I. W. Lyo, K. Jeong, T. G. Kim, J. H. Song, and C. N. Whang, "*Structural characteristics of Y$_2$O$_3$ films grown on oxidized Si(111) surface*",J. Appl. Phys. **89**, 1647 (2001)

[70] M. E. Hunter, M. J. Reed, N. A. El-Masry, J. C. Roberts, and S. M. Bedair, "*Epitaxial Y$_2$O$_3$ films grown on Si(111). by pulsed-laser ablation*", Appl. Phys. Lett. **76**, 1935 (2000)

[71] T. Watahiki, B. P. Tinkham, B. Jenichen, R. Shayduk, W. Braun, K. H. Ploog, "*Praseodymium silicide formation at the Pr$_2$O$_3$/Si interface*", Appl. Surf. Sci. **255,** 758 (2008)

[72] T. Schroeder, T.-L. Lee, L. Libralesso, I. Joumard, and J. Zegenhagen, P. Zaumseil, C. Wenger, G. Lupina, G. Lippert, J. Dabrowski, and H.-J. Müssig, "*Structure and strain relaxation mechanisms of ultrathin epitaxial Pr$_2$O$_3$ films on Si(111)*", J. Appl. Phys. **97**, 074906 (2005)

[73] C. G. Kim, "*Initial growth analysis of Si overlayers on cerium oxide layers* " J. Vac. Sci. Technol. B, **18,** 2650 (2000)

[74] J. T. Jones, E. T. Croke, C. M. Garland, O. J. Marsh, and T. C. McGill, "*Epitaxial silicon grown on CeO₂/Si(111). structure by molecular beam epitaxy*", J. Vac. Sci. Technol. B **16**, 2686 (1998)

[75] Y. Zhao, K. Kita, K. Kyuno and A. Toriumi, "*Mechanisms of and Solutions to Moisture Absorption of Lanthanum Oxide as High-k Gate Dielectric*", ECS Trans. **6**, 141 (2007)

[76] S. Jeon and H. Hwang, "*Effect of hygroscopic nature on the electrical characteristics of lanthanide oxides (Pr_2O_3, Sm_2O_3, Gd_2O_3 , and Dy_2O_3)*", J. Appl. Phys., **93**, 6393 (2003)

[77] J. Kwo, M. Hong, A. R. Kortan, K. T. Queeney, Y. J. Chabal, J. P. Mannaerts, T. Boone, J. J. Krajewski, A. M. Sergent, and J. M. Rosamilia, "*High ε gate dielectrics Gd_2O_3 and Y_2O_3 for silicon*", Appl. Phys. Lett. **77**, 130, (2000)

[78] J. Kwo, M. Hong, A. R. Kortan, K. L. Queeney, Y. J. Chabal, R. L. Opila, Jr., D. A. Muller, S. N. G. Chu, B. J. Sapjeta, T. S. Lay, J. P. Mannaerts, T. Boone, H. W. Krautter, J. J. Krajewski, A. M. Sergnt, and J. M. Rosamilia, "*Properties of high-k gate dielectrics Gd_2O_3 and Y_2O_3 for Si*", J. Appl. Phys. **89**, 3920, (2001)

[79] H. -J. Osten , E. Bugiel and A. Fissel,"*Epitaxial praseodymium oxide: a new high-K dielectric*", Solid-State Electron. **47**, 2161, (2003)

[80] E. Bugiel, A. Fissel, M. Czernohorsky, A. Laha, and H. -J. Osten, "*Integration of Functional Epitaxial Oxides into Silicon: A TEM Investigation*", Microsc. Microanal. **13** (Suppl 3), 304, (2007)

[81] H. D. B. Gottlob, T. Echtermeyer, T. Mollenhauer, J. K. Efavi, M. Schmidt, T. Wahlbrink, M. D. Lemme, H. Kurz, M. Czernohorsky, E. Bugiel, H.-J. Osten and A. Fissel, "*CMOS integration of epitaxial Gd_2O_3 high-k gate dielectrics*", Solid-State Electron. **50**, 979 (2006)

[82] A. Laha, E. Bugiel, H.J. Osten and A. Fissel, "*Crystalline ternary rare earth oxide with capacitance equivalent thickness below 1 nm for high-k application*", Appl. Phys. Lett. **88**, 172107 (2006)

[83] A.Laha, E. Bugiel, J. X. Wang, Q. Q. Sun, A. Fissel, and H. -J. Osten, "*Effect of domain boundaries on the electrical properties of crystalline Gd_2O_3 thin fims*", Appl. Phys. Lett. **93**, 182907 (2008)

[84] J. X. Wang, A. Laha, A. Fissel, D. Schwendt1, R. Dargis, T. Watahiki, R. Shayduk, W.Braun, T. M. Liu and H. -J. Osten, "*Crystal structure and strain state of molecular beam*

epitaxial grown Gd₂O₃ on Si(111) substrates: a diffraction study", Semicond. Sci. Technol. **24**, 045021 (2009)

[85] M. Czernohorsky, E. Bugiel, H. -J. Osten, A. Fissel and O. Kirfel, "*Impact of oxygen supply during growth on the electrical properties of crystalline Gd₂O₃ thin films on Si(001)*", Appl. Phys. Lett. **88**, 152905 (2006)

[86] A. Laha, A. Fissel, H. J. Osten, "*Engineering the interface between epitaxial lanthanide oxide thin films and Si substrates: a route towards tuning the electrical properties*", Microelectron. Eng. **84**, 2282 (2007)

[87] Q.Q. Sun, A. Laha, S. J. Ding, D. W. Zhang, H. J. Osten, and A. Fissel, "*Effective passivation of slow interface states at the interface of single crystalline Gd₂O₃ and Si(100)*", Appl. Phys. Lett. **92**, 152908 (2008)

[88] M. Czernohorsky, D. Tetzlaff, E. Bugiel, R. Dargis, H. -J. Osten, H. D. B. Gottlob, M. Schmidt, M. C. Lemme and H. Kurz, "*Stability of crystalline Gd₂O₃ thin films on silicon during rapid thermal annealing*", Semicond. Sci. Technol. **23**, 035010 (2008)

[89] A. Laha, E. Bugiel, A. Fissel and H -J. Osten, "*Si-nanoclusters embedded into epitaxial rare earth oxides: Potential candidate for nonvolatile memory applications*", Microelectron. Eng. **85**, 2350 (2008)

[90] R. A. McKee, F. J. Walker, J. R. Conner, E. D. Specht and D. E. Zelmon, "*Molecular beam epitaxy growth of epitaxial barium silicide, barium oxide and barium titanate on silicon*", Appl. Phys. Lett. **59**, 782 (1991)

[91] R. A. McKee, F. J. Walker, and M. F. Chisholm, "*Crystalline Oxides on Silicon: The First Five Monolayers*", Phys. Rev. Lett. **81**, 3014 (1998)

[92] R. A. McKee, F. J. Walker and M. F. Chisholm, "*Physical structure and inversion charge at a semiconductor interface with crystalline oxide*", Science, **293**, 468 (2001)

[93] J. Lettieri, thesis, "*Critical issues of complex epitaxial oxide growth and integration with silicon by molecular beam epitaxy*", The Pennsylvania State University, (2002)

[94] Y. Wei, X. Hu, Y. Liang, D. C. Jordan, B. Craigo, R. Droopad, Z. Yu, A. Demkov, J. L. Edwards, Jr., and W. J. Ooms, "*Mechanism of cleaning Si(100) surface using Sr or SrO for the growth of crystalline SrTiO₃ films*", J. Vac. Sci. Technol. B **20**(4), 1402 (2002)

[95] Z. Yu, Y. Liang, C. Overgaard, X. Hu, J. Curless, H. Li, Y. Wei, B. Craigo, D. Jordan, R. Droopad, J. Finder, K. Eisenbeiser, D. Marshall, K. Moore, J. Kulik and P. Fejes, "*Advances in heteroepitaxy of oxides on silicon*", Thin Solid Films, **462–463**, 51 (2004)

[96] X. Hu, Z. Yu, J. A. Curless, R. Droopad, K. Eisenbeiser, J. L. Edwards Jr., W. J. Ooms and D. Sarid, "*Comparative study of Sr and Ba adsorption on Si(100)*", Appl. Surf. Sci., **181**, 103 (2001)

[97] P. W. Peacock and J. Robertson, "Structure, bonding, and band offsets of (100)SrTiO₃–silicon interfaces", Appl. Phys. Lett. **83**, 5497 (2003)

[98] C. J. Först, C. R. Ashman, K. Schwarz and P. E. Blöchl, "The interface between silicon and a high-k oxide", Nature **427**, 53 (2004)

[99] I. N. Yakovkin and M. Gutowski, "*SrTiO₃/Si(001) epitaxial interface: A density functional theory study*", Phys. Rev. B, **70**, 165319 (2004)

[100] X. Zhang and A.A. Demkov, "*A theoretical study of Sr-induced reconstructions of the Si (001) surface*", J. Appl. Phys. **103**, 103710 (2008).

[101] J.W. Reiner, K. F. Garrity, F. J. Walker, S. Ismail-Beigi, and C. H. Ahn, "*Role of strontium in oxide epitaxy on silicon (001)*", Phys. Rev. Lett. **101**, 105503 (2008)

[102] Z. Yu, J. Ramdani, J. A. Curless, C. D. Overgaard, J. M. Finder, R. Droopad, K. W. Eisenbeiser, J. A. Hallmark and W. J. Ooms, "*Epitaxial oxide thin films on Si(001)*", J. Vac. Sci. Technol. B **18**(4), 2134 (2000)

[103] K. Eisenbeiser, J. M. Finder, Z. Yu, J. Ramdani, J. A. Curless, J. A. Hallmark, R. Droopad, W. J. Ooms, L. Salem, S. Bradshaw, and C. D. Overgaard, "*Field effect transistors with SrTiO₃ gate dielectric on Si*", Appl. Phys. Lett. **76**, 1324 (2000)

[104] X. Hu, H. Li, Y. Liang, Y. Wei, Z. Yu, D. Marshall, J. Edwards, Jr., R. Droopad, X. Zhang, A. A. Demkov, K. Moore and J. Kulik, "*The interface of epitaxial SrTiO₃ on silicon: in situ and ex situ studies*", Appl. Phys. Lett., **82**, 203 (2003)

[105] H. Li, X. Hu, Y. Wei, Z. Yu, X. Zhang, R. Droopad, A. A. Demkov, J. Edwards, Jr., K. Moore, W. Ooms, J. Kulik and P. Fejes, "*Two-dimensional growth of high-quality strontium titanate thin films on Si*", J. Appl. Phys. **93**, 4521 (2003)

[106] X. Zhang, A. A. Demkov, Hao Li, X. Hu, Yi Wei and J. Kulik, "*Atomic and electronic structure of the Si/SrTiO₃ interface*", Phys. Rev. B. **68**, 125323 (2003)

[107] Y. Liang, Y. Wei, X. M. Hu, Z. Yu, R. Droopad, H. Li, and K. Moore, "*Heteroepitaxy of SrTiO₃ on vicinal Si(001): Growth and kinetic effects*", J. Appl. Phys. **96**, 3413 (2004)

[108] G. Delhaye, C. Merckling, M. El-Kazzi, G. Saint-Girons, M. Gendry, Y. Robach, and G. Hollinger, "*Structural properties of epitaxial SrTiO₃ thin films grown by molecular beam epitaxy on Si(001)*", J. Appl. Phys. **100**, 124109 (2006)

[109] G. J. Norga, C. Marchiori, A. Guiller, J. P. Locquet, Ch. Rossel, H. Siegwart, D. Caimi, J. Fompeyrine and T. Conard, "*Phase of reflection high-energy electron diffraction oscillations during (Ba,Sr)O epitaxy on Si(100): A marker of Sr barrier integrity*", Appl. Phys. Lett. **87**, 262905 (2005)

[110] G. J. Norga, C. Marchiori, C. Rossel, A. Guiller, J. P. Locquet, H. Siegwart, D. Caimi, and J. Fompeyrine, J. W. Seo and Ch. Dieker, "*Solid phase epitaxy of SrTiO3 on (Ba,Sr)O/Si(100): The relationship between oxygen stoichiometry and interface stability*", J. Appl. Phys. **99**, 084102 (2006)

[111] V. Shutthanandan, S. Thevuthasan, Y. Liang, E. M. Adams, Z. Yu and R. Droopad, "*Direct observation of atomic disordering at the SrTiO₃/Si interface due to oxygen diffusion*", Appl. Phys. Lett. **80**, 1803 (2002)

[112] G. Delhaye, M. El Kazzi, M. Gendry, G. Hollinger, Y. Robach, "*Hetero-epitaxy of SrTiO3 on Si and control of the interface*", Thin Solid Films **515,** p6332 (2007)

[113] J. Q. He, S. Regnery, C. L. Jia, Y. L. Qin, F. Fitsilis, P. Ehrhart, R. Waser, K. Urban and R. H. Wang, "*Interfacial and microstructural properties of SrTiO₃ thin films grown on Si(001) substrates*", J. Appl. Phys. **92**, 7200 (2002)

[114] J. H. Hao, J. Gao, Z. Wang and D. P. Yu, "*Interface structure and phase of epitaxial SrTiO3(110) thin films grown directly on silicon*", Appl. Phys. Lett. **87**, 131908 (2005)

[115] L. V. Goncharova, D. G. Starodub, E. Garfunkel, T. Gustafsson, V. Vaithyanathan, J. Lettieri, and D. G. Schlom, "*Interface structure and thermal stability of epitaxial SrTiO₃ thin films on Si(001)*", J. Appl. Phys. **100**, 014912 (2006)

[116] S. B. Mi, C. L. Jia, V. Vaithyanathan, L. Houben, J. Schubert, D. G. Schlom, and K. Urban, "*Atomic structure of the interface between SrTiO₃ thin films and Si(001) substrates*", Appl. Phys. Lett. **93**, 101913 (2008)

[117] L. Fitting Kourkoutis, C. Stephen Hellberg, V. Vaithyanathan,3 Hao Li, M. K. Parker, K. E. Andersen, D. G. Schlom, and D. A. Muller, "*Imaging the Phase Separation in Atomically Thin Buried SrTiO3 Layers by Electron Channeling*", Phys. Rev. Lett. **100**, 036101 (2008)

[118] X. F. Wang, J.Wang, Q. Li, M. S. Moreno, X. Y. Zhou, J. Y. Dai, Y. Wang and D. Tang, "*Interfacial structure of epitaxial SrTiO₃ on Si: experiments and simulations*", J. Phys. D: Appl. Phys. **42**, 085409 (2009)

[119] J. C. Woicik, H. Li, P. Zschack, E. Karapetrova, P. Ryan, C. R. Ashman and C. S. Hellberg, "*Anomalous lattice expansion of coherently strained SrTiO₃ thin films grown on*

Si(001) by kinetically controlled sequential deposition", Phys. Rev. B, **73**, 024112 (2006)

[120] F. S. Aguirre-Tostado, A. Herrera-Gómez, J. C. Woicik, R. Droopad, Z. Yu, D. G. Schlom, P. Zschack, E. Karapetrova, P. Pianetta, and C. S. Hellberg, "*Elastic anomaly for SrTiO$_3$ thin films grown on Si(001)*", Phys. Rev. B. **70**, 201403(R) (2004)

[121] F. Amy, A. Wan, A. Kahn, F. J. Walker and R. A. McKee, "*Surface and interface chemical composition of thin epitaxial SrTiO3 and BaTiO3 films: Photoemission investigation*", J. Appl. Phys. **96**, 1601, (2004)

[122] A. R. Meier, F. Niu, B. W. Wessels, "*Integration of BaTiO$_3$ on Si (001) using MgO/STO buffer layers by molecular beam epitaxy*", J. Cryst. Growth, **294**, 401 (2006)

[123] D.G. Schlom, J.H. Haeni , J. Lettieri , C. D. Theis, W. Tian, J.C. Jiang, X.Q. Pan, "*Oxide nano-engineering using MBE*", Mater. Sci. Eng. B **87**, 282 (2001)

[124] M.-B. Lee, M. Kawasaki, M. Yoshimoto, and H. Koinuma, "*Heteroepitaxial growth of BaTiO$_3$ films on Si by pulsed laser deposition*", Appl. Phys. Lett. **66**, 1331 (1995)

[125] L. Qiao and X. Bi, "*Effect of different buffer layers on the microstructure and dielectric properties of BaTiO$_3$ thin films grown on Si substrates*", J. Alloys Compd. **477**, 560 (2009)

[126] L. Qiao, X. Bi, "*Domain configuration and phase transition for BaTiO$_3$ thin films on tensile Si substrates*", J. Cryst. Growth **310**, 5327 (2008)

[127] T. Zhao, F. Chen, H. Lu, G. Yang and Z. Chen, "*Thickness and oxygen pressure dependent structural characteristics of BaTiO$_3$ thin films grown by laser molecular beam epitaxy*", J. Appl. Phys. **87**, 7442 (2000)

[128] G.H. Lee, B.C. Shin, I.S. Kim, "*Critical thickness of BaTiO$_3$ film on SrTiO$_3$ (001) evaluated by reflection high-energy electron diffraction*", Mater. Lett. **50**, 134 (2001)

[129] H. P. Sun, W. Tian, X. Q. Pan, J. H. Haeni and D. G. Schlom, "*Evolution of dislocation arrays in epitaxial BaTiO$_3$ thin films grown on (100) SrTiO$_3$*", Appl. Phys. Lett. **84**, 3298 (2004)

[130] M. Kawai, D. Kan, S. Isojima, H. Kurata, S. Isoda, Y. Shimakawa, S. Kimura and O. Sakata, "*Critical thickness control by deposition rate for epitaxial BaTiO$_3$ thin films grown on SrTiO$_3$(001)*", J. Appl. Phys. **102**, 114311 (2007)

[131] B. Jaffe, W. R. Cook and H. Jaffe, *Piezoelectric Ceramics*, Academic, London (1971)

[132] T. Maruyama, M. Saitoh, I. Sakai, T. Hidaka, Y. Yano and T. Noguchi, "*Growth and characterization of 10-nm-thick c-axis oriented epitaxial PbZr$_{0.25}$Ti$_{0.75}$O$_3$ thin films on (100)Si substrate*", Appl. Phys. Lett. **73**, 3524 (1998)

[133] A. Lin, X. Hong, V. Wood, A. A. Verevkin, C. H. Ahn, R. A. McKee, F. J. Walker, and E. D. Specht, "*Epitaxial growth of Pb(Zr$_{0.2}$Ti$_{0.8}$)O$_3$ on Si and its nanoscale piezoelectric properties*", Appl. Phys. Lett. **78**, 2034 (2001)

[134] D. M. Kim and C. B. Eom, V. Nagarajan J. Ouyang, R. Ramesh, V. Vaithyanathan and D. G. Schlom, "*Thickness dependence of structural and piezoelectric properties of epitaxial Pb(Zr$_{0.52}$Ti$_{0.48}$)O$_3$ films on Si and SrTiO$_3$ substrates*", Appl. Phys. Lett. **88**, 142904 (2006)

[135] R. Herdier, M. Détalle, D. Jenkins, D. Remiens, D. Grébille, R. Bouregba, "*The properties of epitaxial PMNT thin films grown on SrTiO$_3$ substrates*", J. Cryst. Growth, **311**, 123 (2008)

[136] A.W. Tavernor, H.-P.S. Li, R. Stevens, "*Production and characterization of composite relaxor ferroelectric multilayer structures*" J. Eur. Ceram. Soc. **19**, 1859 (1999)

[137] S.-E. Park and T.R. Shrout, "*Ultra high strain and piezoelectric behavior in relaxor based ferroelectric single crystals*", J. Appl. Phys. **82**, 1804 (1997)

[138] J. H. Lee, M. R. Choi, W. Jo, J. Y. Jang, M. Y. Kim, "*Structural properties of 0.65Pb(Mg$_{1/3}$Nb$_{2/3}$)O$_3$–0.35PbTiO$_3$ relaxor ferroelectric thin films on SrRuO$_3$ conducting oxides*", Ultramicroscopy, **108**, 1106 (2008)

[139] W. C. Goh, Kui Yao, C. K. Ong, "*Epitaxial La$_{0.7}$Sr$_{0.3}$MnO$_3$ thin films with two in-plane orientations on silicon substrates with yttria-stabilized zirconia and YBa$_2$Cu$_3$O$_{7-\delta}$ as buffer layers*", J. Appl. Phys. **97**, 073905 (2005)

[140] J.-H. Kim, S. I. Khartsev, and A. M. Grishin, "*Epitaxial colossal magnetoresistive La$_{0.67}$(Sr,Ca)$_{0.33}$MnO$_3$ films on Si*", , Appl. Phys. Lett. **82**, 4295 (2003)

[141] J.-H. Kim, A. M. Grishin, and H. H. Radamson, "*The effect of strained Si$_{1-x}$Ge$_x$ and Si$_{1-y}$C$_y$ layers for La$_{0.75}$Sr$_{0.25}$MnO$_3$ films grown on oxide-buffered Si substrates*" J. Appl. Phys. **99**, 014903 (2006).

[142] J.-H. Kim, A.M. Grishin, H.H. Radamson, "*Properties of La$_{0.75}$Sr$_{0.25}$MnO$_3$ films grown on Si substrate with Si$_{1-x}$Ge$_x$ and Si$_{1-y}$C$_y$ buffer layers*", Thin Solid Films **515**, 411 (2006)

143 J. Fontcuberta, M. Bibes, B. Martínez, V. Trtik, C. Ferrater, F. Sánchez and M. Varela, "*Epitaxial growth of magnetoresistive (00h), (0hh), and (hhh) La$_{2/3}$Sr$_{1/3}$MnO$_3$ thin films on (001)Si substrates*", Appl. Phys. Lett. **74**, 1743 (1999)

[144] Z. Trajanovic, C. Kwon, M. C. Robson, K.-C. Kim, M. Rajeswari, R. Ramesh, T. Venkatesan S. E. Lofland, S. M. Bhagat and D. Fork, "*Growth of colossal magnetoresistance thin films on silicon*", Appl. Phys. Lett. **69**, 1005 (1996)

[145] A. K. Pradhan, S. Mohanty, Kai Zhang, J. B. Dadson, E. M. Jackson, D. Hunter, R. R.

Rakhimov, G. B. Loutts, J. Zhang and D. J. Sellmyer, "*Integration of epitaxial colossal magnetoresistive films onto Si(100) using SrTiO₃ as a template layer*", Appl. Phys. Lett. **86**, 012503 (2005)

[146] A. K. Pradhan, J. B. Dadson, D. Hunter, K. Zhang, S. Mohanty, E. M. Jackson, B. Lasley-Hunter, K. Lord, T. M. Williams, R. R. Rakhimov, J. Zhang and D. J. Sellmyer, "*Ferromagnetic properties of epitaxial manganite films on SrTiO₃/Si heterostructures*" J. Appl. Phys. **100**, 033903 (2006)

[147] A. Fissel, A. Laha, E. Bugiel, D. Kühne, M. Czernohorsky, R. Dargis, H.-J. Osten, "*Silicon in functional epitaxial oxides: A new group of nanostructures*", Microelectron. J. **39**, 512 (2008)

[148] A. Fissel, R. Dargis, E. Bugiel, D. Schwendt, T. Wietler, J. Krügener, A. Laha and H.J. Osten, "*Single-crystalline Si grown on single-crystalline Gd₂O₃ by modified solid-phase epitaxy*", Thin Solid Films, **518**, 2546 (2010)

[149] J. W. Seo, Ch. Dieker, A. Tapponnier, Ch. Marchiori, M. Sousa, J.-P. Locquet, J. Fompeyrine, A. Ispas, C. Rossel, Y. Panayiotatos, A. Sotiropoulos, A. Dimoulas, "*Epitaxial germanium-on-insulator grown on (001) Si*", Microelectron. Eng. **84**, 2328 (2007)

[150] A. Giussani, O. Seifarth, P. Rodenbach, H.-J. Müssig, P. Zaumseil, T. Weisemöller, C. Deiter, J. Wollschläger, P. Storck, and T. Schroeder, "*The influence of lattice oxygen on the initial growth behavior of heteroepitaxial Ge layers on single crystalline PrO₂(111)/Si(111) support systems*" J. Appl. Phys. **103**, 084110 (2008)

[151] G. Saint-Girons, C. Priester, P. Regreny, G. Patriarche, L. Largeau, V. Favre-Nicolin, G. Xu, Y. Robach, M. Gendry, and Guy Hollinger, "*Spontaneous compliance of the InP/SrTiO3 heterointerfac*e", Appl. Phys. Lett. **92**, 241907 (2008)

[152] G. Saint-Girons, P. Regreny, J. Cheng, G. Patriarche, L. Largeau, M. Gendry, G. Xu, Y. Robach, C. Botella, G. Grenet and G. Hollinger, "*Competition between InP and In₂O₃ islands during the growth of InP on SrTiO₃*" Appl. Phys. Lett. **104**, 033509 (2008)

[153] J. Cheng, P. Regreny, L. Largeau, G. Patriarche, O. Mauguin, K. Naji, G. Hollinger, G. Saint-Girons, "*Influence of the surface reconstruction on the growth of InP on SrTiO₃(001)*", J. Cryst. Growth, **311**, 1042 (2009)

[154] N. A. Bojarczuk, M. Copel, S. Guha, V. Narayanan, E. J. Preisler, F. M. Ross, and H. Shang, "*Epitaxial silicon and germanium on buried insulator heterostructures and devices*", Appl. Phys. Lett. **83**, 5443 (2003)

[155] G. Saint-Girons, P. Regreny, L. Largeau and G. Patriarche, G. Hollinger, "*Monolithic integration of InP based heterostructures on silicon using crystalline Gd₂O₃ buffers*", Appl. Phys. Lett. **91**, 241912 (2007)

[156] G. Saint-Girons, J. Cheng, P. Regreny, L. Largeau, G. Patriarche and G. Hollinger, "*Accommodation at the interface of highly dissimilar semiconductor/oxide epitaxial systems*", Phys. Rev. B **80**, 155308 (2009)

[157] T. Schroeder, P. Zaumseil, O. Seifarth, A. Giussani, H.-J. Müssig, P. Storck, D. Geiger, H. Lichte and J. Dabrowski, "*Engineering the semiconductor/oxide interaction for stacking twin suppression in single crystalline epitaxial silicon(111)/insulator/Si(111) heterostructures*", New J. Phys. **10**, 113004 (2008)

[158] T. Schroeder, A. Giussani, H. J. Muessig, G. Weidner, I. Costina, Ch. Wenger, M. Lukosius, P. Storck, P. Zaumseil, "*Ge integration on Si via rare earth oxide buffers: From MBE to CVD*" Microelectron. Eng. **86**, 1615 (2009)

[159] Thesis of G. Delhaye, "*Oxydes crystallins à haute permittivité diélectrique épitaxiés sur silicium: SrO et SrTiO₃*", France, (2006)

[160] Thesis of M. E. Kazzi, "*Etude par photoémission (XPS et XPD) d'hétérostructures d'oxydes fonctionnels épitaxiés sur silicium*", France, (2007)

[161] Thesis of L. Becerra, "*Hétérostructures et dispositifs microélectronique à base d'oxydes high-k préparés sur silicium par EJM*", Ecole Central de Lyon, France, (2008)

Chapter II: Epitaxy and characterization principles and methodologies

II.1) Introduction

In this chapter, we will present the physical principles of epitaxy and different methods employed for the oxides growth. We will also introduce different in-situ and ex-situ characterization methods, especially the electrical characterization method.

II.2) Physical principles of epitaxial growth

II.2.1) Atomic process of growth on surfaces

Epitaxial growth refers to the method of depositing thin layers of the required material on a suitably oriented crystalline substrate. Molecular beam epitaxy (MBE) is an ultra-high-vacuum (UHV) technique for growth from the vapor phase of the elements which are deposited on a substrate whose temperature is lower than that of the vapor-solid equilibrium phase of the elements involved. In these conditions, a condensation process therefore takes place on the surface. From a kinetic point of view, the physicochemical interactions between adatoms of vapor phase and substrate plays a dominating role in the growth mechanism, as illustrated in Figure II.1[1].
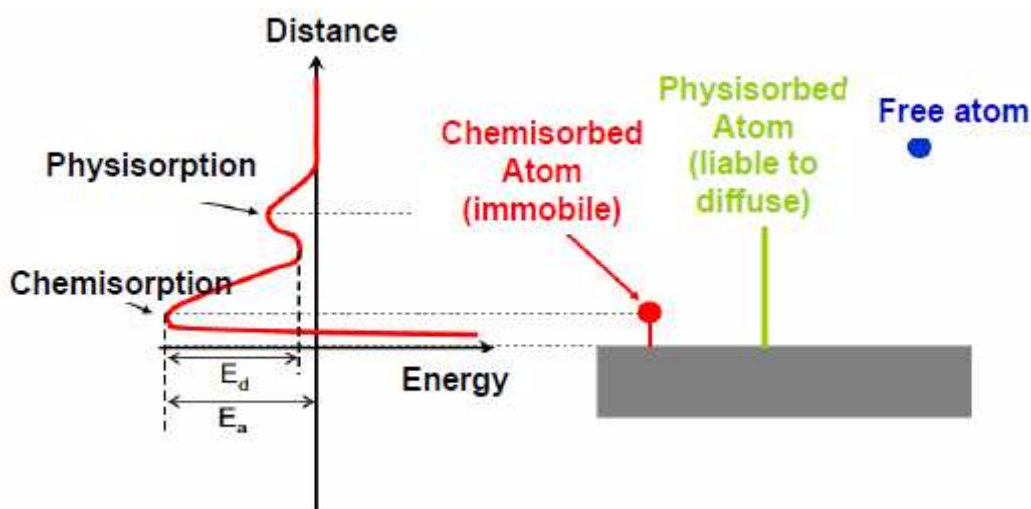
Figure II. 1 Physicochemical interactions between adatoms of vapor phase and substrate

Chemisorption (chemical absorption), in which the electronic structure of bonding atoms or molecules is changed and covalent or ionic bonds form, fixes the adatoms on the surface. The attractive forces are the type occurring in the appropriate chemical bond. In this case, the thermal energy is too small that the mobility of the adatoms is not sufficient to construct a crystal quality. The necessary energy to transfer chemisorption to physisorption is E_d.

Physisorption (physical absorption) is a process in which the electronic structure of the atom or molecule is barely perturbed upon adsorption. The fundamental interacting force of

physisorption is caused by Van der Waals force (~10-100 meV), which is so weak that the adatoms can diffuse easily on the surface permitting the organization of crystal. However, when the thermal energy is too high and larger than E_a, the adatoms desorbs from the surface and re-evaporates. Once the thermal energy falls in the range of $E_d<E<E_a$, the adatoms can move rapidly on the surface without evaporation. They migrate on the surface by jumping from one site to another and then combine together to form metastable nucleis, which are unstable, i.e. they diffuse on the surface. Until the nucleis reach a critical size, which corresponds to the required atom number to obtain a stable collection, they will enlarge and the incorporation starts between them and finally a complete layer forms. This whole atom process of nucleation and growth is depicted in Figure II. 2.
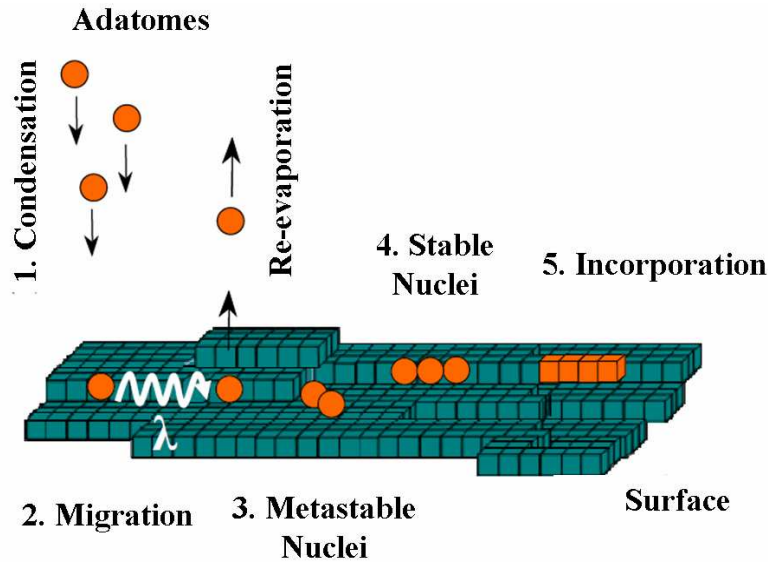
Figure II. 2 Atom process of the nucleation during the epitaxial growth

From this conceptual picture one can identify several basic parameter related to the kinetic growth. The first is the adsorption residence time τ, which is determined by the adsorption energy, E_a, and is conventionally written as:

$$\tau^{-1} = \nu_a \exp(-E_a / kT)$$
<div align="right">Equation II-1</div>

where ν_a the atomic vibration frequency, of order 1-10 THz; k the Boltzman constant and T the surface temperature. The adsorption residence time corresponds to a short time that adatoms stay on the surface, before their re-evaporation. When the kT is sufficient high, the adatoms jump from one place to another over the surface and they migrate with the diffusion coefficient D, which defines the average surface covered by atoms per time unit. D is given by:

$$D = (\nu_d a^2 / 4)\exp(-E_d / kT) \hspace{3cm} \text{Equation II-2}$$

where E_d is the diffusion energy, frequency ν_d is slightly less than ν_a and a is the jumping distance, equal to the surface lattice parameter 0.2~0.5nm.

$D \cdot \tau$ is the area covered by an adatom during its diffusion on the surface. The diffusion length λ, which is the distance traveled by an adatom during its adsorption residence time τ, can be represented by the Einstein relation:

$$\lambda = \sqrt{2\tau D} \hspace{3cm} \text{Equation II -3}$$

II.2.2) Surface, interface energy and growth modes

It is widely accepted that three possible modes of crystal growth on surfaces may be distinguished, as shown in Figure II. 3.

(a)   (b)   (c)
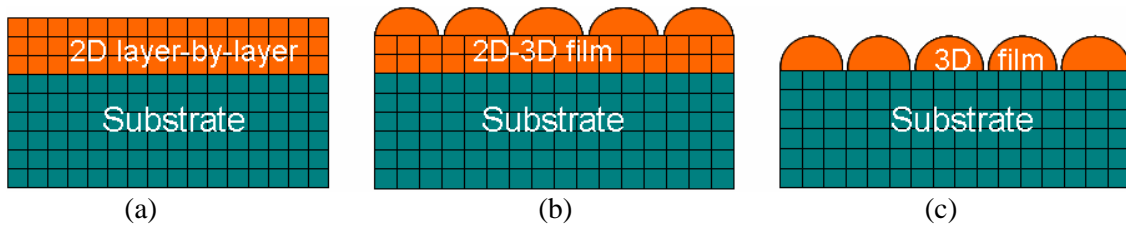
Figure II. 3 Different modes of crystal growth on surfaces: (a) Frank-Van der Merve (2D layer-by-layer); Stranski-Krastanov (layer plus island); (c) Volmer-Weber (3D islands)

- Layer-by-layer or *Frank-Van der Merve* mode. The atoms are more strongly bound to the substrate than to each other, the first atoms to condense form a complete monolayer on the surface, which becomes covered with a somewhat less tightly bound second layer.

- Layer plus island, or *Stranski-Krastanov* mode. After forming the first few monolayers, subsequent layer growth is unfavorable and islands are formed on top of this "intermediate" layer (called wetting layer).

- Island, or *Volmer-Weber* mode. The atoms of the deposit are more strongly bound to each other than to the substrate. Small clusters are nucleated directly on the substrate surface and then grow into islands of the condensed phased.

Surface thermodynamics has been used to describe these modes[1,2]. The condensation process of the adatoms on substrate surface leads to the formation of 3D islands (a contact angle θ with the substrate) or 2D islands (cylindrical platelets, the height of which is a monolayer) on the substrate surface, as shown in Figure II. 4.
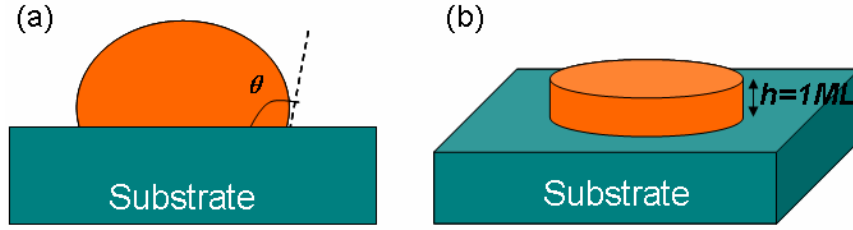
Figure II. 4 Geometry of (a) 3D islands and (b) 2D cylindrical platelet on substrate surface

These islands present a material/substrate interface and a free surface of the epitaxial material. The condensation is thus drived by a competition of the energetic gain of the formation of the solid materials (volume aspect) and the cost related to the formation of the interface and the free surface of deposited materials (surface aspect). Furthermore, in case of a strained material that elastically deforms, a volume cost corresponding to the stored elastic energy in the islands has to be considered. The condensation free enthalpy can be therefore written as follows:

$$\Delta G = V\bullet(E_v - \Delta\mu) + (\gamma_{AB} - \gamma_B)\bullet S_{AB} + \gamma_i \bullet S_i \qquad \text{Equation II -4}$$

where V the island volume; $\Delta\mu$ the chemical potential difference by unit of volume of the island; E_v is the elastic energy stored in the deposited material per unit of volume; S_{AB} and S_i the island/substrate interface and the free surface of the island respectively; γ_{AB} the interface energy and γ_B, γ_i are the surface energies of substrate and island respectively. This equation can be rewritten as:

$$\frac{\Delta G}{\Delta\mu} = V\bullet(\alpha_c - 1) + L\bullet(\alpha_B S_{AB} + S_i) \qquad \text{Equation II -5}$$

where L$= \dfrac{\gamma_i}{\Delta\mu}$ is the homogenous in length, $\alpha_c = \dfrac{E_v}{\Delta\mu}$ and $\alpha_B = \dfrac{\gamma_{AB} - \gamma_B}{\gamma_i}$ are non-dimensional. This equation illustrates the competition:

- between the volume cost to form the islands and the chemical potential difference (α_c). If $\alpha_c > 1$, the free enthalpy is always positive and no condensation occurs, i.e. there is no epitaxial growth; If $\alpha_c < 1$, the condensation could take place and there exists a critic volume V_c less than which the islands are instable, i.e. no stable island exist whose volume is less than V_c.

- between the gain (or cost) to replace the substrate surface by materials/substrate interface and the cost to form the island surface (α_B). According to the theory of Dupré[3], the

relationship between α_B and the contact angle θ is $\cos\theta = -\alpha_B$. Wetting increases when α_B decreases.

If $\alpha_B < -1$, i.e. $\gamma_i + \gamma_{AB} < \gamma_B$, the growth is two-dimensional. This inequality is the so-called Bauer criterion: when the sum of the material surface energy and interface energy is less than substrate surface energy, the growth mode is 2D layer-by-layer (*Frank-Van der Merve*, Figure II. 3(a)) or layer plus island (*Stranski- Krastanov*, Figure II. 3(b));

If $-1 < \alpha_B < 1$, which refers that $\gamma_i + \gamma_{AB} > \gamma_B$ or 0°<θ<180°, the growth follows the 3D island mode (*Volmer-Weber*, Figure II. 3(c)).

If $\alpha_B > 1$, the energy cost to replace the substrate surface by material/substrate interface is greater than the material surface energy and the germination will not occur (no epitaxy).

II.2.3) Heteroepitaxy: elastic deformation and relaxation modes

In this section we will discuss the influence of the lattice mismatch between the epitaxial material and the substrate on the heteroepitaxy process. Since the epitaxial material generally possesses a different lattice constant with respect to the substrate in heteroepitaxy, the lattice mismatch (misfit) is defined as:

$$\varepsilon = \frac{\Delta a}{a} = \frac{a_m - a_s}{a_s} \qquad \text{Equation II -6}$$

with a_m and a_s are lattice constants of the epitaxial material and the substrate, respectively. In particular, in cases that the lattice mismatch is normally very large (this is the case for some oxides/Si shatems), indirect epitaixial relationships can be obtained, as shown in Figure II. 5. These indirect epitaxial relationships must be considered in Equation-6. To accommodate the Si lattice, *x* lattice of the oxide is deposited on Si. Therefore the effective lattice mismatch can be identified:

$$\varepsilon_{eff} = \frac{x \bullet a_m - a_s}{a_s} \qquad \text{Equation II -7}$$
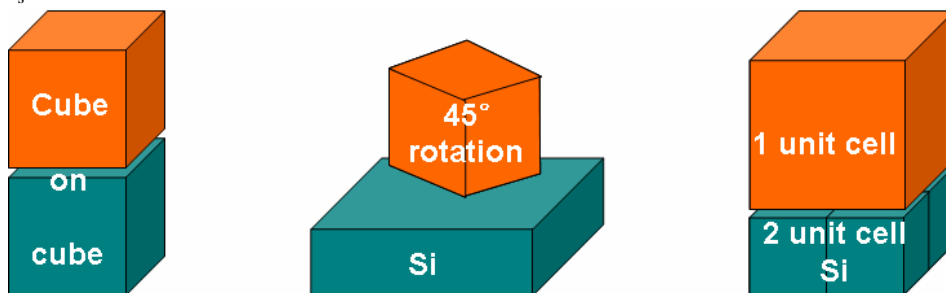
Figure II. 5 Schema of different relationship between epitaxial material and substrate

In the following, standard cube-on-cube growth is considered. At the initial stage of the growth, the substrate imposes its lattice constant to the in-plane lattice constant of epitaxial material at the interface due to its much greater thickness, i.e. $a_{//}=a_s$. Thus the material lattice deforms elastically (as shown in Figure II. 6):
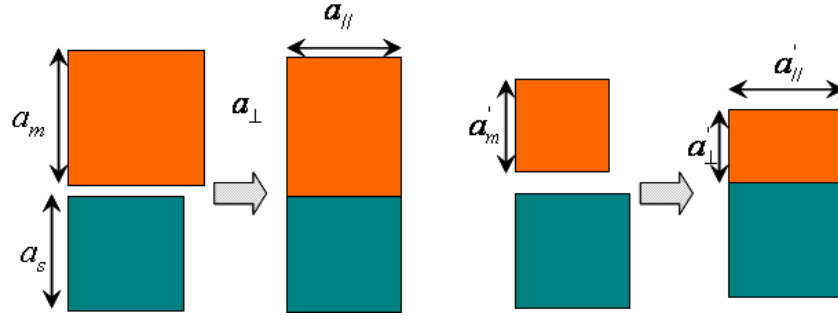
Figure II. 6 Elastic deformation of the epitaxial material lattice on the substrate

If $a_s<a_m$, the lattice is compressively strained with $a_{//}=a_s$ and the perpendicular lattice constant $a_\perp$ increases; If $a_s>a_m$, the lattice undergoes tensile strain, $a_\perp$ decreases. The quadratic deformation of the epitaxial material can be deduced by elastic theory. For the cube-on-cube system, the Poisson's ratio ν describing the tetragonal distortion is given by:

$$\varepsilon_\perp = -\frac{2\nu}{1-\nu}\varepsilon_{//} \quad \Leftrightarrow \quad \frac{a_\perp - a_m}{a_m} = -\frac{2\nu}{1-\nu}\frac{a_{//} - a_m}{a_m} \qquad \text{Equation II -8}$$

Poisson's ratio ν is commonly close to 0.33 for many materials which demonstrate that the volume of the material lattice tends to remain constant during the deformation. Moreover, ν is related to the elastic modulus tensor (C_{ij}) of the material:

$$\nu = \frac{C_{12}}{C_{11} + C_{12}} \qquad \text{Equation II-9}$$

Hereby we have:

$$\frac{a_\perp - a_m}{a_m} = -\frac{2C_{12}}{C_{11}}\frac{a_{//} - a_m}{a_m} \quad \xrightarrow{a_{//}=a_s} \quad \frac{a_m - a_s}{a_s} = \frac{C_{11}}{C_{11} + 2C_{12}}\frac{a_\perp - a_s}{a_s} \qquad \text{Equation II -10}$$

The deformation of the epitaxial material leads to an accumulation of elastic energy E_v in the film. The stored energy E_v increases increasing the film thickness according to Equation-11:

$$E_v = 2G\varepsilon_{//}^2 h\frac{1+\nu}{1-\nu} \qquad \text{Equation II -11}$$

where G the shear modulus with $G=(C_{11}-C_{12})/2$; $\varepsilon_{//}$ lattice mismatch; h the thickness of

epi-layer.

Therefore a critical thickness (or volume for a 3D growth mode) h_c exists, above which the heterostructure becomes instable due to the accumulated elastic energy E_v. They tend to relax to their own bulk lattice constant through a strain relaxation process, plastically or elastically (Figure II. 7).

(a) pseudomorphic growth   (b) plastic relaxat   (c) elastic relaxation
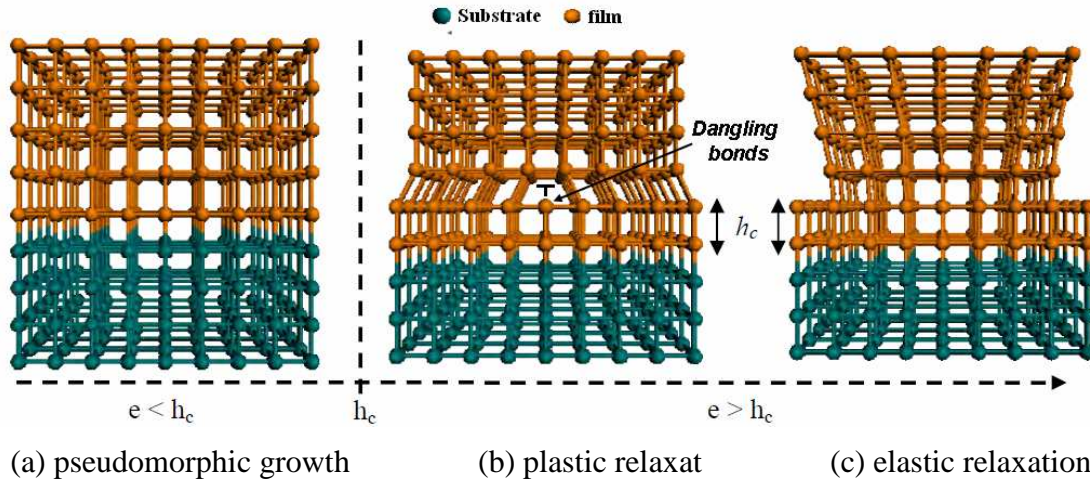
Figure II. 7 Illustration of the relaxation mechanism of the epitaxial film on the substrate

- **Plastic relaxation** (Figure II. 7 (b)). When the film thickness is less than h_c the growth remains pseudomorphic. Once it exceeds the critical thickness h_c, the plastic stress relaxation leads to the generation of the misfit dislocations in the film. The dislocation can be classified with edge dislocation, screw dislocation and mixed dislocation etc. Their formation is generally accomplished by the dislocation motion, i.e. gliding[4] and these defects degrade the film quality (presence of dangle bonds). For a two-dimensional moderately strained film, the critical thickness can be estimated by the Matthews Blakeslee model[5] :

$$h_c = \frac{b(1 - v \cdot \cos^2(\alpha))}{8\pi m \cdot \cos(\lambda)} \cdot \left[\ln\left(\frac{h_c}{b} \right) \right] \qquad\qquad \text{Equation II -12}$$

  where v Poisson ratio, b the Burgers vector of the dislocations, α the angle between the Burgers vector and the projection of dislocation line in interface plane and λ the angle between the Burgers vector and the in-plane direction of the interface. It shows the critical thickness decreases rapidly when the lattice mismatch increases.

- **Elastic relaxation**. The plastic relaxation can be preceded by elastic relaxation. In these

cases islands are formed when the film thickness exceeds a critical 2D-3D transition thickness $h_{2D\text{-}3D}$ (h_c), allowing releasing the elastic energy stored in the film, of the expense of an increase of the surface energy of the system. It corresponds to the grow mode "Stranski- Krastanov". The $h_{2D\text{-}3D}$ can be expressed as:

$$h_{2D-3D} = \frac{1}{a^3} \bullet \left(\frac{\gamma_i \bullet g - \gamma_i^0 \bullet f}{\varepsilon r^2 \bullet (1-R)} \right)^3 \qquad \text{Equation II -13}$$

where γ_i^0 the surface energy of the growing 2D film; γ_i the average energy of the facets of the formed islands; $\varepsilon = \dfrac{Y}{1-v}$,Y and v are Young's modulus and Poisson ratio respectively; r lattice mismatch; R is the relaxation of the free surface (often complex), $g = S_i \bullet V^{-2/3}$ and $f = S_{AB} \bullet V^{-2/3}$ (refer to Equation II-4)

For a strain epitaxial film, if the $h_{2D\text{-}3D}$ is less than plastic h_c, the Stranski- Krastanov growth will be observed. If the growth continues exceeding the plastic critical thickness h_c, the islands will relax plastically by forming misfit dislocations.

Another possible way to obtain a two-dimensional film without threading defects from initially three-dimensional island should be considered. When the germ forms islands on the substrate surface with a network of dislocations at the interface, they are stable because they grow with their own lattice constant. In case that all the germ present the same initial crystallographic orientation and no defect forms when they coalesces, a bidimensional epitaxial layer without threading defects can be attained. This possible process is important for the integration of semiconductor and oxides (Chapter IV).

According to the considerations above, the misfit dislocation is a significant type of defects in the epitaxial film. In fact, several other defects influence the quality of the epilayer. Figure II. 8 exhibits different possible characteristics turned out by epitaxial films. Particularly for the epitaxy of oxides, the oxygen vacancies consist of another important origin of the defects. The objective of epitaxy is to find an optimal strategy to avoid these defects in order to achieve a high quality epitaxial film.

(a) peudomorphic growth   *(b) misorientation*   *(c) dislocation content*

(d) mosaic spread   *(b) curvature*   *(c) inhomogeneity*
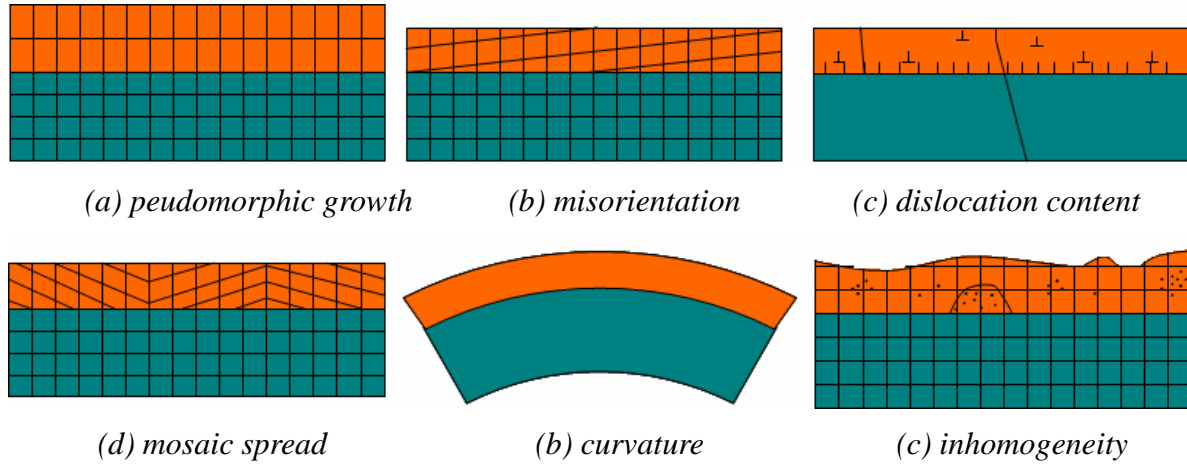
Figure II. 8 Different characteristics of the eptitaxial film.

II.3) Experimental techniques

II.3.1) Molecular Beam Epitaxy

II.3.1.1) Introduction

Since the technique of Molecular Beam Epitaxy (MBE) was first successful used by A. Y. Cho and J. R. Arthur in the late 1960s to fabricate GaAs epilayers[6,7], it has been developed to a versatile tool for growing thin epitaxial structures made of semiconductors, metal or insulators. In comparison to all other epitaxial growth techniques, MBE has several unique advantages:

- Being realized in Ultra High Vacuum (p≤10^{-9}Torr or 1.33×10^{-7}Pa), MBE ensures the high purity of the deposit material. This vacuum condition enables the beam of the mass flow to move toward the substrate with a large mean free path. Given that the residual gas pressure routinely achieved in MBE systems is 10^{-10}~10^{-11}Torr and the mean free path can be calculated by:

$$L = \frac{k_B T}{\sqrt{2}\pi p d^2} = 3.11\times10^{-24}\frac{T}{pd^2} \qquad \text{Equation II -14}$$

with d the molecular diameter, k_B the Boltzmann constant (1.38×10^{-23}JK^{-1}), the mean free path of the material in MBE chamber can reach 10^6 meter whereas the distance between the outlet orifices of the beam sources and the substrate approximately equals 0.2m.

- The composition of the grown epilayer and its doping level depend on the evaporation rates of the appropriate sources. In MBE, the typical growth rate is 1 monolayer/s (for oxides MBE, even lower 1~2 monolayer/min), which is low enough to ensure surface

migration of the impinging species on the growing surface, leading to a very smooth surface of the grown film.

- Thanks to the UHV environment, MBE can be controlled *in situ* by surface sensitive diagnostic methods such as reflection high energy electron (RHEED), ellipsometry, X-ray photoelectron spectroscopy (XPS), Auger electron spectroscopy (AES) and Scanning electron microscopy (SEM). These powerful facilities for control and analysis eliminate much of the guesswork in MBE, and enable the fabrication of sophisticated device structures.

For the study in this thesis, MBE introduces several particular virtues to the epitaxy of oxides on silicon. The first advantage results from the UHV environment. For the application of high-k and functional devices, an abrupt interface between oxides and silicon without silica or silicate is very important. The preparation of the silicon substrate in UHV environment can assure a clean, atomic smooth silicon surface. The second virtue is connected with the low enough growth rate and subtly control of oxygen. Due to the sensitivity of silicon surface to the oxygen, a grow rate of 1 monolayer/min allows us precisely control the introduction moment of oxygen and its partial pressure to effectively prevent the formation of the silica or silicate at the interface simultaneously ensure oxidizing completely the metal elements. The next virtue concerns its intrinsic physical characteristics during the whole growth process. Compared to Atomic Layer Deposition (ALD) or Metal Organic Chemical Vapor Deposition (MOCVD), it is not necessary for MBE to prepare the precursors in advance. The last but no least, the stoichiometry, crystalline quality and the surface morphology of the oxides can be in-situ monitored precisely by RHEED.

Figure II. 9 shows the comparison of different methods of oxides deposition.

	Conformity	*Purity*	*Defects*	*Thickness*	*Surface*
Sputtering	☆	☆ ☆	■ ■		☆ ☆
Metal deposition+Oxydation	☆	☆ ☆	☆	☆ ☆	☆
MOCVD	☆ ☆	☆	☆ ☆	☆ ☆	☆ ☆ ☆
ALD	☆ ☆ ☆	☆	☆ ☆	☆ ☆ ☆	☆ ☆ ☆
MBE	■ ■	☆ ☆ ☆	☆ ☆ ☆	☆ ☆	☆ ☆ ☆

Figure II. 9 Comparison of different oxides deposition methods[8].

(☆ = advantage; ■ = inconvenience)

II.3.1.2) Description of epitaxy reactor for oxides

During this thesis, all the samples were realized in a Riber 2300 reactor adapted to the fabrication of oxides, silicon and germanium. The main building blocks of this machine are schematically presented in Figure II. 10, with their principal functions indicated. This system consists three principal blocks: sample introduction stage, interstage substrate transfer system and MBE chamber.

- *The sample introduction stage* allows a single sample holder of 2 inch diameter substrate to be rapidly loaded or unloaded from the MBE machine. The introduction chamber is equipped with a turbomolecular pump that permits it maintaining a vacuum of 10^{-6}~10^{-7} Torr. A outgasing furnace is also available in the introduction chamber allowing the thermal treatment of the samples.

- Once the substrate is ready in the introduction chamber, it can be transported to *the transfer chamber*, where the vacuum is of the order of 10^{-9} Torr (ionic pumping). Using a transfer cane, we can convey substrates from the transfer chamber to the MBE growth chamber through an isolation gate valve. Furthermore, separate viewports at each process stage allow complete visual access for manipulation.

- In *the MBE growth chamber*, an ionic pump, a turbomolecular pump, a liquid nitrogen cooling system and a titanium sublimation pump are employed to achieve a vacuum down to 1×10^{-10} Torr. Before the introduction of oxygen in the chamber, the ionic pump is turned off and the turbo pump which is more resistant to oxygen is started on work. Here are located all the elements which enable well controlled epitaxial growth. These are beam sources (Knudsen effusion cells) with their individual shutters, the electron gun, a substrate manipulator with heating and continuous rotation facilities, and phosphor screen of the RHEED system, and the pressure control unit (ion gauge and mass spectrometer).
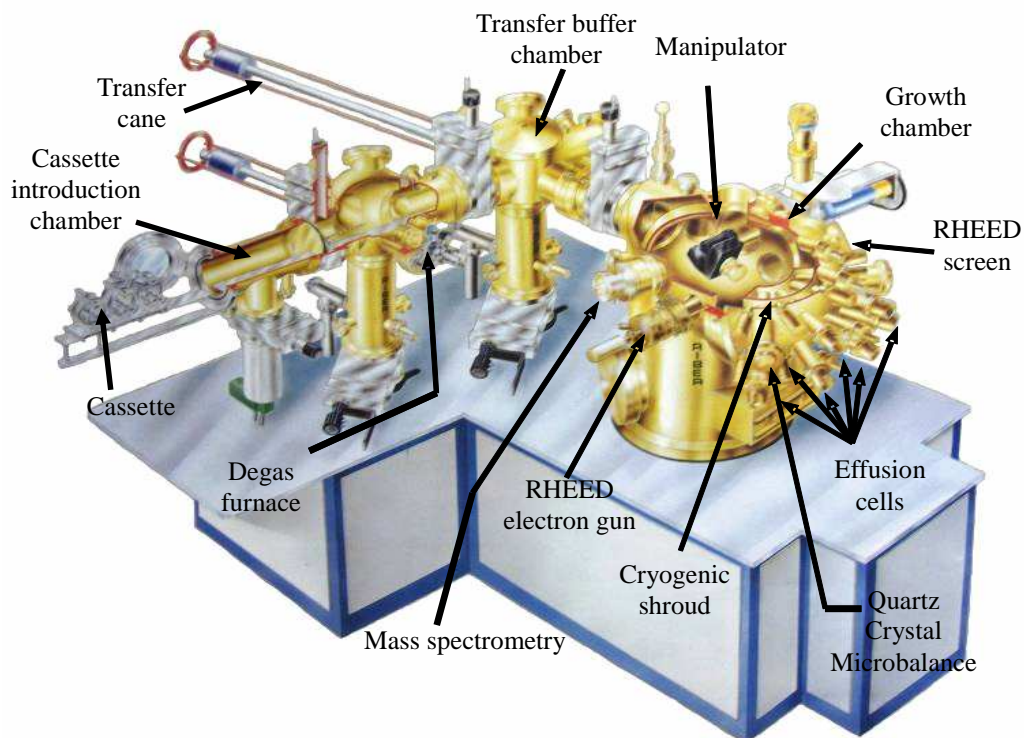
Figure II. 10 Illustration of the main block building of oxide MBE reactor

Effusion cells have a direct impact on the quality of the films grown by MBE (i.e. morphology, purity, composition, uniformity, etc.). In our reactor, we use Knudsen-type effusion cells made of PBN (Pyrolytic Boron Nitride, a refractory material). Standard cells (temperature up to 1500°C) are used for Ba (barium), Sr (strontium), Ge (germanium) and Al (aluminium) and high temperature cells (temperature up to 2000°C) for La (lanthanum) and Ti (titanium). Associated with each cell is a separate refractory metal shutter. The shutters are sited to interrupt the beams between the sources and substrate and to effectively completely shield the substrate from each individual beam when closed.

An electron gun is also available in our reactor. We have four crucibles in our electron gun filled with $LaAlO_3$, Al_2O_3, Gd_2O_3 and Si respectively. When it works, a stream of electrons is accelerated through a field of typically 5~10 kV and focused onto the target surface. Upon impingement, most of the kinetic energy of the electrons is converted into heat and temperatures exceeding 3000°C to evaporate the materials in the crucible. In case of the oxides growth using e-beam gun, an introduction of oxygen is necessary to completely oxidize the metal element because the oxides might partly decompose during the evaporation. Moreover, due the instability of the growth rate using electron gun, it is indispensable to use mass spectrometry or Quartz Crystal Microbalance (QCM) for the real time control of the evaporation.

The <u>manipulator</u> (2 inch) includes a tantalum heater protected by a PBN slab allowing the homogeneity of the heat transition and preventing the deterioration of the filament under an oxygen rich growth environment. The substrate can be heated up to 950°C which is high enough to completely clean $SrTiO_3$ and silicon substrate surfaces. The temperature is measured using a thermocouple (converting heat to electronic signal) and a pyrometer (measuring the thermal radiation, accurate when temperature is higher than 500°C). The substrate holder is made of molybdenum that is very effective to exchange the heat with substrates. During the growth, the manipulator rotates with a constant angular velocity around the axis perpendicular to the surface of substrate to enhance the uniformity of the epilayer.

The <u>RHEED system</u> is sited to in-situ monitor the structure of the growing film on the substrate. A high energy beam of electrons of 30 keV is incident on the substrate at a glancing angle 1°~3°. Therefore the penetration of the beam into the surface is restricted to the outermost few atomic layers, i.e. RHEED reveals the surface structure information of the film. However, it is still a powerful tool to monitor in real time the information such as the crystallization quality, the growth mode, the surface reconstruction and the growth rate. A detailed introduction of RHEED can be found in Appendix A.

The partial pressure of the elements fluxes are measured by a <u>Bayard-Alpert ionization gauge</u>. The species arriving on the gauge are ionized and then collected in form of electronic current. Combined with the RHEED pattern that allows distinguishing different reconstruction features of (Sr, Ba)TiO_3 (Sr/Ba rich or Ti rich), the measured fluxes help us to determine the stoichiometry of the ternary oxides grown by Knudsen effusion cells. Besides the RHEED intensity oscillation, the QCM is also employed to determine the growth rate, especially for the materials grown by electron gun. It measures a mass per unit area by measuring the change in frequency of a quartz crystal resonator. The resonance is disturbed by the addition or removal of a small mass due to oxide growth/decay or film deposition at the surface of the acoustic resonator.

Oxygen is introduced into the reactor via a <u>pressure-regulated plasma chamber</u>, which permits us to precisely control the oxygen partial pressure in the chamber, particularly at the first stage of the oxides growth. Both atomic and molecular oxygen can be used. The atomic oxygen is produced by a Radio Frequency plasma generator with its frequency of 13.56MHz

and power output of 600W.

II.3.1.3) Ex-situ characterization methods

The objective of this thesis is to grow "perfect" crystalline oxides on Si substrate and heterostructures based on oxides/Si template. Therefore we are mainly concerned with the properties of the thin film such as the smoothness of the surface, crystalline perfection of the film, structural parameters of the interface and electrical properties of the thin films. Different ex-situ characterization tools are employed to reveal the information of these properties.

Atomic Force Microscopy (AFM) is one of the most widely used tools for imaging, measuring, and manipulating matter at the nanoscale. It belongs to the Scanning Probe Microscopy (SPM) family whose principle consists in a near field probe imaging a surface by lateral scanning. It can measure a wide range of surface properties on any kind of material, ranging from topography to surface potential, from electrical or magnetic properties. AFM can work with different modes such as tapping mode or contact mode. Based on the contact mode, conductive AFM (C-AFM) which allows the characterization of the conductivity variations across medium- to low- conducting and semiconducting materials, and piezoresponse force microscopy (PFM) which permits nondestructive local measurement of the polarization at nanoscale are developed to meet relative research necessities. The AFM instruments used in this thesis are Veeco CP II and Veeco dimension 3100. More detailed introductions of AFM can be found in Appendix B.

X-ray Diffraction (XRD) is a method of investigating the fine structure of material. X-ray can be used to produce the diffraction pattern because their wavelength λ is typically the same order of magnitude (1~100Å) as the spacing d between planes in the crystal. Following the well-know Bragg's law, the X-ray diffraction results from an electromagnetic wave (the X-ray) impinging on a regular array of scatterers (the repeating arrangement of atoms within the crystal). Our Rigaku diffractometer in INL permits us performing diverse measurements on the samples, such as rocking curve (RC) measurements (out-of-plane and in-plane), reciprocal space mapping (RSM) measurements, X-ray reflection (XRR) and pole figure measurements. For more detailed introductions of XRD, see Appendix C.

X-ray Photoelectron Spectroscopy (XPS) is a method that measures the elemental

composition, empirical formula, chemical state and electronic state of the elements existing within a material. The principle of this method is as following: in a UHV condition, irradiating a material with a beam of X-rays while simultaneously measuring the kinetic energy and number of electrons that escape from the top 1~10nm of the material analyzed. XPS analysis helps us obtain the physico-chemical information of thin film and the interface. With respect to XPS, X-ray PhotoElectron Emission Microscopy (XPEEM) allows conserving the spatial origin of the photoelectrons thanks to electron optics which collect, focus and enlarges the photoelectric signal.

Transmission Electron Microscopy (TEM) is based on the diffraction of electrons when they pass through a very thin sample. Electron diffraction from a crystalline lattice can be described as a kinematic scattering process that meets the wave reinforcement and interference conditions given in the Bragg equation. An image is formed from the interaction of the electrons transmitted through the specimen. The image is magnified and focused onto an imaging device, such as a fluorescent screen, or to be detected by a sensor such as a CCD camera. Derived from TEM, High resolution TEM (HRTEM) which bases on the phase contrast due to the phase modulation of the electron waves by the periodic crystal lattice allows the imaging of the crystallographic structure of a sample at an atomic scale. A TEM can also be modified to a Scanning TEM (STEM), with which the electrons pass through the specimen, however, the electron optics focus the beam into a narrow spot which is scanned over the sample in a raster. By using a STEM and a high-angle detector, it is possible to form atomic resolution images where the contrast is directly related to the atomic number. High-angle annular dark-field imaging (HAADF) is a method of mapping samples in STEM. Based on dominant Z-contrast for distinction of different materials, HAADF images are realized by collecting scattered electrons with an annular dark-field detector in STEM

InfraRed spectroscopy (IR) can be used to identify compounds and investigate sample composition, by exploiting the fact that molecules absorb specific frequencies. These absorptions are resonant frequencies, i.e. the frequency of the absorbed radiation matches the frequency of the bond or group that vibrates. The energies are determined by the shape of the molecular potential energy surfaces, the masses of the atoms, and the associated vibronic coupling.

Rutherford backscattering spectrometry (RBS) is used to determine composition of epitaxial films especially the stoichiometry of the oxides, by analyzing energy loss of light ions (H^+, He^+) at high energies (0.5~5MeV) during their passage through the film.

II.3.2) Electrical characterization methods
II.3.2.1) Post Deposition Annealing (PDA): tubular furnace and RTA

One of the main objectives is to obtain small EOT values and simultaneously low leakage current by exploring the system of high k oxide (Gd_2O_3) on silicon substrate. In order to study the thermal stability of the Metal Insulator Semiconductor (MIS) structure as well as to observe the influence of PDA on the dielectric properties of the samples tested, the pre-metallization annealings were performed. All these annealing treatments were carried out after the samples taken out from epitaxy chamber exposed to air, while before the metallization of the oxides/Si system to avoid the possible problems resulting from the interdiffusion between dielectric oxides and metal gates. Two PDA have been performed on the MIS structures.

The first PDA type concerns the utilization of a carbolite horizontal tubular furnace with a maximum operating temperature of 1200°C. It is composed of a cylindrical tube and a pure sintered alumina nacelle. Three arrivals gas are connected to the furnace: oxygen, nitrogen and forming gas (mixed with 96% N_2 and 4% H_2). Due to the small internal diameter of the tube and in order to prevent weakening it, the ramp rate to increase the temperature is only 6°C/min. This low ramping time is one of the drawbacks of this furnace. Particularly, the temperature decreases slowly after one turns off the furnace, which strongly extends the annealing time. For instance, an annealing at 300°C for 5 minutes will become an annealing during which the temperature remains 250~300°C for 30minutes.

The second furnace in service for PDA is a RTA (Rapid Thermal Annealing) furnace. The furnace (Jipelec Jet Star 100SR Processor) allows attaining ~1000°C during several seconds (100°C/s). The standard procedure is as follows:
1) putting samples in the chamber under vacuum; then introducing the desired gas desired (oxygen, nitrogen or argon are available) into the chamber;
2) launching the annealing process while conducting a continuous sweep under the selected gas;

3) the temperature is dropped by draining the gas used for the annealing

The annealing duration of RTA is much shorter than the tubular furnace and makes very rapid "spike" annealing type similar to that used in industry, particularly for the dopant activation.

II.3.2.2) The choice of substrates and gate metals

The Metal-Oxide-Semiconductor capacity is the most useful device to characterize the electrical properties of the dielectric materials and the interface quality between the silicon substrate and the oxides gate insulator. Once the oxides/Si samples are elaborated in the MBE chamber and undergone post growth thermal treatments, they are metallized to fabricate MOS capacity in the clean room environment of INL.

The silicon substrates used are (001) and (111) oriented, and doped by boron (type P). The dopage concentration ranges from 10^{16} to 10^{18} cm^{-3}, corresponding to resistances ranging from 1Ω·cm to 0.01Ω·cm. For the high-k application, the dopage of the substrate should not be too elevated ($\leq 10^{16}$ cm^{-3}) so that the inversion phenomenon of the MOS structure is not hindered. A too high dopage makes the Fermi level of the silicon too close to the valence band, impeding the minority porters to participate the depletion and inversion of the capacity. In contrary, for the application as a template of functional oxides, a high dopage concentration is necessary to facilitate the characterization of the polarization of the piezo- (ferro-)electric films on the top.

The gate metal has an important impact on the capacities properties. The metals employed in the microelectronic industry include metal alloys such as TiN[9] or TaN[10], or FUSI (Fully SIlicide[11]) such as NiSi[12]. A low temperature solution was developed at INL to prevent the impact of gate metals fabrication to the electrical behaviors of the dielectric oxides. Following the work of L. Becerra[13], the top gate metal selected in this thesis is Au/Ni. In fact, different attempts were carried out on the metals such as aluminum, gold or nickel. Figure II. 11 presents the C-V and I-V measurements with these gate metals.
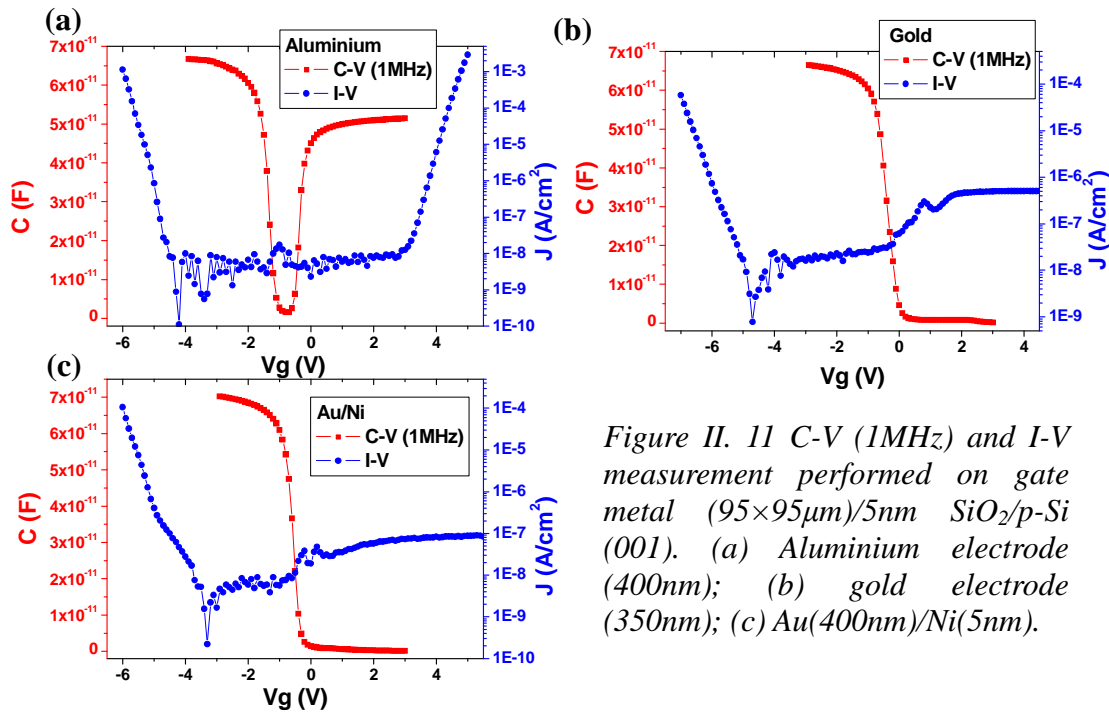
(a)

(b)

(c)

Figure II. 11 C-V (1MHz) and I-V measurement performed on gate metal (95×95µm)/5nm SiO₂/p-Si (001). (a) Aluminium electrode (400nm); (b) gold electrode (350nm); (c) Au(400nm)/Ni(5nm).

As shown in Figure II. 11 (a), the MOS with aluminium electrode demonstrates an abnormal behavior. The C-V curve ascends up in the inversion regime, which should not appear given that the measurement is performed at a high frequency 1MHz. The similar phenomenon also appears for I-V measurement that presents an increase when the voltage exceeds 3V. The rising up of I-V curve can be explained by low intensity saturation current caused by the lack of available minority porters. The irregular behavior is probably connected with the fixed charge or incorporated impurities in aluminium.

The capacitor with gold electrode demonstrates better results (Figure II. 11 (b)). The C-V curve shows no rising up in the inversion regime and the I-V saturates for the positive bias voltages. At low frequency (not shown), the C-V curve increases in the inversion regime because of the generation of the porters. In addition, different from aluminium, the gold does not oxidize in the air.

Finally we decided to choose the bi-layer electrode with a 400nm-gold on top of 5nm-nickel. The results obtained are comparable with those obtained without nickel (Figure II. 11 (c)). The capacity measured in accumulation is about 69pF for a 95×95µm size surface, which is exactly consistence with the theoretical capacity of a 5nm-SiO₂ film (62pF), considering the approximation of our measurements. However, being aware that the gold is

not adapted to the industrial integration given that this metal cannot endure high temperature (poor coherence, diffusion, formation of droplets), all the metal gates of the MOS devices studied in this thesis are composed by a stack of Au/Ni.

II.3.2.3) Fabrication of MOS capacities by lift-off method

The method "lift-off" is employed to deposit the metal gate Au/Ni onto oxides/Si samples. This method uses only lithography without direct etching procedure that might have undesirable effects on the insulator layers. The lift-off process is described as following:

- cleaning the oxides surface rapidly with deionized water and drying with N_2.
- deposition of an adhesion promoter which facilitates the adhesion of the photoresist with the oxides surface using a turnplate.
- deposition of photoresist AZ 5214 at a velocity of 5500 round/min for 30s.
- pre-baking on the heated plate at 110°C for 1 minute to drive off excess solvents and to promote the polymerization of the photoresist.
- Exposition for 1.4 seconds through a metal mask (called "capa") constituted by the square motifs with side lengths from 95µm to 580µm. The instrument used is a Karl Süss MJB3 UV300 SUSS with an exposition wave length of 300nm.
- baking at 110°C for 1 minute in order to reverse the photoresist.
- exposition of the whole plate for 10 second.
- developing the photoresist by agitating the samples in the acetone for 1 minute then rinsing in deionized water.
- post-baking at 110°C for 1 minute to harden the photoresist and eliminate excess solvents.
- introduction the samples masked by photoresist to a Leybold evaporation chamber under vacuum condition.
- deposition of 3nm nickel and 250nm gold successively under vacuum of ~10^{-6} Torr. The metal material are placed in nacelles in graduated form and heated by the law of Joule until the evaporation. The growth rate is monitored by a QCM. The metal layers cover the remaining resist as well as parts of the sample that were cleaned of the resist in the previous developing step.
- lift-off is accomplished by immersing the samples in the acetone. The photoresist is washed out together with the metals covering on it and only the metals in the "hole" have the direct contact with the oxides surface. Thus the pattern of the metal electrodes is the same as that of the mask.

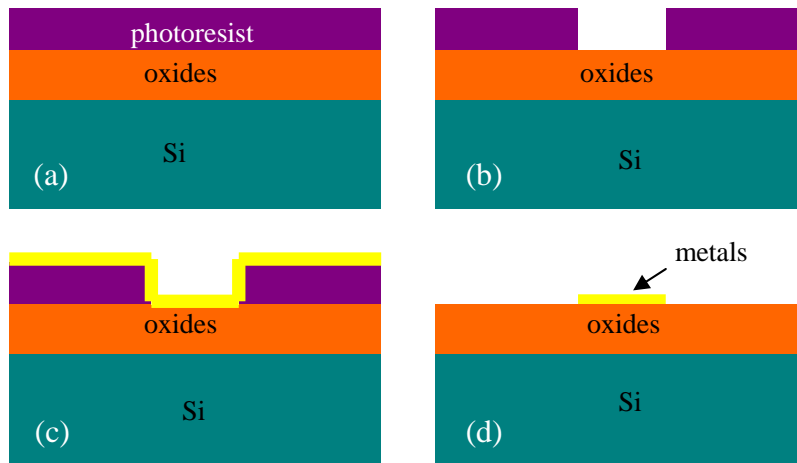The main procedures of lift-off method are illustrated in Figure II. 12.

Figure II. 12 The principle processes of lift-off method: (a) sample with photoresist AZ5214; (b) exposing and developed;(c)deposition of metals and (d) lift-off.

Finally, the Au/Ni electrodes form the same pattern as the mask used, as shown in Figure II. 13.
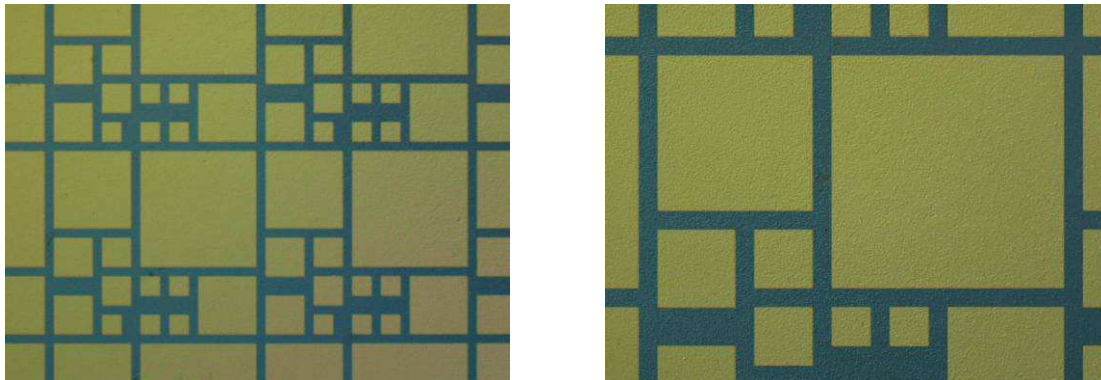
Figure II. 13 Images photoed by optic microscope (zoom ×26 at left and ×52 at right) of an oxides/Si sample metalized by Au/Ni and the squares shows the pattern of the metal electrodes.

II.3.2.4) C-V and I-V measurements

In this section we will describe the C-V and I-V measurements for Metal-Oxide -Semiconductor (MOS) structures in detail. The electrical characterization of both the dielectric and ferroelectric oxides films are realized by this method.

Figure II. 14 Schematic drawing of electrical characterization for MOS devices.

Figure II. 14 illustrates the principle of electrical measurements for MOS devices. The bottom electrode is realized by painting silver at the back of Si substrate. A Karl Suss manual probe station equipped with a HP 4284A impedance meter and a HP 4156B pA-meter is used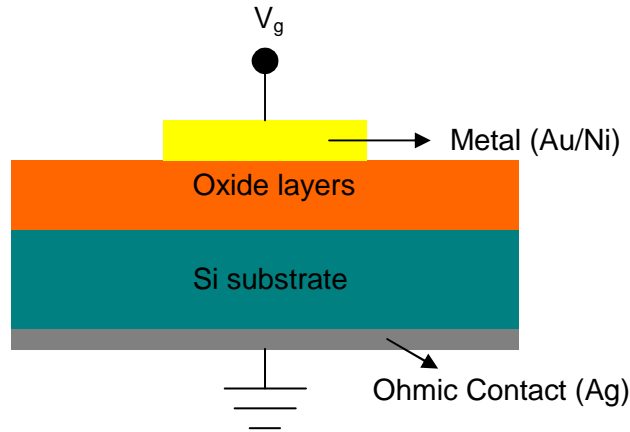 for C-V and I-V measurements. This station is placed in a Faraday cage in order to accomplish the measurement in obscurity and prevent at most outside disturbances. It is however possible to light up the sample to help the generation of minority porters. The station is placed on a vibration-proof table.

All measurements are performed at room temperature and on the different sizes of electrode to prevent the errors that might result from area scaling. However, it should be noted that even for the smallest electrode area size used in this study ($100 \times 100 \mu m^2$) are sufficient large, compared to the thicknesses of oxide films (less than 50nm), to neglect the effect of electric field broadening at electrode edges.

C-V measurement were performed at f=10kHz~1MHz, sweeping from inversion to accumulation and back. I-V measurement were performed firstly from zero to positive and then from zero to negative bias voltage till breakdown.

Figure II. 15 shows the actual equivalent circuit (at left) for C-V measurements. Due to the probe-electrode contact, silicon-back electrode (silver) and resistance of bulk silicon, a series resistance R_s has to be considered. The impedance meter ANGILENT HP 4284A provides parameters of two equivalent models namely the series model (C_{ms}, R_{ms}) and the parallel model (C_{mp}, R_{mp}) for this circuit, as shown in Figure II. 14 at right. Depending on the

gate voltage applied to capacity, this apparatus can deliver different pairs of specific values of the electrical circuit[14]: C_{ms}, R_{ms}, C_{mp}-G_{mp} (G_{mp} is the conductance measured in parallel mode), C_{mp}-D (D is the dissipation factor), etc ... In this work, all the couples measured will be C_{ms}-R_{ms} and C_{mp}-G_{mp}.
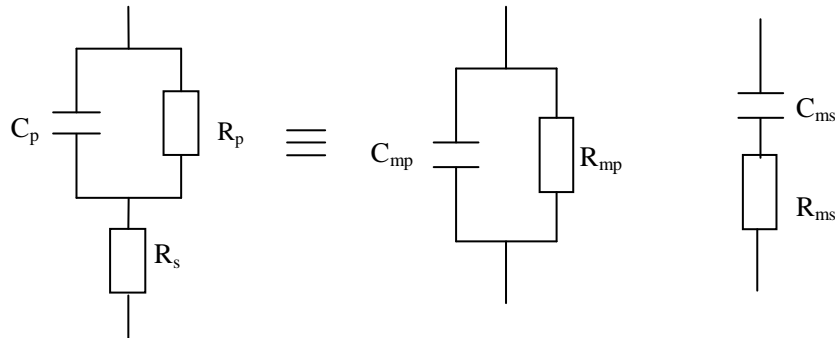

Figure II. 15 Actual circuit for C-V measurement considering series resistance R_s and equivalent parallel and series models provided by HP4284A.R_{mp} and R_{ms} are the leakage or loss resistance in the dielectric layer.

II.3.2.5) Determination of EOT of high-*k* dielectrics using TCV program

Figure II. 16 shows typical C-V measurement curves both at low and high frequencies.
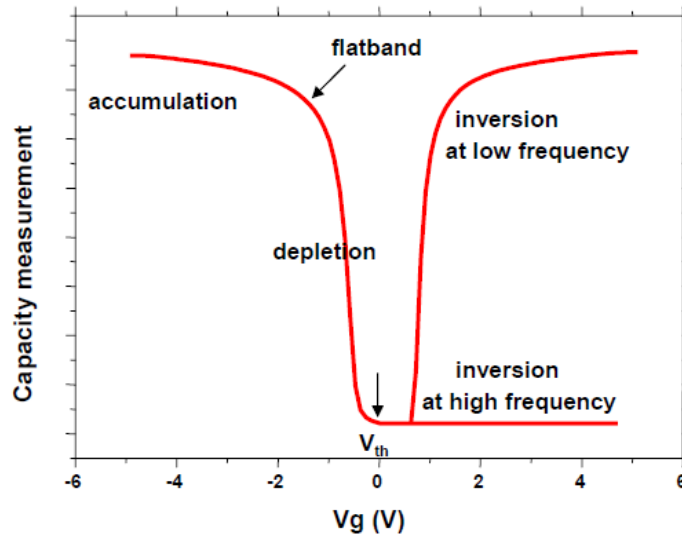
Figure II. 16 Typical C-V curves depending on the applied bias voltage, measured at both low and high frequencies.

When the bias voltage V_g is performed on the grid of MOS structure, three modes could be produced depending on the voltage values. The first is accumulation regime, where V_g<V_{FB} (flatband voltage). In this regime the majority porters in the Si substrate, i.e. the holes, are attracted towards to the oxides/Si interface and form an accumulation layer by the

electrical effect. The second is depletion regime ($V_g > V_{FB}$), where the holes are repelled from the surface of the silicon to the volume of the substrate by the positive charge applied to the grid. Last one is inversion regime ($V_g >> 0$), where all the holes are deserted at the Si surface therefore the minority porters electron becomes the majority porters at the Si surface leading to the inversion of the substrate type at the surface.

In this thesis, all the EOT values of the high-k dielectrics are extracted by using a homemade (at INL) TCV simulation program, which is developed by Christophe Busseret, Nicolas Baboux, Carole Plossu et Alain Poncet[15, 16]. The TCV program permits the reconstruction of the C-V curves based on the experimental data by using the parameters such as substrate type, doping concentration, working function of silicon and metal electrode, effective mass of the oxide, fixed charge Q and D_{it} etc.

In a MOS device, the capacity measured is actually a sum of three terms corresponding three series capacities:

$$\frac{1}{C} = \frac{1}{C_{oxide}} + \frac{1}{C_{grid}} + \frac{1}{C_{substrate}}$$ Equation II -15

In terms of thickness, it can be represented by the relation[17]:

$CET=EOT+t_{grid}+t_{substrate}$ Equation II -16

where CET (Capacitive Equivalent Thickness) is the total thickness corresponding to the measured capacity; t_{grid} (0.5Å for metals) is the depleted zone of the grid; and $t_{substrate}$ results from the 2 dimensional electron gas which is formed at the dielectric/Si interface (appearance of discrete energy levels)[18] but not strictly confined at the interface and therefore generates a complementary thickness approximately several angstroms. (Figure II. 17 (a))

For the samples with thick dielectric films, the t_{grid} and $t_{substrate}$ can be generally neglected and we have CET=EOT. However, if one's objective is to obtain very low EOT values that require thin oxide films, the differences between CET and EOT has to be considered. TCV is a program allowing fitting the experimental C-V measurements taking count in quantum effect which appears for the thin dielectric films. It permits extracting directly the EOT values. (Figure II. 17 (b))
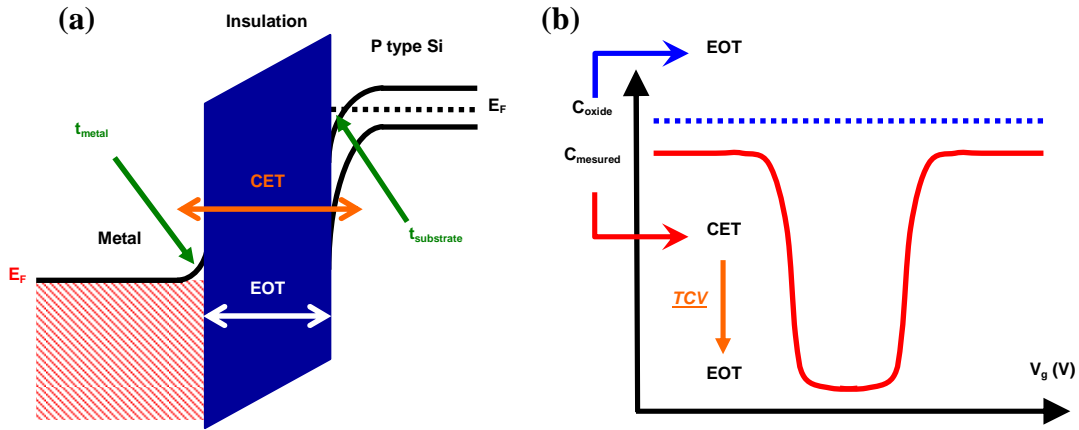
Figure II. 17 (a) Band diagram illustrating the distinction between CET and EOT; (b) Principle of EOT determination using TCV simulation program.

II.3.2.6) Determination of other crucial parameters for high-*k* dielectric

Different from the MOS with SiO_2 layers, the electrical measurements of the MOS structures with high-*k* dielectric layers requires some specific attentions. Except for EOT, some other crucial parameters can be extracted from the C-V measurements:

- Flatband voltage (V_{FB})
- Interface and oxide charges

- **_V_{FB} determination._**

In the MOS structure, the electrons migrate from the metal with higher Fermi level (small work function) to the semi-conductor substrate with lower Fermi level (large work function) through the interface, to align the Fermi levels in different materials, which leads to the curvature of the energy bands. If the applied voltage exactly compensates the difference of the work function between metal and semiconductor, the curvature of the energy bands will disappear. This applied voltage is called flat band voltage V_{FB}. For a ideal MOS system, V_{FB} can be represented as:

$$V_{FB} = \phi_m - \phi_s = \phi_{ms}$$
<div align="right">Equation II -17</div>

To extract V_{FB} from the experimental data, $(1/C^2)=f(V)$ can be traced. In the depletion regime, it is possible to fit part of this curve with a straight line. The intersection of this line with the horizontal axis gives the value of V_{FB}, in consistent with the equation:

$$\frac{1}{C^2} = \frac{2}{qN_A\varepsilon_{sc}S^2}(V - V_{FB})$$
<div align="right">Equation II -18</div>

The calculation of the slope of the line can also obtain the doping concentration N_A of the

substrate, since the dielectric constant ε_{sc} of the semiconductor and the electrode size S are known.

However, this method is only valid for the ideal condition, i.e. the sample has very few defects. In fact the existence of the defects is unavoidable. Different types of charges localize at different position of the MOS structure and have different effect on the C-V behavior of the device. As shown in Figure II. 18, four types of charges can be identified in a MOS structure: interface trapped charges (Q_{it}), fixed oxide charges (Q_f), oxide trapped charges (Q_{ot}) and mobile oxide charges (Q_m). V_{FB} can be influenced by these charges. Thus Eq. II-17 can be modified by[19]:

$$V_{FB} = \phi_{ms} - \frac{Q_f}{C} - \gamma \frac{Q_m}{C} - \gamma \frac{Q_{ot}}{C} - \gamma \frac{Q_{it}(\phi_s)}{C}$$
<div align="right">Equation II -19</div>

where ϕ_s the surface potential, γ the charge distribution factor.

The V_{FB} can be calculated by this equation if the amount of charges in oxide and at the interface and ϕ_{ms} are known.   For the electrode Au/Ni used in this study, nickel is the metal in direct contact with the dielectric. The ϕ_{ms} is theoretically very close to -0.5V (taking the work function of Ni is 4.5eV and the Si doping is 10^{16}cm^{-3}). In practical, the C-V curve is stretched out due to Q_{it} and shifted from the theoretical curve by due to Q_f and Q_m. The V_{FB} determination methods in the literatures have major difficulties for high-k dielectrics because of high leakage current, high D_{it} and high oxide charges. Therefore in this thesis, TCV simulation program is used to facilitate the extraction of V_{FB}.
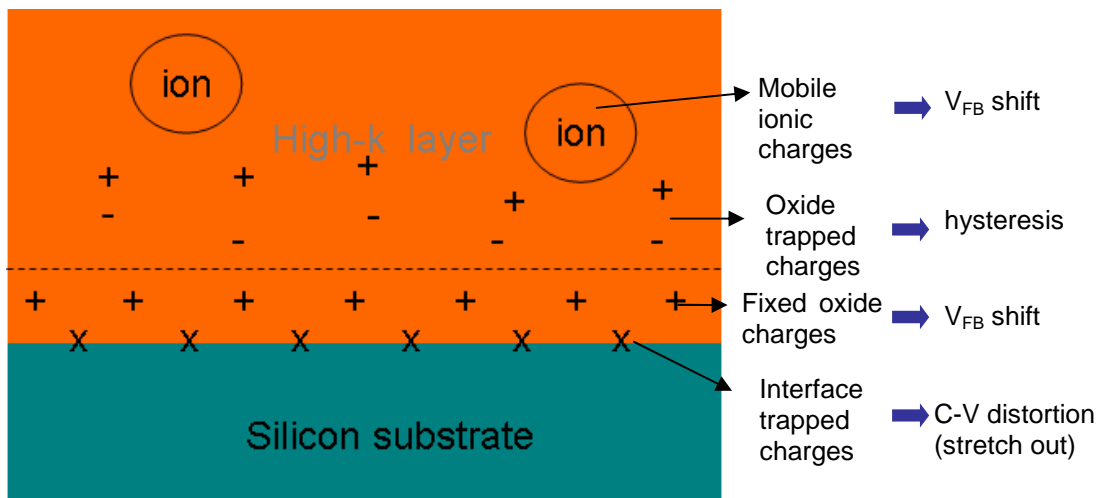

Figure II. 18 Different types of charges existing in the MOS structure and their effects to the C-V behavior of the device.

- $\underline{D_{it}\ determination.}$

Interface trapped charges can be described by the interface state density D_{it}, which is one of the major problems of high-k dielectrics CMOS compared to SiO_2 based MOS that possesses a much lower D_{it}. Interface trapped charges are caused by structural defects, defects resulting from oxidation, impurities at interface and radiation effects (or any other effect that causes bond breaking at silicon interface)[20]. Neglecting the leakage current and the series resistance, the interface state density can be obtained by:

$$D_{it} = \frac{2.5}{q}(\frac{G_p}{\omega})_{max} \qquad\qquad \text{Equation II -20}$$

and $\quad \dfrac{G_P}{\omega} = \dfrac{\omega \cdot G_{mp} \cdot C_{ox}^2}{G_{mp}^2 + \omega^2 (C_{ox} - C_{mp})^2}$ $\qquad\qquad$ Equation II -21

where $(G_p/\omega)_{max}$ represents the maximum of the plot $(G_p/\omega) = f(\omega)$ for a selected voltage; ω the angular frequency $(\omega = 2\pi f)$ and C_{ox} the oxide capacity at the accumulation regime, calculated by a method Dual Frequency Correction (DFCR), which is proposed by Yang and Hu[21].

If the measurement is performed at high frequency, the interface states will not have adequate time to response the change of applied voltage. In order to extract the interface state density, it is necessary to perform the measurement at high and low frequency. DFCR method permits correcting the C-V measurements to achieve more precise EOTs.

- $\underline{Q_{ot}\ determination.}$

Oxide trapped charges (Q_{ot}) are distributed throughout the oxide. Q_{ot} is defined by the shift of flatband voltage, which can be represented as[19]:

$$\Delta V_{FB} = V_{FB}(Q_{ot}) - V_{FB}(Q_{ot} = 0) = -\gamma \frac{Q_{ot}}{C} \qquad\qquad \text{Equation II -22}$$

Assuming that the V_{FB} shift is only caused by Q_{ot} and $\gamma = 1$, ΔV_{FB} is then:

$$\Delta V_{FB} = -\frac{Q_{ot}}{C} = -\frac{Q_{ot}}{3.9\varepsilon_0 S} EOT \qquad\qquad \text{Equation II -23}$$

Therefore Q_{ot} can be determined by the slop of the plot of ΔV_{FB} versus EOT and the change in C-V hysteresis (ΔV_{FB}) can be used to compare the results from the measurement of different layer thicknesses.

II.3.2.7) Determination of parameters for MFIS structure

The ferroelectric layer in the MFIS (Metal Ferroelectric Insulator Semiconductor) structure adds a memory function to the MOS capacitor. The regions of operation described previously are the same, since they refer to the condition of the semiconductor. Due to the hysteretic nature of the ferroelectric, both *Capacitance-Voltage* (C-V) and *Conductance-Voltage* (G-V) curves also demonstrate hysteretic as shown in Figure II. 19. The width of the hysteresis loop is referred to as "memory window" and can have a maximum value C_0 (for the saturated hysteresis), which can be represented as:

$$C_0 = \frac{\varepsilon_0 \varepsilon_r S}{d}$$

Equation II -24

where ε_0 dielectric constant in vacuum (8.85×10^{-12}F/m); ε_r the relative dielectric constant of the ferroelectric film; S the electrode area and d the film thickness.

Thus the ε_r of the ferroelectric film can be roughly estimated (considering the SiO$_2$ insulator layer is normally quite thin). In addition, an index to the amount of polarization is the memory window.
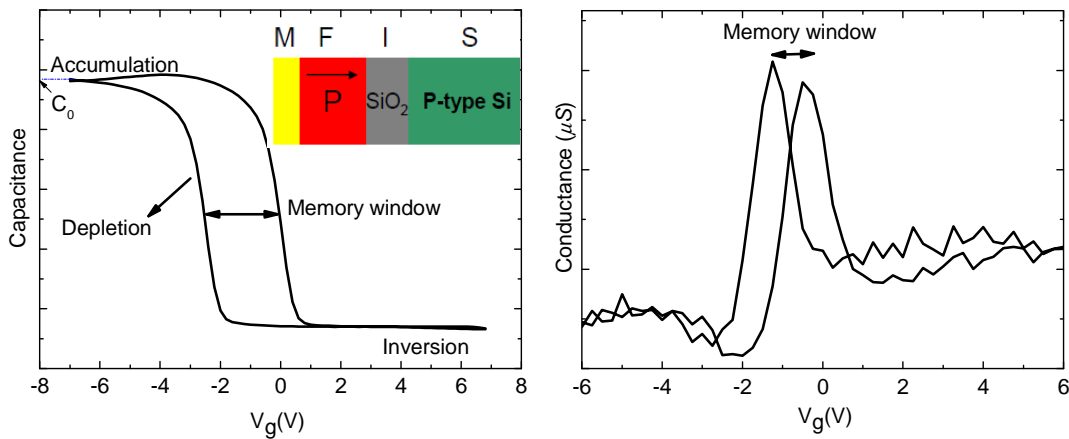

Figure II. 19 C-V curve (left, inset shows the MFIS structure) and G-V curve (right) of MFIS capacitor

II.4) Conclusion

In this chapter, we discussed briefly the physical principles of epitaxial growth. We also introduced the growth and characterization methodologies of the crystalline oxide thin films on Si substrate. In particular, the electrical characterization method as well as the extraction of

different parameter for high-k dielectrics has been explained.

II.5) Reference

[1] G. Saint-Girons, HDR, "*Epitaxie des systemes heterogenes*", Ecole Centrale de Lyon and University of Lyon 1, (2009).

[2] E. Bauer, "*Phaenomenologische Theorie der Kristallabscheidung an Oberflaechen (Phenome- nological theories of crystal deposits on surfaces)*", Z. Kristallogr, **110**, 372 (1958)

[3] A. Dupré, "*Théorie Mécanique de la Chaleur*", Gauthier-Villars, Paris, 369, (1869)

[4] A. E. Romanov and J. S. Speck, "*Stress relaxation in mismatched layers due to threading dislocation inclination*", Appl. Phys. Lett. **83**, 2569, (2003)

[5] J.W. Matthews, A.E. Blakeslee and S. Mader, "*Use of misfit strain to remove dislocations from eptaxial thin films*", Thin Solid Films **33**, 253, (1976)

[6] A.Y. Cho, "*Film Deposition by Molecular Beam Techniques*", J. Vac. Sci. Tech. **8**, S31, (1971)

[7] A. Y. Cho and J. R. Arthur, "*Molecular Beam Epitaxy*", Prog. Solid State Chem. **10**, 157, (1975)

[8] J. Robertson, "*High dielectric constant gate oxides for metal oxide Si transistors*", Rep. Prog. Phys. **69**, 327 (2006)

[9] S. Kim, E. Yoon, M. Kim, S. Suk, M. Li, L. Jun, C. Oh, K. Yeo, S. Lee, Y. Choi, N.-Y. Kim, Y.-Y. Yeoh, H.-B. Park, C. Kim, H.-M. Kim, D.-C. Kim, H. Park, H. Kim, Y. Lee, D.-W. Kim, D. Park, B.-I. Ryu, "*TiN/HfSiO$_x$ Gate Stack Multi-Channel Field Effect Transistor (McFET) for Sub 55nm SRAM Application*", VLSI Technology, Digest of Technical Papers, 72, (2006)

[10] B.H. Lee, R.Choi, L. Kang, S. Gopalan, R. Nieh, K. Onishi, Y. Jeon, W.-J. Qi, C. Kang, J.C. Lee, "*Characteristics of TaN gate MOSFET with ultrathin hafnium oxide (8Å-12Å)*", IEDM, p39, (2000)

[11] E.P. Gusev, C. Jr. Cabral, B.P. Linder, Y.H. Kim, K. Maitra, E. Cartier, H. Nayfeh, R. Amos, G. Biery, N. Bojarczuk, A. Callegari, R. Carruthers, S.A. Cohen, M. Copel, S. Fang, M.Frank, S. Guha, M. Gribelyuk, P. Jamison, R. Jammy, M. leong, J. Kedzierski, P. Kozlowski, V. Ku, D. Lacey, D. LaTulipe, V. Narayanan, H. Ng, P. Nguyen, J. Newbury, V. Paruchuri, R. Rengarajan, G. Shahidi, A. Steegen, M. Steen, S. Zafar, Y. Zhang, "*Advanced Gate Stacks with Fully Silicided (FUSI) Gates and High-K Dielectrics: Enhanced Performance at Reduced Gate Leakage*", Tech. Digest IEDM, p79, (2004)

[12] M.A. Gribelyuk, C. Jr. Cabral, E.P. Gusev, V. Narayanan, "*Interfacial microstructure of NiSi$_x$/HfO$_2$/SiO$_x$/Si gate stacks*", Thin Solid Films **515**, 13, 5308, (2007)

[13] Thesis of L. Becerra, "*Hétérostructures et dispositifs microélectronique à base d'oxydes high-k préparés sur silicium par EJM*", Ecole Central de Lyon, France, (2008)

[14] G.A. Brown, "*Electrical measurement issues for alternative gate stack systems*", tiré de "*High dielectric constant materials*" de H.R. Huff et D.C. Gilmer, Springer series in Advanced Microelectronics, p521, (2004)

[15] C. Busseret, N. Baboux, C. Plossu, A. Poncet, "*Ultra fast full quantum Capacitance and Current-Voltage calculations of MOS capacitors*", Proceedings SISPAD, IEEE, (2006)

[16] P. Palestri, N. Barin, D. Brunel, C. Busseret, A. Campera, P.A. Childs, F. Driussi, C. Fiegna, G. Fiori, R. Gusmeroli, G. Iannaccone, M. Karner, H. Kosina, A.L. Lacaita, E. Langer, B. Majkusiak, C. Monzio Compagnoni, A. Poncet, E. Sangiorgi, L. Selmi, A.S. Spinelli, J. Walczak, "*Comparison of Modeling Approaches for the Capacitance–Voltage and Current–Voltage Characteristics of Advanced Gate Stacks*", IEEE Trans. on Elec. Dev. **54**, 1, 106, (2007)

[17] J. Robertson, "*High dielectric constant gate oxides for metal oxide Si transistors*", Rep. Prog. Phys. **69**, 327, (2006)

[18] Thesis of W. Li, "*Characterization of High-κ Gate Stacks in Meatl-Oxide-Semiconductor Capacitors*", North Carolina State University, (2000)

[19] D.K. Schroder, "*Semiconductor Material and Device characterization*", 2nd ed., Chapter 6, p347, John Wiley & Sons, New York (1988)

[20] E. H. Nicollian and J. R. Brews, "*MOS Physics and Technology*", Chapter 6 and 7, p285 and p319, John Wiley & Sons, New York (1982)

[21] K.J. Yang, C. Hu, "*MOS Capacitance Measurements for High-Leakage Thin Dielectrics*", IEEE Transactions on Electron Devices **46**, 7, 1500, (1999)

Chapter III: Epitaxial growth of crystalline oxides on Si: SrTiO$_3$ and Gd$_2$O$_3$

III.1) Introduction

We will discuss the epitaxial growth of two crystalline oxides-SrTiO$_3$ and Gd$_2$O$_3$ on Si substrate. Epitaxy of these oxides requires a clean and atomic flat silicon surface. We thus first compare different pre-growth treatment for Si substrate. In particular, for the epitaxial growth of perovskite SrTiO$_3$ on Si, we present the Sr-assisted method of the Si surface preparation.

Then we will present the direct growth of crystalline SrTiO$_3$ on Si (001) substrate with no amorphous interfacial layer. The optimal strategy of the direct growth of SrTiO$_3$ on Si will be identified and the SrTiO$_3$ thin film grown at optimal condition will be characterized in detail, including the early stage of the growth and the strain relaxation process of the film.

In order to achieve the "substrate-like" SrTiO$_3$ films on Si substrate, different optimized strategies will be compared and we will that show a substrate-like quality SrTiO$_3$ film on Si (001) can be obtained.

Finally the epitaxial growth of Gd$_2$O$_3$ on Si substrate will be discussed. We will focus on Gd$_2$O$_3$ thin film grown on Si (111), because this system leads to very good oxide structural quality. The influence of oxygen pressure and growth temperature will be discussed and we will show that monocrystalline Gd$_2$O$_3$ can be grown on Si (111) with a sharp interface.

III.2) Preparation of silicon surface

A clean, smooth and atomic level flat Si substrate surface is a fundamental requirement for the high quality epitaxial growth of the thin film. In this section, we will introduce the preparation of silicon surface before the epitaxy of oxides films.

III.2.1) Chemical treatment of Si substrate

The most common used treatment of Si substrate before epitaxy consists in a diluted HF etching process[12]. HF selectively etches SiO$_2$ without attacking the Si substrate surface. Typically, HF is diluted in de-ionized (DI) water to slow down the etch rate, with dilution ratios ranging from 1:1 H$_2$O: HF to 100:1 H$_2$O:HF. For particular critical etching, HF might be diluted with ammonium fluoride (NH$_4$F) to promote more uniform liquid coverage on the silicon surface, which is then called Buffered Oxide Etch (BOE). At INL, we use the

commercial (*Honeywell*) AF 7:1 modified BOE (15% NH_4F and 5.2%HF), the etching rate of which is 70nm/min. In order to identify an optimal preparation method of silicon substrate, we study the Si surface prepared at different conditions, using *in-situ* RHEED and *ex-situ* AFM. Four chemical treatments are described in Figure III. 1. All chemicals used are of electronic grade. The resistivity of the distilled, de-ionized water is 18MΩ.cm.

Method	Details
(a) No HF treatment	Degreasing (ultrasonic cleaning for 10min in ethanol) → nitrogen gas flow 1min
(b) BOE treatment alone	BOE dip 10s → DI-water rinse 30s → nitrogen gas flow 1min
(c) BOE plus UV ozone treatment	Ultraviolet ozone cleaning 20min→BOE dip 30s → DI-water rinse 90s → nitrogen gas flow 1min → Ultraviolet ozone cleaning 2min
(d) Standard industrial treatment	Degreasing (ultrasonic cleaning for 5min in trichloroethylene, acetone and ethanol respectively) → diluted HF solution (1HF:25H₂O) dip 30s→ DI-water rinse 1min→ diluted sulfuric acid (1 H_2SO_4: $1H_2O_2$) dip10min→ DI-water rinse 5min→ diluted hydrochloric acid (3HCL: 1H₂O: 1H₂O₂) dip 10min → DI-water rinse 5min→diluted HF solution (1HF:25H₂O) dip 30s → DI-water rinse 1min → nitrogen gas flow 1min → Ultraviolet ozone cleaning 2min

Figure III. 1 List of chemical treatment tested

Once the chemical treatments are finished, the Si substrate is introduced into our RIBER 2300 MBE chamber and annealed in UHV condition. The base pressure in the chamber is 2×10^{-10} Torr and it raises up to $2\sim3\times10^{-9}$ Torr during annealing. The annealing temperature which is monitored by both thermocouple and infrared pyrometer is increased from 300°C to ~950°C in 100°C, 4~5min steps and is stabilized at 950°C for 30 minutes. During this step, possible residual carbon impurities on surface may react with Si to form silicon carbide (*β*-SiC) nanoparticles, leading to the observation of a set of characteristic spots on the RHEED pattern. This reaction typically occurs for temperatures larger than 750°C~800°C.

Ex-situ AFM has also been employed to observe the substrate surfaces. Figure III. 2 presents the RHEED patterns after annealing and AFM results of the Si (001) substrates treated by different treatments.
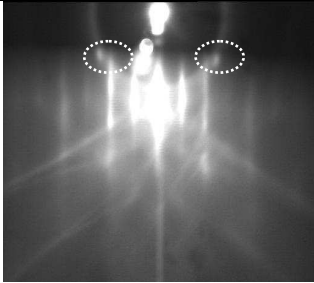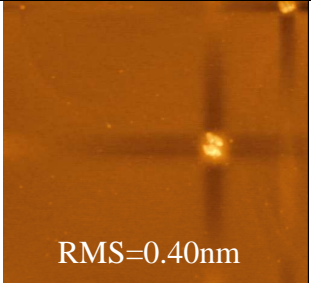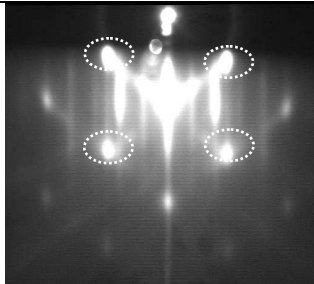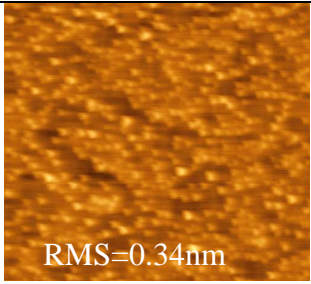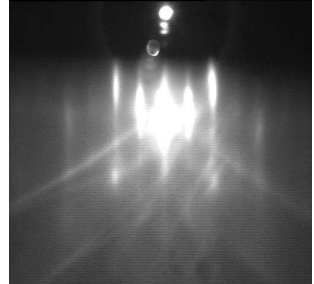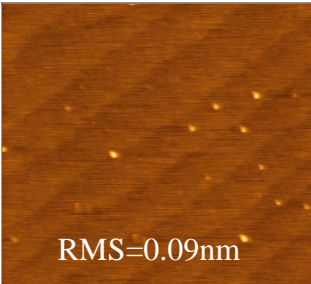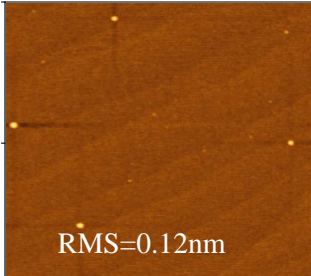
Methods	RHEED along Si[110]	AFM ($1{\times}1\mu m^2$)
(a) No HF treatment		RMS=0.40nm
(b) BOE treatment alone		RMS=0.34nm
(c) BOE plus UV ozone treatment		RMS=0.09nm
(d) Standard industrial treatment		RMS=0.12nm

Figure III. 2 RHEED patterns along Si [110] azimuth and $1{\times}1\mu m^2$ AFM images of Si(001) substrates treated by different preparation methods.

According to the RHEED patterns along Si [110] azimuth, all the Si (001) substrates present a (2×1) reconstructed surface after the annealing in UHV, which corresponds to silica (SiO₂) free surfaces. As for many semiconductor surface reconstructions, this (2×1) reconstruction allows reducing the surface energy by forming surface chemical bonds[3]. The

surface energies of the ideal (1×1) and (2×1) reconstructed surfaces are 2.58J/m^2 and 1.51J/m^2 respectively[4]. In the case of the Si (001) surface, surface atoms form dimmers along the [110] rows, leading to periodicity doubling along the [110] direction[5,6]. Figure III. 3 (a), (b) shows the models of the ideal (1×1) and (2×1) reconstructed Si (001) surface, top view (upper) and side view (below). Figure III. 3 (c) shows a STM image of (2×1) reconstructed Si (001) surface[7], in which two different colors correspond to two terraces: the dimmer orientation rotates of 90° from one terrace to the neighboring one.

| (a) | (b) | (c) |
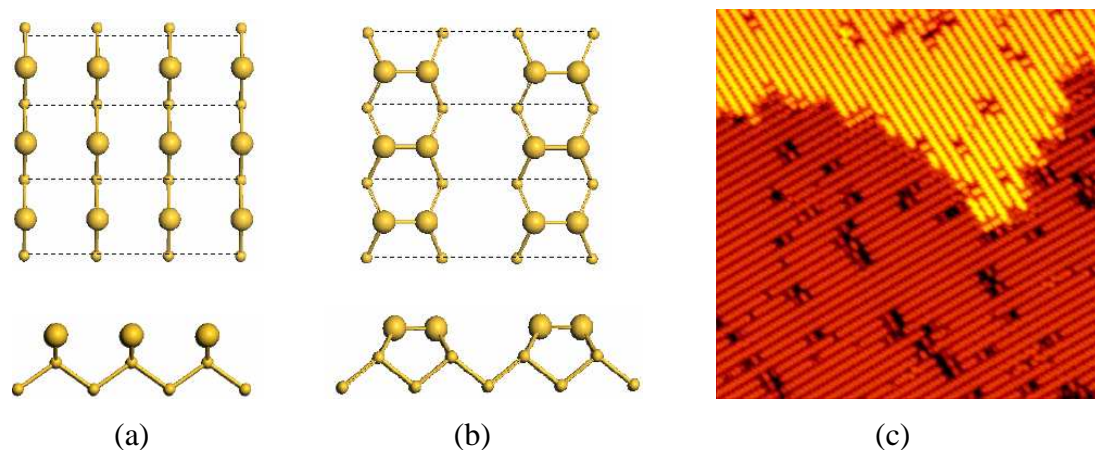
Figure III. 3 Si (001) reconstruction models: (a) Ideal (1×1) surface, (b) (2×1) reconstructed surface, top view (upper) and side view (below).The larger spheres represent the atoms at the first layer, in which the more yellow ones indicate the atoms buckled up[4]. And (c) STM image of (2×1) reconstructed surface including two terraces[7].

On the RHEED patterns of Figure III.2, spots related to the formation of *β*-SiC (circled by dotted line) next to the Si streak lines are observed for the silicon surfaces treated using the "no HF" and "BOE alone" methods. For the "no HF" treatment, the presence of *β*-SiC is related to the reaction of carbon impurities initially present at the Si/SiO₂ interface or at the SiO₂ surface with silicon during high temperature annealing. For "BOE alone" method, we find that the relative intensity of the spots corresponding to SiC is stronger than that observed for the "no HF" treatment. This suggests that additional carbon is absorbed on the bare Si surface during the transfer to the epitaxial chamber after chemical treatment. HF treatment is known as passivating the Si surface by saturating dangling bonds (formation of Si-H or Si-OH bonds)[8]. In our case, this passivation is not perfect, resulting in adsorption of carbonic impurities, which are very difficult to be desorbed[9]. Figure III. 4 shows a model of the "BOE alone"-treated silicon surface and possible chemisorption sites for carbonic impurities.

On the other hand, for the Si surface treated by "BOE plus UV ozone" and "Standard

industrial" methods, the implementation of a UV ozone process after BOE treatment has been found to effectively decrease the carbonic impurities: the RHEED show clear, ordered patterns without any β-SiC spot. In addition, the presence of Kikuchi lines indicates a clean, smooth surface. The UV ozone process (2min) removes the carbonic impurities in form of Si-O-C or Si-C and converts the terminated surface into a ~1nm SiO_2 layer that protects Si surface during transfer to the reactor.

The AFM images of Figure III.2 confirm the good quality of the surfaces treated by method (c) and (d). We can clearly observe the atomic steps of silicon and their RMS values are as low as 0.09 nm and 0.12nm respectively. The "BOE plus UV ozone" treatment which is much easier to perform than standard industrial treatment leads to a clean and atomic flat surface with an even smaller RMS. In contrast, the Si surfaces treated by method (a) and (b) have relative high RMS values and there is no presence of atomic steps. SiC nanoparticles are clearly observed in these images, the density of which is the highest for treatment (b), thus confirming the RHEED analysis.
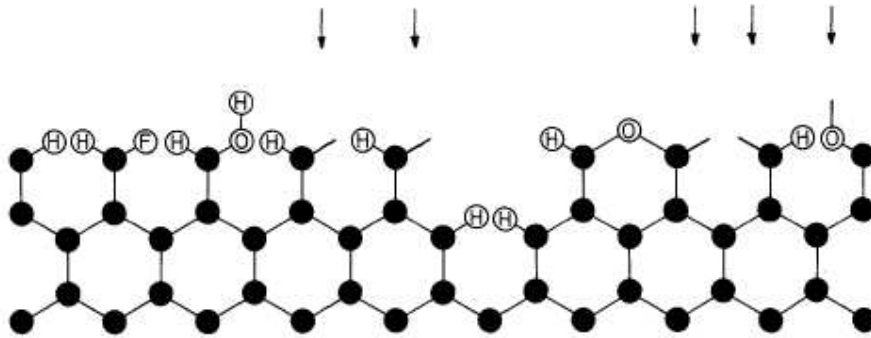
Figure III. 4 Model of "BOE alone"-treated silicon surface. Arrows indicate the chemisorption sites for the carbonic impurities (Ref.8).

In case of (111)-oriented silicon substrate, the Si surface treated by the method "BOE plus UV ozone" following with the annealing at ~1000°C also demonstrates good quality, as revealed by RHEED and AFM characterizations (Figure III. 5).

RHEED along Si[110]	RHEED along Si[211]	AFM (1×1μm^2)

RMS=0.35nm
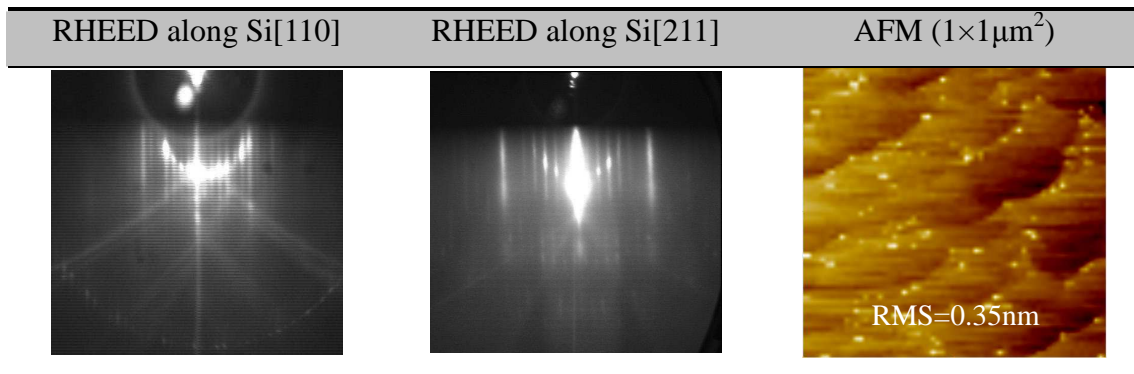
Figure III. 5 RHEED patterns and 1×1 μm^2 AFM image of Si (111) substrate treated by "BOE plus UV ozone" methods.

The RHEED pattern exhibits clear, well ordered streak lines of silicon without any β-SiC spots. The presence of Kikuchi lines indicate a very smooth surface and Laue zones are obseved. Si presents a (7×7) reconstructed surface, which reversibly turn to a (1×1) unreconstructed surface below about 850°C.[3]. The surface energies of (1×1) and (7×7) Si surfaces are 2.23 J/m^2 and 1.42 J/m^2 respectively. The (7×7) reconstruction is described in Figure III. 6.

(a) *(b)*
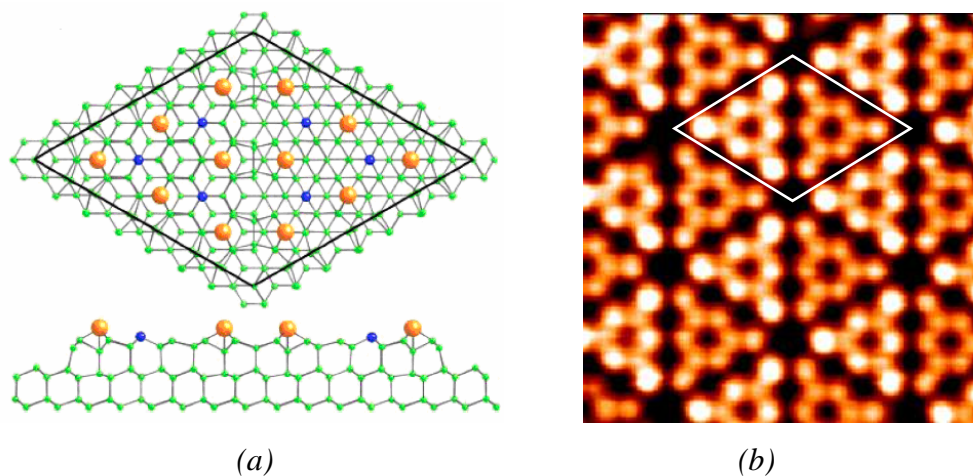
Figure III. 6 (a) Top view (upper) and side view (below) of (7×7) reconstructed Si (111) surface model; (b) Experimental STM image (Ref.10).

The Si (001) and Si (111) surfaces treated by "BOE plus UV ozone" consist of the starting point of all the subsequent oxides epitaxial growth on silicon substrates.

III.2.2) Strontium passivated Si (001) surface

A great challenge of the growth of oxides on Si substrate is to manage completely

oxidizing the metal elements of the oxides without forming silica or silicates at the oxide/Si interface. For this purpose, we use a strontium-assisted passivation method developed by Motorola[11] to clean, passivate the silicon surface and ultimately obtain a template with a Sr/Si (2×1) surface reconstruction that allows the epitaxial growth of SrTiO₃ on Si (001). The detailed process of is shown in Figure III. 7.

(a) Sr deposition

(b) Sr promoted SiO desorption and SiO₂/Si interface reaction:
$$SiO_2 + Si \rightarrow 2SiO \uparrow \quad and$$
$$SiO_2 \rightarrow SiO \uparrow + O^+ + e^-$$

(c) Pit formation was suppressed by Sr passivation. SiO₂ decomposition continues.
$$SiO_2 \rightarrow SiO \uparrow + O^+ + e^-$$

(d) Cleaned Sr terminated Si(001) surface
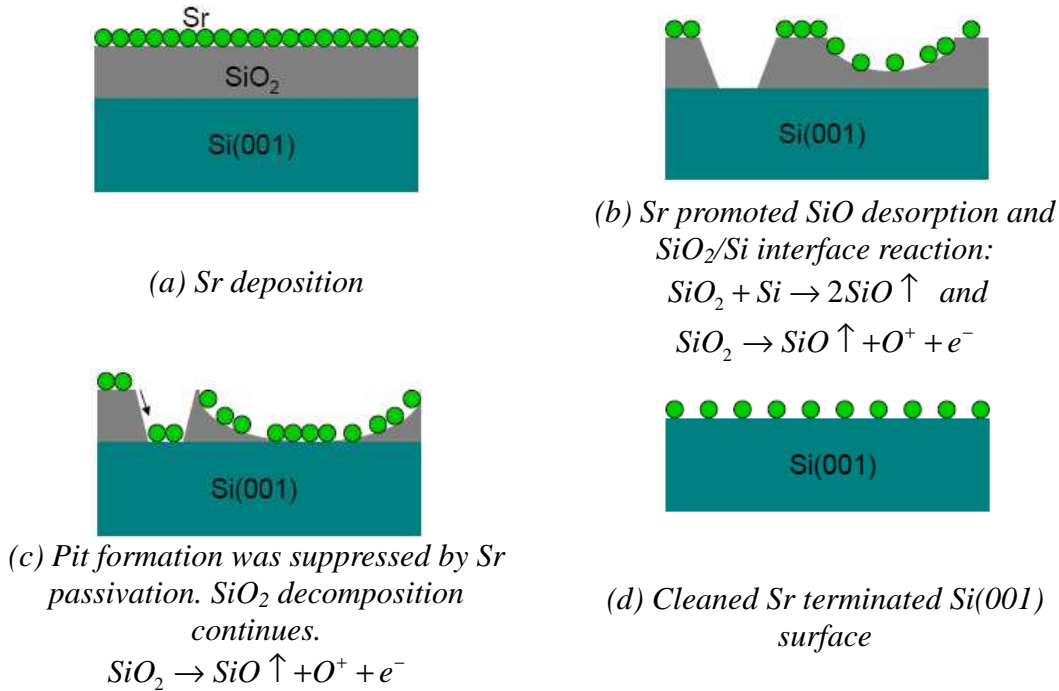
Figure III. 7 Mechanism of deoxidation using strontium (Ref.11).

After the preparation with "BOE plus UV ozone" method, the silicon surface is covered by ~1nm-thick silica. Then a small amount (2ML) Sr is deposited on the SiO₂-Si surface in UHV at 600°C followed by an annealing at 750°C for 30min. During the annealing process, Sr or SrO acts as a catalyst to promote the decomposition of SiO₂:

$$SiO_2 + Sr(SrO) \rightarrow SiO(g) + O + Sr(SrO)$$

Once the SiO₂ is removed and Si surface is exposed to the vacuum, the Sr diffuses into the void and passivates the Si surface. This process results in an oxygen- and carbon- free, atomically smooth surface and leaves 1/6~1/3 ML Sr on the silicon surface, which can be characterized by a Si surface observed at 600°C, as shown in Figure III. 8. The ×2, ×3 and ×6 feature of the RHEED pattern along Si[110] orientation corresponds to a mixture of (3×2) and c(6×2) phases of Sr/Si system.
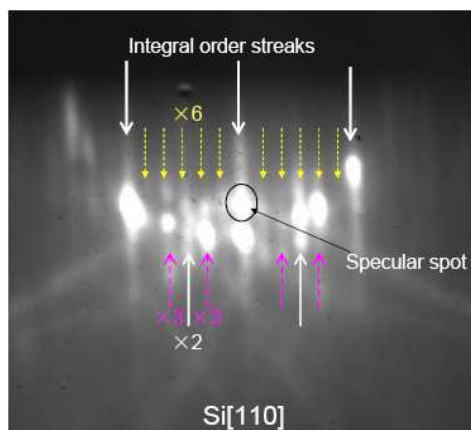
Figure III. 8 Reconstruction of Si surface covered by 1/6~1/3 ML Sr

Adding strontium on this at 600°C modifies the reconstruction, which turns to a ×2 feature along Si [110] direction, corresponding to 1/2 ML Sr-coverage on the silicon surface (Figure III. 9). After exposition to oxygen for 1min at approximately 400°C, this (2×1) phase surface remains stable and forms a half monolayer SrO on silicon surface, ultimately serving as a template for the subsequent growth of SrTiO₃ on Si(001). Figure III. 10 shows the model of 1/2 ML Sr covered Si surface and the experimental STM image.

Figure III. 9 RHEED patterns of Si surface covered by 1/2 ML Sr, which lead to a ×2 reconstruction along [110] direction.
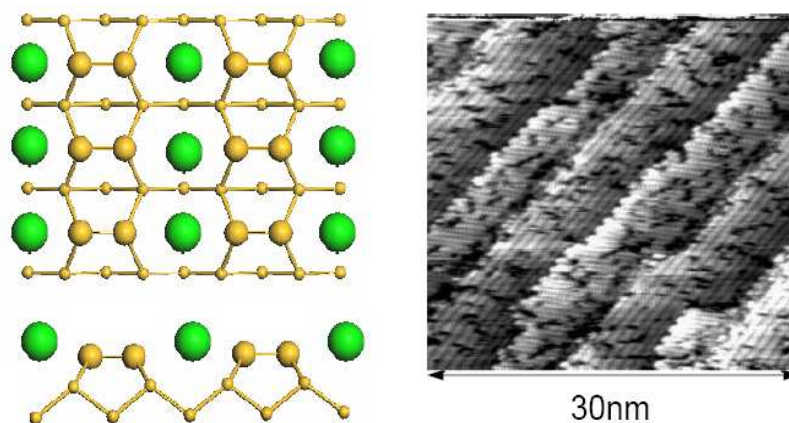
Figure III. 10 Top view (left upper) and side view (left below) of the model of Si surface covered by 1/2 ML Sr and a STM image (Ref.12) (right)

88

III.3) Epitaxial growth "window" of SrTiO₃/Si (001)

III.3.1) Introduction

Strontium Titanate (SrTiO₃, STO) possesses a perovskite-type structure (*Pm3m*) and the lattice mismatch between STO (a_{STO}=3.905Å) and Si (a_{Si}= 5.431 Å) is fairly small (1.69%) with STO unit cell rotated 45° around Si surface [001] axis, as shown in Figure III. 11(a). The surface energy of SrO-terminated STO and the STO-Si interface energy are 0.801 J/m^2 and 0.574 J/m^2 (Ref.13). Considering that the Si surface energy is 1.7 J/m^2 (Ref.13), we obtain $\gamma_{Si} > \gamma_{STO} + \gamma_{interface}$, i.e. STO wets the Si surface[13]. Therefore the epitaxial growth of 2D STO layer on Si is theoretically possible. Furthermore, STO is predicted to be thermodynamically stable on Si up to 1000K[14]. Figure III. 11(b) shows a model of the epitaxial growth of STO on Sr-passivated Si surface (covered with 1/2 ML SrO layer) that we discussed in last section.
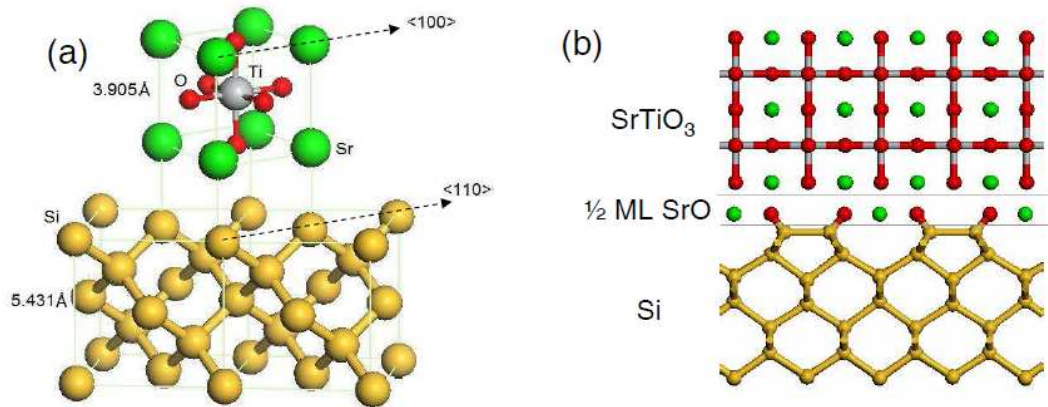
Figure III. 11 The model of (a) Epitaxy relationship between STO and Si (001) substrate; (b) epitaxial growth of STO on 1/2 ML SrO covered Si substrate.

STO presents a high dielectric constant of 300, a band gap of 3.3eV and its conductive and valence bandoffsets with respect to Si are -0.14eV and 2.4eV. STO is paraelectric at room temperature and becomes ferroelectric at -238°C. At approximately -168°C, STO undergoes a transition from cubic phase to tetragonal phase[15], with a small distortion value c/a=1.0005 and this transition is related to the rotation of the oxygen octahedrons[16].

In this section, we will firstly introduce the homoepitaxy of STO. This work has been well developed at INL by G. Delhaye. We will show how STO/STO homoepitaxy allows fixing the oxide stoichiometry and determining the growth rate. In the second and third part, we will study the influences of growth temperature and oxygen partial pressure to the STO/Si system and identify the optimal growth condition. Then we will discuss the strain relaxation

process, particularly at the early stages of the growth, of the STO film grown under optimal condition.

III.3.2) Homoepitaxy of SrTiO₃

III. 3.2.1) Preparation of the STO substrate

A SrTiO$_3$ (001) surface has two possible terminations: SrO and TiO$_2$, since the crystal consists of an alternating stack of these two atomic planes. Calculations predict different surface energies for the two possible terminations: 0.801 J/m^2 for SrO and 2.127 J/m^2 for TiO$_2$ respectively[17,18]. In order to achieve a perfect, i.e. well-defined surface on an atomic scale, as well as a single terminated surface, the cleaning method developed by Kawasaki et al.[19] is generally employed, which consists in a treatment of the SrTiO$_3$ substrates with an NH$_4$F buffered HF solution (BHF) with pH 4.5 leading to a uniform TiO$_2$-terminated surface. Some detailed researches[20,21] demonstrates that this TiO$_2$ termination on the surface is incomplete, whose fraction was estimated to be 88±2%. In INL, we use a chemical treatment including a short dip (30s) in the commercial BOE solution introduced in III. 2. 1), following with a rinse in DI water for 10 seconds. Then the substrate is introduced into the epitaxy chamber for an annealing at 650°C under an O$_2$ partial pressure of 1×10^{-6}Torr for 1 hour, allowing minimizing the formation of oxygen vacancies in the material[21] and the carbonic pollution[22] on the surface. Ex-situ AFM measurement has been performed for the STO substrate after chemical and thermal treatments, revealing its surface morphology, as shown in Figure III. 12.

(a)   *(b)*   *(c)*
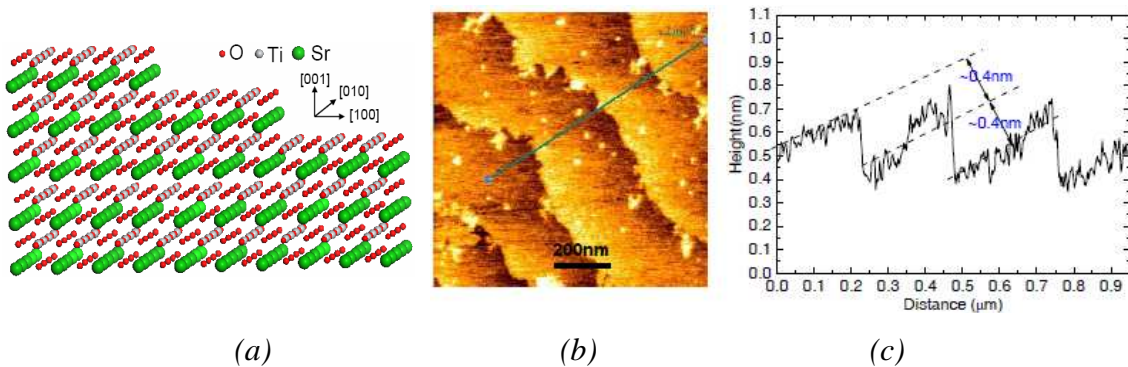
Figure III. 12 (a)Model of the TiO₂-terminated STO surface; (b)experimental 2μm×2μm AFM image showing a step-terrace structure of STO surface and (c) the vertical profile of the line marked in (b),exhibiting the height of the step is 0.4nm, i.e. a unit cell of STO.

The AFM image exhibits a flat and well-defined STO surface with a step-terrace structure and the step height equals to 0.4nm corresponding to one unit cell STO. The TiO$_2$-terminated

terrace edges meander along the two crystallographic axes [100] and [010][23]. The RMS of the STO surface is 0.29nm. Figure III. 13 shows the RHEED patterns of STO substrate before homoepitaxial growth. We can observe that the streak lines are well-defined with clear Kikuchi lines, which demonstrates a flat and good crystal quality surface. The half-order fractional streaks appear along both [100] and [010] directions, demonstrating a two domain (2×1)+(1×2) surface reconstruction, which corresponds to a TiO_2 or TiO_x (x is slightly smaller than 2) terminated STO surface. This is due to the creation and organization of the oxygen vacancies during the annealing process. In essence, for different treatment methods and annealing temperatures STO surface exhibits different reconstruction phases. In addition to the above-mentioned (1×1) and (2×1)+(1×2) reconstructions, several other reconstructions are also reported[24,25,26,27,28,29,30,31,32,33,34,35,36], such as (2×1), c(4×2), c(4×4), (4×4) c(6×2), (6×2), (√5×√5)-R26.6°, (√13×√13)-R33.7°. Generally, the higher order (larger primary unit cell) reconstruction usually requires higher annealing temperature and thus higher density of the bulk oxygen vacancy[37].
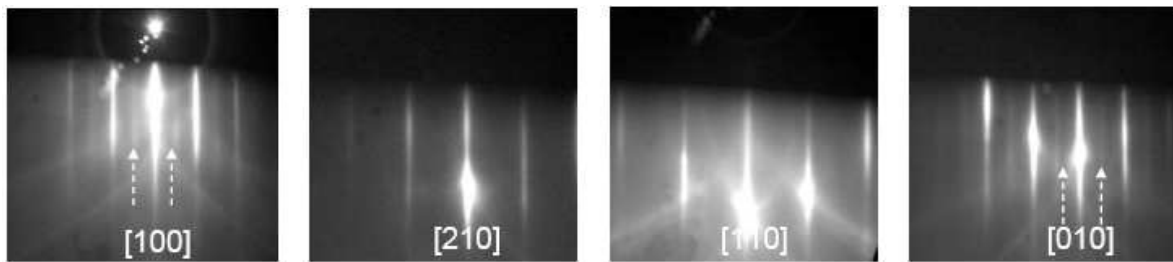
Figure III. 13 RHEED patterns of the STO substrate after the chemical treatment and annealing process. The arrows shows ×2 reconstruction along [100] and [010] directions.

III. 3.2.2) Epitaxial growth of STO on STO substrate

The configuration of our MBE chamber allows depositing STO by two methods: co-deposition (sending all the elements Sr, Ti and O simultaneously) and layer-by-layer deposition (growing alternatively the SrO plane and TiO_2 plane). Because the presence of Sr promotes titanium oxidation (see I.3.2), codeposition method is used in this study. This method has been studied[38] by Gabriel Delhaye during his PhD thesis and the results lead to the optimal growth condition of the homoepitaxy of STO as following:

(1) <u>Growth temperature</u>: between 450°C~750°C

Homoepitaxy can be performed between 250°C to 750°C and all the RHEED patterns show a streak-feature revealing monocrystalline epitaxial growth. This means the crystallization temperature of STO is as low as 250°C. Nevertheless, when the temperature is

lower than 450°C, the Bragg spots gradually cover the streak lines from the beginning of the growth, exhibiting the appearance of 3D structure leading to more rough surfaces.

(2) Oxygen partial pressure: 5×10^{-7} Torr~1×10^{-5} Torr

As shown in Figure I. 20 (chapter I), in order to completely oxidize the metals of strontium and titan, the oxygen partial pressure should be 1×10^{-7} Torr and 1×10^{-6} Torr respectively. Although the presence of Sr in codeposition method will make the oxidization of Ti easier, the PO$_2$ should be higher than 5×10^{-7} Torr. In addition, due to the configuration of our MBE chamber, PO$_2$ is technically limited to 1×10^{-5} Torr. In this range of oxygen pressure, there is no significant variation of RHEED patterns.

(3) The growth rate: 1~3 ML/min

Too high growth rates lead to amorphous STO growth due to limited adatom surface diffusion. In our case, because of the intrinsic characteristic of Ti evaporation cell, the growth rate is limited between 1~3 ML/min. The variations of RHEED patterns for these two growth rate demonstrate no evident difference.

In this optimal growth condition, a high quality, two-dimensional monocrystalline STO could be homoepitaxial grown on STO substrate. Sr/Ti stoichiometry can be finely tuned during homoepitaxy by monitoring RHEED reconstructions (Ref. 38): a ×2 reconstruction is observed along the [100] STO azimuth when the surface is Ti-rich, while a ×2 reconstruction is observed along the [110] STO azimuth when the surface is Sr-rich. (Figure III. 14). By adjusting the Sr and Ti fluxes, ×1 reconstructions are achieved for both [100] and [110] azimuths, which represents a good stoichiometry of STO film. Furthermore, the growth rate could be measured by recording the intensity oscillation of the specular spot.
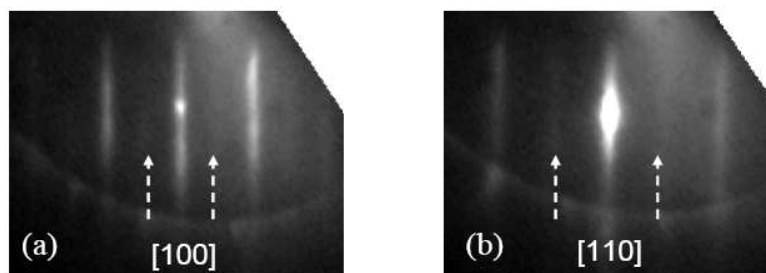

Figure III. 14 RHEED pattern of (a) TiO₂-rich and (b) SrO-rich STO film surface.

III.3.3) SrTiO₃/Si (001): growth temperature dependence

Generally speaking, in order to achieve a two-dimensional growth for an epitaxial system with small lattice mismatch, two conditions have to be satisfied: 1) thermodynamically, the

epitaxial film has to wet the substrate, which is the case of SrTiO$_3$/Si system as discussed in section III.3.1; 2) kinetically, the growth temperature has to be sufficient to confer to adatoms sufficient surface mobility to build the growing crystal. Too low temperatures lead to amorphous layers. Particularly for the epitaxial growth of oxides on Si substrate, due to the presence of oxygen and to the reactivity of Si with this element[39], two additional conditions have to be considered: 1) the growth temperature has to be not too high to avoid reactions between the oxide and Si; 2) the chemical potential of oxidants, i.e. oxygen (molecular or atomic) pressure has to be limited to prevent the oxidation of Si surface but high enough to form the required phase of the oxide (oxidization of the metallic atoms of the oxide lattice, but not of the Si surface).

Abovementioned analysis suggests that an epitaxial growth "window" concerning the suitable growth temperature and the oxygen partial pressure exist for the heteroepitaxy of SrTiO$_3$ on Si (001) substrate. In this section, we discuss the temperature dependence of STO/Si system.

In order to protect the Si surface from oxidatizing and achieve the required oxygen stoichiometry, a strategy including the meticulous oxygen control has been used, as illustrated in Figure III. 15. The Si surface is clean and highly-ordered covered with 1/2 ML-thick Sr after Sr-assisted deoxidization process. The oxygen with $P_{O2}=2\times10^{-8}$ is introduced to the MBE reactor via a pressure-regulated plasma chamber by controlling a needle valve to form 1/2ML SrO as a template for the STO growth. For the initial 2ML STO, the Sr and Ti are codeposited under an ambience of $P_{O2}=5\times10^{-8}$ Torr, which is raised up to 2×10^{-7} Torr~1×10^{-6} Torr for the subsequent Sr and Ti atom fluxes.
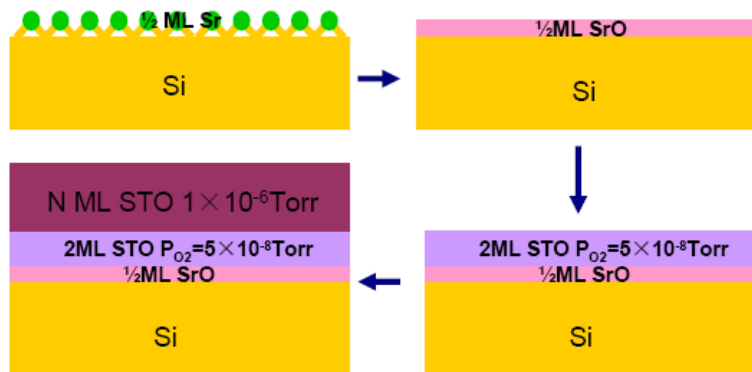
Figure III. 15 The sequent oxygen control strategy of STO epitaxy

With this sequent oxygen control strategy, STO thin films are deposited on silicon substrate at different temperatures from 340°C~500°C. The characteristics such as RHEED, TEM, XRD and IR are employed to study the crystallization, surface of the film and the interface between STO and silicon.

III.3.3.1) RHEED

Two series of 4nm-thick and 45nm-thick STO films are grown on Si (001) substrate, at different temperatures. Figure III. 16 shows the final RHEED patterns of these samples along STO [100] azimuth.

340°C	360°C	420°C	450°C	500°C
4nm				
45nm				
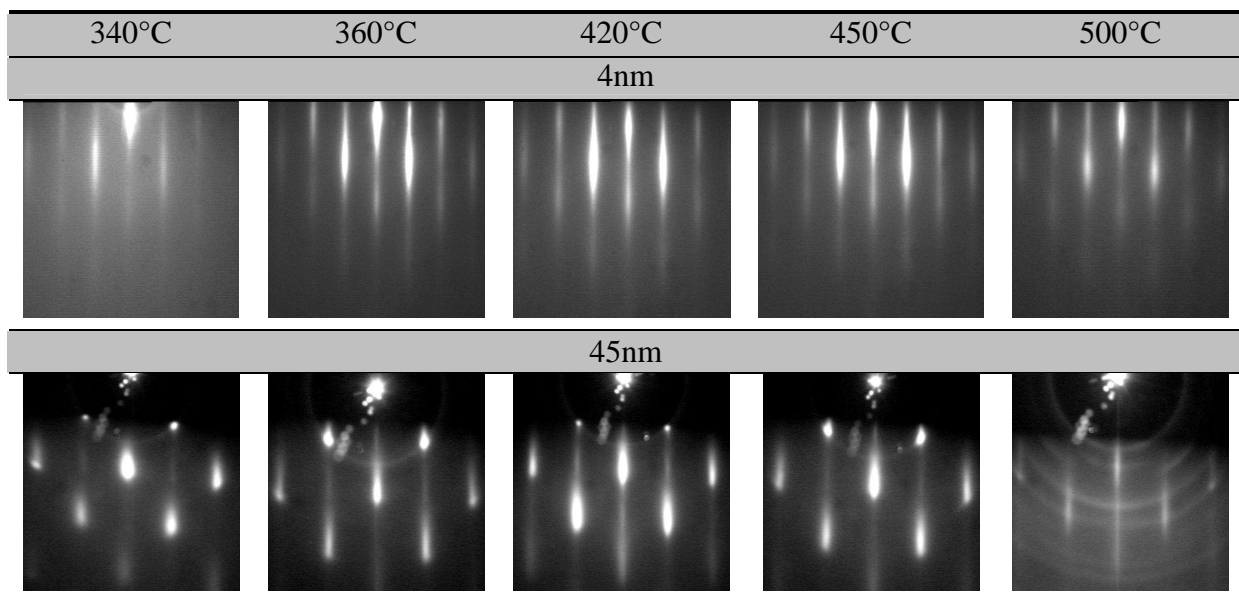
Figure III.16 Variation of RHEED patterns of STO film (4nm and 45nm) grown at different temperatures.

We firstly discuss the 4nm-thick samples. Apparently, the growth of STO film on silicon demonstrates strong temperature dependence. For the two extreme temperatures (340°C and 500°C), the RHEED patterns exhibit both streak lines and diffuse halo, suggesting the coexistence of crystalline and amorphous phases. These similar RHEED patterns result from different mechanism: a too low temperature (340°C) leads to partially amorphous STO layer due to the limited mobility of the surface adatoms (see II.2.1); while a too high temperature (500°C) induces a reaction between the deposited film and the underlying substrate, leading to the formation of an amorphous silicate interface.

For the samples grown between 360°C and 450°C, all the RHEED patterns displays a

clear, well-defined streak line feature, suggesting the two-dimensional single crystalline quality of STO films. One has to notice here that RHEED only provides information on the first few monolayers below the surface of the growing film.

As the film thicknesses increase to 45nm, the RHEED patterns of samples grown at 360°C~450°C displays a feature of streaks line covered by Bragg spots, suggesting the increase of the surface roughness and the 3D growth mode of the films. This behavior is consistent with the STO homoepitaxy for which the optimal temperature is 550°C (see III. 3.2.2)[38]. At too low temperature, intensity oscillation of the specular spot on RHEED is rapidly damped due to limited adatom mobility. The RHEED pattern of the sample grown at 500°C displays Debye-Scherrer rings indicating the polycrystalline growth. It is surprisingly that the sample grown at 340°C undergoes a transition from an amorphous-crystalline mixture phase to single crystalline phase as the film thickness increases (~20ML, not shown here) and simultaneously follows a 3D growth mode (spotty feature on RHEED).

III.3.3.2) TEM

The 4nm-thick samples grown at 360°C and 450°C were examined by TEM, (Figure III. 17 (a) and (b)) The sample grown at 360°C presents a good structural quality and an atomically abrupt interface with silicon. In contrast, a ~1.2nm-thick amorphous silicate layer is formed at the interface between STO grown at 450°C and the Si substrate, as already described elsewhere[40,41]. According to these results, 360°C appears as the optimal temperature for growing high quality STO/Si layers with an abrupt heterointerface.
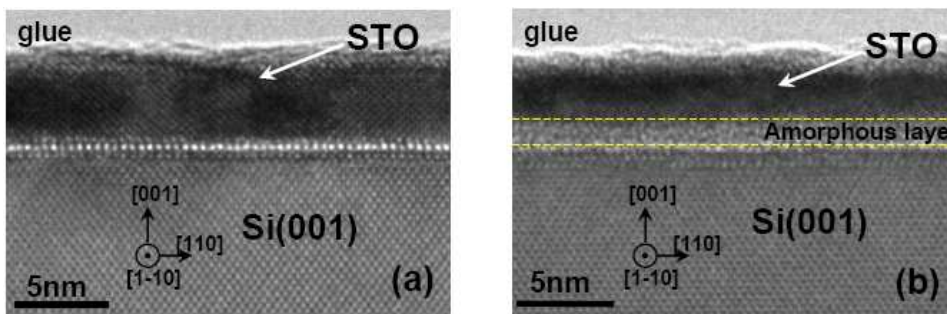
Figure III. 17 High-resolution TEM cross-sectional view of STO/Si(001) grown at (a)360°C and (b) 450°C, with the Si directions denoted inset.

Figure III. 18 shows the diffraction pattern corresponding to Figure III. 17(a). The crystal orientation of STO with respect to Si can be deduced from this figure and as expected, the

epitaxy relationship is defined as [110] STO (001)//[100] Si (001).
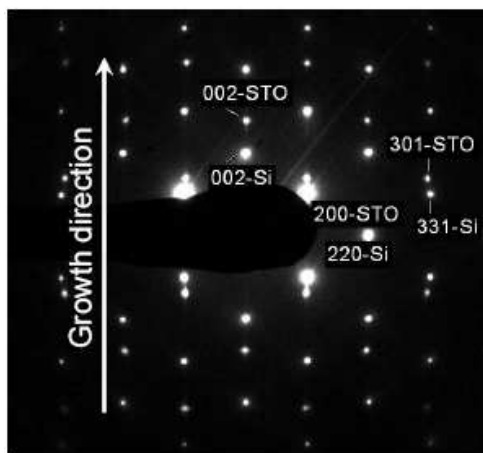
Figure III. 18 High resolution TEM diffraction pattern of the STO/Si(001) sample grown at 360°C.

III.3.3.3) XRD

To further investigate the structural quality of the STO films grown at different temperature, 45nm-thick samples have been characterized by high-resolution X-ray diffraction. Figure III. 19 displays the 2θ-ω scans recorded around the STO 002 out-of-plane Bragg reflection for the samples grown at 340°C 360°C, 420°C and 500°C respectively. The sharp, intense peak at $2\theta=69.13°$ is the Si 004 Bragg reflection. The STO samples grown at 340°C, 360°C and 420°C present good crystalline quality with the STO 002 peaks appearing at $2\theta=46.29°$, 46.34° and 46.27° respectively. However, for the 500°C sample the STO 002 peak intensity is much less than that of the other samples, due to lower crystal quality. These results are consistent with the RHEED observation. The out-of-plane lattice parameters extracted from Figure III. 19 for the sample of 340°C, 360°C and 420°C are 3.919±0.002Å, 3.915±0.002Å and 3.921±0.002Å respectively. These will be discussed below.
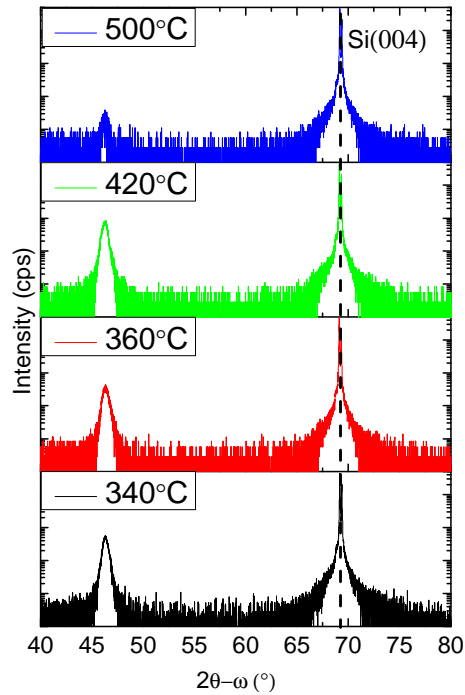
Figure III. 19 High resolution X-ray diffraction measurements around STO (002) diffraction condition for the STO/Si samples grown at different temperatures.

In-plane diffraction was also used to characterize the samples. Figure III. 20 shows the corresponding data (in linear scale) collected around the in-plane STO 200 Bragg reflections. For the sample grown at 500°C, we observe a sharp, intense peak at $2\theta_\chi=47.30°$ corresponding to the 220 diffraction of the underlying silicon substrate and no STO 200 reflection is observed. In agreement with out-of-plane measurement results, this suggests a poor STO structural quality for this sample. For the other three samples, the STO 200 peaks are much more intense than the Si 220 peaks revealing a good STO structural quality. The in-plane lattice parameter extracted for the samples grown at 340°C, 360°C and 420°C are 3.931±0.01Å, 3.933±0.01Å and 3.945±0.01Å respectively.
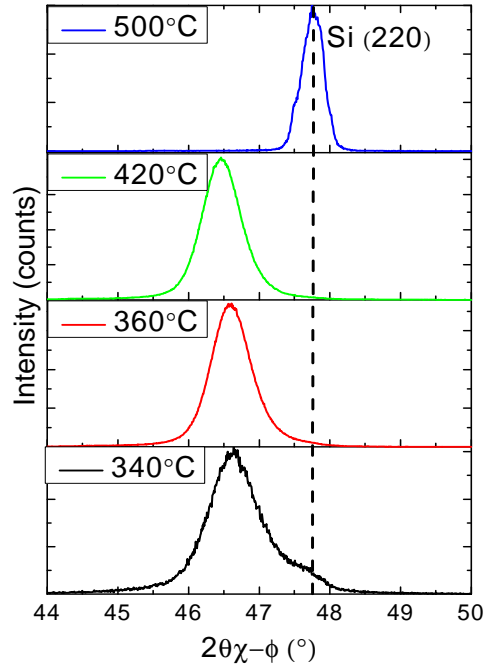
Figure III. 20 High resolution XRD data collected around in-plane STO (200) Bragg diffraction condition for the STO/Si samples grown at different temperatures.

Both of in-plane and out-of-plane lattice parameters are larger than that of bulk STO (3.905Å). We attribute this anomalous behavior to a combined influence of thermal expansion and defects existing in the STO epitaxial films. Let us assume the STO films entirely relax to their bulk in-plane lattice constant at growth temperature (340°C, 360°C and 400°C), which can be calculated by:

$$a_{//}^{GT} = a_0 \times \left[1 + (T_G - 20) \times \alpha_{STO}\right]$$ Equation III-1

where T_G the growth temperature, $a_{//}^{GT}$ the in-plane lattice parameter at the growth temperature, a_0 the bulk STO lattice constant (3.905Å) and α_{STO} the thermal expansion coefficient of STO ($9 \times 10^{-6} K^{-1}$) [42]. Because the underlying silicon substrate imposes a clamping effect to the STO film, the STO will obey the thermal expansion coefficient of Si when cooled to room temperature (20°C). The in-plane STO lattice parameters can thus be written as:

$$a_{//}^{20°C} = a_{//}^{GT} \times \left[1 + (20 - T_G) \times \alpha_{Si}\right]$$ Equation III-2

where α_{Si} the thermal expansion coefficient of Si ($2.5 \times 10^{-6} K^{-1}$) [42].

The theoretical in-plane lattice parameters of STO grown at 340°C, 360°C and 400°C are 3.913Å, 3.914Å and 3.915Å respectively. These values are larger than a_{bulk}, indicating that

differential thermal expansion leads to tensile strain in the STO layers at room temperature. According to the elasticity theory, the relationship between in-plane and out-of-plane lattice parameters is given by:

$$\frac{a_\perp - a_0}{a_0} = -2\frac{C_{12}}{C_{11}} \cdot \frac{a_{//} - a_0}{a_0} \qquad \text{Equation III-3}$$

where C_{12} and C_{11} are the macroscopic elastic constants of STO[43] with $C_{12}=3.175\times10^{-12}$ dynes/cm² and $C_{11}=3.175\times10^{-12}$ dynes/cm². And $\gamma=C_{12}/(C_{11}+C_{12})$ is called Poisson's ratio that describes the tetragonal distortion of the film due to the strain. The $a_\perp$ predicted by elastic theory as well as all the theoretical and experiment data are listed in Figure III. 21.

Comparing the experimental and calculation data in Figure III. 21, we find that both STO grown at 340°C, 360°C and 420°C present the same $a_\perp/a_{//}$ values as that of fully relaxed STO layers, which tends to indicates that these layers are fully relaxed on Si at the growth temperature. However, both in-plane and out-of-plane lattice parameters are larger than those predicted by thermal expansion and elastic theory (considering the experimental errors). The experimental unit cell volumes ($V=a_{//}^2 \cdot a_\perp$) obtained are larger than the calculated ones. It is probably related to the presence of defects in the STO film such as misfit dislocations and oxygen vacancies, which could increase the lattice constant[44, 45, 46]. The volume of a vacancy in ionic solids is in general larger than the atomic volume of the missing ion[47]. It has to be noted that we observe weak temperature dependence for the lattice parameters of 45nm single crystalline STO films due to the relative large thickness and the interface conditions play no longer a critical role for the structure quality of the STO layers.

Temperature		*340°C*	*360°C*	*420°C*
Experiment Data	*$a_\perp$($\pm$0.002Å)*	*3.919 Å*	*3.915 Å*	*3.921 Å*
	$a_{//}$ ($\pm$0.01Å)	*3.931 Å*	*3.933 Å*	*3.945 Å*
	$a_\perp/a_{//}$	*0.9969*	*0.9954*	*0.9937*
	Unit cell Volume (Å³)	*60.56*	*60.56*	*61.02*
Calculation results (if STO is entirely relaxed on Si)	*$a_\perp$(Å)*	*3.900*	*3.899*	*3.898*
	$a_{//}$ (Å)	*3.913*	*3.914*	*3.915*
	$a_\perp/a_{//}$	*0.9967*	*0.9963*	*0.9958*
	Unit cell Volume (Å³)	*59.72*	*59.72*	*59.74*

Figure III. 21 Experimental and theoretical data of STO lattice parameters

III.3.3.4) IR (work of W. Peng, collaboration with SOLEIL)

The Infrared transmission measurements were performed at AILES infrared beamline,

Synchrotron SOLEIL, on the samples discussed in the previous sections. The high brightness of the synchrotron radiation allows obtaining significant IR signal on our thin STO layers. The IR spectra were recorded under vacuum using a Bruker E55 Fourier transform spectrometer with resolution of $1 cm^{-1}$ and a bolometer to cover the $20\sim600 cm^{-1}$ spectral region . Figure III. 22 (a) and (b) show the IR transmission spectra of the STO/Si samples grown at 340°C~500°C with thicknesses of 4nm and 45nm, respectively. The absorbance was calculated using the transmission through a Si (001) substrate as a reference.

In Figure III. 22 (a) (4nm-thick samples), the spectrum of STO grown at 360°C clearly shows transverse optical (TO) modes at 155 cm^{-1} (TO_1), 199 cm^{-1} (TO_2) and 555 cm^{-1} (TO_4). Compared to equivalent phonons observed in ceramics[48], the peak positions of thin layers are shifted to higher energy (see Figure III. 22 (c)), supporting a mismatch induced stressed structure. As the epitaxial temperature increases from 360°C to 420°C, these phonon modes shift to lower frequency, indicating an increase of the interatomic bond length. It demonstrates that the STO film grown at higher temperature (420°C) is less strained (i.e. less tetragonally deformed) than that grown at 360°C on silicon substrate. In addition, the intensities of the TO_1, TO_2 and TO_4 modes corresponding to the 420°C sample are weaker than those of the 360°C sample, indicating larger crystalline disorder in the layer grown at 420°C.. In the spectra corresponding to the STO layers grown at 340°C, 450°C and 500°C the STO phonon modes are not visible, which indicates that the well ordered STO portion dramatically decreases in these thin films. Meanwhile, several interface modes at $260 cm^{-1} \sim 480 cm^{-1}$ are present in all spectra except for the 360°C grown sample, which is in good agreement with the our RHEED and TEM results (no interface layer formed at 360°C). These interface modes can be attributed to the formation of the amorphous silicate interfacial layer[49,50].

Interestingly, for the spectrum of the 360°C sample, three extra modes appear at 25 cm^{-1}, $58 cm^{-1}$ and $81 cm^{-1}$ respectively. These low energy modes can be induced either by the formation of tetragonal STO phases or by the stabilization of the soft mode[48,51]. It is well known that the bulk STO crystal undergoes a phase transition from the cubic *Pm$\bar{3}$m* perovskite structure (at room temperature) to tetragonal phase with *I4/mcm* symmetry[52] when T is below 105 K. This transition involves the rotation of TiO_6 octahedra[53]. According to previous IR reflectivity study on STO ceramics[48] as a function of temperature, TO_1 mode position shows a progressive shift from 93 cm^{-1} at room temperature to 15 cm^{-1} at 15 K (see

Figure III. 22 (c)). In the case of thin films, it is widely reported that the biaxial strain imposed by underlying substrates can induce the cubic-tetragonal phase transition thus ferroelectricity in STO epitaxial films[54,55]. For the STO/Si system with a lattice mismatch of 1.7%, our IR results suggest that different tetragonal structures (as demonstrated by the various TO modes) are present in the STO film commensurately grown on silicon. Evidently, the vibrational modes can be a great guide in determining the precise structure of thin layers. The interpretation however, is hampered by the complexity of the spectra. *ab initi*o periodic method are underway to predict the vibrational spectra of both SrTiO₃ bulk and thin layer which will allow verifying the assignment of these low energy modes.

In Figure III. 22 (b) from 45nm-thick samples, the TO_1, TO_2 and TO_4 modes appear in the spectra of all the temperatures due to the much larger film thickness. However, the TO_1 peak in spectrum 500°C is quite broadened, which is very likely caused by the eventually polycrystalline film feature. Compared to the 4nm-thick thin films, the TO_1 modes of 360°C and 420°C spectra of 45nm-thick STO layers are evidently shifted to lower energy (see Figure III. 22 (c)) which attests the relaxation of the STO films as the thickness increases, thus confirming our XRD results (previous section). Comparing the TO_1 modes taken from spectra 340°C, 360°C and 420°C, one can observe that TO_1 mode of spectrum 420°C shifts to lower frequency with respect to those of 340°C and 360°C, indicating the STO layer grown at 420°C is more relaxed than those grown at 340°C and 360°C, consistently with our XRD measurements (Figure III. 21). Furthermore, there is no significant difference in the interface mode region for all the spectra of different temperatures, which reveals that the STO component takes a majority portion in the epitaxial film and the signals of the interface mode become much weaker comparing with those in 4nm-thick films. These results are in good agreement with prior RHEED and XRD measurements.
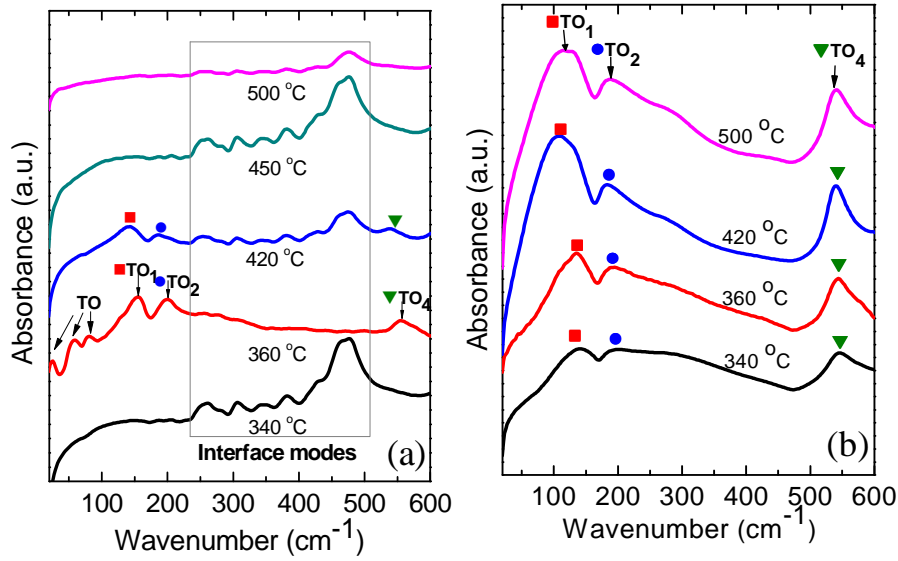
STO	Crystal Structure	TO$_1$ (E_g)	Soft (A_{1g})	TO$_2$ (E_g)	TO$_4$ (E_g)
Bulk (15 K)	Tetragonal	15	42	172	548
Bulk (100 K)	Tetragonal	46	/	173	548
Bulk (300 K)	Cubic	93	/	176	548
4nm-film (360°C)	Tetragonal & Cubic	25 155	58 81	199	555
45nm-film (360°C)	cubic	135	/	193	542
4nm-film (420°C)	Cubic	142	/	185	540
45nm-film (420°C)	Cubic	108	/	185	540

(c)

Figure III. 22 Infrared transmission spectra of epitaxial STO films on Si grown at different temperatures (a)4nm-thick films and (b)45nm-thick films. Squares, circles and triangles denote the transverse optic modes of TO₁, TO₂ and TO₄ respectively. (c) IR active TO modes of STO. All numbers are in cm⁻¹. Bulk STO data are determined by infrared reflectivity (Ref.48).

III.3.3.5) Influence of initial oxygen partial pressure

The oxygen partial pressure, in particular at the early stage of the growth, is another parameter to achieve a coherent interface between STO film and Si substrate. Therefore a series of 9ML-thick STO/Si(001) samples grown at the optimal temperature 360°C under different oxygen partial pressures at the initial growth stage (0~3ML) have been investigated using XPS. Figure III. 23 (a)~(c) display the experimental scans and the fit of the Si *2p* core levels of the STO/Si samples grown under initial oxygen partial pressure of 2×10^{-8}Torr,

5×10^{-8}Torr and 8×10^{-8}Torr. As a reference, spectrum (d) was recorded from a Si substrate with its native SiO_2 layer on the surface. In this spectrum, the Si *2p* peak is centered at around 99.3eV and the SiO_2 peak is located at about 103.2eV, consistently with literature data[41]. For the spectrum (a), taken from the sample grown under $PO_2 = 2 \times 10^{-8}$Torr, the peak centered around 101.7eV which can be assigned to Si^+, Si^{2+} or Si^{3+} species[56] indicates the formation of a silicate at the interface. In spectrum (b), recorded for the STO/Si sample grown under $PO_2 = 5 \times 10^{-8}$Torr, the signal arises principally from the silicon substrate with only a relatively weak peak centered at approximately 101.2eV indicating the presence of Si-O-Sr bonds at the interface[56]. This indicates that the STO/Si interface is abrupt at the atomic scale, which is in good agreement with the present TEM analysis (Figure III. 17(a)). Spectrum (c) is taken from the sample grown under $PO_2 = 8 \times 10^{-8}$Torr. The experimental data can be fitted using two components corresponding to SiO_x species. The peak centered at around 101.7eV suggests the formation of silicate phase while the other one centered at 103.3eV, which is much more intense, indicates the formation of SiO_2 at the interface.

These results clearly demonstrate that the oxygen partial pressure plays a critical role for the interface reaction during the first growth stage. Decreasing the oxygen pressure results in a pronounced intensity of silicate (or silicide), which is consistent with the study of STO/(Ba,Sr)O/Si system performed by G. J. Norga et al. (Ref.57). In Ref.57, both $SrSiO_3$ and $TiSi_x$ interfacial layers form when the oxygen pressure is less than the optimal value 7×10^{-8}Torr. Meanwhile, increasing the oxygen pressure leads to the oxidation of the silicon surface. The optimized oxygen partial pressure during the initial growth stage is 5×10^{-8}Torr for the STO/0.5ML-SrO/Si(001) system.
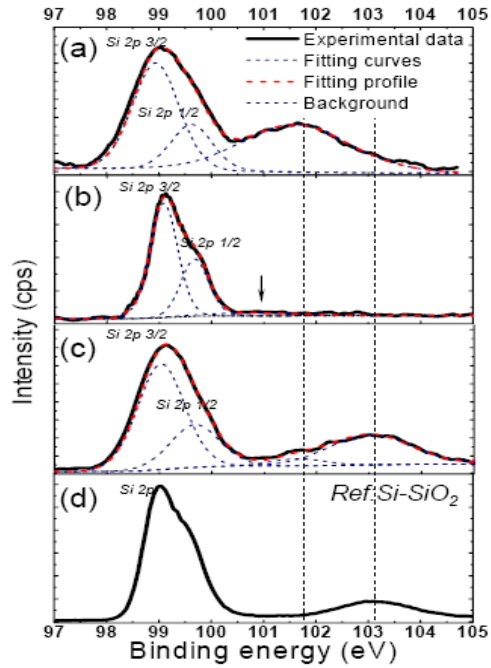
Figure III. 23 The XPS scans in the Si 2p region of 9ML-thick STO/Si(001) samples grown under different initial oxygen partial pressure (a) 2×10^{-8}Torr, (b) 5×10^{-8}Torr (c) 8×10^{-8}Torr and a reference spectrum of Si substrate with native SiO₂ on the surface.

According to the analysis above, we can thus obtain the epitaxy window of STO/Si system, as sketched in Figure III. 24. Both of the too elevated and too low growth temperatures lead to amorphous interfacial layer between STO and silicon and the optimal temperature is around 360°C. At the optimal temperature, too high or too low initial oxygen partial pressures (for the first 2ML~4ML STO) result in the formation of amorphous interfacial layer and the optimal oxygen partial pressure is 5×10^{-8}Torr. In contrary, a higher oxygen pressure 5×10^{-7}Torr~1×10^{-6}Torr is required for the following growth to achieve the good stoichiometry of SrTiO₃. Compared to the optimal growth conditions of STO/STO homoepitaxy that are ~550°C and 1×10^{-6}Torr, the optimal growth conditions of heterosystem STO/Si fall in a regime of relative low temperature and low initial oxygen partial pressure.
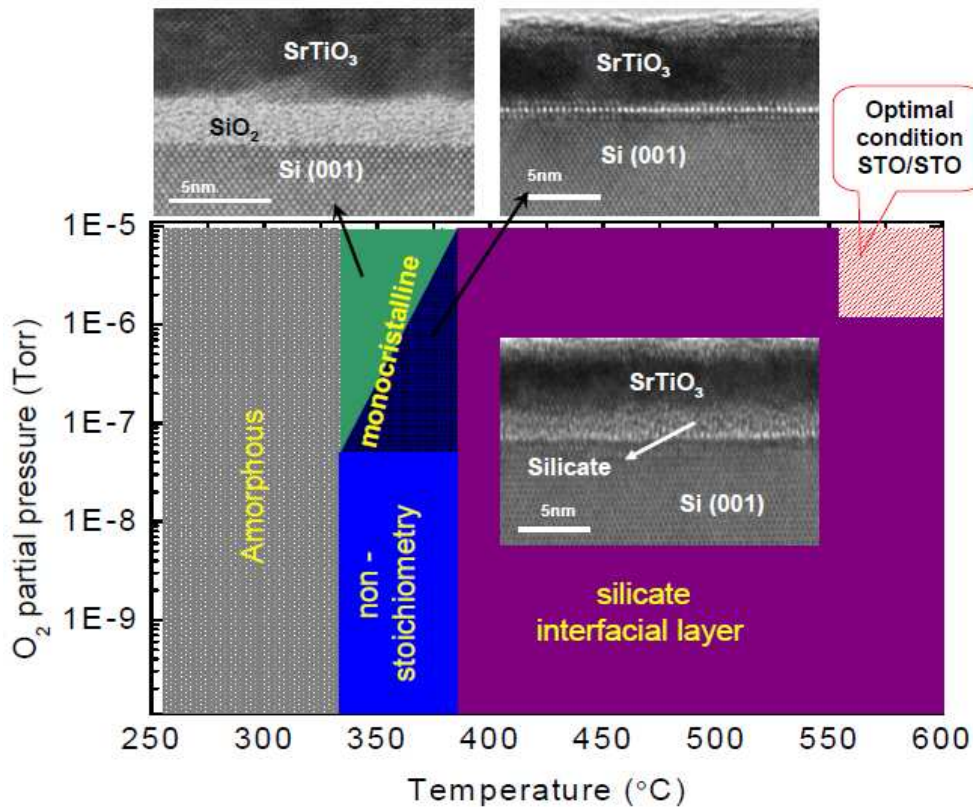
Figure III. 24 Diagram of STO/Si(001) system P_{O2}-T.

III.3.4) SrTiO₃ film grown under optimal conditions

In the previous section, we discussed the impacts of growth temperature and initial oxygen partial pressure on the heteroepitaxy of STO on Si (001). Optimized material quality and abrupt interface if obtained at T = 360°C with an initial O_2 partial pressure of 5×10^{-8}Torr for the first 2ML of STO. In this section, we will analyze the structural properties of STO films grown under the optimal growth conditions in further details.

III.3.4.1) Two-phased STO, strain relaxation

The XRD out of plane 2θ-ω scans recorded around the STO 002 reflection for five samples with the thicknesses of 10ML, 14ML, 24ML, 42ML and 118ML are displayed in Figure III. 25 (a) (in reciprocal space units: q = 1/d where d is the distance in the real space along the growth axis). The spectra of the four thinner samples (10, 14, 24 and 42 ML) present Pendellösung fringes attesting for the good crystallinity and flatness of the STO layers. The main diffraction peak progressively shifts towards large q values increasing the STO thickness beyond 14 ML, indicating a decrease of the STO out of plane lattice parameter. At 118 ML, Pendellösung fringes are no longer detected due to a degradation of the STO quality

associated to plastic relaxation (see below).
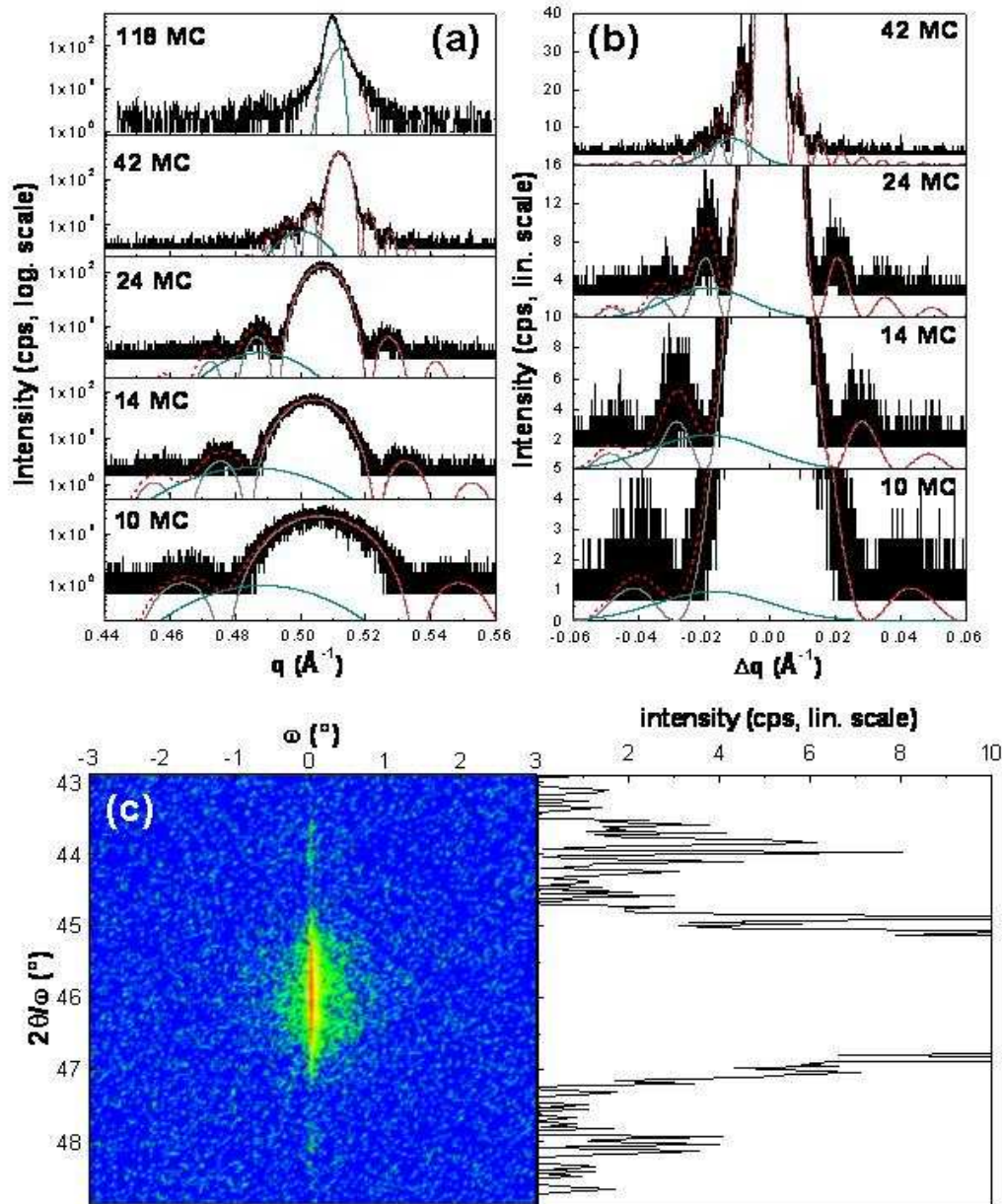
Figure III. 25 (a): 2θ-ω scans of the STO 002 reflection for 10, 14, 24, 42 and 118 ML thick STO/Si layers. Grey, dark cyan and red-dashed lines: fit of the peaks. q = 1/d is the interatomic distance in the growth direction. (b) Zooms in linear scale on the Pendellösung fringes of the spectra of (a). Δq is the offset with respect to the center of the cardinal sinus contribution. (c): Reciprocal space map of the STO 002 reflection, and 2θ-ω profile of the map for ω = 0.

Interestingly, the Pendellösung fringes are not symmetric for the 10, 14, 24 and 42 ML samples. The XRD spectra cannot be fitted using a simple cardinal sinus function, and a

shoulder peak at low q value must be added, as shown in Figure III. 25 (b). A good agreement between experimental data and fitted curves is obtained by using a sum of a cardinal sinus (for the main diffraction peak and the Pendellösung fringes) and a Gaussian function (for the low q shoulder). Such a dissymmetry of the diffraction spectrum can result from geometric effects (strong mosaicity of the STO layer, possible misalignment between the STO layer and the Si substrate). To test this hypothesis, a reciprocal space map of the STO 002 reflection of the 24 ML thick sample was recorded using a Ge 200 two bounces analyzer on the diffracted beam (Figure III. 25 (c)). This allows strongly reducing the detection acceptance angle, thus removing possible parasitic diffraction due to geometric effects. The profile extracted for the reciprocal space map of Figure III. 25 (c) at $\omega= 0$ is also dissymmetric, indicating that this dissymmetry is related to the presence in the layers of two different STO domains having two different out of plane parameters (designated as c in the following). The 002 STO peak of the 118 ML thick sample can also clearly be decomposed into two components, as shown in Figure III. 25 (a).

In-plane diffraction was used to record the $2\theta_\chi$-φ spectra corresponding to the 110 STO reflections. The $2\theta_\chi$ angle in in-plane configuration is equivalent to the 2θ angle in the out-of-plane configuration, so that in-plane $2\theta_\chi$-φ scans are equivalent to 2θ-ω out-of-plane scans. 110 STO reflections are particularly interesting because 100 Si reflections, that are theoretically located in the same angular region, are forbidden due to diffraction selection rules. Diffraction from STO only is thus collected around the 110 STO reflections. A deconvolution into two Gaussian peaks was required to fit these $2\theta_\chi$-φ scans, as shown in Figure III. 26. The bimodal character of the diffraction peaks is clear for the 10, 14 and 24 ML samples, and becomes less clear for larger thicknesses. However, even for the 42 and 118 ML thick layers, a better fit was obtained using two Gaussian peaks rather than one.
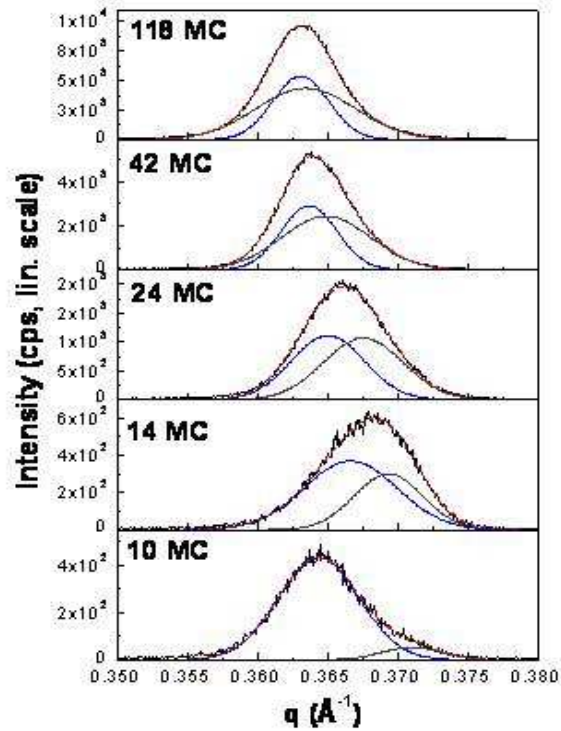
Figure III. 26 In-plane 2θχ-φ scans of the STO 110 reflections for 10, 14, 24, 42 and 118 ML thick STO/Si layers. Dark-grey, blue and red-dashed lines: fit of the peaks. q = 1/d is the interatomic distance in the growth plane.
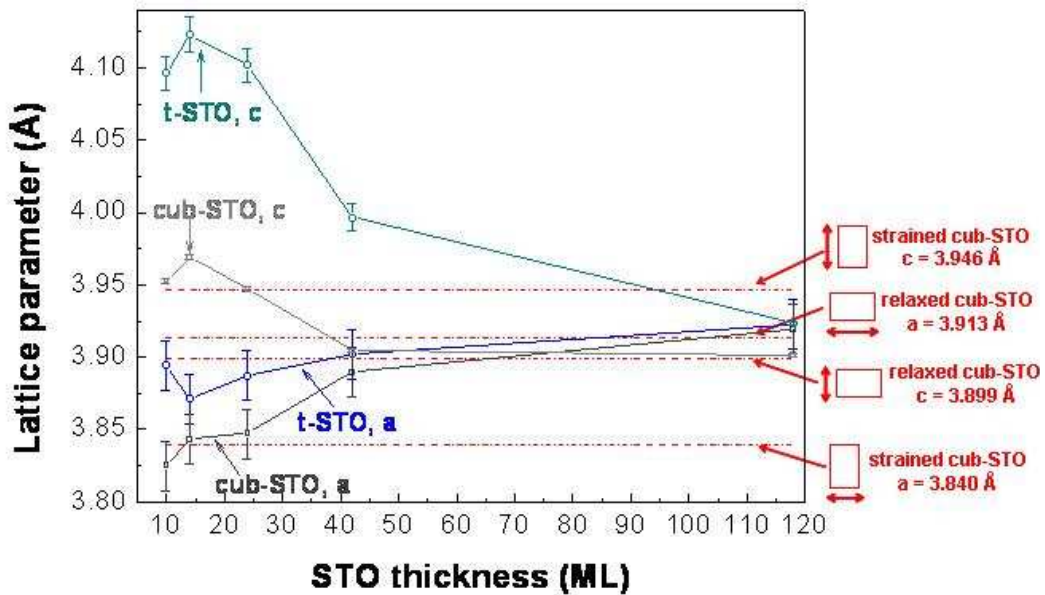
Figure III. 27 Evolution of the in-plane (a) and out-of-plane (c) STO lattice parameters as a function of the STO thickness in ML, as deduced from XRD experiments. Grey and dark lines correspond to the evolution of c and a, respectively for the cubic STO phase, and dark cyan and blue lines correspond to the evolution of c and a, respectively for the tetragonal t-STO phase. Red-dashed lines : calculated values for c and a for fully strained and fully relaxed

cubic STO, taking into account the influence of the Si substrate on the thermal expansion of STO during the temperature ramping down step after growth.

This analysis indicates that the STO layers contain two STO domains having two different in-plane lattice parameters (designated as a in the following) and two different out-of-plane lattice parameters c. The lattice parameter values extracted from in- and out-of-plane XRD experiments are plotted in Figure III. 27. In this figure, the red dash-dotted lines represent the values calculated for in- and out-of-plane lattice parameters of fully strained and fully relaxed (bulk) cubic Pm3m STO. The calculation is based on the elastic theory considering thermal expansion effect, as discussed in detail in previous section III. 3.3.3. As a consequence, thin STO layers grown on Si substrates undergo additional thermal deformation after epitaxy, when the temperature is ramped from the growth temperature (360°C) down to room temperature (20°C). As described in Ref.58 for the GaAs/Si system, the in-plane lattice parameter of STO is submitted to the Si thermal expansion coefficient, while the effective STO out-of-plane thermal expansion coefficient depends on the thermal expansion coefficients of Si and STO as well as on STO elastic constants, and rates 1.315×10^{-5} °C^{-1}. This anisotropic contraction leads to built-in tensile strain at room temperature in STO thin layers relaxed on Si at growth temperature (for such relaxed layers, a is larger than c). The dark and light gray experimental curves in Figure III. 27 labeled "cub-STO a" and "cub-STO c", respectively correspond to the same STO domain: for thicknesses lower than 24 ML, the corresponding experimental values for a and c correspond to the calculated values for "standard" STO crystallizing in the cubic Pm3m perovskite structure and fully strained on the Si substrate. For this STO phase, designated as cub-STO in the following, plastic relaxation starts between 24 and 42 ML, leading to a decrease of c and an increase of a. For the 118 ML, the experimental values of a and c matches that calculated for bulk cubic Pm3m STO (on condition that differential thermal expansion is taken into account), showing that the cub-STO phase is fully plastically relaxed for this thickness. According to these experimental results, the critical thickness for plastic relaxation of STO on Si is between 24 and 42 ML.

The remaining set of lattice parameters (blue and dark cyan curves in Figure III. 27 labeled t-STO a and t-STO c, respectively) correspond to a second STO phase, designated as t-STO in the following. Obviously, this t-STO phase does not correspond to cubic Pm3m STO:

the associated c values for the 10, 14 and 24 ML thick STO layers are around 4.1 Å, which is much larger than the expected c value for cubic STO even strained on Si, and the associated a values does neither match that expected for cubic STO strained on Si, nor that expected for bulk cubic Pm3m STO. It corresponds to a tetragonal STO phase, the origin of which will be discussed in further details in the next section. The tetragonality (c/a-1) as a function of the deposited STO thickness and the evolution of c as a function of a are plotted for both cub-STO and t-STO phases in Figure III. 28. For the cub-STO phase, the tetragonality corresponds to that expected for cubic Pm3m STO strained on Si for thicknesses below 24 ML, and tends toward that expected for fully relaxed STO for larger thicknesses. Moreover, the evolution of c as a function of a matches that expected from linear elasticity for cubic Pm3m STO (black dash-dotted line in Figure III. 28 (b)). For the t-STO phase, the tetragonality is around 0.06 for thicknesses below 24 ML, and tends toward that expected for fully relaxed *cubic* STO for larger thicknesses. For this t-STO phase, the evolution of c as a function of a presents two regimes: for thicknesses below 24 ML, the experimental points are aligned along a line that can be easily fitted (dark gray dash-dotted line in Figure III. 28 (b)) using a Poisson-type relationship of the form:

$$c = a_b - 2 \times \frac{C_{12}}{C_{11}} \times (a - a_b)$$

where a_b, C_{12} and C_{11} are the bulk lattice parameter and elastic constants of the t-STO phase, respectively. The fit in Figure III. 28 (b) leads to $a_b \sim 4.0$ Å and $C_{12}/C_{11} \sim 0.46$, which strongly differs from the values for cubic Pm3m STO ($a_b = 3.905$ Å and $C_{12}/C_{11} = 0.323$). Interestingly, for the 42 and 118 ML thick STO layers, the evolution of c as a function of a for the t-STO phase deviates from that predicted by Poisson relationship and tends towards that measured for the cub-STO phase. This evolution, as well as that of the tetragonality, suggests that the t-STO phase undergoes a progressive tetragonal to cubic phase transition for deposited thicknesses larger than 24 ML, which corresponds to the thickness above which the plastic relaxation of the cub-STO phase starts.
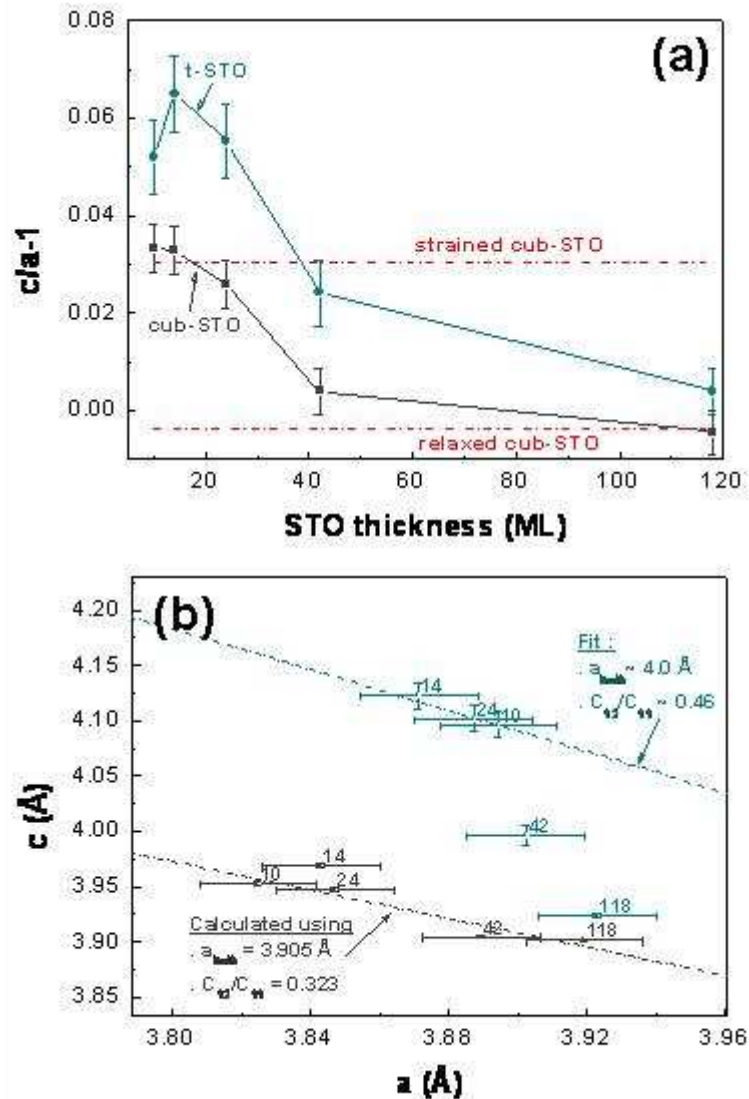
Figure III. 28 (a) : Evolution of the tetragonality (c/a-1) as a function of the STO thickness for the cub-STO phase (dark grey) and the t-STO phase (dark cyan). Red-dashed lines: calculated tetragonalities for fully strained and fully relaxed cubic STO, taking into account the influence of the Si substrate on the thermal expansion of STO during the temperature ramping down step after growth. (b): evolution of c (out-of-plane lattice parameter) as a function of a (in-plane lattice parameter) as a function of the STO thickness for the cub-STO phase (dark grey) and the t-STO phase (dark cyan). Dark-grey dash-dotted line: elasticity theory prediction for cubic STO (elastic parameters indicated on the graph). Dark cyan dash-dotted line: fit on the three smallest thicknesses for the t-STO phase (fit parameters indicated on the graph).

In order to further precise the experimental results detailed above, the 10 ML thick STO/Si sample was studied by high-resolution TEM (Figure III. 29). A high-resolution

cross-sectional view of this sample is displayed in Figure III. 29 (a). The STO layer is flat and its interface with Si is abrupt at the atomic scale. The image contrast in the STO region presents clear heterogeneities, attesting for slight crystallographic disorder. More precisely, well defined bright zones (as zone 1 in Figure III. 29 (a)) coexist with darker zones (as zone 2). The electron diffraction pattern corresponding to the image of Figure III. 29 (a) is displayed in Figure III. 29 (b). In the in-plane (horizontal) direction, the Si 220 and STO 200 diffraction spots are superimposed, as expected from the indirect epitaxial relationship between STO and Si. In the growth (vertical) direction, the STO 002 diffraction spot appears clearly. Interestingly, this diffraction spot is doubled, indicating that the STO presents two distinct c parameters. The values of these c parameters, as extracted from the diffraction pattern are $3.95 \pm 3 \times 10^{-2}$ Å and $4.10 \pm 2 \times 10^{-2}$ Å for the bright external spot and the less bright internal spot, respectively. These values match that measured by X-ray diffraction for the c-parameters of the strained cub-STO and the t-STO phases in the 10 ML thick sample, respectively. The Fourier transform of the image of Figure III. 29 (a) is displayed in Figure III. 29 (d). In this Fourier transform image, the in-plane STO 200 diffraction spot is no longer masked by the Si 220 diffraction spot, and both reflections can be distinguished, as shown by the zoom in the corresponding region (Figure III. 29 (e)). The two diffraction spots correspond to a values of $3.845 \pm 8 \times 10^{-3}$ Å and $3.899 \pm 8 \times 10^{-3}$ Å. The smallest of these values correspond to the Si 110 interatomic distance and to the a value for strained cub-STO, while the largest corresponds to the a value measured by XRD for the t-STO phase. This TEM analysis thus confirms the presence of the two STO phases in the 10 ML thick samples, and also confirms the a and c values measured by XRD.
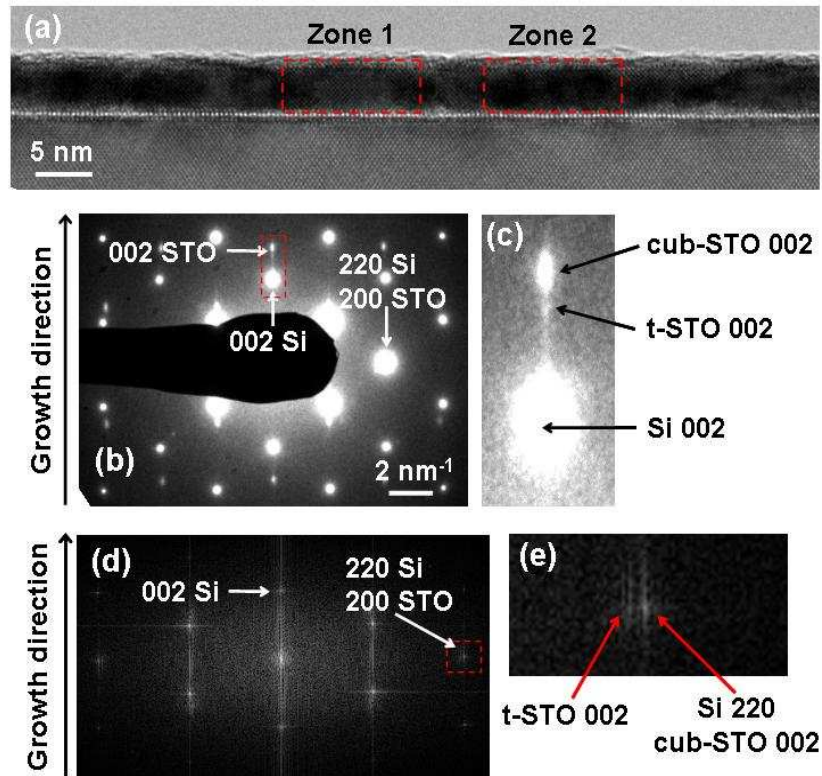
Figure III. 29 (a) High-resolution TEM cross-sectional view of the 10 ML thick STO/Si layer. (b) : corresponding electronic diffraction pattern. (c) Zoom around 002 Si and 002 STO out of plane reflections (squared zone in (b)). (d) : Fourier-transform of the image of Figure 29(a), and (e), zoom around the 002 in-plane reflections (squared zone in (d)).

III.3.4.2) Formation of the two STO phases

Further information can be extracted from the analysis of the TEM image of Figure III. 29 (a): the Fourier-transform images corresponding to zone 1 and 2 are displayed in Figure III. 30. The horizontal line profiles recorded along the <200> axis in these Fourier transform images are compared in this figure. This graph shows that STO has not the same in-plane lattice parameter in zone 1 and in zone 2. In zone 1 (bright zone in Figure III. 29 (a)), the a value extracted from the Fourier-transform image of Figure III. 30 is $3.85 \pm 1.5 \times 10^{-2}$ Å, which is close to that expected for STO strained on Si (3.840 Å). In zone 2 (darker zone in Figure III. 29 (b)), the a value for STO is $3.90 \pm 1.5 \times 10^{-2}$ Å, very close to that measured by XRD for the t-STO in-plane lattice parameter in this sample, namely $3.89 \pm 2 \times 10^{-2}$ Å. This analysis allows concluding that bright zones in Figure III. 29 (a) correspond to coherently strained cubic Pm3m STO, while darker zones in Figure III. 29 (a) correspond to tetragonal STO.
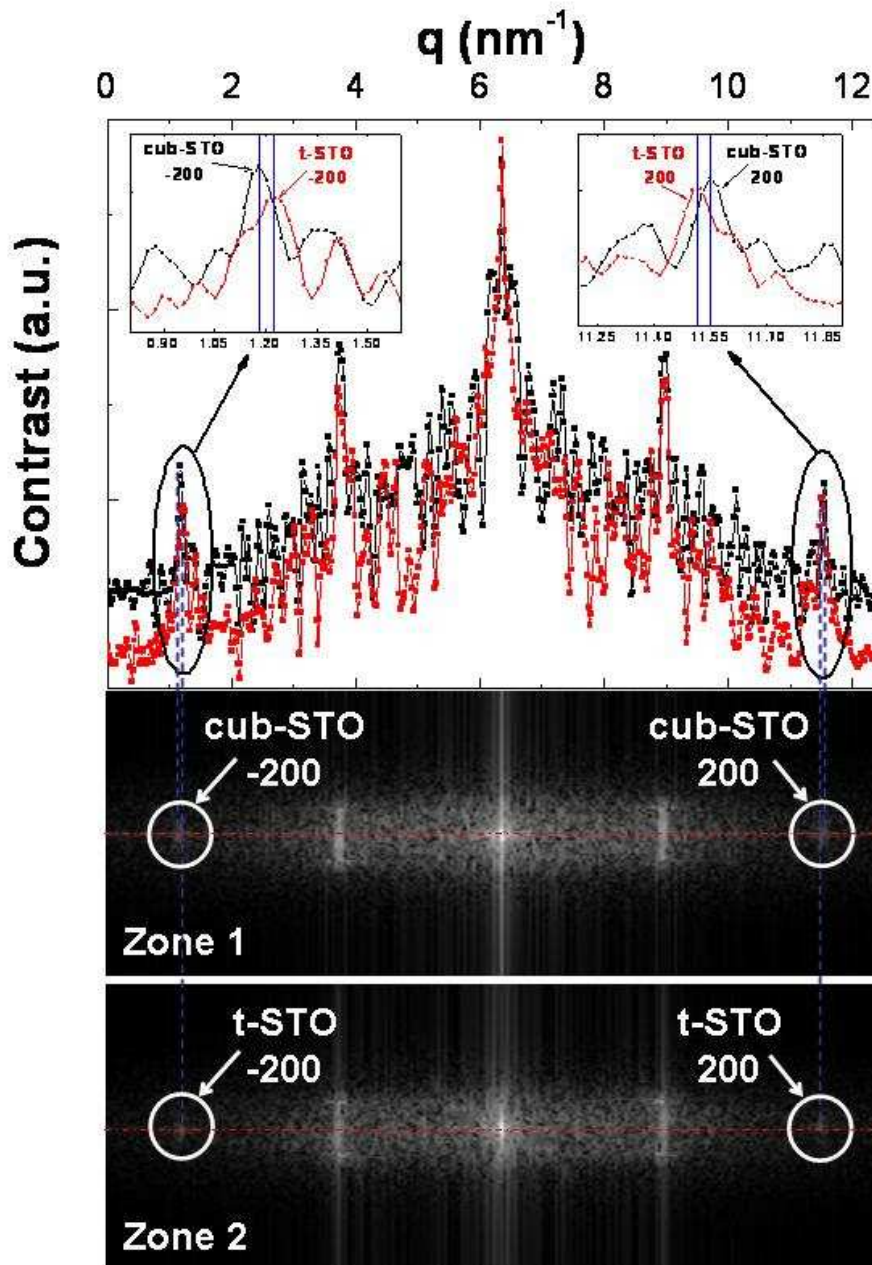
Figure III. 30 Fourier transform images of zone 1 and 2 in Figure III. 29 (a), and associated profiles along the [200] in-plane axis. Insets of the graph: zooms around the STO -200 and STO 200 reflections.

According to Figure III. 29 (a), the extension of these STO domains is of the order of ten or a few tens nanometers. They are separated by vertical boundaries, leading to a (quite disturbed) columnar like morphology. Both STO domains are present in approximately same proportions in the 10 ML sample, according to Figure III. 29 (a). Both STO phases are very similar from a chemical point of view, so that the difference in the TEM contrast between the

STO domains cannot be interpreted as resulting from chemical effects. Tetragonal STO domains are darker because they are slightly misoriented with respect to the Si substrate (mosaicity), oppositely to perfectly oriented coherent cubic STO domains. This mosaicity also leads to a quite low contribution of the t-STO phase in the heavily angularly resolved out-of-plane XRD spectra of Figure III. 25. Oppositely, the in-plane experiments summarized in Figure III. 26 have been carried out using a much lower angular resolution. In these in-plane spectra, the relative intensities of the peaks corresponding to cubic and tetragonal STO is much more representative of the volumic proportion of these domains in the samples.

The t-STO phase thus presents a more pronounced mosaicity than the well ordered coherent cub-STO phase. The coexistence of a well ordered and a more disordered STO phase appears clearly in the ω-scans of the STO 002 reflection plotted in Figure III. 31. Up to 24 ML, i.e. as long as the cub-STO phase remains coherently strained on Si, these ω-scans present a sharp central contribution corresponding to a well ordered STO phase, and a much broader contribution corresponding to STO with strong mosaicity. According to the TEM analysis described above, the well ordered STO phase leading to the sharp central contribution in the ω-scans correspond to coherently strained cub-STO (bright zone 1 in Figure III. 29 (a)), while the broader contributions in the ω-scans (due to stronger mosaicity) correspond to the more disorder t-STO phase (dark zone 2 in Figure III. 29 (a)). Very similar results as that displayed in Figure III. 31 have been published in Ref.59. In this article, the authors attribute the sharp portion of the STO 002 ω-scans to the presence of coherently strained STO, which is consistent with our analysis. Oppositely, in Ref.59, the origin of the broader contribution (which is reported by the authors for STO thicknesses as low as 5 ML) is not clearly discussed and is attributed to a relaxed portion of the STO layer. According to our experimental results, the plastic relaxation critical thickness for the cub-STO/Si systems exceeds 24 ML, which excludes the presence of a STO relaxed portion in 5 ML thick layers. The disordered STO portion in thin layers (up to 24 ML) corresponds to the t-STO phase, as clearly shown by our experimental results. Above 24 ML, plastic relaxation of the cub-STO phase occurs, leading to the disappearance of sharp contribution in the ω-scans of Figure III. 31: plastically relaxed cub-STO presents a strong mosaicity due to the presence of threading defects associated to plastic relaxation.
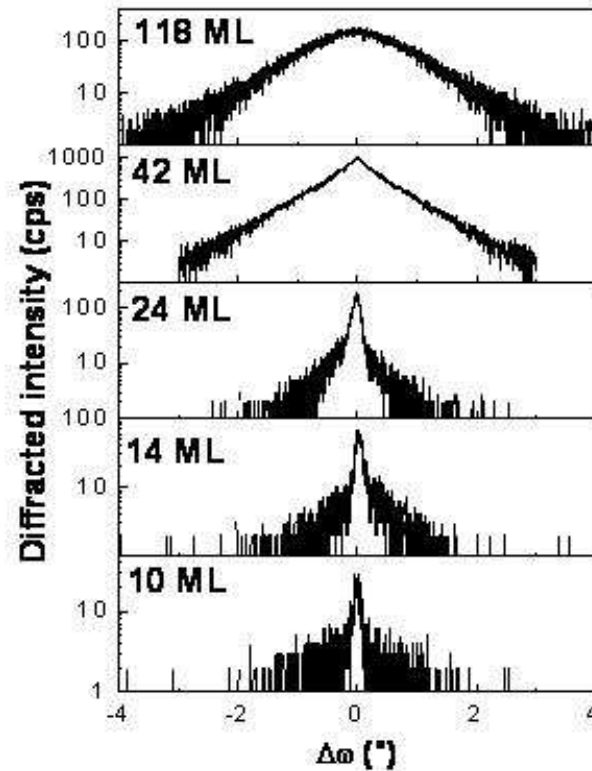
Figure III. 31 ω-scans of the STO 002 reflections for 10, 14, 24, 42 and 118 ML thick STO/Si layers.

The evolution of the RHEED pattern at the early stages of STO growth is presented in Figure III. 32 (a). Pattern (i) corresponds to the (2×1)-reconstructed Si surface before growth, while patterns (ii), (iii) and (iv) were recorded after the growth of 0.8, 2 and 5 ML, respectively. The contrast of the diffraction lines in pattern (ii) is low, due to the presence of a relatively bright background. This indicates that STO is initially partly amorphous, as described in Ref.60. The amorphous part of STO then recrystallizes, leading to brighter diffraction line contrast in patterns (ii), (iii) and (iv).
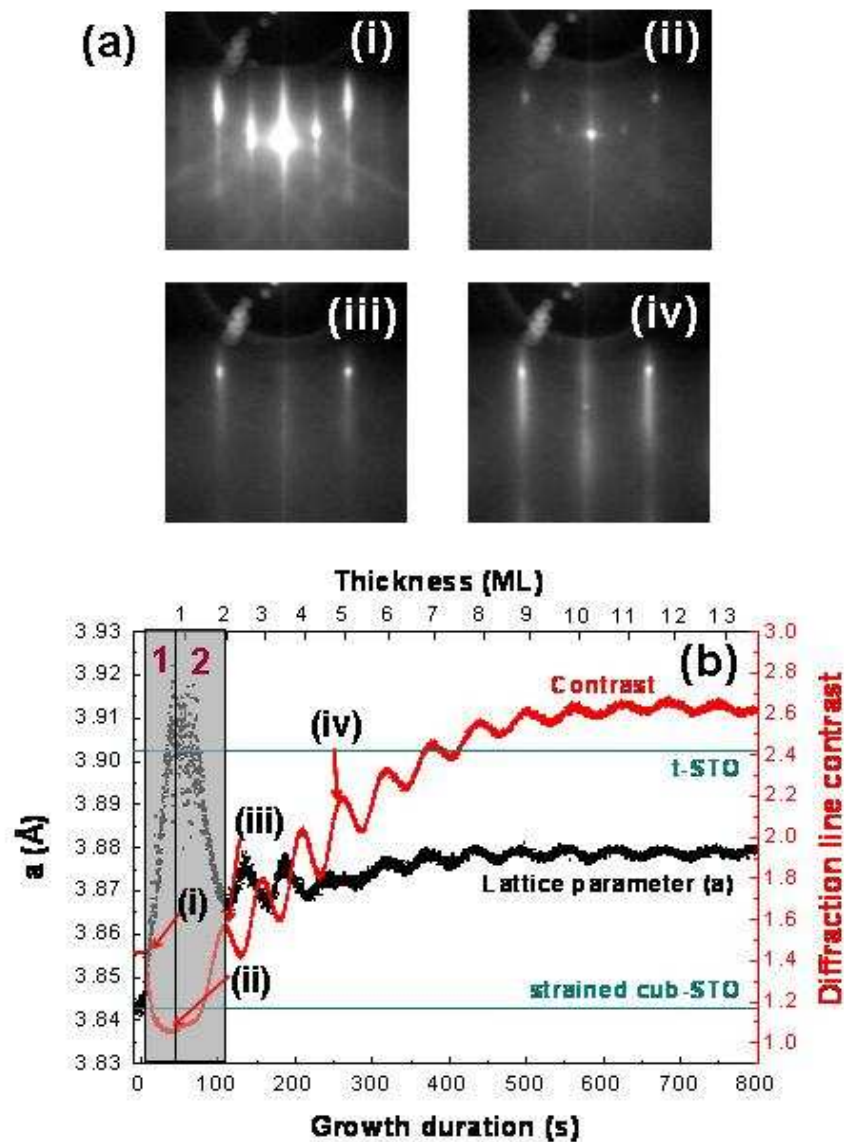
116

Figure III. 32 (a) RHEED patterns recorded along the Si [110] azimuth before STO growth (i), and after 50 (ii), 110 (iii) and 250 s (iv) of STO growth. (b) : red circles : evolution of the RHEED contrast (ratio between the diffraction line intensity and the background intensity) as a function of the deposition time. The points arrowed (i), (ii), (iii) and (iv) correspond to the RHEED patterns of (a). black squares : evolution of the STO in-plane lattice parameter, as deduced from the spacing between STO diffraction lines, a a function of the deposition time. Dark cyan lines: in-plane lattice parameters for fully strained cub-STO and for t-STO at 360°C, as deduced from XRD and TEM measurements and taking into account the influence of the Si substrate on the thermal expansion of STO during the temperature ramping down step after growth.

The evolution of the RHEED diffraction line contrast and of the STO in-plane lattice

parameter a (as deduced form the spacing of the RHEED diffraction lines) are plotted in Figure III. 32 (b). The diffraction line contrast was measured by normalizing the diffracted intensity with respect to the background intensity (recorded between 2 diffraction lines). It decreases as compared to that measured for the substrate during the first ~0.8 ML STO (zone 1 in Figure III. 32(a)), and re-increases between 0.8 and ~2 ML. Intensity oscillations are then observed, indicating the onset of a two-dimensional layer-by-layer growth mode after ~2 ML. The evolution of the RHEED contrast between 0.8 and 2 ML is driven by the proportion of amorphous STO in the growing layer : the RHEED contrast decreases between 0 and 0.8 ML (zone 1) due to the increase of the background intensity, and increases above 2 ML (zone 2) due to a decrease of the background intensity. Beyond 2ML, the background intensity remains constant and the evolution of the RHEED intensity is mostly driven by the variation of the diffraction line intensity. This shows that amorphous STO is formed on the surface simultaneously with crystalline STO up to 0.8 ML, and that the amorphous STO part recrystallizes between 0.8 and 2 ML. Interestingly, the evolution of the STO in-plane lattice parameter a is correlated to that of STO crystallinity. Between 0 and 0.8 ML, a increases from the Si value (3.843 Å along the 110 azimuth at the growth temperature to approximately 3.9 Å. This value is very close to that measured by XRD and TEM for the in-plane lattice parameter of the t-STO phase (~3.903 ± 8×10⁻³ Å at the growth temperature if one considers that the in-plane lattice parameter of t-STO is submitted to the thermal expansion coefficient of Si during the temperature ramp-down after growth). This shows that the initially crystalline part of STO is the t-STO phase. Between 0.8 and 2 ML, when the amorphous STO part recrystallizes, it starts contributing to RHEED diffraction. In this region (zone 2) the STO in-plane lattice parameter decreases and reaches ~3.865 Å at 2ML. This shows that the in-plane lattice parameter of recrystallized STO is smaller than that of the initially crystalline t-STO phase. Considering the TEM and XRD results detailed above, the recrystallized (and initially amorphous) STO portion correspond to the coherently strained cub-STO phase. Due to its limited resolution, RHEED does not allow discriminating both STO lattice parameters: beyond 0.8 ML, when both STO phases coexist under their crystalline form in the deposited layer, the lattice parameter measured by RHEED is an average lattice parameter resulting from the contribution of both these phases. Above 2 ML, when the initially amorphous phase is fully recrystallized, the surface lattice parameter starts oscillating. These surface lattice parameter oscillations are characteristic for the growth of a coherently strained material[61]. The simultaneity between lattice parameter oscillation start and full recrystallization of the

initially amorphous STO phase further confirms that the initially amorphous STO phase recrystallizes into the coherently strained cub-STO phase between 0.8 and 2 ML. The formation of a coherently strained material by recrystallization of its amorphous phase on a substrate may *a priori* sound anti-intuitive. However, as mentioned in the introduction, the formation of coherently strained STO on Si by recrystallization of amorphous STO has already been reported earlier by several groups[40,42,62], and is a standard technique for fabricating STO on Si (so-called "kinetically controlled" STO growth).

III.3.4.3) Discussion on the origin of the t-STO phase

At room temperature or even at its growth temperature on Si (360°C), the stable bulk STO phase is the cubic Pm3m phase. Bulk STO undergoes an extensively studied antiferrodistorsive phase transition at ~105 K, and is ferroelectric with a tetragonal I4/mcm structure below this temperature.[63] This phase transition leads to a rotation of the TiO_6 octahedrons of the perovskite structure.[64] It is associated to an increase of the tetragonality (c/a-1) of the STO lattice which turns form 0 above 105 K to a few 10^{-4} at 50K[65,66]. Pressure has been shown to strongly modify the critical temperature of this transition for bulk STO[67], and strain related to mismatched epitaxial growth is also known as impacting the transition[68,69,70]. A T_c as high as 293K has thus been reported for a thin STO/DyScO₃ epitaxial layer.[71] However, the tetragonality reported in the studies mentioned above never exceeds 10^{-3}, and is much smaller than that reported here (between 5×10^{-2} and 7×10^{-2} for t-STO, when the total STO thickness is below 24 ML).

For the STO/Si(001) systems, Aguirre-Tostado et al.[72] have reported tetragonality values of 1.5×10^{-3} for STO thicknesses up to 40 Å, while Woicik et al[73] have reported a value of was found to be fully strained on Si, i.e. to present exactly the same in-plane lattice parameter as that of Si. In both cases also, the formation of a tetragonal STO phase was attributed to the simultaneous influence of the strain and of an internal polarization related to the presence of interface defects (such as oxygen vacancies) and surface adsorbates. Finally, in both cases, STO was described as single-phased.

It is likely that similar effects are at the origin of the formation of the t-STO phase in our samples, even if our experimental results significantly differ from that reported in Ref. 72 and.73 In our samples, grown by direct deposition of partly crystalline STO (as in the low

temperature step of the kinetically-limited method), two STO phases coexist. The t-STO phase, while not commensurate to Si (it presents a larger in-plane lattice parameter as that of Si) is crystalline as soon as growth begins while the cub-STO phase results from the spontaneous crystallization of initially amorphous STO. Moreover, the t-STO phase is clearly present for STO thicknesses up to 24 ML (~96 Å), which is much larger than the maximal thicknesses of 40 and 20 Å reported in Ref. 72 and 73, respectively. In our growth conditions, the amount of oxygen provided at the early stages of the growth is insufficient to fully oxidize the entire material. In this O-poor environment, O segregation effects (enhanced by the presence of an elevated concentration of O vacancies) are liable to take place, leading to an inhomogeneous repartition of the O atoms (and O vacancies) at the very beginning of the growth that may be at the origin of the formation of the two STO phases. In the end, the fact that the t-STO phase is not coherent with the Si substrate (which indicate that it is not fully strained on Si) while the cub-STO phase is fully strained on Si indicates that epitaxial strain does not play a major role in the formation of a t-STO phase.

III.3.4.4) THz IR evidence of the two-phased STO and relaxation

The samples discussed in the previous section were also studied by IR measurements, on the SOLEIL AILES beamline in collaboration with Prof. P. Roy. The results of the 14, 24, and 118 ML thick samples are plotted in Figure III. 33. For these samples, all the TO modes (TO_1, TO_2 and TO_4) shift to lower energies when the film thickness increases from 14ML to 114ML, which corresponds to the plastic relaxation of the cubic STO phase. For the 14ML film several extra TO modes (including soft modes) are observed appear in the THz range (20~100 cm^{-1}) which shows that cubic STO phase, as well as unpolarized and polarized tetragonal (ferroelectric, corresponding to soft modes) STO phases coexist in the film. For the 24ML STO film, a single extra TO mode (non soft mode) remains indicating that the tetragonal phase portion STO decreases (no polarized phase) but still can be detected. However, when the film thickness reaches 118ML, no extra TO mode exists suggesting the STO film is entirely relaxed. These results are in good agreement with our XRD analysis: a tetragonal STO portion exists in the films up to at least 24 ML, and disappears for larger thicknesses. Moreover, this analysis allows concluding that two tetragonal STO phases (namely polarized and unpolarized) coexist in the 14ML-thick films.
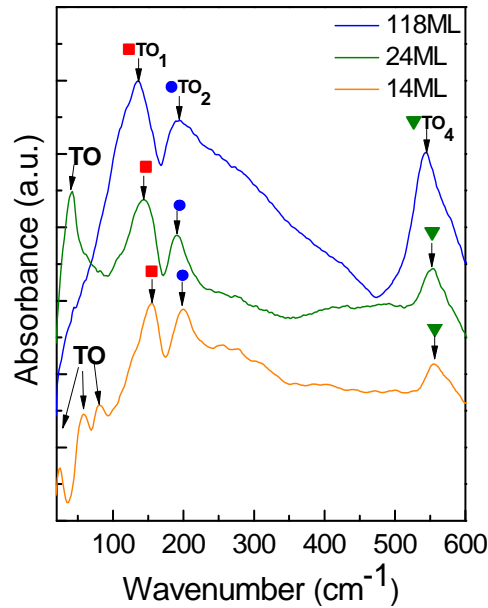
Figure III. 33 Evolution of the IR transmission spectra of STO films grown under optimized condition as the film thickness increases.

III.3.4.5) Evolution of the surface morphology of the STO film

In this section, we investigate the evolution of the surface morphology as the STO film thickness increases. Figure III. 34 shows the RHEED patterns and corresponding AFM 1×1μm images of STO films with different thicknesses (this sample series is the same as that discussed in the previous sections). These experiments highlight the effects of plastic relaxation of STO morphology: below 42 ML, the films are flat. Roughness then increases above 24 ML (critical thickness for plastic relaxation according to our XRD experiments), due to the onset of plastic relaxation and related formation of defects in the STO layers.
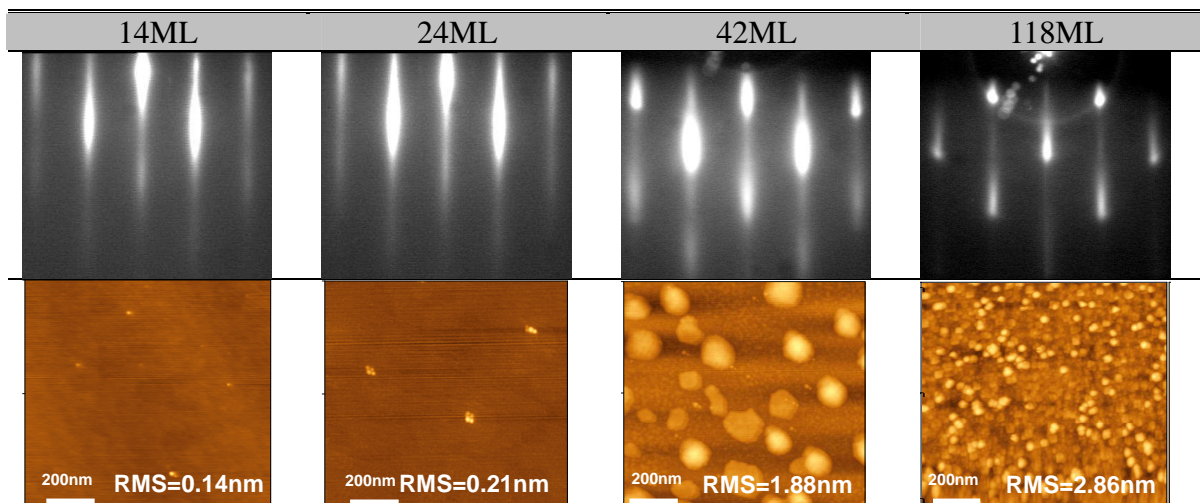
Figure III. 34 Evolution of the surface morphology of the STO films as the thickness increases: RHEED patterns (upper) and AFM 1×1μm images (below, inset shows the RMS values)

III.3.5) Summary

Our experimental results give some clarifying elements on the STO/Si interface, morphology, STO crystallinity and strain relaxation process. According to our analysis, the STO growth shows temperature and oxygen partial pressure dependence. The optimized epitaxy window is 360°C and initial $P_{O2}=5\times10^{-8}$Torr. For the STO films grown under the optimized condition, STO is two-phased. A cubic STO phase is formed by recrystallization of initially amorphous STO. This STO phase is coherently strained on Si and obeys elasticity laws (with the elastic constants of bulk cubic Pm3m STO) up to 24 ML. Above this thickness, plastic relaxation starts leading to fully relaxed STO at 118 ML. The tetragonal t-STO phase is crystalline as soon as growth begins and remains tetragonal (with a tetragonality of 5×10^{-2} to 6×10^{-2}) up to at least 24 ML. Further increase of STO thickness leads to a progressive reduction of the tetragonality of the t-STO phase that tends to 0 for large STO thicknesses. Despite the apparent simultaneity between plastic relaxation of the strained cub-STO phase and diminution of the tetragonality of the t-STO phase (which requires further experimental confirmation, by studying STO/Si layers with intermediate thicknesses), epitaxial strain is not likely to be the main driving force for the formation of the t-STO phase: O vacancies associated with O segregation at the early stages of the growth are more likely at the origin of this phenomenon. Improving the STO structural quality requires:

-further understanding and control of the origin of the formation of these two phases, in order to obtain single phased STO

-increasing the STO growth temperature: at 360°C, STO is initially partly amorphous. The optimal growth temperature for STO/STO homoepitaxy is 550°C.

III.4) Towards substrate-like quality SrTiO₃ thin films on Si (001)

III.4.1) Alternative strategies of Si surface passivation

One of the principal objectives of this thesis consists in the development of perfect STO epitaxial film on silicon substrate and the comprehension of the issues related to system thermodynamics, oxidation kinetics and knowledge of interfacial structures. In order to improve the crystalline and surface quality of the STO film epitaxially grown on silicon substrate, we discuss in this section several different Si passivation strategies and their influence on the STO structural quality.

III.4.1.1) Silicate (Sr$_2$SiO$_4$) buffer layer

Since R. C. McKee *et al*[74,75,76] firstly pointed out the crucial role of Sr termination layers in the preparation of crystalline oxide-semicondutor heterostructures, the growth of alkaline earth oxides (SrO, (Ba,Sr)O) on silicon were intensely studied, particularly during the first stages of their growth on Si. Y. Liang[77] *et al* reported an investigation of a two-dimensional silicate-like layer (Sr$_2$SiO$_4$) on Si (001) surface. This layer remains stable at high temperature ~450°C in oxygen rich environment with oxygen partial pressure up to 5×10^{-7} Torr hence can possibly be used as an interfacial template for the subsequent growth of single-crystalline perovskites. We have further studied[78] the structural and chemical behavior of the crystalline Sr$_2$SiO$_4$ layer and it is found that this silicate decomposes to SrSiO$_3$ at higher temperature 600°C due to internal reactions and/or by reaction with the substrate.

In this thesis, we examine firstly the growth of STO on 2D silicate layer reported by Y. Liang (Ref. 77). This process consists in forming the silicate and subsequently growing STO at around 550°C. The process details and the RHEED patterns obtained along Si[110] azimuth at each step are shown in Figure III. 35. After treatment by BOE plus UV ozone (III.2.1), the silicon surface is covered by ~1nm thick SiO$_2$ layer. An annealing at 950°C for 1 hour is performed to obtain a clean (2×1) reconstructed Si surface. Strontium is then added to the silicon surface from 1/3ML (×3 reconstruction) to 1/2ML (×2 reconstruction) at 600°C. The substrate temperature is then ramped down to 160°C and the 1/2ML Sr is oxidized under oxygen partial pressure of 5×10^{-8}Torr. A 2D single crystalline Sr$_2$SiO$_4$ layer is formed by increasing the temperature to 550°C, which is revealed by a clear, well-define RHEED pattern with Kikuchi lines. STO is deposited on this silicate buffer layer at 550°C with oxygen partial pressure 5×10^{-7}Torr. We observe that the STO film remains amorphous until 4ML and exhibits both crystalline and amorphous phases when the thickness is 20ML, which suggests the possible reaction between the deposited STO and Si substrate and the formation of amorphous interfacial layer. Therefore the 1/2ML silicate layer cannot passivate silicon surface at high temperature and high oxygen partial pressure.

It is very likely that the 1/2 ML silicate layer is too thin to prevent the interfacial reaction. According to the results of Ref. 38, the Sr$_2$SiO$_4$ layer is formed during the epitaxial growth of SrO on silicon substrate when the growth temperature is higher than 500°C, and remains single crystalline and 2D up to 6ML. We have thus investigated the growth of this silicate as a
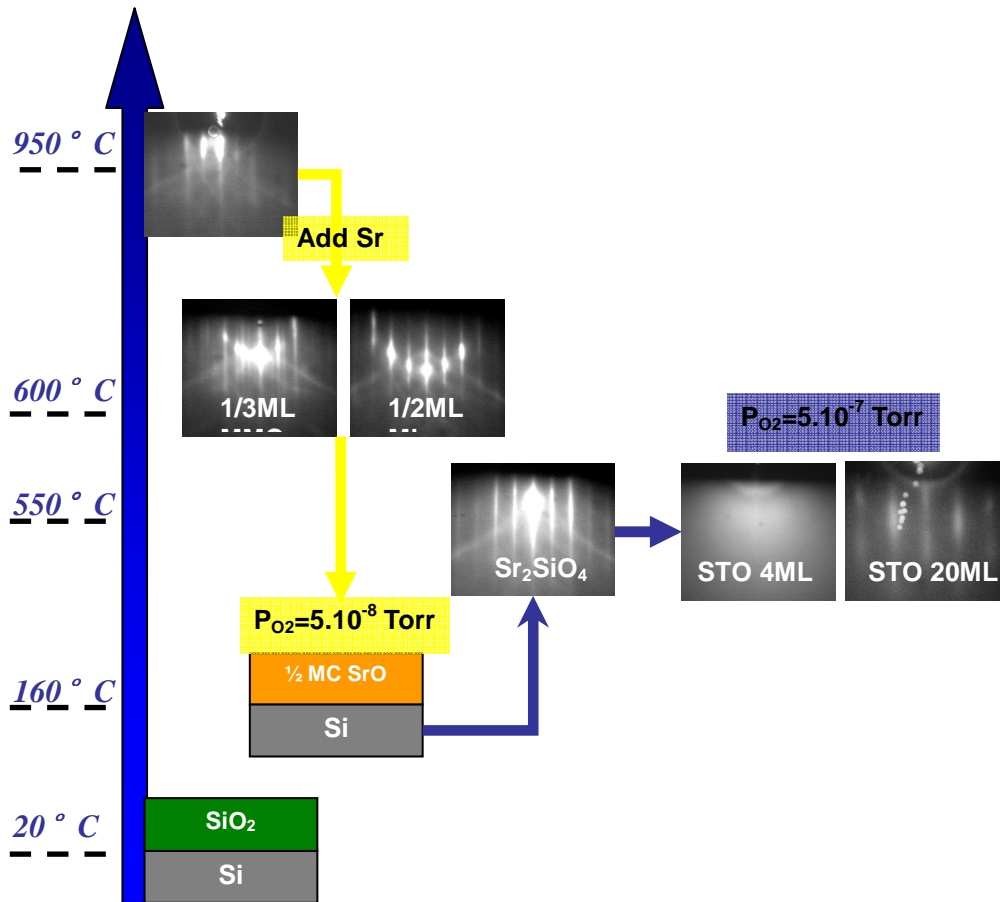
function of the growth temperature.

Figure III. 35 Growth processes of STO/SrSiO₄/Si(001) system. The RHEED patterns are all taken along Si[110] azimuth.

10ML silicate layers are deposited at 500°C~750°C with a Sr flux of 9×10^{-9}Torr and oxygen partial pressure of 1×10^{-8}Torr (optimized condition of SrO epitaxy, see Ref. 38). Figure III. 36 shows the RHEED patterns along Si [110] azimuth of the 10ML-silicate on silicon substrate. At 500°C, the RHEED displays only diffuse halo suggesting a completely amorphous feature of the deposited layer. It has to be noted that the growth always begins from a crystalline phase but the portion of amorphous phase continuously increases and covers the entire surface at the end of the growth. As the temperature increases to above 650°C, the crystalline phase (streak lines) can still be observed for the 10ML film. Nevertheless, at the extreme temperature 750°C the growth mode turns into three dimensional one.
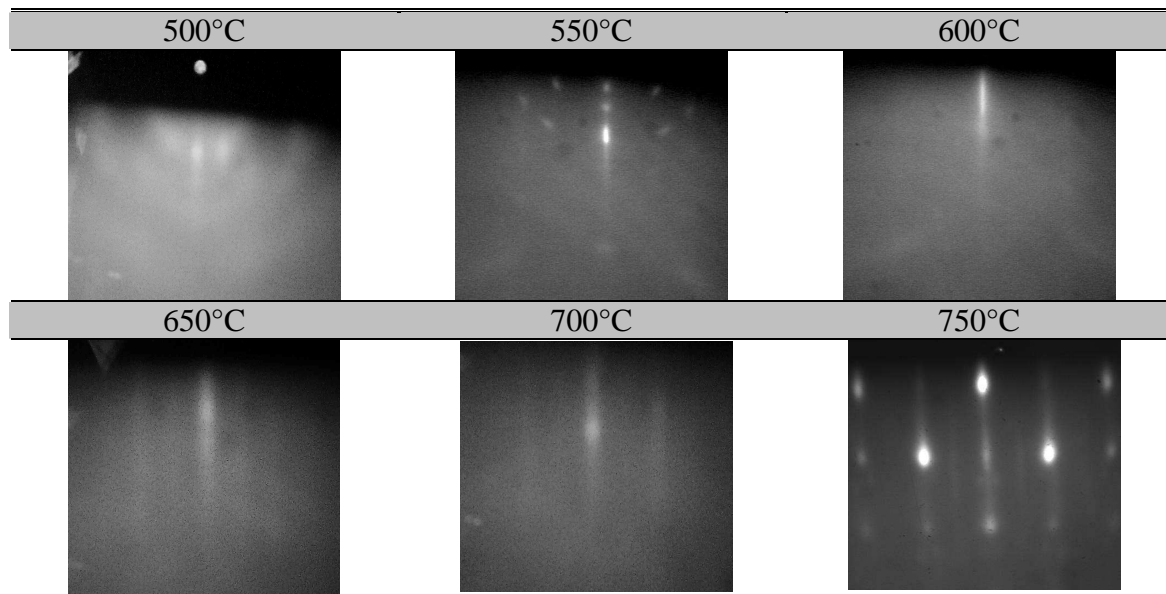
Figure III. 36 RHEED pattern along Si [110] azimuth of 10ML silicate layers at different temperatures

Based on these observations we conclude that the initial 2D single crystalline silicate layers cannot be grown on Si at any temperature. It is not surprising because neither the two Sr_2SiO_4 phases (α and β) structurally matches silicon[79], considering that Sr_2SiO_4-α has an orthorhombic (group space N°62 Pmnb) phase with a=5.682Å, b=7.090 Å, c=9.773 and Sr_2SiO_4-β possesses a monoclinic (group space N°14 P121/n1) phase with a=5.663Å, b=7.084 Å, c=9.767 Å[80]. Therefore the initial crystalline silicate layer is likely a pseudomorphic phase and stable only within few monolayers.

We examine the quality of STO films grown on 2ML-thick silicate buffer layers at 550°C~650°C. Figure III. 37 exhibits the evolutions of RHEED patterns along Si[110] azimuth for the STO growth on silicate/Si (001) template. We observe that 2ML silicate layers grown at 550 °C show clear streak lines attesting the single crystalline feature. The RHEED pattern of 10ML-STO grown at the same temperature displays clear, streak lines feature suggesting single crystalline growth. However, the initial 5ML STO shows partly amorphous feature revealing the formation of interfacial layer. For higher temperatures, the RHEED patterns show coexistence of streaks and the diffuse halo suggesting both crystalline and amorphous phases. The RHEED patterns of STO films deposited on these silicate layers demonstrate spots and Debye-Sherrer rings suggesting 3D and polycrystalline growth modes.
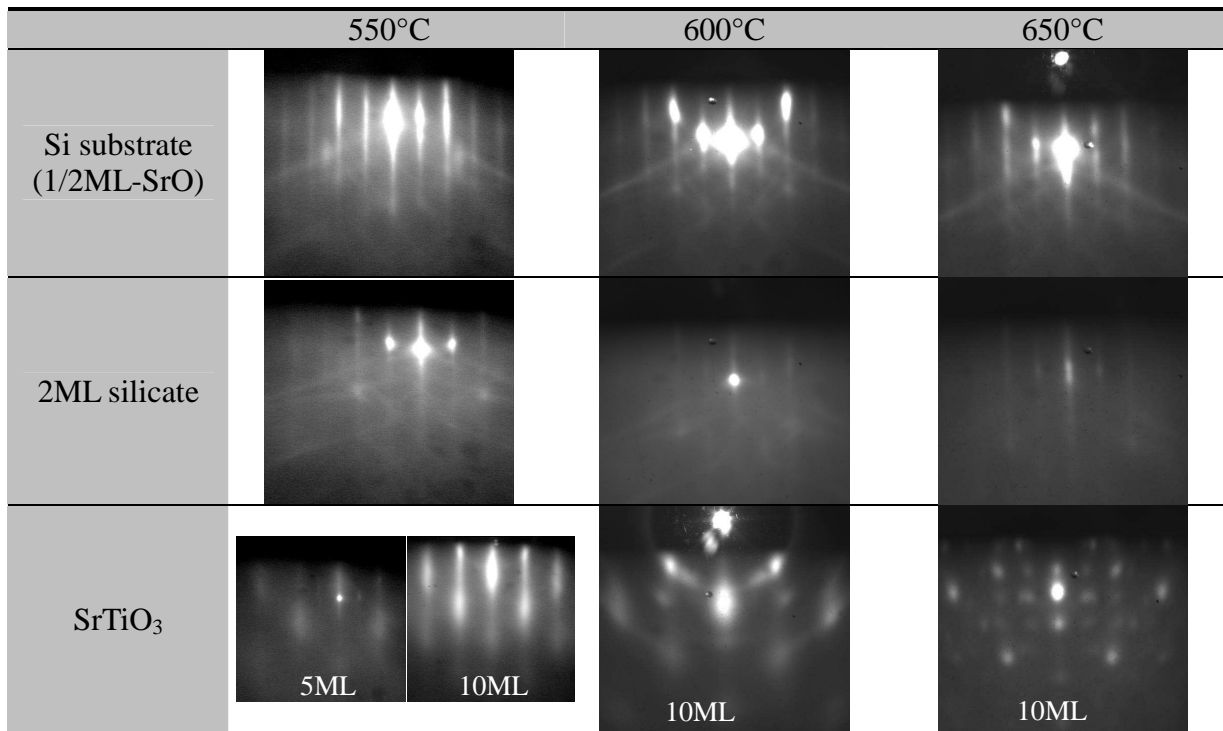
Figure III. 37 RHEED patterns along Si [110] azimuth of the STO growth on silicate/Si(001) template at different temperatures.
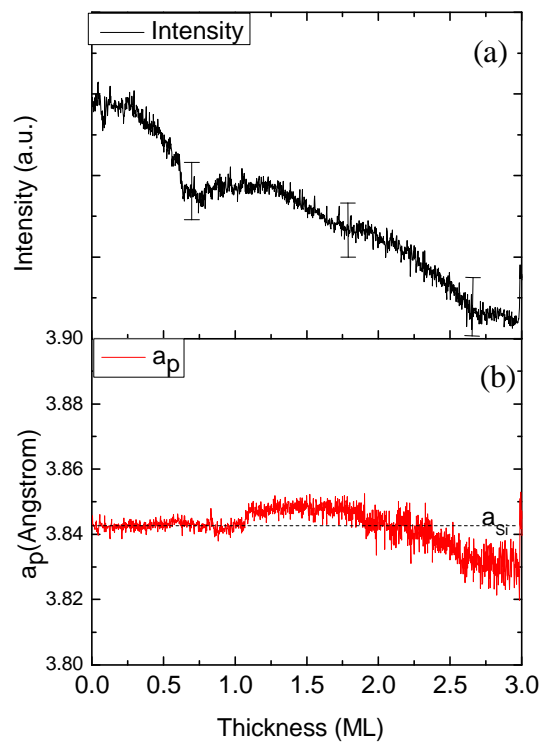

Figure III. 38 Evolutions of (a) RHEED intensity of the specular spot and of (b) the silicate lattice parameter (deduced from RHEED diffraction line spacing)

Figure III. 38 (a) and (b) respectively shows the evolutions of RHEED intensity of the

specular spot and of the silicate lattice parameter during the silicate growth at 550°C. The RHEED intensity undergoes a continuous decline during the growth and the oscillations show that 3ML-thick silicate film is deposited. The a_p remains constant and equals to that of the silicon substrate value (3.845Å at the growth temperature 550°C) suggesting a pseudomorphic growth of silicate film on Si.

The crystallographic quality of a 60ML-thick STO/2ML-silicate/Si sample grown at 550°C was examined by XRD 2θ-ω measurement, as shown in Figure III. 39. The intense sharp peak locating at 2θ=69.13° corresponds to the Si 004 reflection. The Si 002 peak (2θ=32.95°) that should be extinct also appears probably due to the interdiffusion of the atoms at the silicate/Si interface. The STO (001), (002) and (004) peaks appear at 2θ=22.75°, 46.56° and 104.44°, exhibiting good quality of single-crystalline STO film, in good agreement with the RHEED observations.
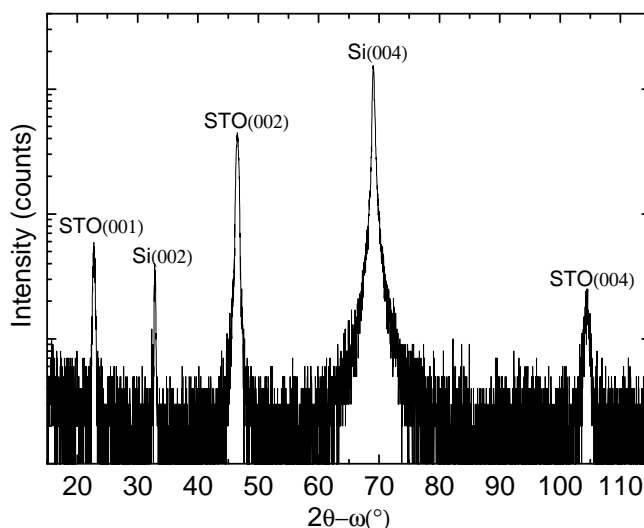
Figure III. 39 XRD 2θ-ω scan of the STO film grown on silicate/Si(001) template at optimized growth condition.

Compared to the STO grown on Sr-passivated Si surface at ≥500°C, which is polycrystalline, the 2D single-crystalline STO film can be epitaxially grown on silicate/Si(001) template at 550°C. Nevertheless, an amorphous interfacial layer forms at the interface and the STO recrystallizes after 5ML.

III.4.1.2) (Ba,Sr)O-passivated Si(001)

In addition to SrO, the binary oxide BaO was also been envisaged and explored as a

buffer layer for the heteroepitaxy of perovskite oxides on silicon[81,82]. In particular, the mixed compound $(Ba_{1-x},Sr_x)O$ attracts intense researches[83,84,85] due to the possibility to tune its lattice parameter between that of BaO(5.534Å) and that of SrO(5.140Å). According to the Vegard Law[86], the compound $(Ba_{0.72}Sr_{0.28})O$ adopts the same lattice parameter as that of silicon (5.431 Å) at room temperature. Hence lattice-matched epitaxy could be envisaged between $(Ba_{0.72}Sr_{0.28})O$ and Si and also between $(Ba_{1-x},Sr_x)O$ and STO by progressively changing the alloy composition.

The growth condition of the mixture $(Ba_{0.72}Sr_{0.28})O$ has been detailed investigated in the thesis of G. Delhaye[38] at INL. The optimized growth condition of $(Ba_{0.72}Sr_{0.28})O$ can be summarized as following:

(1)   Low growth temperature (60°C). At such low temperature, the mobility of the metal species is limited leading to a homogeneous mixed compound in case of co-deposition.

(2)   Oxygen partial pressure of 1×10^{-8}Torr. This critical oxygen partial pressure guarantees the complete oxidation of the metal species while prevents the formation of the phases of BaO_2 and SrO_2.

(3)   The stoichiometry of the mixture $(Ba_{0.72}Sr_{0.28})O$ is determined by the measurement of Quartz Crystal Microbalance.

RHEED patterns along Si[110] and Si[100] of a 19ML $(Ba_{0.72}Sr_{0.28})O$ film are shown in Figure III. 40. The high contrast, well-ordered streak lines exhibit good single crystalline quality of the layer. In addition, the epitaxial relationship between $(Ba_{0.72}Sr_{0.28})O$ and Si can be defined as [100] $(Ba_{0.72}Sr_{0.28})O$ (001)//[100]Si(001).
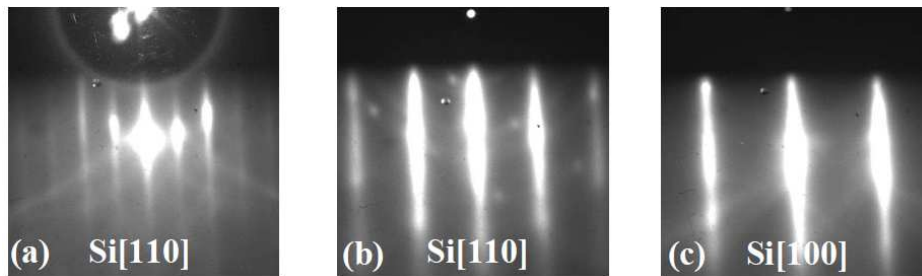

Figure III. 40 RHEED patterns of (a)1/2MLSr covered Si surface, (b)(Ba,Sr)O[110] surface along Si[110]direction and (c) (Ba,Sr)O[100] along Si[100]direction.

Figure III. 41 (a) shows the evolution of the RHEED intensity of the specular spot during

the growth of the $(Ba_{0.72}Sr_{0.28})O$ sample grown under optimized condition. The plotting displays oscillation at the beginning of the growth suggesting layer-by-layer growth mode, which transforms to 3D growth revealed by the disappearance of the oscillations. The evolution of the lattice parameter of $(Ba_{0.72}Sr_{0.28})O$ is plotted in Figure III. 41 (b): it oscillates in phase opposition with respect to the RHEED intensity. This behavior corresponds to the non-tetragonal deformation of the $(Ba_{0.72}Sr_{0.28})O$ takes place at the free edges of the two-dimensional islands formed during the layer-by-layer growth, as explained in III 3.5. The lattice parameter of $(Ba_{0.72}Sr_{0.28})O$ remains similar to that of silicon, indicating that good lattice-matched $(Ba_{0.72}Sr_{0.28})O$ epitaxial film has been grown on Si(001).
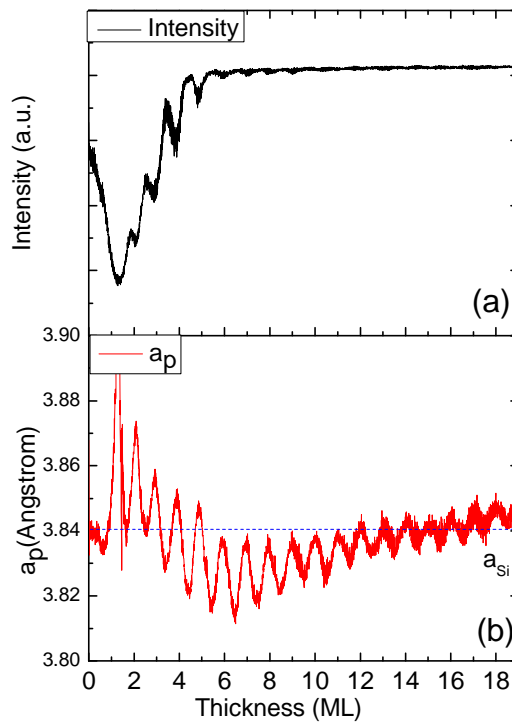
Figure III. 41 Evolution of the intensity of the RHEED diffraction lines (a), and of the $(Ba_{0.72}Sr_{0.28})O$ lattice parameter (b) (as deduced form RHEED diffraction line spacing).

In order to investigate the stability of $(Ba_{0.72}Sr_{0.28})O$ thin film on silicon substrate, the interface of the as-deposited 5ML sample and a sample annealed at 380°C for 10min under UHV are probed by XPS[87]. Figure III. 42 shows the XPS spectra of Si *2s* of the two samples. An high energy shoulder appears on the the Si *2s* peak after the annealing of 380°C, which corresponds to the presence of silicate and silica at the interface. These results demonstrate that the (Ba,Sr)O layer is thermodynamically instable on silicon even at such low temperature of 380°C, which make (Ba,Sr)O not suitable as a passivation layer on silicon for the subsequent STO growth at relative high temperatures (550°C).
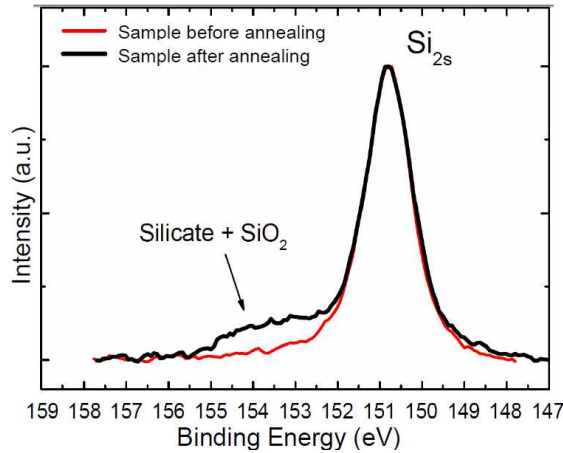
Figure III. 42 XPS Si 2s spectra[87] of the as-deposited sample and the sample annealed at 380°C for 10min under UHV.

III.4.1.3) Summary

In this section, we have examined two other passivation methods in addition to 1/2 ML-SrO to achieve the commensurately epitaxial growth of STO on silicon without the recrystallization process. However, none of these two techniques effectively passivate silicon surface at the relative high temperature 550°C, the optimal growth temperature for STO homoepitaxy. Other strategies should be identified to attain this objective.

III.4.2) "2 steps" growth approach

Given that the strategies discussed above could not be used to passivate silicon surface at high temperature, a "2 steps" growth approach has been explored in this thesis. It is detailed in this section. The STO epitaxial film grown under the optimal condition identified in III. 3 (360°C and initial oxygen partial pressure of 5×10^{-8}Torr) is firstly annealed under UHV at 550°C to be used as a buffer layer (first step). Further STO epitaxy is then performed at 550°C, and under an oxygen partial pressure of $5\times10^{-7}\sim1\times10^{-6}$Torr. This process is illustrated in Figure III. 43.
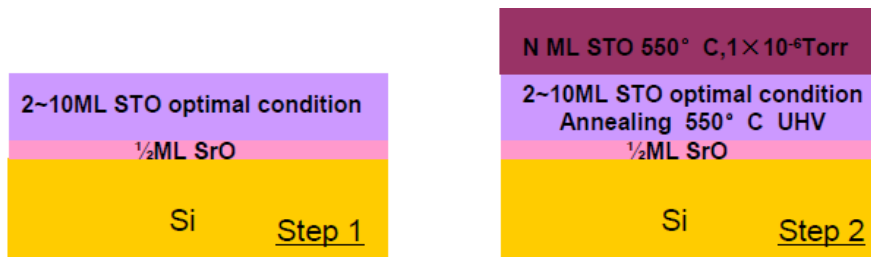

Figure III. 43 Illustration of "2 steps"approach of epitaxial growth of STO. Left panel shows step 1 of the STO growth under optimized condition and right panel displays step 2 of an

annealing and the epitaxy at high temperature and high oxygen partial pressure.

III.4.2.1) Influence of STO buffer layer thickness: crystallinity

As discussed in the following, the "2 steps" approach is a compromise between STO structural quality (crystallinity, defects) and interface abruptness. The STO grown at the first step presents an abrupt interface with silicon and is expected to act as a buffer layer role to prevent Si from oxidization at high temperature and under high oxygen partial pressure. Because the oxygen might diffuse through the STO buffer layer to the STO/Si interface and lead to the formation of silica amorphous layer, we investigate the influence of STO buffer layer thickness to the quality of the samples.

A series of 45nm-thick STO/Si samples (grown at 550°C under 5×10^{-7} Torr of oxygen except for the STO buffer) with 2ML, 5ML and 10ML STO buffer layer (grown at 360°C) have been fabricated. The evolutions of the RHEED patterns recorded along the Si[110] azimuth are shown in Figure III. 44.

As shown in the figure, all the films are grown on flat, 1/2ML-SrO covered silicon substrates. At the first step, STO was deposited under optimal conditions defined in the section III. 3. The 2ML STO buffer exhibits both amorphous and crystalline phases, while the 5ML and 10ML thick STO buffers present improved crystallinity due to recrystallization at 360°C (see section III. 3.4.2). For 2ML STO, after annealed at 550°C under UHV, it is obvious that the diffuse halo vanishes and the RHEED pattern shows clear streak lines features, suggesting good crystallinity of the STO layer. For 5ML and 10ML samples, the streak lines displays higher contrast and better defined feature after annealing treatment. In the end of the growth, all the samples exhibit well-defined streak lines feature with a "×2" reconstruction RHEED patterns, suggesting high quality single-crystalline TiO₂-terminated STO epitaxial layers.
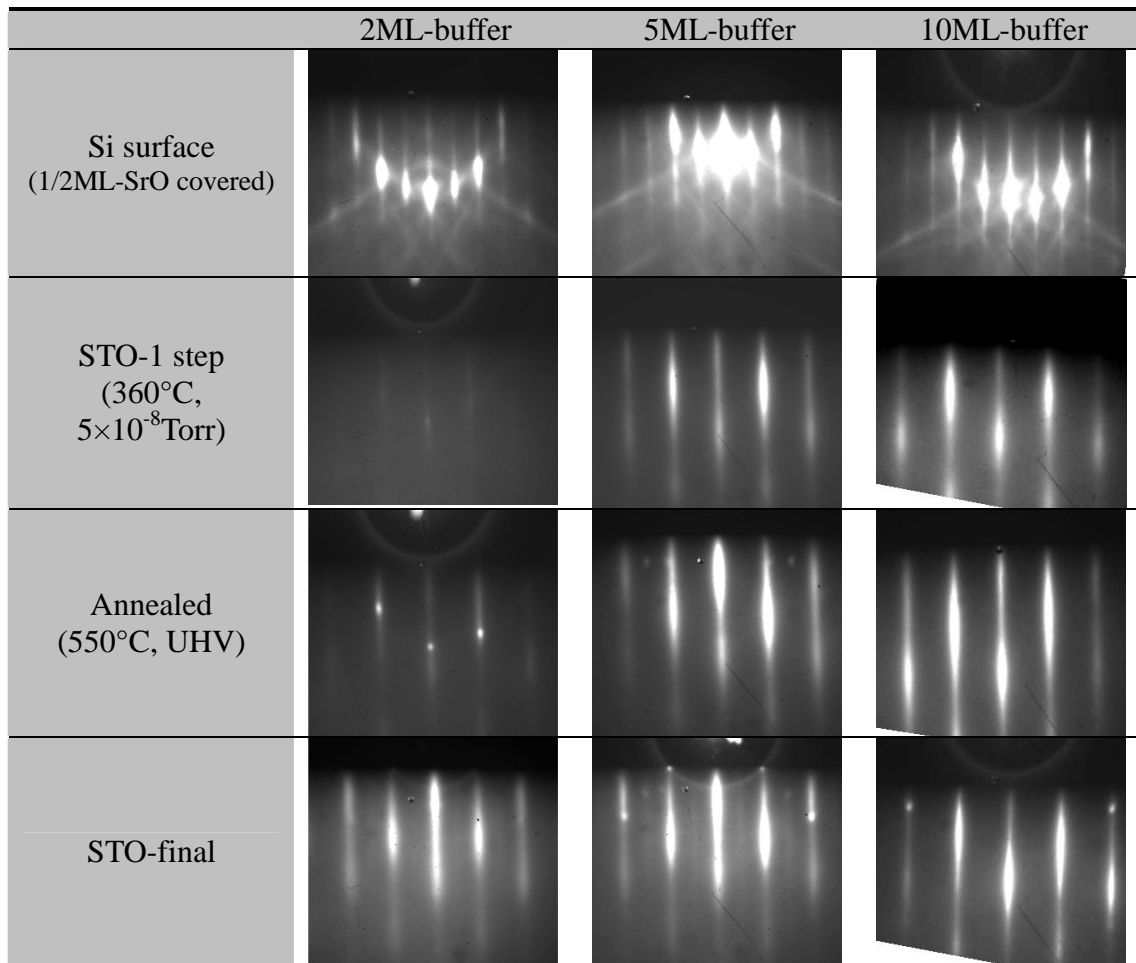
Figure III. 44 RHEED patterns along Si [110] azimuth of "2 steps" STO films with different buffer STO thicknesses.

HRXRD measurements were performed to further study the crystalline quality of the 45nm STO layers. Figure III. 45 shows the typical 2θ-ω scans and ω scans (rocking curves) recorded the around STO 002 reflections for the different samples.. The 2θ-ω scans of the three samples exhibit the similar feature. The STO 002 peak centered at 2θ=46.58°, corresponding to an out-of-plane lattice parameter $a_\perp$=3.896Å, indicates that the STO films are fully relaxed on the silicon substrate, considering the thermal expansion mismatch (see III.3.3.3). STO 003 peaks arising at 2θ=72.3° can also be observed for the samples with 5ML buffer and 10ML buffer, indicating high quality crystallinity of these films. The rocking curves however show that increasing the buffer layer thickness to 10 ML reduces the mosaicity of the STO film. It is very likely that thicker buffer layers result in better interface quality thus better crystallinity.
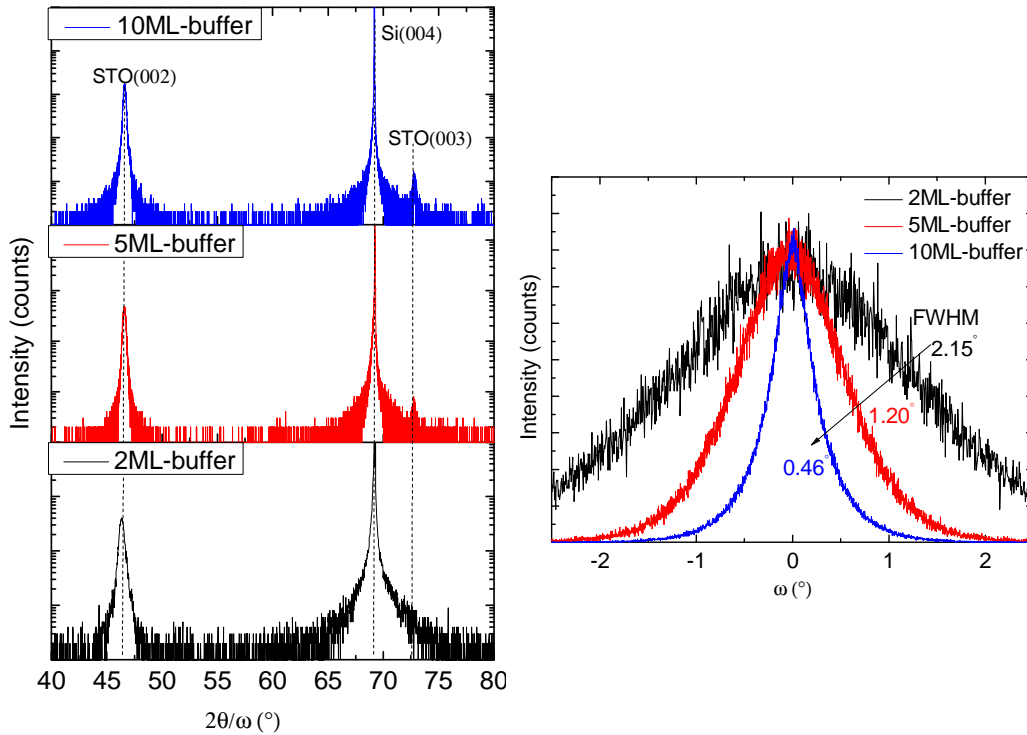
Figure III. 45 X-ray 2θ-ω scans in log scale (left panel) and ω rocking curve scans around STO (002) in linear scale of (right panel) for a series of STO films "2 steps"

III.4.2.2) Interface and surface quality

The "2 steps" samples have also been examined by HRTEM measurements to clarify both crystallization and interface qualities. Figure III. 46 (a) and (b) shows the HAADF-STEM and HRTEM cross-sectional view images of the 2ML-buffer sample respectively.
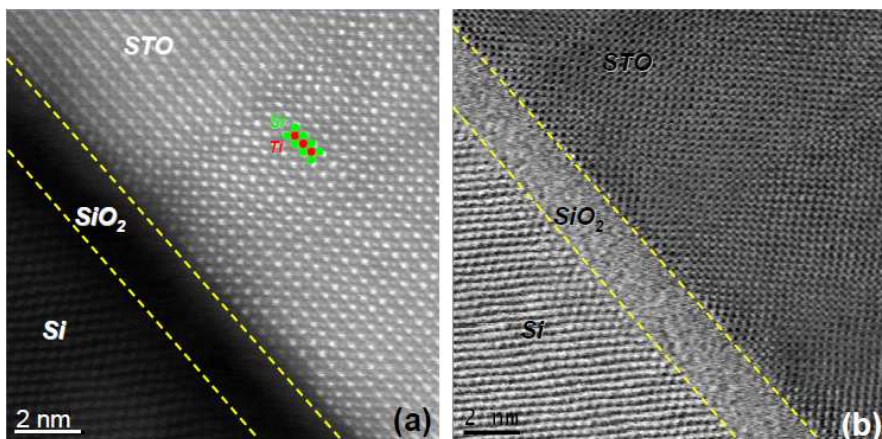

Figure III. 46 (a) HAADF-STEM and (b) HRTEM cross-sectional view images of 2ML-buffer sample.

From the TEM images we can clearly observe that an approximately 2nm SiO_2

amorphous layer forms at the interface. In addition, surprisingly, this 2nm-SiO_2 amorphous does not disappear as the buffer thickness increases to 5ML and 10ML (not shown here). According to an earlier study (Ref. 42), the silica layer forms at the second step of the growth, i.e. the oxygen ($P_{O2}=5\times10^{-7}\sim1\times10^{-6}$Torr) diffuses through the grown STO layer to the silicon surface at such high temperature (550°C). Regarding to the STO layer quality, the highly uniform contrast displayed by the images verify a good crystallinity of the STO epitaxial film. We can clearly observe the strontium and titan atoms in the HAADF-STEM images.

The surface morphology of the "2 steps" samples are also explored by AFM non-contact measurement. They all demonstrate an atomically flat surface. Figure III. 47 shows a 4μm×4μm AFM image of 2ML-buffer sample, with the RMS of 0.11nm.
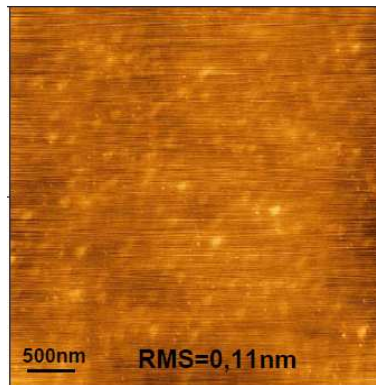

Figure III. 47 4μm×4μm AFM image of 2ML-buffer "2 steps" STO/Si(001) sample.

III.4.3) Strategy of multi-step recrystallization growth

H. Li et al. in 2003 reported a kinetically controlled sequential deposition method for the STO/Si system with an abrupt interface[62]. This method consist of an initial deposition of amorphous 2ML STO at low temperature (200°C) and low oxygen partial pressure ($1\sim5\times10^{-8}$Torr) then annealing at 600°C and UHV, following with the repeat of this process till 10ML STO is obtained. They announced that this 10ML STO could maintain its integrity for subsequent further STO growth at high temperature (550°C) and high oxygen partial pressure ($\geq1\times10^{-7}$Torr). Therefore we investigate this method in this section.

Figure III. 48 shows the evolution of the RHEED patterns of the STO films at each step. After annealing at 550°C under UHV , well-defined steak lines RHEED pattern can be observed for the originally amorphous 2ML STO. By repeating the recrystallization process, 10ML high quality single crystalline STO layer is obtained. Based on this 10ML buffer STO

layer, 105ML STO film is subsequently deposited at 550°C and oxygen partial pressure of 1×10^{-6}Torr. The final film shows the similar RHEED pattern as those grown using "2 steps" method, indicating a high quality single crystalline TiO$_2$-terminated STO film.
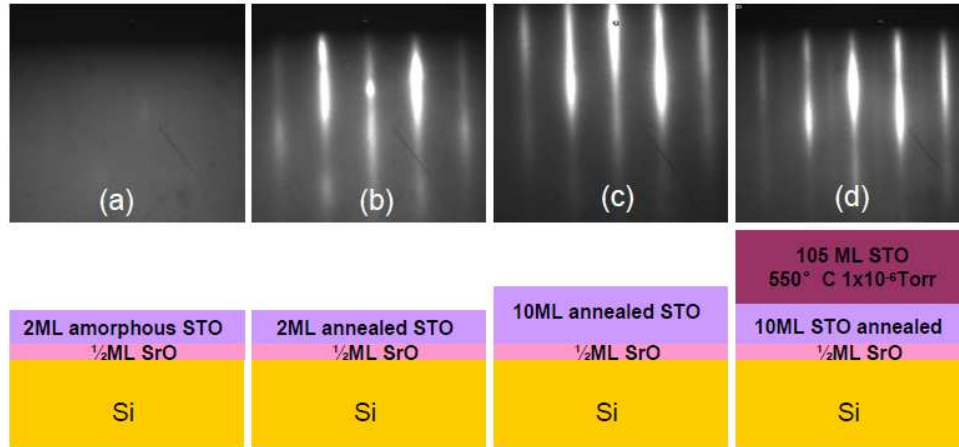

Figure III. 48 Evolution of RHEED patterns (upper) for each step of STO deposition using kinetically controlled sequential method in Ref 62.

XRD *2θ-ω* measurements were performed on this 45nm-thick sample, as shown in Figure III. 49 (a). The STO 002 peak appears at 2θ=46.60° (with a FWHM=0.22°), in the same position as that observed for STO grown by the "2 steps" method, which suggests STO is totally relaxed. The corresponding rocking curve ω (Figure III. 49 (b)) presents a FWHM of 0.14°, which attests for the excellent structural quality of the STO layer.

Considering the finite thickness of the STO sample (~45nm), the FWHM of $2θ_B/2$ of perfect crystallite can be estimated by Scherrer formula:

$$t = \frac{0.89\lambda}{B\cos\theta_B}$$

where t the crystallite thickness, λ the X-ray wavelength (1.54059Å), B full width at half max (FWHM) and $θ_B$ the Bragg angle (rad). Comparing the FWHM of calculation value (0.18°) and experimental one, a "substrate-like" STO epi-layer is obtained on Si(001) substrate. The surface morphology of this STO layer is characterized by AFM (4μm×4μm), which shows atomically flat quality with RMS=0.16nm, as is demonstrated in Figure III. 50.

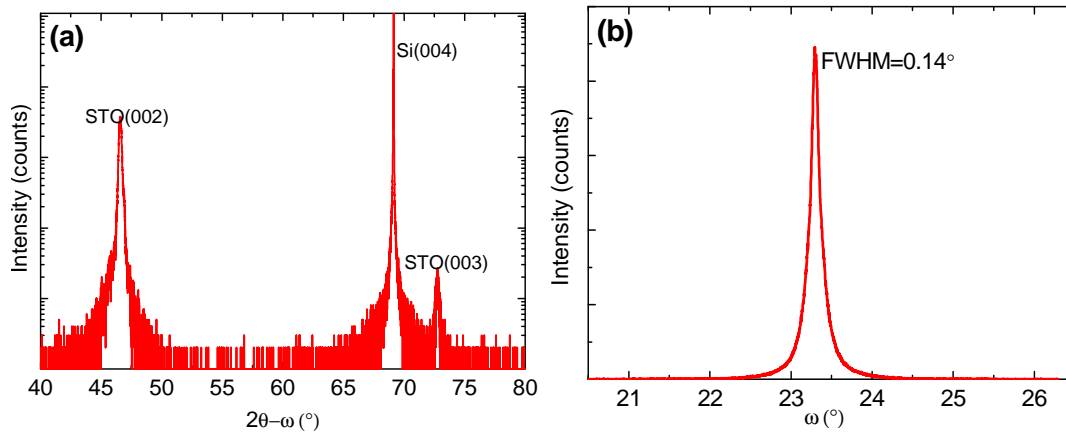*Figure III. 49 (a) Typical 2θ-ω scans in log scale (a) and ω rocking curve scans around STO (002) in linear scale of (b) "recrystallized" STO films*

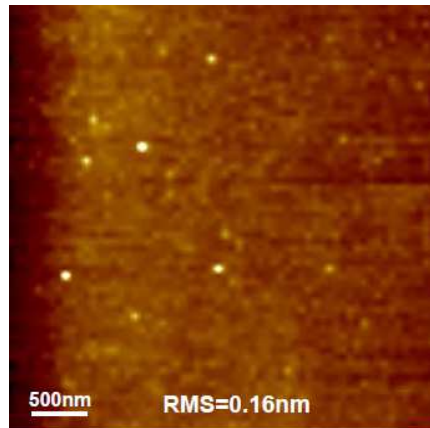*Figure III. 50 4μm×4μm AFM image of "recrystallinzed" STO/Si(001) sample*

Figure III. 51 (a) and (b) show the TEM cross-sectional images of the recrystallized 10ML thick STO buffer layer (taken from Ref.62) and of our final 45nm-STO film. The 10ML recrystallized STO buffer presents an abrupt interface with Si and the subsequent growth of STO at 550°C and O_2 partial pressure of 1×10^{-6}Torr lead to the formation of a ~2nm-thick amorphous SiO_2 layer at the interface. This behavior is similar to that of the STO/Si sample grown by "2 steps" method. Oxygen diffuses through the growing film resulting in the formation of interfacial SiO_2.
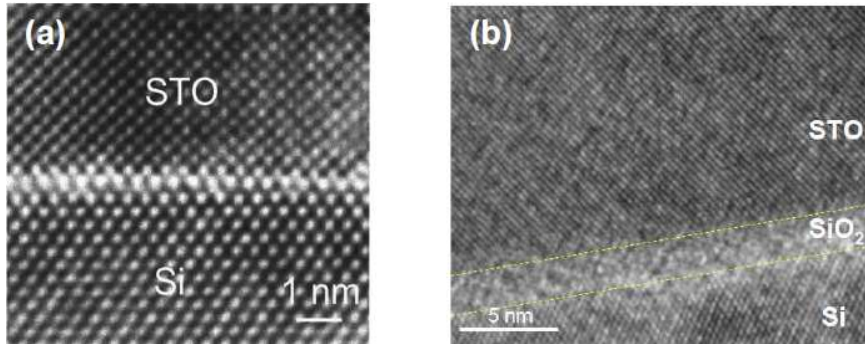
Figure III. 51 TEM cross-sectional images of (a) 10ML-recrystallized STO buffer (Ref. 62) and (b) ~45nm-thick final STO epi-layer grown at 550°C and $P_{O2}=1\times10^{-6}$Torr.

III.4.4) Conclusion

In this section, several strategies are compared to optimize STO structural quality while maintaining an acceptable interface structure between STO and Si. Neither the silicate nor (Ba,Sr)O layer could play the passivation role therefore "2 steps" and "recrystallization" methods were developed and a "substrate-like" STO epi-layer has been obtained. Although a ~2nm-thick SiO_2 interfacial layer forms even for the 10ML-thick buffer samples due the diffusion of the oxygen, we succeeded in strongly improving the STO structural quality.

Figure III. 52 shows the X-ray reciprocal space maps (RSM) around both STO (002) (symmetric) and STO (103) (asymmetric) Bragg reflections, for the ~45nm samples grown under the optimal conditions for low temperature (360°C and $PO_2=5\times10^{-8}$Torr then 1×10^{-6}Torr) and by "2 steps" and "recrystallization" methods. This figure clearly shows how we have improved STO structural quality. Except for the sample grown by "recrystallization" method which displays intense and circle spots in the RSM maps, all the other samples shows ellipse diffuse spots feature in the maps, which suggest the high mosaicity of these STO samples. Comparing the "recrystallization" sample with the "360°C" sample, the FWHM of the rocking curve in ω of STO (002) is improved from 1.4° to 0.14°, which obviously shows that the crystalline quality of the STO film is significantly developed owing to our optimization for the growth condition.
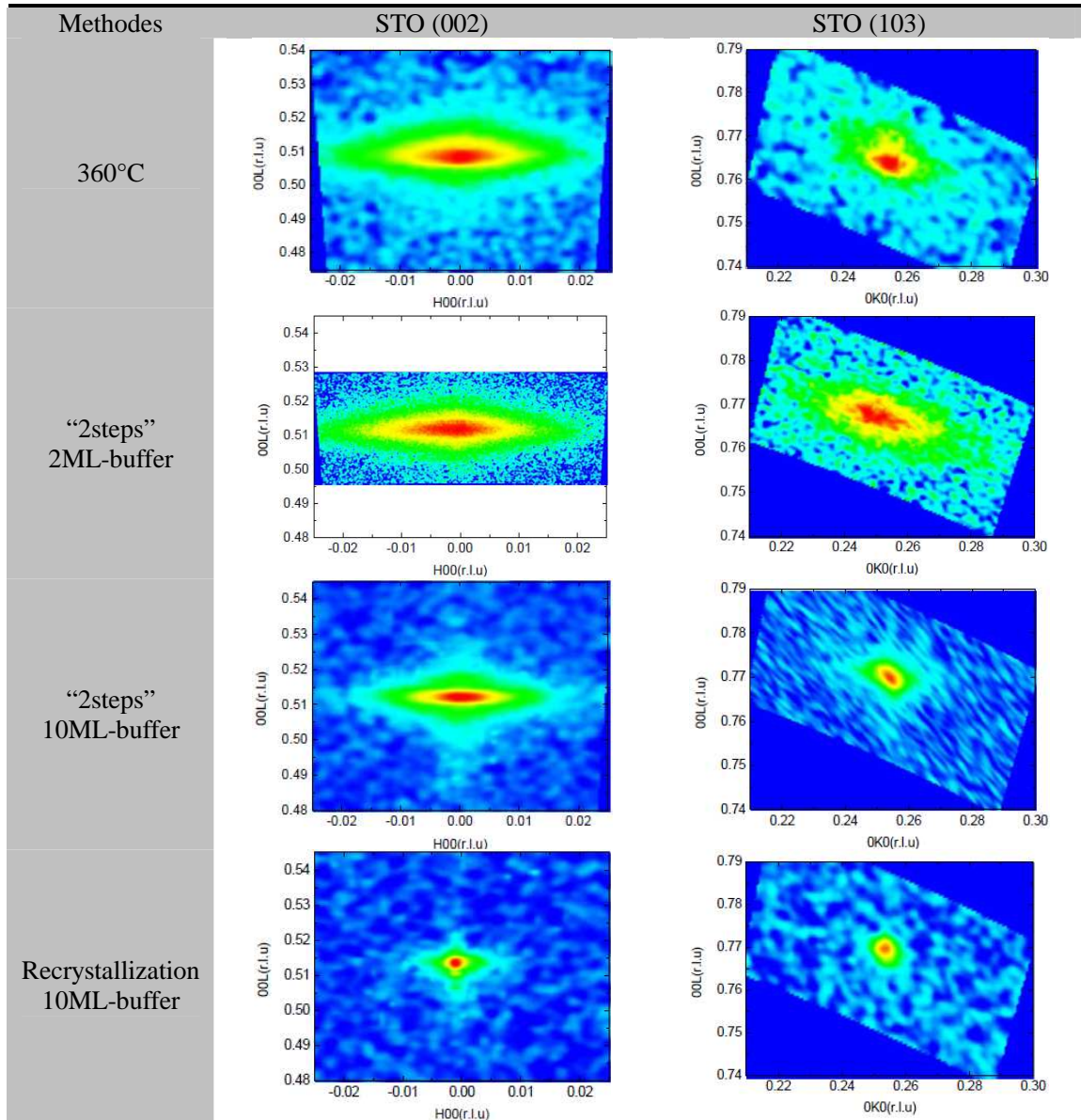
Figure III. 52 Reciprocal space maps along STO (002) and STO(103) Bragg conditions of STO epitaxial films fabricated by different growth strategies. Intensities from low to high: blue, green, yellow, red.

III.5) Epitaxial growth of Gd₂O₃ on Si (111)

III.5.1) Introduction

Gadolinium oxide (Gd$_2$O$_3$) which belongs to the rare earth oxides family presents a cubic bixbyite Mn$_2$O$_3$ (II) structure (group space $Ia\bar{3}$) in which the unit cell includes eight unit cells of an incomplete and distorted fluorite structure, as shown in Figure III. 53 (a). As mentioned in I.3.1, it is identified as a promising candidate for the future high-k gate dielectric due to its several outstanding properties: (1) high dielectric constant; (2) thermodynamic stability on Si;

(3) lattice-match growth when 2 unit cells of Gd_2O_3 deposited on one Si unit cell (lattice mismatch 0.44%) and (4) high bandgap of 5.3eV and large conduction and valence band offset of 1.8eV and 2.4 eV respectively with respect to Si, as shown in Figure III. 53 (b). Particularly, compared to the Gd_2O_3 films with bidomain structure on Si(001) substrate, the Gd_2O_3 films on Si(111) exhibits highly perfect crystallinity which turns out quite appealing for its potential application to the realization of monolithic integration of functional oxides and semiconductors on the silicon substrate. We will focus on the study of Gd_2O_3/Si(111) system in this section, including elucidate the growth condition and the structural quality of the Gd_2O_3 epitaxial films.
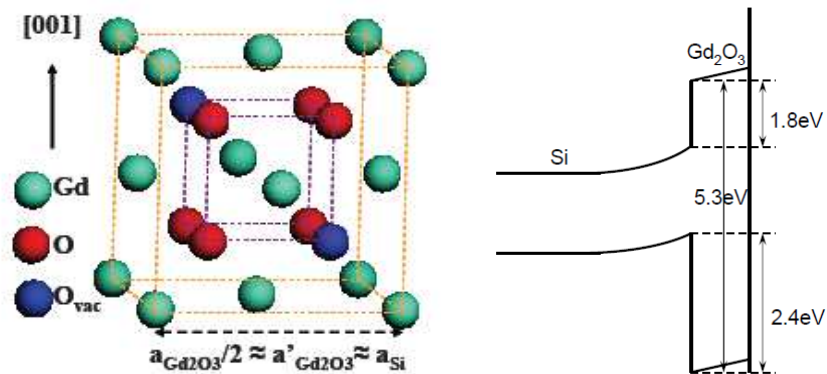

Figure III. 53 (a) Lattice structure of Gd₂O₃ and (b) schematic band alignment for Gd₂O₃/Si heterostructure

III.5.2) Influence of the growth temperature

The Gd_2O_3 films studied in this section were prepared using electron beam evaporation of commercial granular Gd_2O_3 target on p-type Si (111) substrates (10^{15} cm^{-3} dopant concentration). The film deposition started from an atomically flat silicon surface (see III.3.1). Similarly to the $SrTiO_3$ growth, the O_2 partial pressure is precisely controlled in the range of UHV (~5×10^{-10}Torr) during the first stage to avoid any interface parasitic phase formation. The growth rate is 2~3Å/min, monitored by the QCM. After 2 monolayers growth of Gd_2O_3, the O_2 pressure was ramping up to 1×10^{-6}Torr in order to insure the oxygen stoichiometry in the oxide film.

A series of ~5nm-thick Gd_2O_3 films were deposited at different temperatures ranging from 650°C~750°C. Figure III. 54 shows the RHEED patterns (along Si [1-10] azimuth) and the corresponding AFM images (1μm×1μm) The RHEED images of the 680°C and 700°C samples exhibit streaky lines, indicating good crystallinity of the films. A ×4 surface

reconstruction can be observed for the sample deposited at 700°C, likely due to the presence and organization oxygen vacancies at the film surface.. Compared to those grown at 680°C or 700°C, the films grown at extreme temperatures (650°C and 700°C) are partially amorphous feature (diffuse halo between the diffraction streaks). At 750°C, the 7×7 reconstruction of Si remains through the whole growth process, which could be attributed to an important desorption of Gd_2O_3 at such a high temperature. AFM images show that the Gd_2O_3 layers deposited between 650°C and 700°C have a surface of good quality with an RMS of less than 1nm.
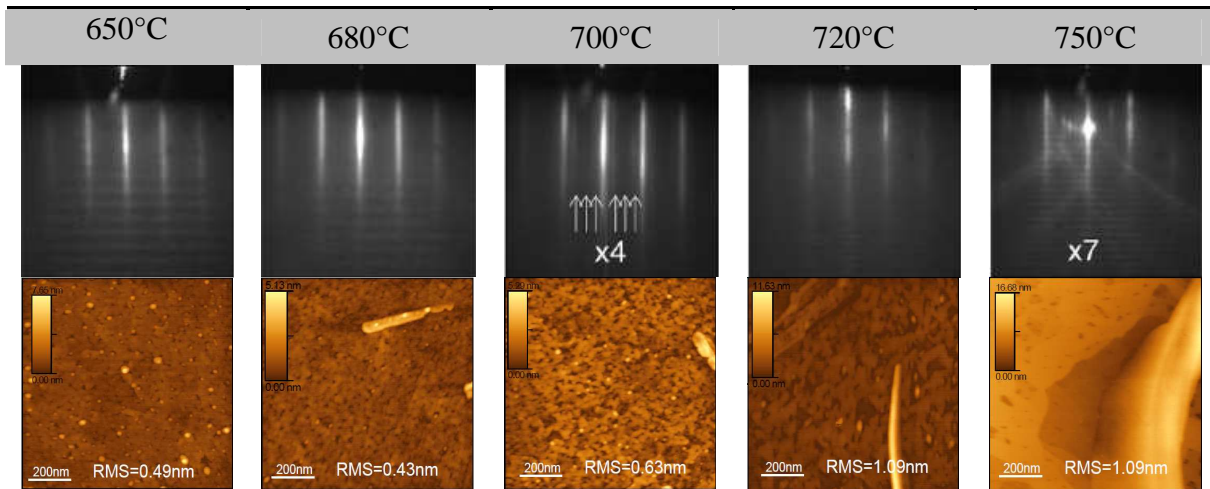

Figure III. 54 RHEED pattern along Si[1-10] azimuth and AFM images of Gd₂O₃ films gorwn on Si (111) at respectively 650°C, 680°C, 700°C, 720°C and 750°C.

III.5.3) Influence of oxygen partial pressure (Thesis of C. Merckling)

A crucial parameter to succeed in high quality growth without any interface layer formation is the oxygen partial pressure. A high enough oxygen chemical potential is needed to avoid the silicidation of the Si surface, which will lead to a Volmer–Weber growth of Gd_2O_3 because of its wetting behavior on Si surface[88]. Figure III. 55 shows the RHEED patterns (along Si[1-10] and Si[-211] respectively) of the Gd_2O_3 film grown at 700°C without the introduction of oxygen (~5×10⁻¹⁰Torr), in which the spotty feature reveals clearly the three-dimensional growth mode. The AFM image shows a higher RMS with respect to the sample grown within O_2 ambient indicating higher surface roughness. On the other hand, too high oxygen pressure, particularly at the initial stage, might oxidize the Si surface leading to a formation of interfacial SiO_x phase.
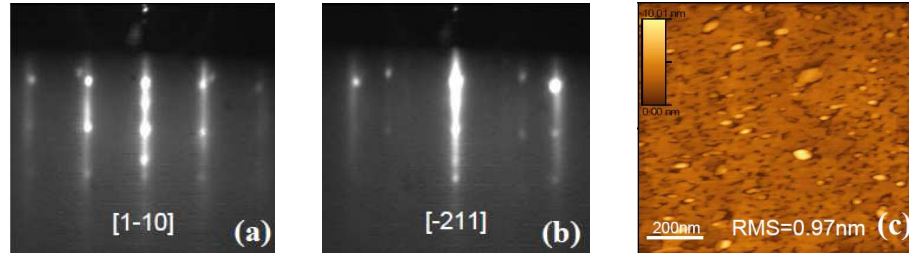
Figure III. 55 RHEED patterns of the Gd₂O₃ film grown in UHV along (a)[1-10] azimuth and (b)[-211] azimuth; And 1μm×1μm AFM image with RMS of 0.97nm.

Figure III. 56 (a), (b) and (c) show the TEM cross-sectional images of $Gd_2O_3/Si(111)$ grown at 700°C with different oxygen partial pressures. It is apparent that the silicide (Gd_xSi_y) inclusions can be observed along the interface for the Gd_2O_3/Si sample (a) grown in UHV. Oppositely, the introduction of too high oxygen partial pressure at the very beginning of the growth (b) leads to a silicate ($Gd_xSi_yO_z$) interfacial layer. With our meticulate oxygen control including first 2ML film grown in UHV and subsequently under $PO_2=1\times10^{-6}$Torr, the interface (c) is found to be abrupt at atomic scale. The epitaxial relationship between Gd_2O_3 and Si (111): $[-110]Gd_2O_3(111)//[1-10]Si(111)$, with one Gd_2O_3 unit cell on two Si unit cells, as shown in Figure III.56 (d). The oxide layer is rotated by 180°C around the [111] axis with respect to the underlying silicon substrate.
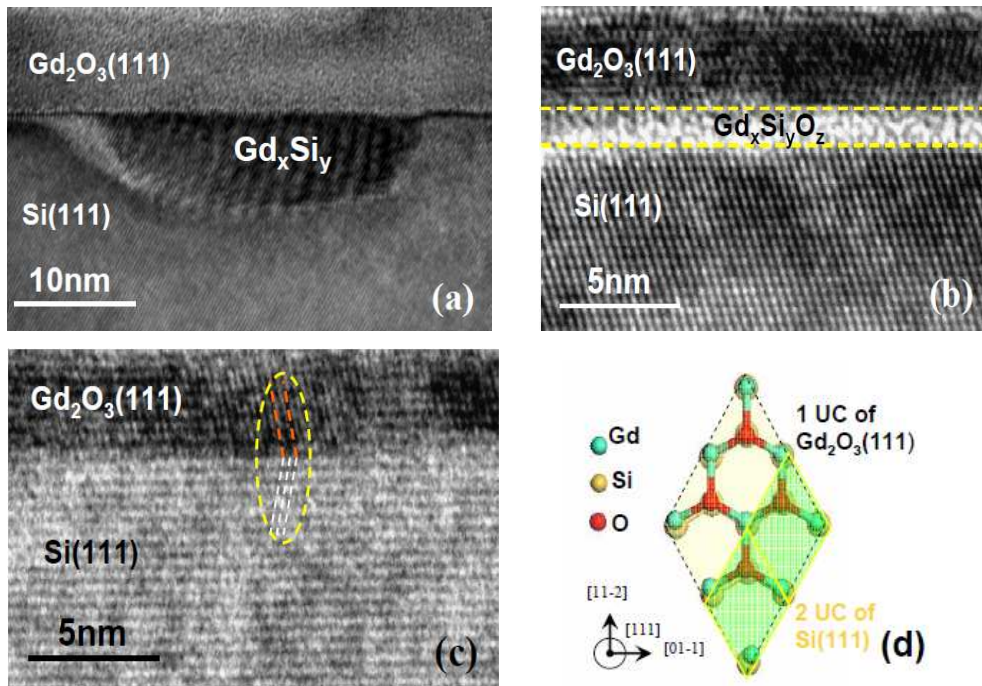

Figure III. 56 HRTEM cross-sectional images of Gd₂O₃/Si(111) samples grown under (a) UHV; (b)P_{O2}=1×10^{-6}Torr and (c)UHV for first 2ML and then P_{O2}=1×10^{-6}Torr. (d) illustration of epitaxial relationship between Gd₂O₃ and underlying Si (111).

According to the analysis above, we can therefore obtain the epitaxy window of Gd_2O_3 on the silicon substrate. The PO_2-Temperature diagram can be illustrated in Figure III.57.
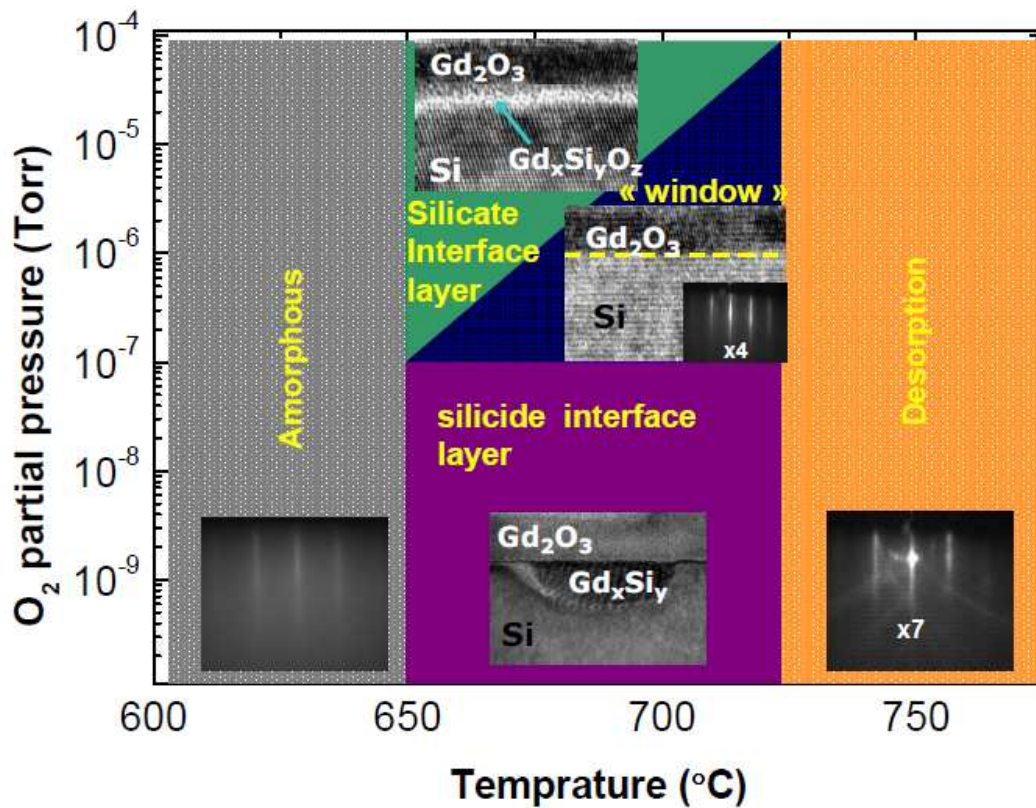

Figure III. 57 P_{O2}-T diagram of Gd_2O_3/Si(111) system

III.5.4) Evaluation of structural quality by XRD

The structural quality of the Gd_2O_3/Si(111) samples was investigated by high-resolution X-ray diffraction. Figure III. 58 shows a 2θ-ω scan around the Si (111) Bragg reflection as well as the fitting data of a 6.7nm-thick Gd_2O_3/Si (111) sample grown at 700°C. The intense and sharp peak observed at 2θ=28.44° corresponds to the Si 111 substrate reflection. According to the fitting curve, the Gd_2O_3 222 peak is located at 2θ=28.87° with a Full Width at Half Maximum (FWHM, Δ(2θ)) ~1.2°. Pendellösung fringes appear at both shoulders of the Gd_2O_3 peak, indicating a high uniformity, flatness and crystal quality of the Gd_2O_3 film. The out-of-plane lattice parameter of this 6.7nm-thick Gd_2O_3 can be extracted from 2θ=28.87°:10.704Å, indicating that Gd_2O_3 is under tensile strain (pseudomorphic growth on Si).
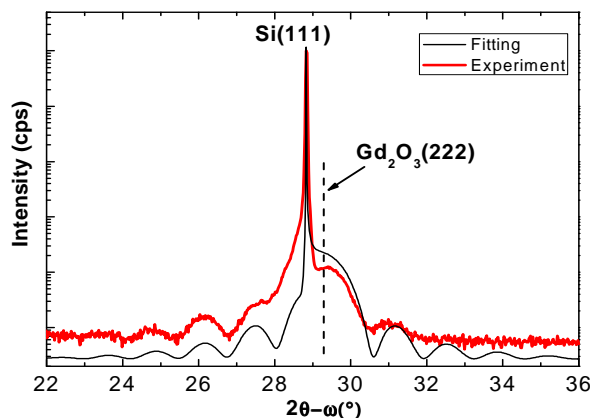
Figure III. 58 X-ray 2θ-ω scan and the fitting data around the Si (111) reflection of a 6.7nm-thick Gd₂O₃ layer grown on Si (111).

III.5.5) Conclusion

In summary, we identified the optimal growth condition of Gd_2O_3 growth on Si (111) substrate and the Gd_2O_3 epitaxial film present high crystalline quality as well as an abrupt interface with respect to silicon. The relationship between Gd_2O_3 and Si is defined as [-110] Gd_2O_3 (111)//[1-10]Si(111), with one Gd_2O_3 unit cell on two Si unit cells. The growth remains pseudomorphic for a 6.7nm-thick layer.

III. 6) Reference

[1] T. Sakamoto, T. Takahashi, E. Suzuki, A. Shoji, H. Kawanami, Y. Komiya and Y. Tarui, Surf. Sci. **86**, 102 (1979)

[2] T. Takahagi, I. Nagai, A. Ishitani, H. Kuroda and Y. Nagasawa, J. Appl. Phys. 64, 3516 (1988)

[3] F. Liu, M. Hohage, M.G. Lagally, Encyclopedia of Applied Physics, Wiley-VCH Verlag GmbH, London, p.321 (1999)

[4] G. H. Lu, M. Huang, M. Cuma and F. Liu, "*Relative stability of Si surfaces: A first-principles study*",Surf. Sci. **588**, 61 (2005)

[5] R. M. Tromp, R. J. Hamers, J. E. Demuth, "Si(001) Dimer Structure Observed with Scanning Tunneling Microscopy", Phys. Rev. Lett. **55**, 1303 (1985)

[6] R. J. Hamers, R.M. Tromp, J. E. Demuth, "Scanning tunneling microscopy of Si(001)", Phys. Rev. B **34**, 5343 (1986)

[7] http://www.rhk-tech.com/results/Low-Temperature-STM-image-of-Si%28100%29.php

[8] T. Takahagi, I. Nagai, A. Ishitani, H. Kuroda and Y. Nagasawa, J. Appl. Phys. 64, 3516 (1988)

[9] M. Suemitsu, T. kaneko and Nobuo Miyamoto, "*Low temperature silicon surface cleaning by HF etching/Ultraviolet ozone cleaning method (I)*", J. J. Appl. Phys. **28**, 2421 (1989)

[10] Y. L. Wang, H.-J. Gao, H. M. Guo, H. W. Liu, I. G. Batyrev, W. E. McMahon, and S. B. Zhang, "*Tip size effect on the appearance of a STM image for complex surfaces: Theory versus experiment for Si(111)-(7×7)*", Phys. Rev. B, **70**, 073312 (2004)

[11] Y. Wei, X. Hu, Y. Liang, D. C. Jordan, B. Craigo, R. Droopad, Z. Yu, A. Demkov, J. L. Edwards, Jr., and W. J. Ooms, "*Mechanism of cleaning Si(100) surface using Sr or SrO for the growth of crystalline SrTiO₃ films*", J. Vac. Sci. Technol. B **20**, 1071 (2002)

[12] R. Droopad, Z. Yu, H. Li, Y. Liang, C. Overgaard, A. Demkov, X. Zhang, K. Moore, K. Eisenbeiser, M. Hu, J. Curless, J. Finder, "*Development of integrated heterostructures on silicon by MBE*", J. Crys. Growth **251**, 638 (2003)

[13] X. Zhang, A.A. Demkov, H. Li, X. Hu, Y. Wei, and J. Kulik, Phys. Rev. B **68**, 125323 (2003).

[14] D.G. Schlom, J.H. Haeni, "*A thermodynamic approach to selecting alternative gate dielectrics*", MRS Bulletin **27**, **3**, 198 (2002)

[15] P. A. Fleury, J. F. Scott and J. M. Worlock, "*Soft phonon modes and the 110K phase transition in SrTiO₃*", Phys. Rev. Lett., **21**, 16 (1968)

[16] M. E. Lines and A. M. Glass, "*Principles and applications of ferroelectrics and related materials*", edited by O. U. Press (1977)

[17] A. A. Demkov, "*Investigating alternative gate dielectrics: A theoretical approach*", Phys. Stat. Sol. B **226**, No.1, 57 (2001)

[18] K. Johnston, M. R. Castell, A. T. Paxton and M. W. Finnis, "*SrTiO₃ (001) (2×1) reconstructions: First-principles calculation of surface energy and atomic structure compared with scanning tunneling microscopy images*", Phys. Rev. B **70**, 085415-1 (2004)

[19] M. Kawasaki, K. Takahashi, T. Maeda, R. Tsuchiya, M. Shinohara, O. Ishiyama, T. Yonezawa, M. Yoshimoto and H. Koinuma, "*Atomic control of SrTiO₃ crystal surface*", Science **266**, 1540 (1994)

[20] T. Ohnishi, K. Shibuya, M. Lippmaa, D. Kobayashi, H. Kumigashira, M. Oshima and H. Koinuma, "*Preparation of thermally stable TiO₂ terminated STO (100) substrate surfaces*", Appl. Phys. Lett. **85**, 272 (2004).

[21] T. Nishimura, A. Ikeda, H. Namba, T. Morishita and Y. Kido, "*Structure change of TiO₂-terminated SrTiO₃ (001) surfaces by annealing in O₂ atmosphere and UHV*", Surf. Sci. **421**, 273 (1999).

[22] M. Yoshimoto, H. Ohkubo, N. Kanda and H. Koinuma, "*Two-dimensional epitaxial growth of SrTiO₃ films on carbon-free clean surface of Nb-doped SrTiO₃ substrate by Laser Molecular Beam Epitaxy*", Jpn. J. Appl. Phys. **31**, 3664 (1992)

[23] J. Fompeyrine, R. Berger, H. P. Lang, J. Perret, E. Mächler, Ch. Gerber, and J.-P. Locquet, "*Local determination of the stacking sequence of layered materials*", Appl. Phys. Lett. **72**, 1699 (1998)

[24] J. E. T. Andersen and P. J. Møller, "*Impurity‐induced 900°C (2×2) surface reconstruction of SrTiO₃(100)*", Appl. Phys. Lett. **56**, 1847 (1990).

[25] T. Matsumoto, H. Tanaka, T. Kawai, and S. Kawai, "*STM-imaging of a SrTiO₃(100) surface with atomic-scale resolution*",Surf. Sci. **278**, L153 (1992).

[26] M. Naito and H. Sato, "*Reflection high-energy electron diffraction study on the SrTiO₃ surface structure*", Physica C **229**, 1 (1994).

[27] Q. D. Jiang and J. Zegenhagen, "*SrTiO₃(001) surfaces and growth of ultra-thin GdBa₂Cu₃O₇₋ₓ films studied by LEED/AES and UHV-STM*", Surf. Sci. **338**, L882 (1995).

[28] Q. D. Jiang and J. Zegenhagen, "*c(6×2) and c(4×2) reconstruction of SrTiO₃(001)*", Surf. Sci. **425**, 343 (1999)

[29] G. Charlton, S. Brennan, C. A. Muryn, R. McGrath, D. Norman, T. S. Turner, and G. Thornton, "*Surface relaxation of SrTiO₃(001)*", Surf. Sci. **457**, L376 (2000)

[30] T. Kubo and H. Nozoye, "*Surface Structure of SrTiO₃(100)- (√5×√5)-R26.6°*", Phys. Rev. Lett. **86**, 1801 (2001)

[31] A. Kazimirov, D. M. Goodner, M. J. Bedzyk, J. Bai, and C. R. Hubbard, "*X-ray surface diffraction analysis of structural transformations on the (001) surface of oxidized SrTiO₃*", Surf. Sci. **492**, L711 (2001)

[32] M. R. Castell, "*Scanning tunneling microscopy of reconstructions on the SrTiO₃ (001) surface*", Surf. Sci. **505**, 1 (2002)

[33] K. Johnston, M. R. Castell, A. T. Paxton, and M. W. Finnis, "*SrTiO₃(001) 2×1 reconstructions: First-principles calculations of surface energy and atomic structure compared with scanning tunneling microscopy images*", Phys. Rev. B **70**, 085415 (2004)

[34] V. Vonk, S. Konings, G. J. van Hummel, S. Harkema, and H. Graafsma, "*The atomic*

surface structure of SrTiO₃(001) in air studied with synchrotron X-rays", Surf. Sci. **595**, 183 (2005)

[35] F. Silly, D. T. Newell, and M. R. Castell, "*SrTiO₃ (001) reconstructions: the (2×2) to c(4×4) transition*", Surf. Sci. **600**, 219 (2006)

[36] R. Herger, P. R. Willmott, O. Bunk, C. M. Schlepütz, B. D. Patterson, B. Delley, V. L. Shneerson, P. F. Lyman, and D. K. Saldin, "*Surface structure of SrTiO₃ (001)*", Phys. Rev. B **76**, 195435 (2007)

[37] N. Erdman and L.D. Marks, "*SrTiO₃ (001) surface structures under oxidizing conditions*" Surf.Sci. **526**, 107 (2003)

[38] Thesis of G. Delhaye, "*Oxydes crystallins à haute permittivité diélectrique épitaxiés sur silicium: SrO et SrTiO₃*", France, (2006)

[39] E. G. Keim, L. Wolterbeek, and A. van Silfhout, "*Adsorption of atomic oxygen (N₂O) on a clean Si (100) surface and its influence on the surface state density: A comparison with O₂*", Surf. Sci. **180**, 565 (1987)

[40] G. J. Norga, C. Marchiori, C. Rossel, A. Guiller, J. P. Locquet, H. Siegwart, D. Caimi, and J. Fompeyrine, J. W. Seo and Ch. Dieker, "*Solid phase epitaxy of SrTiO₃ on (Ba,Sr)O/Si(100): The relationship between oxygen stoichiometry and interface stability*", J. Appl. Phys. **99**, 084102 (2006)

[41] Xiaoming Hu, H. Li, Y. Liang, Y. Wei, Z. Yu, D. Marshall, J. Edwards, Jr., R. Droopad, X. Zhang, A. A. Demkov, K. Moore and J. Kulik, "*The interface of epitaxial SrTiO₃ on silicon: in situ and ex situ studies*", Appl. Phys. Lett. **82**, 203 (2003)

[42] G. Delhaye, C. Merckling, M. El-Kazzi, G. Saint-Girons, M. Gendry, Y. Robach, and G. Hollinger, L. Largeau and G. Patriarche, "*Structural properties of epitaxial SrTiO₃ thin films grown by molecular beam epitaxy on Si(001)*", J. Appl. Phys. **100**, 124109 (2006)

[43] R. O. Bell and G. Rupprecht, "*Elastic Constants of Strontium Titanate*", Phys. Rev. **129**, 90 (1963)

[44] E. J. Tarsa, E. A. Hachfeld, F. T. Quinlan, J. S. Specka, and M. Eddy, "*Growth-related stress and surface morphology in homoepitaxial SrTiO₃ films*", Appl. Phys. Lett. **68**, 490 (1996)

[45] L. S. –J. Peng, X. X. Xi, B. H. Moeckly and S. P. Alpay, "*Strain relaxation during in situ growth of SrTiO₃ thin films*", Appl. Phys. Lett. **83,** 4592 (2003)

[46] M. Hiratani, K. Imagawa and K. Takagi, "*Insufficient oxidation in pulsed laser deposition*",

J. Appl. Phys. **78**, 4258 (1995)

[47] M J. Gillan and A. B. Lidiard, in Computer Simulation of Solids, edited by C. R. A. Catlow and W. C. Mackrodt p.32 (Springer, New York 1982)

[48] J. Petzelt, T. Ostapchuk, I. Gregora, I. Rychetsky, S. Hoffmann-Eifert, A. V. Pronin, Y. Yuzyuk, B. P. Gorshunov, S. Kamba, V. Bovtun, J. Pokorny, M. Savinov, V. Porokhonskyy, D. Rafaja, P. Vanek, A. Almeida, M. R. Chaves, A. A. Volkov, M. Dressel, and R. Waser, "*Dielectric, infrared, and Raman response of undoped SrTiO₃ ceramics: Evidence of polar grain boundaries*", Phys. Rev. B **64**, 184111 (2001)

[49] E. Knittle, Q. Williams, American Mineralogist. "*High-pressure Raman spectroscopy of ZrSiO₄: Observation of the zircon to scheelite transition at 300 K*", **78,** 245 (1993).

[50] B. Manoun, R. T. Downs and S. K. Saxena, American Mineralogist. "*A high-pressure Raman spectroscopic study of hafnon, HfSiO₄*", **91,** 1888 (2006).

[51] D. A. Tenne, I. E. Gonenli, A. Soukiassian, D. G. Schlom, S. M. Nakhmanson, K. M. Rabe and X. X. Xi, "*Raman study of oxygen reduced and re-oxidized strontium titanate*", Phys. Rev. B **76**, 024303 (2007)

[52] P. A. Fleury, J. F. Scott and J. M. Worlock, "*Soft Phonon Modes and the 110°K Phase Transition in SrTiO₃*", Phys. Rev. Lett. **21**, 16 (1968)

[53] K. A. Müller, W. Berlinger and F. Waldner, "*Characteristic Structural Phase Transition in Perovskite-Type Compounds*", Phys. Rev. Lett. **21**, 814 (1968)

[54] A. Antons, J. B. Neaton, K. M. Rabe and D. Vanderbilt, "*Tunability of the dielectric response of epitaxially strained SrTiO3 from first principles*", Phys. Rev. B **71**, 024102 (2005)

[55] F. He, B. O. Wells and S.M. Shapiro, "*Strain Phase Diagram and Domain Orientation in SrTiO₃ Thin Films*", Phys. Rev. Lett. **94**, 176101 (2005)

[56] B. V. Crist, *The elements and native oxides*, Handbook of Monochromatic XPS spectra Vol. **1**. (XPS International, 1999).

[57] G. J. Norga, C. Marchiori, C. Rossel, A. Guiller, J. P. Locquet, H. Siegwart, D. Caimi, and J. Fompeyrine, J. W. Seo and Ch. Dieker, "*Solid phase epitaxy of SrTiO3 on (Ba,Sr)O/Si(100): The relationship between oxygen stoichiometry and interface stability*", J. Appl. Phys. **99**, 084102 (2006)

[58] N. Lucas, H. Zabel, H. Morkoç and H. Unlu, Appl. Phys. Lett. **52**, 2117, (1988)

[59] P. M. Warusawithana, C. Cen, C. R. Sleasman, C. J. Woicik, Y. Li, L. F. Kourkoutis, J. A.

Klug, H. Li, P. Ryan, L. P. Wang, M. Bedzyk, D. A. Muller, L. Q. Chen, J. Levy and D. G. Schlom, "*A ferroelectric oxide made directly on silicon*", Science, **324**, 367 (2009)

[60] G. Niu, G. Saint-Girons, B. Vilquin, G. Delhaye, J.-L. Maurice, C. Botella, Y. Robach, and G. Hollinger, "*MBE of SrTiO₃ on Si(001): early stages of the growth and strain relaxation*", Appl. Phys. Lett., 95, 062902 (2009)

[61] J. Massies and N. Grandjean, "*Oscillation of the lattice relaxation in layer-by-layer epitaxial growth of highly strained materials*", Phys. Rev. Lett. **71**, 1411, (1993).

[62] H. Li, X. Hu, Y. Wei, Z. Yu, X. Zhang, R. Droopad, A. A. Demkov, J. Edwards, Jr., K. Moore, W. Ooms, J. Kulik and P. Fejes, "*Two-dimensional growth of high-quality strontium titanate thin films on Si*", J. Appl. Phys. **93**, 4521 (2003)

[63] R.A. McKee, F.J. Walker and M.F. Chisholm, "*Physical Structure and Inversion Charge at a Semiconductor Interface with a Crystalline Oxide*", Science **293**, 468, (2001).

[64] K. A. Müller, W. Berlinger and F. Waldner, "*Characteristic Structural Phase Transition in Perovskite-Type Compounds*", Phys. Rev. Lett. **21**, 814 (1968)

[65] R. Loetzsch, A. Lübke, I. Uschmann, E. Förster, V. Grosse, M. Thuerk, T. Koettig, F. Schmidl and P. Seidel, "*The cubic to tetragonal phase transition in SrTiO₃ single crystals near its surface under internal and external strains*", Appl. Phys. Lett. **96**, 071901, (2010)

[66] L. Cao, E. Sozontov and J. Zegehagen, " *Cubic to Tetragonal Phase Transition of SrTiO₃ under Epitaxial Stress: An X-Ray Backscattering*", Phys. Stat. Sol. (a) **181**, 387, (2000)

[67] M. Guennou, P. Bouvier, J. Kreisel and D. Machon, "*Pressure-temperature phase diagram of SrTiO₃ up to 53 GPa Study*", Phys. Rev. B **81**, 054115 (2010)

[68] A. Antons, J.B. Neaton, K.M. Rabe and D. Vanderbilt, " *Tunability of the dielectric response of epitaxially strained SrTiO₃ from first principles*", Phys. Rev. B **71**, 024102, (2005)

[69] F. He, B.O. Wells and S.M. Shapiro, "*Strain Phase Diagram and Domain Orientation in SrTiO₃ Thin Films*", Phys. Rev. Lett. **94**, 176101, (2005)

[70] N.A. Pertsev, A.K. Tagantsev and N. Setter, "*Phase transitions and strain-induced ferroelectricity in SrTiO₃ epitaxial thin films*", Phys. Rev. B **61**, R825, (2000)

[71] J.H. Haeni, P. Irvin, W. Chang, R. Uecker, P. Reiche, Y.L. Li, S. Choudury, W. Tian, M.E. Hawley, B. Craigo, A.K. Tagantsev, X.Q. Pan, S.K. Streiffer, L.Q. Chen, S.W. Kirschoefer, J. Levy and D.G. Schlom, "*Room-temperature ferroelectricity in strained SrTiO₃*", Nature **430**, 758 (2004).

[72] F.S. Aguirre-Tostado, A. Herrera-Gomez, J.C. Woicik, R. Droopad, Z. Yu, D.G. Schlom, P.

Zschack, E. Karapetrova, P. Pianetta and C.S. Hellberg, "*Elastic anomaly for SrTiO₃ thin films grown on Si(001)*", Phys. Rev. B **70**, 201403(R), (2004).

[73] J. C. Woicik, H. Li, P. Zschack, E. Karapetrova, P. Ryan, C. R. Ashman and C. S. Hellberg, "*Anomalous lattice expansion of coherently strained SrTiO₃ thin films grown on Si(001) by kinetically controlled sequential deposition*", Phys. Rev. B, **73**, 024112 (2006)

[74] R. A. McKee, F. J. Walker, and M. F. Chisholm, "*Crystalline Oxides on Silicon: The First Five Monolayers*", Phys. Rev. Lett. **81**, 3014 (1998).

[75] R. A. McKee, F. J. Walker, M. Buongiorno Nardelli, W. A. Shelton, and G. M. Stocks, "*The Interface Phase and the Schottky Barrier for a Crystalline Dielectric on Silicon*", Science **300**, 1726 (2003)

[76] R. A. McKee, F. J. Walker, J. R. Conner, and R. Raj, "*BaSi₂ and thin film alkaline earth silicides on silicon*", Appl. Phys. Lett. 63, 2818 (1993).

[77] Y. Liang, S. Gan, and M. Engelhard, "*First step towards the growth of single-crystal oxides on Si: Formation of a two-dimensional crystalline silicate on Si(001)*", Appl. Phys. Lett., **79**, 3591 (2001)

[78] M. El Kazzi, G. Delhaye, C. Merckling, E. Bergignat, Y. Robach, G. Grenet, and G. Hollinger, "*Epitaxial growth of SrO on Si (001): Chemical and thermal stability*", J. Vac. Sci. Technol. A **25**(6), 1505 (2007)

[79] J.-P. Doumerc, "*Oxydes à forte permittivité diélectrique pour la réalisation de diélectrique de grille dans les MOSFET*", internal report, Project Nano 2008, Institut de Chimie de la Matiere Condensee de Bordeaux (2005)

[80] Catti, M., Gazzoni, G., Ivaldi, "*Structures of twinned β-Sr₂SiO₄ and of α'-Sr₁.₉Ba₀.₁SiO₄*", Acta Cryst. **C 39**, 29-34(1983)

[81] R. A. McKee, F. J. Walker, J. R. Conner, e. D. Specht and D. E. Zelmon, "*Molecular beam epitaxy growth of epitaxial barium silicide, barium oxide, and barium titanate on silicon*", Appl. Phys. Lett. **59**, 782 (1991)

[82] F. Amy, A. Wan, A. Kahn, F. J. Walker and R. A. McKee, "*Surface and interface chemical composition of thin epitaxial SrTiO₃ and BaTiO₃ films: Photoemission investigation*", J. Appl. Phys. 96, 1601 (2004)

[83] J. Lettieri, J. H. Haeni, D. G. Schlom, "*Critical issues in the heteroepitaxial growth of alkaline-earth oxides on silicon*", J. Vac. Sci. Tech. A, 20, 1332 (2002)

[84] G. J. Norga, A. Guiller, C. Marchiori, J. P. Locquet, H. Siegwart, D. Halley, C. Rossel, D.

Caimi, J. W. Seo, and J. Fompeyrine, "*Growth of perovskites with crystalline interfaces on Si(100)*", Mat. Res. Soc. Symp. Proc. **786**, E 7.3.1(2004)

[85] J. Zachariae and H. Pfnür, "*Growth conditions, stoichiometry, and electronic structure of lattice-matched SrO/BaO mixtures on Si (100)*", Phys. Rev. B **72**, 075410-1 (2005)

[86] L.Z. Vegard, "*Gitterkonstanten von Mischkristallen*", Z. Phys. **5**,17 (1921)

[87] Thesis of M. El. Kazzi, "*Etude par photoémission (XPS et XPD) d'hétérostructures d'oxydes fonctionnels épitaxiés sur silicium*", France, (2007)

[88] A. Fissel, D. Kühne, E. Bugiel, H.J. Osten, " *Cooperative solid-vapor-phase epitaxy: An approach for fabrication of single-crystalline insulator/Si/insulator nanostructures*", Appl. Phys. Lett. **88**, 153105 (2006)

Chapter IV: Integration of versatile functionalities on Si based on oxide/Si system

IV.1) Introduction

The integration of epitaxial functional oxides and semiconductors on silicon opens the opportunities for the integration of novel memory, sensing, electric, optical signal processing and photonic elements on microelectronic platforms.

Firstly, the high-κ oxides themselves could serve as the gate dielectric of the future 22nm and sub-22nm CMOS nodes by replacing traditional SiO_2 gate dielectrics.

Secondly, Field-Effect Transistor (FET) devices with increased speed and functionality (FeFET, spinFET, MottFET) can be realized by replacing conventional SiO_2 gate dielectric with functional oxides. Smart sensors such as highly sensitive bio-chemical sensors can be developed, which based on static strain-free membranes and cantilevers made of high performance piezoelectric oxide films. Other devices such as integrated micro-electromechanical systems (MEMS) and ferroelectric random access memories (FeRAM) can also be envisaged.

Thirdly, the integration of Ge on Si via oxide buffer layers might circumvent the difficulty of direct Epitaxy due to the large lattice mismatch which leads to extended defects in the Ge layer. Thus devices such as modulators, heteroepitaxial injection lasers, photodetectors, waveguide and solar cell based on the good physical properties of Ge (or III-V semiconductors) could be married with the characteristics of the silicon manufacturing processes. Higher mobility tunnel could also be realized for the future CMOS with Ge layer on oxides/Si template.

IV.2) Dielectrics

IV.2.1) A promising candidate: Gd_2O_3

We have discussed in prior chapters the unparalleled properties of crystalline Gd_2O_3 as an alternative gate dielectric for the future CMOS technique. With the purpose of further clarifying the choice of Gd_2O_3 in this work, we compare Gd_2O_3 with other candidates in terms of EOT and leakage current. The direct tunneling current of the MOS structure can be calculated by the following equation[1]:

$$J_g = \frac{q^2}{16\pi^2\hbar\Phi_B}F_{ox}^2\times\exp\left[-\frac{4}{3}\frac{\sqrt{2m_{ox}q}\Phi_B^{3/2}}{\hbar F_{ox}}\left(1-\left(1-\frac{V_{ox}}{\Phi_B}\right)^{3/2}\right)\right] \qquad \text{Equation IV-1}$$

$$J_g = \frac{A}{\Phi_B}F_{ox}^2\times\exp\left[B\left(1-\left(1-\frac{V_{ox}}{\Phi_B}\right)^{3/2}\right)\right]=\frac{1,54\times10^{-6}}{\Phi_B}F_{ox}^2\times\exp\left[-6,83\times10^9\left(1-\left(1-\frac{V_{ox}}{\Phi_B}\right)^{3/2}\right)\right] \qquad \text{Eq. IV-2}$$

where V_{ox} of absolute value and $F_{ox}=\dfrac{V_{ox}}{e_{phys}}=\dfrac{V_{ox}\times\kappa_{SiO_2}}{EOT\times\kappa_{High-\kappa}}$.

The values demonstrated in the following table are then injected in this equation and Figure IV. 1 displays the results obtained with a gate voltage V_{ox} of 1.5V.

	SiO₂	*Al₂O₃*	*LaAlO₃*	*HfO₂*	*Gd₂O₃*
$\Phi_{B\ (/Si)}$ (eV)	3,1	2,8	1,8	1,5	1,8
κ	3,9	10	20	24	20
m^*	0,5	0,35	0,3	0,17	0,29
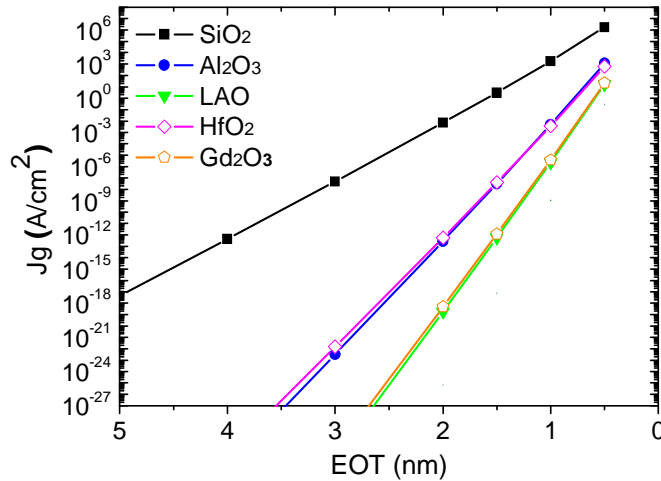
Figure IV. 1 Current densities calculated as a function of equivalent thickness of SiO₂ (gate voltage of 1.5V) for different dielectric candidates (Ref. 2).

We can observe that the curves of LaAlO₃ and Gd₂O₃ are almost superposed and towards to the lowest leakage current. Although all these high-κ oxides possess much lower leakage currents than SiO₂, Gd₂O₃ is the most promising in terms of scaling among the candidates illustrated in Figure IV. 1. Another promising candidate LaAlO₃ (in amorphous phase) has been previously studied at INL. At an EOT value of 1nm, the leakage current of Gd₂O₃ is 6 decade less than HfO₂, which thus attests the choice of Gd₂O₃ as the possible high-κ gate dielectric for sub-22nm nodes.

IV.2.2) Electrical characterization of as-deposited $Gd_2O_3/Si(111)$ samples

In this section, we will focus on the dielectric characterization of the $Gd_2O_3/Si(111)$ samples. The growth parameters and the structural quality of the samples are presented in III.5. In order to evaluate the real potential of the deposition technique, we firstly study the as deposited samples without any PDA process. A MOS structure of $Au/Ni/Gd_2O_3/Si(111)$ was fabricated by lift-off method and a Karl Suss manual probe station equipped with a HP 4284A impedance meter and a HP 4156B pA-meter is used for C-V and I-V measurements, as introduced in detail in the section II.3.2.

IV.2.2.1) Influence of growth temperature

A series of ~3nm $Gd_2O_3/Si(111)$ samples were fabricated at different temperatures in order to investigate the influence of growth temperature to the electrical properties. Figure IV. 2(a) shows the typical experimental C-V curves measured at a frequency of 100 kHz for Gd_2O_3 thin films grown on Si(111) at 650°C, 680°C and 700°C. For the sample grown at 720°C, the leakage current density was too high to measure any C-V characteristics. As discussed in the previous chapter, at 750°C, the temperature is too high for Gd_2O_3 absorption onto Si surface. For the investigated film thickness, quantum mechanical effects are no more negligible. In this case, capacitance equivalent thickness (CET) which can be calculated directly is bigger than EOT. The EOT was therefore extracted by fitting the experimental C-V data with realistic quantum simulations. Figure IV. 2(b) shows a fitting example for the sample grown at 700°C. For the ~3 nm-thick films grown at 650°C, 680°C and 700 °C, the EOT values extracted are respectively equal to 0.90, 1.15 and 0.73 nm. The sample deposited at 700°C turns out to have the best EOT. For the layers grown at 650°C, 680°C and 700°C, their dielectric constants are respectively 13, 11 and 12 which are less than the bulk value 20 but very close to the results obtained for the Gd_2O_3 thin films in the literature[3,4]. For the samples presented in the present work with Au/Ni top electrode, the theoretical flatband voltage V_{FB} is -0.5V. The positive shift of the V_{FB} for all the C-V curves suggests the presence of charge traps in the oxide film and the interface.

Figure IV. 3 shows J-V characteristics of the $Gd_2O_3/Si(111)$ MOS capacitors grown at different temperatures. At $|V_g - V_{FB}| = 1$ V, the leakage current through the sample deposited grown at 700°C is 1.1×10^{-1} A/cm^2, which satisfies the ITRS recommendations for the 32 nm node (J<10^{+2}A/cm^2)[5].
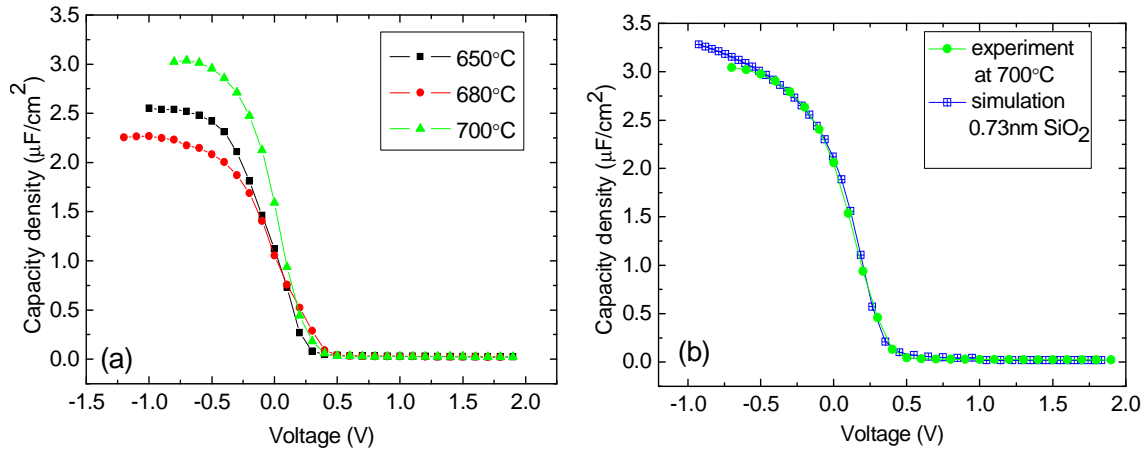
Figure IV. 2 (a) Room temperature C-V curves (f=100kHz) obtained for Gd$_2$O$_3$/Si (111) MOS capacitors grown at different temperatures; (b)TCV fitting of the C-V curve of the sample grown at 700°C. The EOT value extracted is 0.73nm.
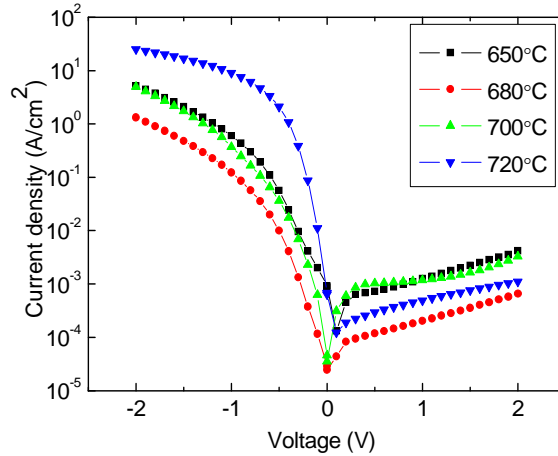
Figure IV. 3 Room temperature J-V curves of Gd$_2$O$_3$/Si (111) MOS capacitors grown at different temperatures.

IV.2.2.2) Influence of deposited film thickness

Au/Ni/Gd$_2$O$_3$/Si (111) MOS structures with different oxides physical thicknesses were characterized and their EOT values as a function of the physical thicknesses are plotted in Figure IV. 4 (a). From the slope of the plot, the dielectric constant of the Gd$_2$O$_3$ films grown on *p*-type Si (111) was κ=12, which is calculated by:

$$EOT = t_{high-\kappa} \frac{\kappa_{SiO_2}}{\kappa_{high-\kappa}} \Rightarrow \kappa_{Gd_2O_3} = t_{Gd_2O_3} \frac{3.9}{EOT} \qquad \text{Equation IV-3}$$

Tunneling AFM (TUNA) is employed to investigate the leakage current in the Gd$_2$O$_3$ dielectric films (performed by Waël Hourani at INL, INSA.). Similar to Conductive AFM

(C-AFM), TUNA is a secondary imaging mode derived from contact AFM, which characterizes ultra-low currents (<1 pA) through the thickness of thin films. The gate voltage is applied on the samples (negative on the substrate and positive on the point) with a ramp of 0~-10V and 0.5V/sec. The current limit is -80pA. The results are shown in Figure IV. 4 (b). We can observe that the threshold voltage to breakdown the insulator layer increases from 5V to 7.6V as the film thickness increases from 2.7nm to 6.2nm. It is reasonable since the EOT of the high-κ oxide layer (thus its capacity) enhances with the increase of the film thickness.
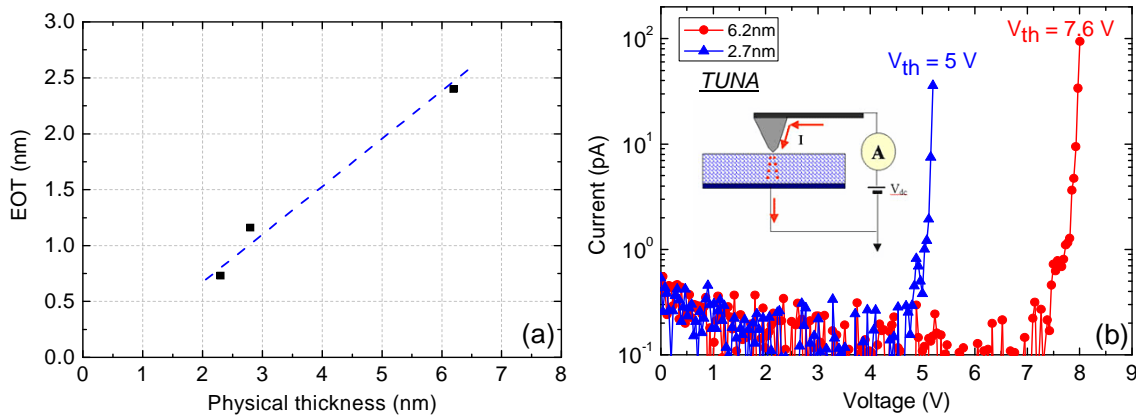

Figure IV. 4 (a) Evolution of the EOTs of the Gd_2O_3 films as a function of the physical thickness; (b) TUNA I-V curves of Gd_2O_3/Si MOS structure with different dielectric film thickness, inset illustrates the principle of TUNA.

IV.2.2.3) Leakage current and frequency measurement

The leakage current through a MOS capacitor can be modeled by a resistance R in parallel with capacity. An ideal insulator owes quite low leakage current thus the R can be regarded as infinite. However, in practice the dielectrics always contain defects leading to the leakage current which affects the C-V characterization of MOS capacitor.

Experimentally, the frequency of the measurement influences the C-V characterization. A too low frequency will inevitably lead to an immediate deterioration of the C-V characterization, as shown in Figure IV. 5. These problems are attributed to the excessive leakage current, as we will discuss in the following.

The MOS capacity can be simply modeled as below:

C_p: Gate dielectric capacity

R_p: dielectric leak resistance

R_s: Series resistance (substrate, contact dots)
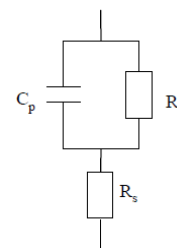
In order to determine these three parameters, it is necessary to establish a relationship between this model and the measured parameters in parallel mode:

We can obtain that

$$R_{mp} = \frac{(1 + R_s G_p)^2 + R_s^2 C_p^2 \omega^2}{G_p(1 + R_s G_p) + R_s C_p^2 \omega^2}$$ Equation IV-4

and $$C_{mp} = \frac{C_p}{(1 + R_s G_p)^2 + R_s^2 C_p^2 \omega^2}$$ Equation IV-5

According to the equations, the C_{mp} and R_{mp} are dependent with the measurement frequency.

When $\omega \to 0 \Rightarrow R_{mp} \to R_s + R_p$ and $C_{mp} \to \left(\frac{R_p}{R_s + R_p}\right)^2 C_p$
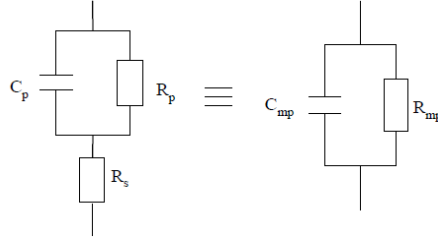
When $\omega \to \infty \Rightarrow R_{mp} \to R_s$ and $C_{mp} \to 0$

Figure IV. 5 shows the C_{mp}-V_g and R_{mp}-V_g curves of different frequencies obtained from a 2.8nm-thick Gd_2O_3/Si(111) sample. The variation of C_{mp} can be clearly observed as a function of the frequency. We can observe platforms in the accumulation regime for all the C_{mp}-V curves. The platform level decreases from 2.12µF/cm^2 to 1.27µF/cm^2 as the frequency increases from 10kHz to 1MHz, indicating a non-negligible series resistance R_s.

The approximation value of R_s can be obtained from the R_{mp}-V_g curves because R_{mp} tends toward to R_s with the high frequency limitation. The saturation at high frequency can be obviously observed in Figure IV. 5 and $R_s \approx 1422\Omega$.

n order to determine R_p, we consider the quasi-static I=f(V_g) measurement performed on the same sample. By applying the Ohm's law to the measurement, we obtain the variation of the total resistance, i.e. R_s+R_p, as a function of the gate voltage. Knowing R_s, the variation of R_p=f(V_g) can then deduced from the variation of R_s+R_p=f(V_g).
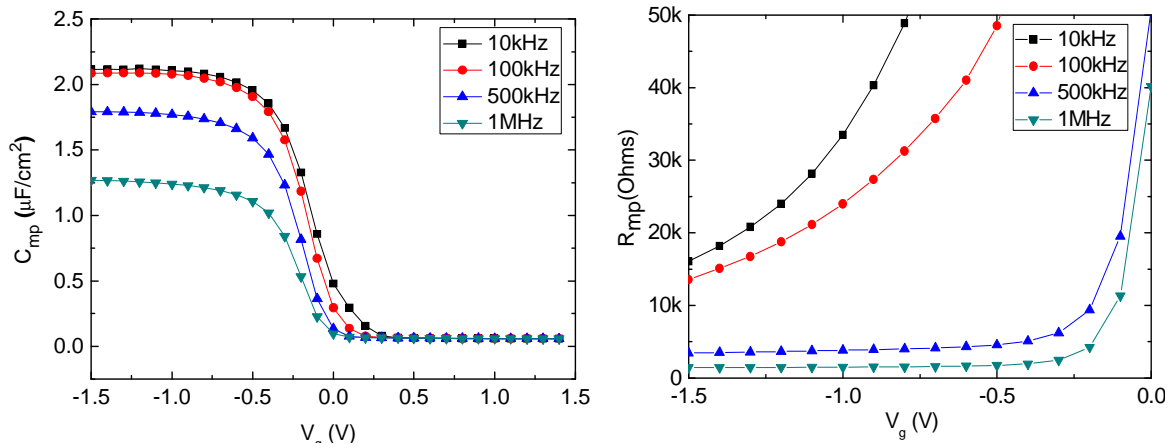
Figure IV. 5 C_{mp}-R_{mp} obtained from the measurement of different frequencies in parallel mode on a Gd$_2$O$_3$/Si(111) sample.

The leakage current measured for V_G-V_{FB}=-1V is used as parameter to compare the Gd$_2$O$_3$/Si samples with silicon oxide having the same EOT. $J_{leakage}$ v.s. EOT is illustrated in Figure IV. 6. Obviously the Gd$_2$O$_3$/Si samples have a leakage current density which is several orders of magnitude smaller than SiO$_2$ at the same EOTs[6].
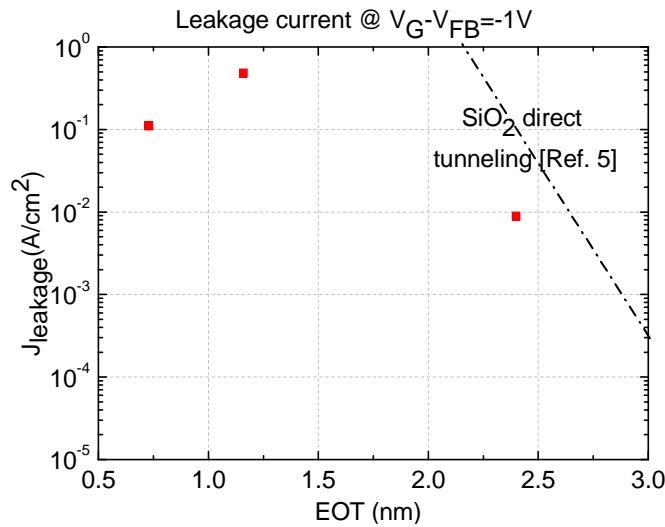
Figure IV. 6 Leakage current density v.s. EOT of Gd$_2$O$_3$ compared with SiO$_2$.

IV.2.2.4) Determination of defects in the films

Although we have obtained good EOT value with low leakage current, the electrical quality of the Gd$_2$O$_3$/Si(111) samples is not perfect, several bulk and interface defects exist: interfaces trapped charges D_{it}, fixed and mobile charges. These defects present themselves by the distortion of the C-V curves including hysteresis and V_{FB} shift, etc. The methods to determine these crucial parameters were introduced in II.3.2.5 and we will analyze the

Gd_2O_3/Si system in detail.

According to Equation 20 (Chapter II), we have:

$$D_{it} = \frac{0.4(G_p / \omega)}{qA}$$ Equation IV-6

Where G_p is the peak conductance in the parallel C-V measurement (f=10kHz) configuration, A is the top electrode area and q is the elementary charge.

Figure IV. 7 illustrates the G-V curves obtained based on the data for f=10kHz represented in Figure IV. 5. Considering the electrode area is 100×100 μm^2, the D_{it} value of the 2.8nm-thick $Gd_2O_3/Si(111)$ sample can be deduced: $2.58 \times 10^{+11}$eV^{-1}·cm^{-2}. And the D_{it} of the sample with EOT=0.73nm is $3.28 \times 10^{+11}$eV^{-1}·cm^{-2}.
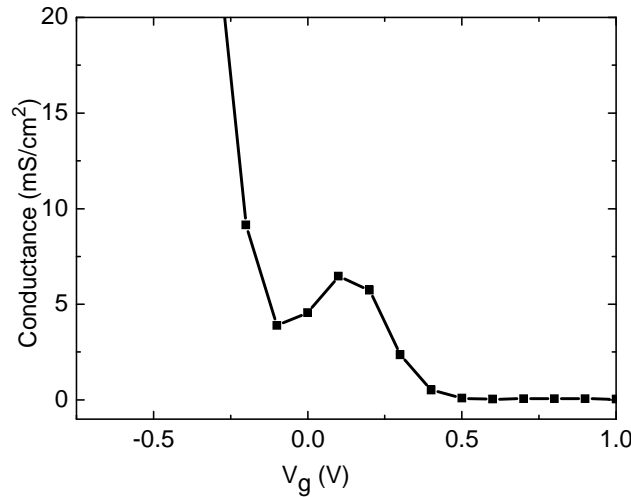
Figure IV. 7 G-V plot of a 2.8nm-thick Gd_2O_3 showing the G_p that is used for D_{it} calculation.

The C-V and I-V sweeps show hysteresis due to the oxide trapped charges Q_{ot} in the Gd_2O_3 film. Figure IV. 8 (a) (b) show the hysteresis feature of the C-V and I-V sweeps respectively for the $Gd_2O_3/Si(111)$ sample with EOT=0.73nm. Figure IV. 8 (c) shows the V_{FB} shift (due to fixed oxide charges) of the same sample with the reference of simulation data.
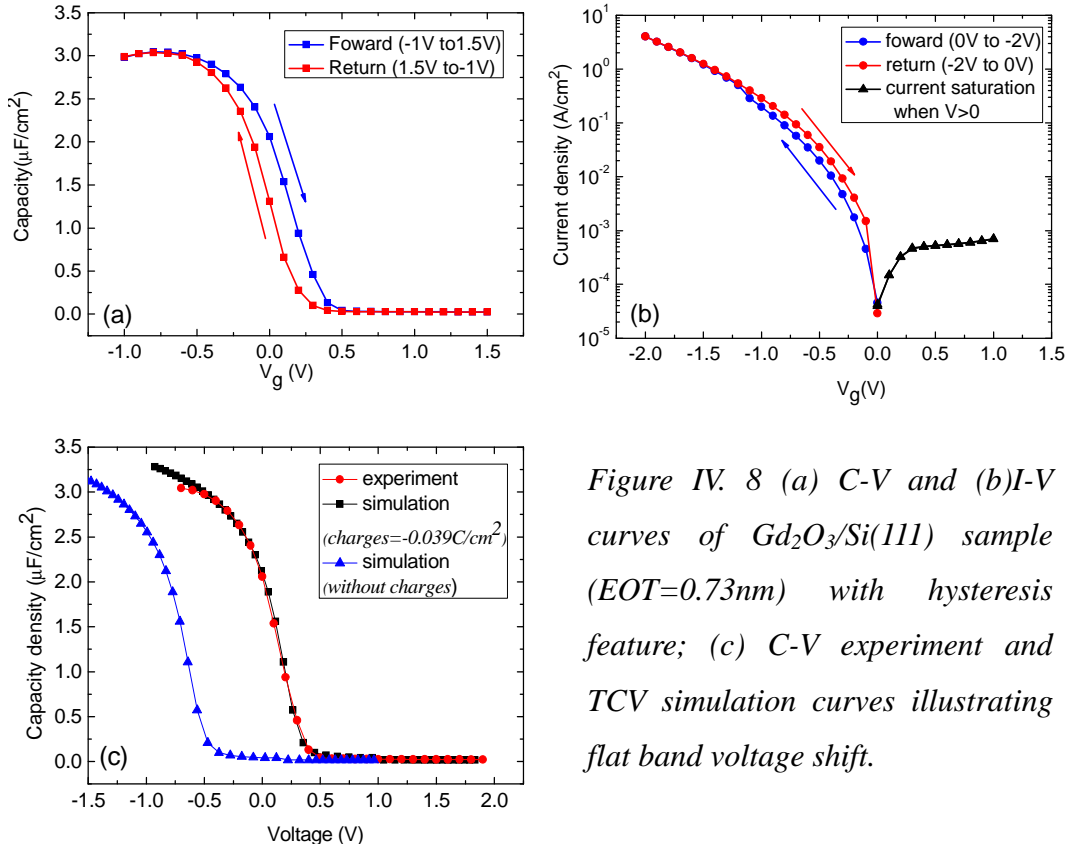
Figure IV. 8 (a) C-V and (b)I-V curves of Gd_2O_3/Si(111) sample (EOT=0.73nm) with hysteresis feature; (c) C-V experiment and TCV simulation curves illustrating flat band voltage shift.

Therefore different optimizing methods were carried out in order to decrease the defect density in the oxides films thus develop their electrical performances. We will focus on the impacts of these strategies on the Gd_2O_3/Si samples.

IV.2.3) Influence of the oxidant type

The majority defects in the oxide films fabricated by MBE are oxygen vacancies thereby atomic oxygen with higher oxidizing potential is used during the film growth in order to improve the stoechiometry. The influence of the oxygen types on the electrical properties of the samples was explored by TUNA measurements (performed by Waël Hourani, INL-INSA). Figure IV. 9 (a) shows the I-V measurements in range of 0~-10V(0.5V/sec) for the Gd_2O_3/Si(111) samples grown in molecular and atomic oxygen ambiences respectively. For the films grown under O_2 and atomic oxygen with the same physical film thickness 2.7nm, the threshold voltage of the latter (6V) is higher than the former (5V), indicating the sample grown under atomic oxygen possesses better dielectric quality. As the sample thickness decreases to 1.1nm (atomic oxygen ambience), the V_{th} also decreases to 5.1V. The impact of atomic oxygen can be presented more directly by TUNA current maps. Figure IV. 9 (b) and (c) shows the 1μm×1μm TUNA current maps of a 6.2nm-thick sample grown under O_2 ambience

and a 2.7nm-thick sample grown under atomic oxygen ambience respectively. For the sample grown under O_2 with an applied voltage of -7.2V and a current scale of 5.0pA (bright)~-20pA(dark), intense leakage current spots can be observed in the map. However, for the sample grown under atomic oxygen with an applied voltage of -6.4V and a current scale of 5.0pA (bright)~-10pA(dark), only randomly distributed leakage current spots are visible demonstrating better dielectric property. In addition, it has to be noted that the Gd_2O_3 layer grown under atomic oxygen is much thinner than that grown under O_2 (2.7nm v.s. 6.2nm), which further suggests the positive impact of atomic oxygen growth ambience on the dielectric property of the Gd_2O_3 layer.
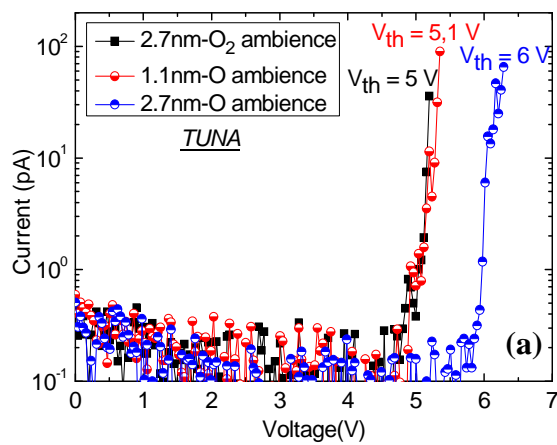
Figure IV. 9 (a) TUNA I-V curves of $Gd_2O_3/Si(111)$ samples grown under molecular and atomic oxygen ambience; 1μm×1μm TUNA current maps of $Gd_2O_3/Si(111)$ samples grown under (b) O_2 and (c) atomic oxygen ambience.
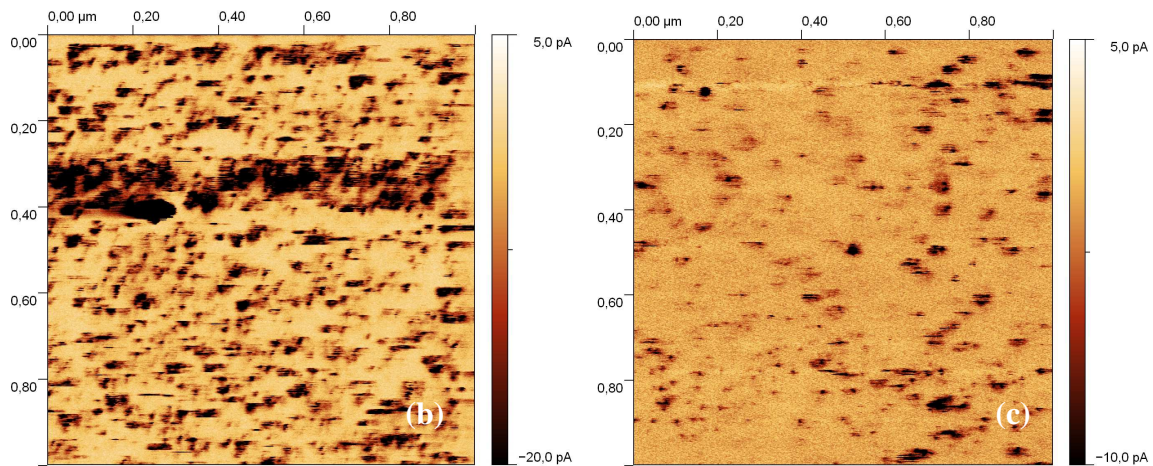
IV.2.4) Influence of post deposition annealing

Post Deposition Annealing (PDA) in different conditions, including a PDA in a tubular furnace and a Rapid Thermal Annealing (RTA) under different gas atmosphere were performed for the samples grown at 700°C to improve their electrical quality and investigate their structural stability.

IV.2.4.1) Annealing in a tubular furnace

Figure IV. 10 (a) shows the forward and reverse bias sweeps (at 100 kHz) for a 2.3nm-thick Gd_2O_3 film, both as-deposited sample and that annealed at 200°C under O_2 atmosphere for 30 minutes in a tubular furnace. A clockwise loop ($\Delta V=0.1V$) can be observed for the measurement of as-deposited sample, indicating electrical charge phenomenon depending on the applied voltage[7] which is probably caused by oxygen vacancies. The flat band voltage (V_{FB}) extracted from the C-V curve of as-deposited sample is -0.3V, which is much larger than the theoretical V_{FB} (-0.5V) of the Ni gate MOS capacitors without any oxide charge. The positive shift ($\Delta V_{FB}=0.2V$) between the theoretical and experimental V_{FB} values reveals a large amount of negative charges in the dielectric films and at the interface. The measurement of the annealed sample displays a significant decrease of the hysteresis ($\Delta V=0V$) and the ΔV_{FB} (0V), indicating that this PDA method under O_2 atmosphere effectively decreased the charge density of the as-deposited layer and developed the interface states at the Gd_2O_3/Si interface. It is very likely that the oxygen vacancies are refilled during the annealing process. At the same time, the EOT is only slightly disturbed, given that the EOT of the PDA sample is 0.9nm which is a little larger than that of as-deposited one (0.73nm). Figure 5 (b) shows the J-V measurements. At $|V_g-V_{FB}|=1V$, the leakage current density of as-deposited and PDA samples are $1.02\times10^{-1}A/cm^2$ and $4.04\times10^0A/cm^2$ respectively, both of which are consistent with the recommendation of ITRS for 32nm node.

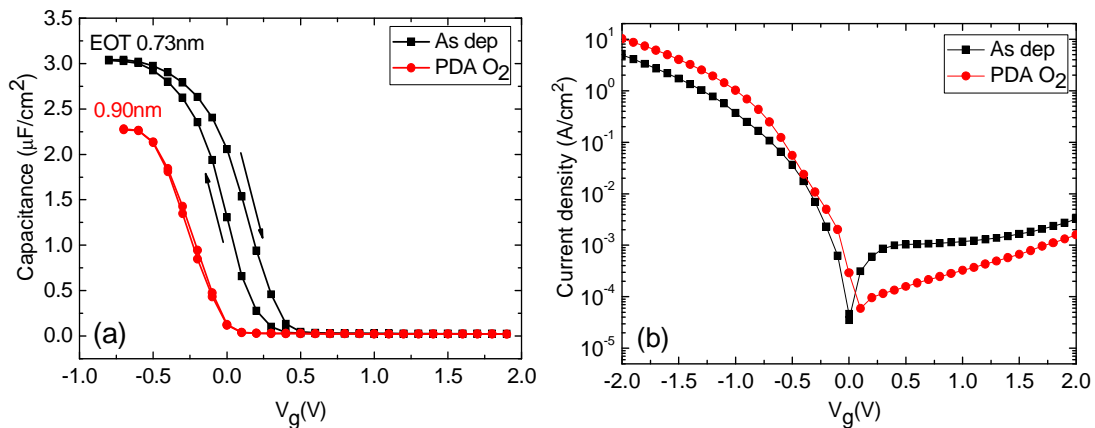*Figure IV. 10 (a) C-V measurements at f=100 kHz for the as-deposited Gd_2O_3 film grown at 700°C and the same sample treated by a 200°C PDA process under O_2 in a tubular furnace. (b)corresponding J-V measurements.*

IV.2.4.2) Annealing in a RTA furnace

As Rapid Thermal Annealing (RTA) is the most used method in the treatment of high-κ materials, we have tried different RTA processes on our Gd_2O_3 films, 400°C RTA under nitrogen, forming gas (96%N_2/ 4%H_2) and O_2 atmospheres have also been performed on a 2.54 nm Gd_2O_3 film (EOT=0.82nm) grown at 700°C under atomic oxygen ambience. The treatment includes an increase of temperature at the rate of 100°C/min and the temperature is maintained at 400°C for 1 second with a subsequent cooling with an introduction of the considered gas during the annealing.

Figure IV. 11 (a) shows the C-V curves measured at 100 kHz for as-deposited and RTA samples in N_2, forming gas, O_2 ambiences respectively. As-deposited sample shows EOT of 0.82nm with a hysteresis loop of $\Delta V=0.25V$ and a $V_{FB}=-0.3V$ ($\Delta V_{FB}=0.2V$). Different gas ambiences present different impacts on the annealed samples. The annealing in O_2 ambience yields a almost similar EOT value (0.86nm) compared to as-deposited one (0.82nm), while effectively reduce the charges in the film: the hysteresis loop and V_{FB} of the O_2-annealed sample are reduced to $\Delta V=0.1V$ and $\Delta V_{FB}=-0.1V$ respectively. The annealing under N_2 and forming gas atmosphere result in increased EOT values (1.8nm and 1.4nm) but effectively decrease the hysteresis ($\Delta V=0V$ and 0.1V) and ΔV_{FB} (-0.25V and -0.2V).

The J-V measurements are shown in Figure IV. 11(b). At $|V_g-V_{FB}|=1V$, the leakage current density of the as-deposited, N_2-annealed, forming-gas-annealed and O_2-annealed samples are $1.11\times10^{-2}A/cm^2$, $6.03\times10^{-1}A/cm^2$, $1.62\times10^{0}A/cm^2$ and $4.78\times10^{-1}A/cm^2$ respectively. The RTA samples demonstrate stable J-V performance with respective to the as-deposited sample.
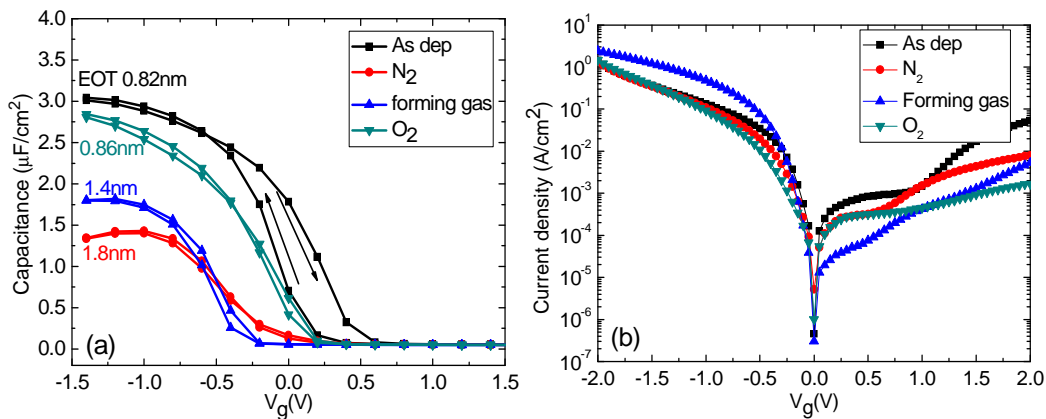

Figure IV. 11 (a) C-V measurements at f=100 kHz for the as-deposited and RTA under N_2, forming gas and O_2 Gd_2O_3 films and (b) corresponding J-V measurements.

IV.2.5) Influence of the substrate orientation

In order to investigate the influence of the substrate orientation on the electrical properties of Gd_2O_3, a 2.5nm-thick Gd_2O_3 film is deposited on Si(001) substrate to compare with that on Si (111) substrate. Figure IV. 12 (a) shows the C-V characteristics of Gd_2O_3 films on Si(001) and Si(111) substrate. The physical film thicknesses are 2.5nm and 2.7nm respectively. Compared to that of Gd_2O_3/Si(111) that displays a typical capacity behavior, the C-V curve of Gd_2O_3/Si(001) sample exhibits an abnormal large depletion region following a quick breakdown of the capacity, which might be explained by the comparison of their J-V characteristics: as shown in Figure IV. 12 (b), the leakage current density of Gd_2O_3/Si(001) sample is larger by 1~2 orders of magnitude than that of Gd_2O_3/Si(111) sample. This result is probably due to the presence of the grains between the two orthogonal in-plane orientations of Gd_2O_3 on Si (001) (see Ref. 8), the joints of which can serve as the channels of the leakage current.
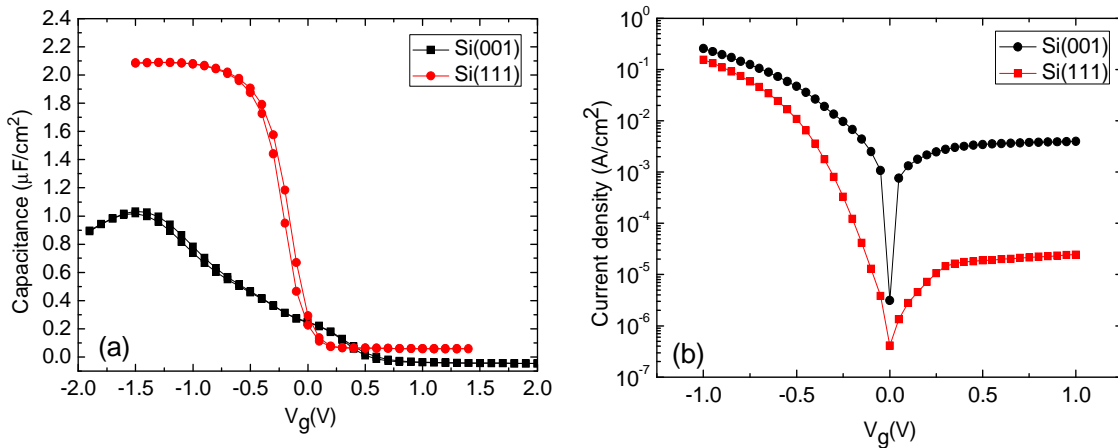
Figure IV. 12 (a) C-V measurements at f=100 kHz for the Gd_2O_3 films on Si(001) and Si(111); (b) corresponding J-V measurements.

IV.2.6) Conclusion

The crystalline Gd_2O_3 thin films on Si substrate demonstrate good dielectric properties. With this high-κ oxide, low ETO values (0.73nm in this work) can be obtained with a leakage current value consistent with the ITRS recommendations (J<300 A/cm^2 for a 7Å EOT of the 16nm node in the category of "low operating power technology requirements"). Gd_2O_3 has been proved to be one of the most promising candidates for gate dielectric materials of future 22nm and sub-22nm MOSFET technique.

The electrical properties of the as-deposited samples are far from perfect and require further optimization. Different strategies are performed to develop the performance of Gd_2O_3/Si MOS structure. The employment of the atomic oxygen during the growth could effectively decrease the leakage current in the Gd_2O_3 layers. Both PDA by tubular furnace and RTA improve the dielectric qualities of the samples. In particular, the RTA under O_2 atmosphere can effectively reduce the charge density in the dielectric films while retain almost the same EOT value of the sample, thus turns itself to be a good PDA treatment for the Gd_2O_3/Si samples. Figure IV. 13 shows the best performances $J_g=f(EOT)$ of Gd_2O_3 films in the literature, in which the results of this work are also demonstrated. It is evident that the above-mentioned results are at the cutting edge of the state of the art of world.
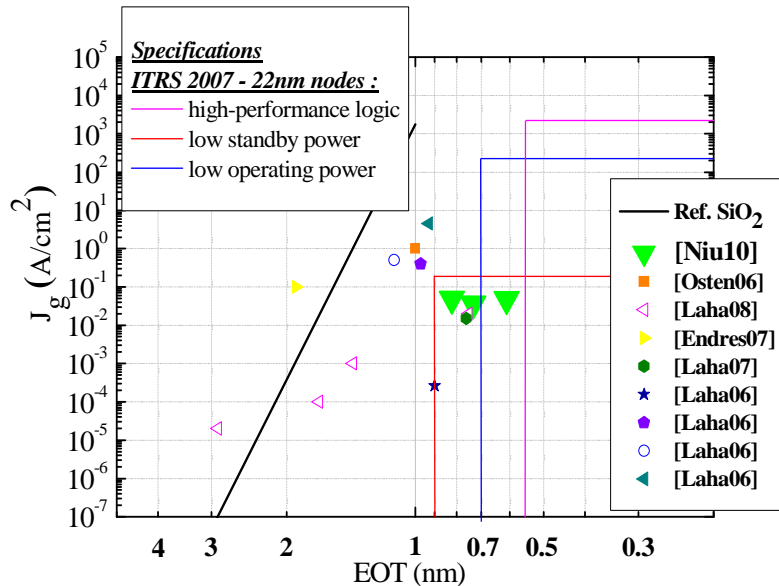
Figure IV. 13 International state of art of Gd_2O_3/Si system for $V_g=+/-1V$. The green triangles note the results obtained in this thesis.

IV.3) Piezo-(Ferro -) electrics

Piezo-(Ferro-)electrics is one of the most important properties of the alkaline earth titanates, which possess the same perovskite structure. A ferroelectric is generally defined as a material whose intrinsic lattice polarization P can be reversed through the application of an external electric field E that is greater than the coercive field E_c. All ferroelectrics are piezoelectric. Not all materials with electrical hysteresis are ferroelectric: as discussed in last section, dielectric films have an extrinsic hysteresis due to mobile charged defects. And *p-n* junctions can also exhibit hysteresis.

In order to demonstrate our $SrTiO_3/Si(001)$ can be used as a template for functional oxide integration on silicon, we investigated the electrical properties of four perovskite oxides on the $SrTiO_3/Si(001)$ template: $SrTiO_3$, $BaTiO_3$, $Pb(Mg, Nb)$-$PbTiO_3$, $Pb (Zr, Ti)O_3$ using different film deposition processes: MBE, sol-gel, laser-MBE.

IV.3.1) SrTiO$_3$

Bulk cubic crystal $SrTiO_3$ does not show any ferroelectricity. However, the biaxial strain imposed by the underlying substrate on the coherently epitaxial $SrTiO_3$ films might induce cubic to tetragonal phase transition leading to ferroelectricity. In fact, several recent works have reported this strain induced or enhanced ferroelectricity in the epitaxial thin films[9,10,11]. Thanks to the commensurate epitaxy of $SrTiO_3$ on Si, as demonstrated in Chapter III, the ferroelectricity is thus envisaged in our $SrTiO_3$ thin film. We performed I-V measurements on the Au/Ni/STO/*p*-Si structure in order to explore its electrical behavior.

Figure IV. 14 displays the typical I-V behaviors at 300K of STO/*p*-Si heterostructure grown at 360°C with respectively thicknesses of 4ML and 10ML. The Au/Ni electrode area is 100μm×100μm. According to the results of Chapter III, the interface between STO and Si is coherent and the STO is principally strained on Si substrate with such thin thicknesses. Surprisingly, the STO/*p*-Si structure shows well-rectified I-V characteristic of *p-n* diode instead of ferroelectric one. We attribute this behavior to the oxygen vacancies in the STO film. In fact, electrical properties of STO can be changed from insulator to *n*-type semiconductor by reducing it to $SrTiO_{3-x}$[12,13,14] or doping impurity ions[15,16]. STO thin films prepared by vacuum processes usually contain oxygen vacancies which can form positive space charge under high electric fields by detrapping electrons. Then STO films will possess characteristics of the *n*-type semiconductors.

Let us look at the I-V curves in the Figure IV. 14. The *p*-Si/*n*-$SrTiO_{3-x}$ heterojunctions with 4ML and 10ML demonstrate similar striking rectifications. Under forward bias (positive pole dc voltage applied on the *p*-Si), the current is initially quite small (1.6μA and 2.0μA at 0.3V for 4ML and 10ML STO respectively) and begins to increase very quickly after the voltage exceeds 0.35V. However, it remains very small even under large reverse bias. At V=-2V, the current of 4ML and 10ML STO/Si junctions are -2.8×10^{-4}μA and -6.1μA respectively.

167
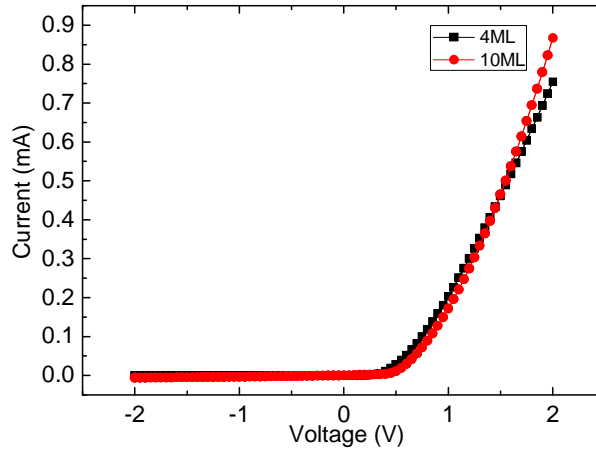
Figure IV. 14 Typical I–V characteristic of p-Si/n-SrTiO$_{3-x}$ junctions diode at 300 K.

The observed phenomena can be explained by considering the band structure of the *p*-Si/*n*-SrTiO$_{3-x}$ heterojunction[17], as shown in Figure IV. 15. Values of work function [χ(Si)=4.05eV and χ(STO)=3.9eV] and band gap [E$_g$(Si)=1.12eV and E$_g$(STO)=3.3eV] were taken to construct the band structure. The band offset of conduction band at *n*-SrTiO$_{3-x}$/*p*-Si interface is E$_c$=χ(STO)- χ(Si)=-0.15eV and that of valance band is E$_v$=[χ(STO)-χ(Si)]+[E$_g$(STO)- E$_g$(Si)]=2.03eV. An energy barrier is formed at the interface of STO/Si. Under forward bias condition (a positive pole of dc voltage applied on the *p*-Si), the applied voltage reduces the energy barrier and electrons in the conduction band of *n*-SrTiO$_{3-x}$ may inject into that of *p*-Si. By using an iterative method to solve the Poisson equation and Boltzmann formulas self-consistently[18], the energy barrier height can be obtained as 0.4eV, which is comparable to the threshold voltage (0.35V) under the forward bias voltage.

Figure IV. 15 Schematic band structure for p-Si/n-SrTiO$_{3-x}$ heterojunction.

One question remains: why cannot we observe ferroelectric behavior? One can suppose

that the too high leakage current avoid measuring any hysteresis loops. Indeed the polarization switch current is less than 100pA while the leakage current of the STO/Si heterostructure is about 1mA.

IV.3.2) BaTiO₃

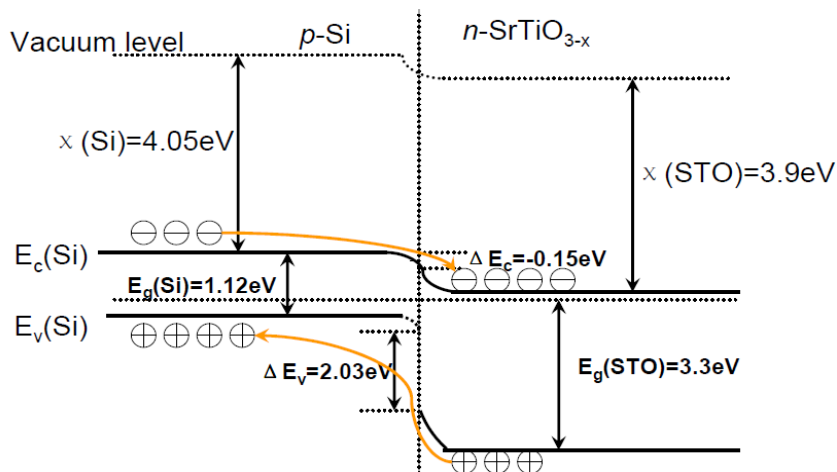Barium titanate (BaTiO$_3$, BTO) is a classical ferroelectric material which was extensively investigated in bulk form in the past[19]. Recently the BTO thin films have also attracted numerous study not only because of its simple chemical composition and remarkable properties (high dielectric constant, non-linear optical properties and positive/negative temperature coefficient effects), but also due to its lead-free and environmental-friendly characteristics, which have become increasingly important from a long term point of view[20]. It is a tetragonal ferroelectric at room temperature with a=3.989Å and c=4.029Å and a Curie temperature of 393K.

IV.3.2.1) BaTiO₃/Nb-doped STO (001)

To well investigate the heteroepitaxy of BTO on Nb-STO, the Nb doped STO substrates are firstly used before the deposition of BTO on STO/Si templates. The conductive Nb:STO wafers (10mm×10mm, 0.5wt%, provided by MaTeck) have the similar crystal structure with pure STO but can be served as an bottom electrode, i.e. they are electrically conducting.

It has been reported that the ferroelectric performance of BTO films are highly influenced by the film thickness due to the size effect and stressing[21,22] or the oxygen pressure due to the generation of oxygen vacancies[23,24]. Therefore a series of BTO films with the thickness ranging from 4nm to 50nm under various oxygen partial pressures from 1×10^{-6}Torr to 1×10^{-5}Torr are deposited on Nb-doped STO substrate to investigate their influences on the structural and electrical properties of BTO.

Before the growth of BTO, the Nb-doped STO substrate is prepared with the same method as explained in III. 3.2.1. Figure IV. 16 displays the RHEED patterns along both BTO[100] and [110] azimuths of a 50nm BTO film grown at 620°C and PO$_2$=1×10^{-6}Torr on the Nb-doped STO substrate. The growth temperature of the heteroepitaxy of BTO on STO was optimized by a previous thesis at INL (G. Delhaye, 2007), which ranges from 550°C to 650°C. Clear, well-defined streak lines can be observed indicating a single crystalline BTO layer with good quality. Both [100] and [110] directions show 1×1 reconstruction during the

whole growth process, suggesting good stoichiometry of Ba and Ti. If the Ti/Ba ratio is different from 1, special reconstructions appear on the RHEED pattern.
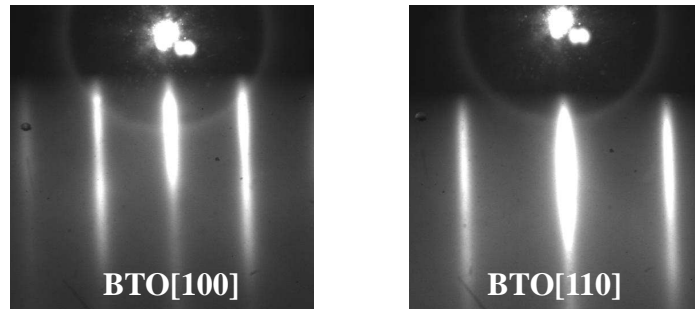
Figure IV. 16 RHEED patterns along BTO[100] and BTO[110] azimuths of 50nm-BTO/Nb-STO sample grown at 620°C and $PO_2=1\times10^{-6}$Torr.
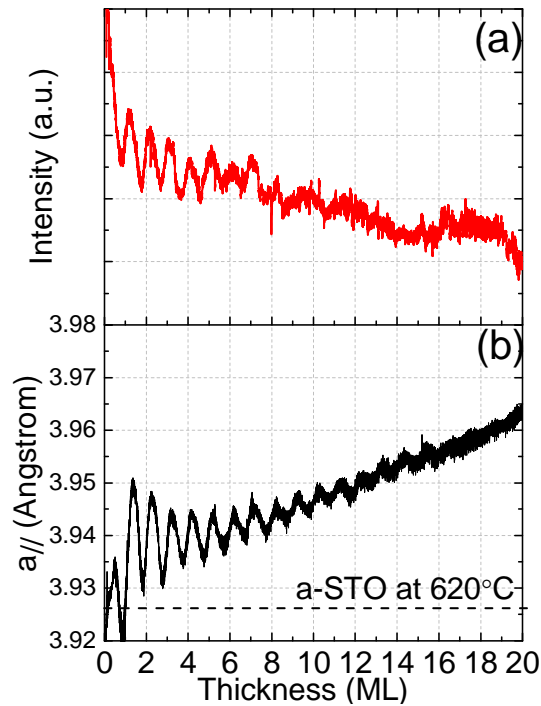
Figure IV. 17 Evolutions of (a) the intensity of the RHEED specular spot and (b) the in-plane parameter of the growing BTO film.

The intensity variation of the RHEED specular spot observed during the epitaxial growth of BTO film is shown in Figure IV.17 (a). The intensity variation has an oscillatory behavior which indicates a 2D layer-by-layer growth mode. The growth rate can be estimated to be 0.01ML/s by analyzing the oscillation.

The evolution of the BTO in-plane lattice parameter is plotted by recording the distance between the streak lines along [110] direction, as shown in Figure IV.17 (b). It also exhibits oscillatory behavior due to the evolution of the deformation of 2D islands during the growth.

Considering the lattice mismatch between BTO and STO is +2.2%, the minimum of the $a_{//}$ corresponds to the moment when one whole layer is complete while the maximum represents the half complete layer, which is in contrary with the intensity oscillation.

The oscillations persist up to approximately 16ML (6.4nm) and then disappear, which indicates a transition from 2D to 3D growth mode. This result shows a critical thickness of 6.4nm for BTO epitaxial layer on STO substrate. The critical thickness of BTO/STO system can be theoretically calculated following the formulation of Matthew and Blakeslee:

$$h_c = \left[\ln\left(\frac{h_c}{b}\right) + 1 \right] \bullet \left[\frac{b(1 - v \cos^2 \alpha)}{2\pi f (1+v)\cos \lambda} \right]$$
Equation IV-7

where h_c is the critical thickness, b is $a\sqrt{2}$, f is 2ε (ε is lattice mismatch between BTO and STO, 2.2%), v is the Poisson ratio, α is the angle between dislocation line and its Burgers vector and λ is the angle between the slip direction and that direction in the film plane which is perpendicular to the line of intersection of the slip plane and the interface.

In this BTO/STO system, the main type of the misfit dislocations are interfacial edge dislocations with Burgers vector **b**=**a**<100>[25,26]. The critical thicknesses calculated range form 2.4 to 11nm[27] due to the different dislocation slip systems used in the calculations. And the results obtained experimentally by other groups using XRD[25,28], RHEED[27] and HRTEM[26] also range from 2nm to 10nm, which generally depend on the growth conditions. Our result is in good agreement with previous work.

The crystalline qualities of the BTO films with different thicknesses are examined ex-situ by HRXRD measurements. Figure IV. 18(a) shows an instance for a 50.7nm-thick BTO/STO sample. In the typical 2θ/ω scan we can observe sharp, intense BTO *00l* peaks appear at the left side of the STO *00l* peaks, indicating the c-oriented BTO film on STO substrate. The Pendellösung fringes demonstrate highly uniform feature of the BTO film. The inset shows a rocking curve in ω around BTO(002) Bragg condition with a FWHM=0.09° confirming the good crystalline quality of the BTO epitaxial film. The BTO film thicknesses were determined by XRR measurement. Figure IV. 18 (b) shows the reflectivity curve and the fitting for the 50.7nm sample. It can be observed that the curve is quite well fitted by the Rigaku software and the corresponding fitting parameters are listed in the inset table. Two BTO layers are found: one 10.8nm layer close to substrate (commensurate layer) and one 39.9nm layer on the

surface (partial relaxed layer). Moreover, the oscillations of the measured reflectivity curve and the good fit of the simulation curve suggest an uniform growth along the surface normal direction. The AFM image (1μm×1μm) displays an atomic flat surface of the sample, as shown in Figure IV. 18 (c).
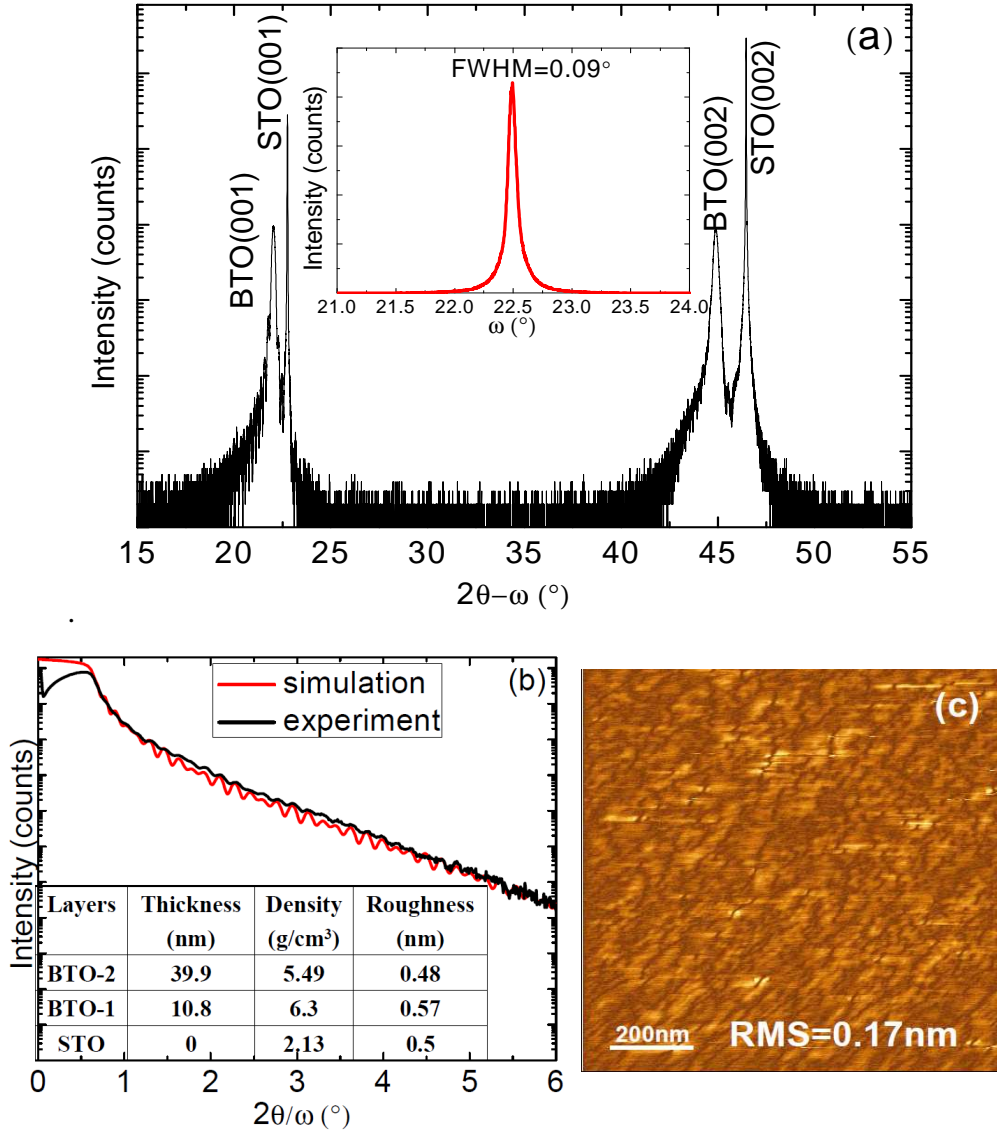
Figure IV. 18 (a)Room temperature 2θ/ω scan of a 50.7nm BTO/STO sample. Inset shows rocking curve in ω around BTO (002) Bragg condition with a FWHM=0.09°. (b) XRR measurement (simulation and experimental data, inset shows the information of layers) and (c) 1μm×1μm AFM image (RMS=0.17nm) for the same sample.

From the 2θ/ω scan around BTO (002) reflection the out-of-line BTO lattice parameter can be extracted and the in-plane lattice parameters can be obtained form the BTO (202) measurements (not shown). The evolution of the lattice parameters (*c* and *a*) of the BTO films

as a function of thickness is plotted in Figure IV. 19 (a). The in-plane lattice parameters are equal to the STO lattice constant when the thickness is less than 10nm, indicating the pseudomorphic growth of BTO film. This behavior well consists with our RHEED observations and prior reports. Once the thickness exceeds 10nm, the BTO film plastically relaxes on STO substrate by forming misfit dislocations and with the thickness of 50nm it is almost completely relaxed on STO.

Figure IV. 19 (b) compares the evolution of *c/a* ratio and unit cell volume of BTO film with those of bulk one (noted by dashed lines). For the coherent epitaxial BTO layers (less than 10nm), the *c/a* ratios are much larger than the bulk one resulted from the enhancement of the tetragonality of the BTO cells according to Poisson's elastic law. And their unit cell volumes are less than the bulk one. As the film thickness increases, the BTO film progressively relaxes thus the *c/a* ratio continues to decrease and is very close to bulk one for 50nm-thick film. The unit cell volume of BTO. In addition, the volumes of the relaxed BTO films are larger than the bulk one.
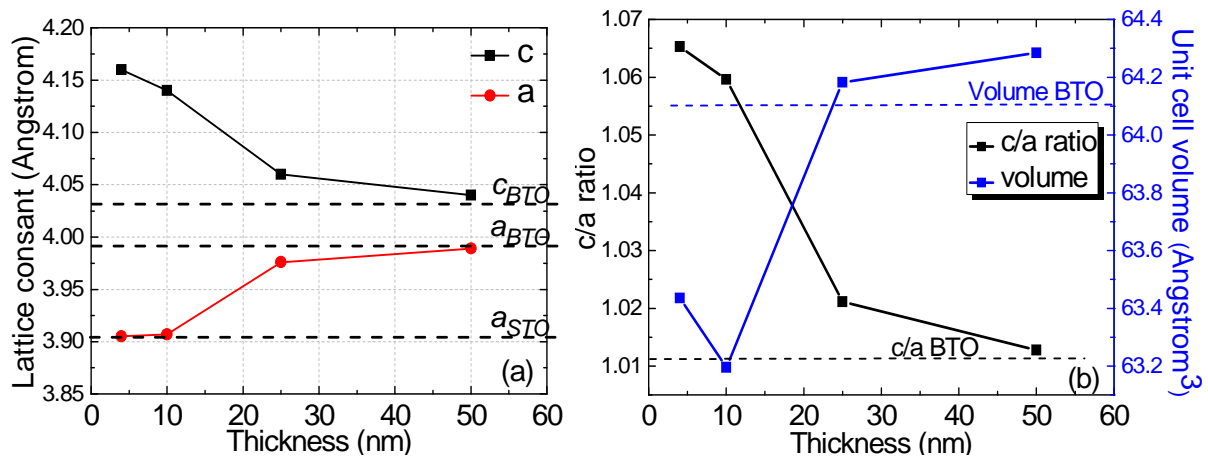
Figure IV. 19 Evolution of (a) lattice parameters c and a; (b) c/a ratio and unit cell volume of BTO epitaxial film as a function of thickness.

In essence, the lattice parameters of BTO unit cells are determined by two mismatch effects: lattice mismatch and thermal expansion mismatch. The lattice mismatch between BTO and STO is +2.2%. Let us now discuss the thermal expansion mismatch effect. During the cooling process from the growth temperature (620°C) to room temperature (20°C), both BTO epitaxial film and STO substrate are contracted due to the thermal expansion effect. Meanwhile BTO also undergoes the cube-tetragonal transition during this cooling process. According to D. Taylor et al.[29], the thermal expansion coefficients of BTO and STO are

1.7×10^{-5} and 9×10^{-6} respectively. In the case that BTO is pseudomorphically grown on STO substrate (less than 10nm), the in-plane lattice parameter of BTO will always equal to that of STO (3.905Å) and under the other extreme condition that the BTO is totally relaxed on STO, during the growth process BTO follows its own thermal expansion coefficient but it will follow the STO thermal expansion coefficient instead during the cooling process due to the clamping effect imposed by underlying STO substrate. Hence the in-plane lattice parameter of the entirely relaxed BTO can be calculated as 4.008 Å, which confirms that 50nm-thick film (a=3.990 Å) is almost entirely relaxed.

Evidently, the abovementioned relaxation mechanism related to lattice mismatch and thermal expansion mismatch can quite well explain the evolution of the lattice parameter of BTO. However, it cannot fully explain the fact that the unit volumes of partial relaxed BTO are larger than the bulk one. We attribute this anomalous enlargement of the unit cell volume to the oxygen vacancies existing in the BTO films. The similar behavior has been reported for $PbTiO_3$[30] and $BaTiO_3$ prepared by Laser-MBE[31]. According to the discussion about $PbTiO_3$[30], the +2 charged oxygen vacancy (V_O^{2+}) is energetically more favorable along the **c** axis than in the (a-b) plane. In this case, subject to the Coulombic interaction, the nearest two Ti^{4+} and four Pb^{2+} neighbor cations of a V_O^{2+} defect are displaced away from the V_O^{2+} while the nearest eight O^{2-} neighbor anions are attracted towards it. The displacements of Ti^{4+} and Pb^{2+} cations are along **c** axis and **a** axis, respectively. The magnitude of the displacements from ideal tetragonal positions of Ti, O, and Pb atoms are, respectively, 0.021, 0.004, and 0.016 nm. Resulting from these displacements, the unit cell volume of $PbTiO_3$ is enlarged. The $BaTiO_3$ possesses similar perovskite structure with $PbTiO_3$ thus the enlargement of the lattice volume can be explained in the same way.

In order to reduce the oxygen vacancies in the BTO epitaxial films, the plasma induced atomic oxygen has been used during the growth and different oxygen partial pressures are employed to investigate its impact on BTO films. Figure IV. 20 shows the $2\theta/\omega$ scans around the BTO (002) Bragg condition for the BTO/STO samples (45nm~50nm) grown under different oxygen conditions. From curve (a) to (e), the oxygen conditions are molecular oxygen 1×10^{-6}Torr plus atomic oxygen 8×10^{-6}Torr annealing (650°C, 1hour), atomic oxygen 1×10^{-6}Torr plus atomic oxygen 8×10^{-6}Torr annealing (650°C, 1hour), atomic oxygen 1×10^{-6}Torr, atomic oxygen 5×10^{-6}Torr and molecular oxygen 1×10^{-6}Torr respectively. The

intense sharp peak located at 2θ=47.3° is the STO(002) reflection. For the BTO grown in molecular oxygen ambience (a) and (e), only one BTO (002) peak arises at the left side of the STO peak, revealing good crystalline c-axis oriented BTO lattices. However, for the BTO films grown in atomic oxygen ambience (b), (c) and (d), two BTO (002) peaks appear together indicating both **c**-axis and **a**-axis oriented BTO lattices. The **c/a** domains structure forms during the cubic-tetragonal phase transition during the cooling process when the temperature decreases to less than 120°C. Therefore the alignment of the BTO lattices in atomic oxygen ambience is not as highly-ordered as that in molecular oxygen ambience. The 90° domains in these c/a-axis oriented films might decrease the piezoelectricity of the BTO film[32] thus should be avoided. We choose the condition (a) as the optimized oxygen condition, i.e. growth under molecular oxygen 1×10^{-6}Torr following by an annealing under atomic oxygen 8×10^{-6}Torr (1hour). Figure IV. 21 displays the reciprocal space maps around both STO (002) and STO (103) Bragg conditions. The more intense spots represent the STO reflections. According to the RSM measurement around BTO 103 reflection, the 50nm BTO film is partially relaxed on STO substrate.
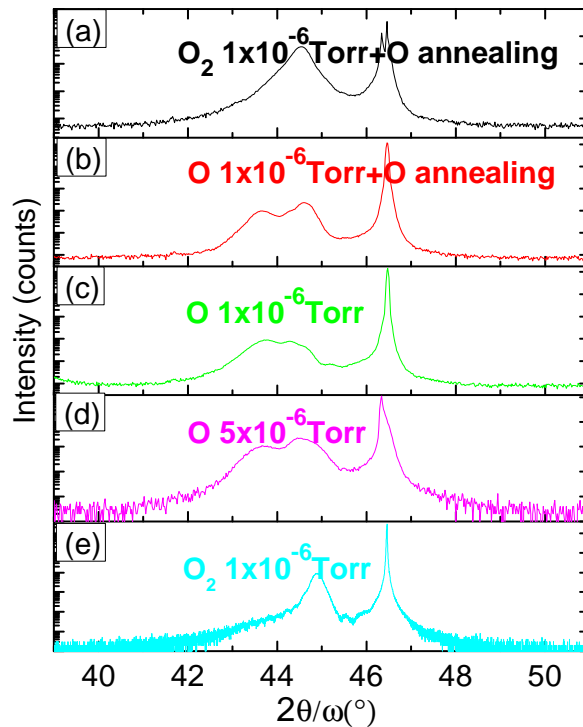

Figure IV. 20 Typical 2θ/ω scans around BTO (002) reflection for ~50nm BTO/STO (001) samples grown in different oxygen ambiences.
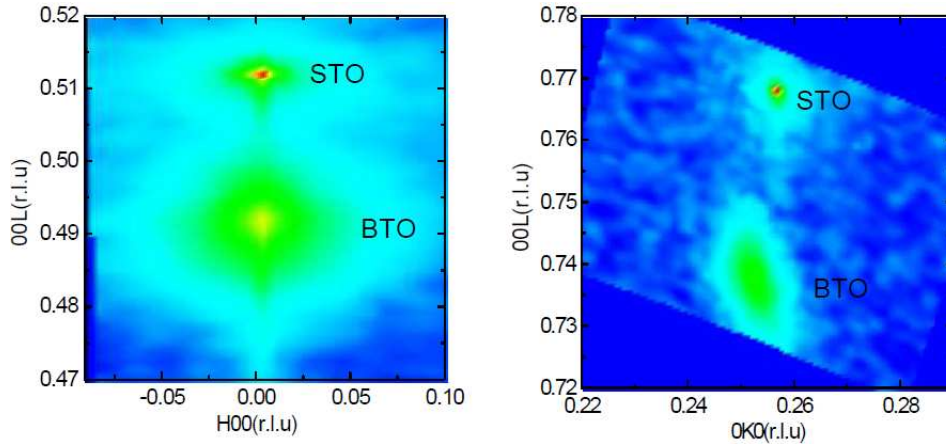
Figure IV. 21 Reciprocal space maps around STO 002 (left panel) and STO 103 (right panel) Bragg conditions. Intensities from low to high: blue, green, yellow, red.

The Au/Ni/BTO/Nb-STO structure is fabricated using the BTO/STO samples grown in molecular (O_2) and atomic (O) oxygen ambiences (both are in-situ post-annealed under atomic oxygen atmosphere) respectively. Au/Ni and Nb-STO are respectively used as top and bottom electrodes.

The I-V characteristics realized on a $100 \times 100 \mu m^2$ electrode of the two samples are shown in Figure IV. 22 (a). It is surprisingly that the sample grown in O_2 ambience which is c-axis oriented shows a rectifying behavior with a threshold voltage V_{th}=-0.7V. This result reveals that the oxygen vacancies in the BTO film grown in O_2 ambience are non-negligible although an in-situ PDA in atomic oxygen ambience was subsequently performed. The oxygen vacancies in the film lead to a p-BTO/n-STO (Nb doped) junction structure, which shows a rectification characteristic. The current remains very small even under large reverse bias. At V=2V, the current is 2.7µA.

In contrary, the sample grown in O ambience which possesses both c-axis and a-axis oriented BTO shows hysteresis characteristic for dc voltage loop ranging from -2→0→2→0→-2V, exhibiting the ferroelectric switch (butterfly behavior). In the inset the current is plotted in logarithmic scale, where the I-V characteristic is found symmetric for positive and negative bias. Figure IV. 22 (b) shows the corresponding C-V curve for the sample grown in O ambience. The hysteresis of the curve for a voltage loop of -3→0→3→0→-3V confirms the ferroelectric quality of the BTO film and the two peaks at V=0.2V and V=-0.8V reveal the polarization reverses of the ferroelectric BTO film.

176

Furthermore, as the positive bias increases the capacitance tends to a constant C_0 which can be described as:

$$C_0 = \frac{\varepsilon_0 \varepsilon_r S}{d}$$

Equation IV-8

where ε_0 dielectric constant in vacuum (8.85×10^{-12}F/m); ε_r the relative dielectric constant of BTO; S the electrode area($100 \times 100 \mu m^2$) and d the BTO film thickness (50nm). Considering that C_0 is equal to 2.6×10^{-10}F (at V=2.8V) the ε_r of BTO film can be estimated as 147.
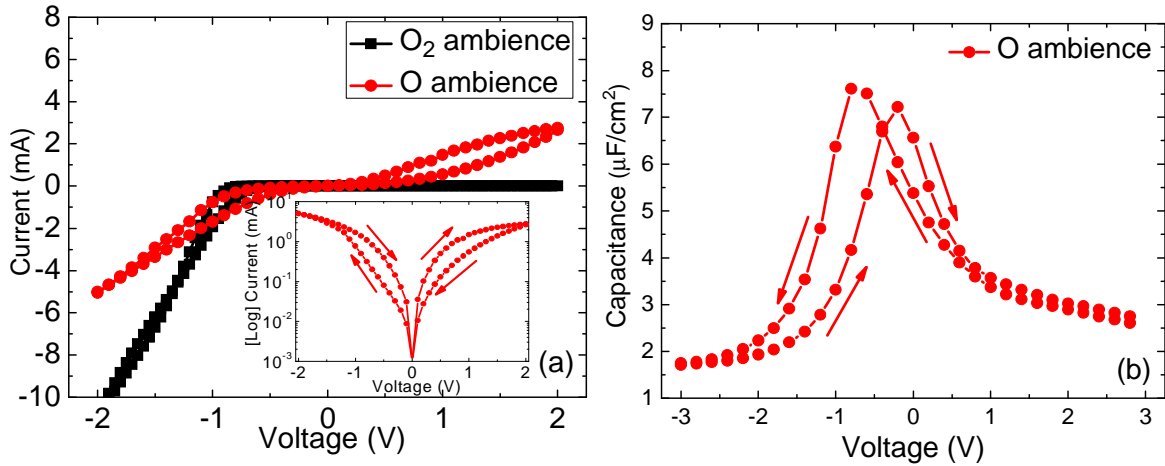
Figure IV. 22 (a) Typical I-V characteristics of the BTO/Nb-STO samples grown in molecular and atomic oxygen ambiences, inset shows log scale of the O-ambience I-V curve; and (b) corresponding C-V characteristic at f=1MHz for the sample grown in atomic oxygen ambience. The electrode area is 100μm×100μm.

Several ex-situ PDA treatments are performed on the BTO films grown in O_2 ambience in purpose of refilling the oxygen vacancies and inducing ferroelectrics of the film. The RTA annealing in O_2 atmosphere at 400°C is firstly examined, which turns out to affect very slightly the electrical properties of the BTO film. The annealing in a PLD chamber at 600°C under oxygen partial pressure of 100 Pa is then attempted.

In this thesis, BTO thin films are principally prepared by MBE at INL while Pulsed Laser Deposition (PLD) is also employed for the comparison. The growth of BTO films by PLD was carried out at IEF, Paris-Sud University, in Orsay. We perform the deposition using a KrF excimer laser (λ = 248 nm) at 620°C and P_{O2}=120mTorr. Laser energy was set up to 200 mJ to have a maximum fluence of 3 J/cm^2 on the target. The electrical properties of BTO sample grown in O_2 ambience (sample a), annealed (in PLD chamber) BTO sample grown in O_2

ambience (sample b), BTO sample grown in O ambience (sample c) and BTO sample by PLD (sample d) are investigated and compared by Piezoresponse Force Microscopy (PFM, performed by Prof. Brice Gautier, INL-INSA). For the BaO-terminated ferroelectric BTO with a tetragonal structure, the ferroelectric distortion lies along the c axis, with P$^-$ polarization giving a net negative surface fixed charge, as illustrated in Figure IV.23 left panel (upper). The mechanism of PFM is also illustrated in Figure IV.23 left panel (lower). 10μm×10μm polarized ferroelectric domains have been written by the conductive point of PFM (+10V) in d.c. (writing) mode on the samples (a), (b), (c) and (d). Then a voltage of -10V is applied on 5μm×5μm areas in the center of the polarized domains. The right panel of Figure IV. 23 shows the typical amplitude signals observed in the a.c. (reading) mode (V=1V), in which all the samples show electrical contrast. However, it can be seen that the poling region of sample (a) is not stable. The contrast at the bottom of the square poling region disappears during the subsequent reading process which only takes 2~5min. Therefore the electrical contrast in PFM image of sample a is induced probably by the charges in the film instead of the ferroelectricity of the BTO film, which is in good agreement with our macro electrical characteristic results. For the other three samples, the poling regions are stable and can be re-detected even after 3 hours (not shown here). Moreover, it is thought that the film has undergone a phase transition to a single ferroelectric domain with a P$^-$ imprint at room temperature, which is confirmed by the PFM writing because it was easier for P$^+$ followed by P$^-$ poling, showing that the film has actually a P$^-$ imprint.
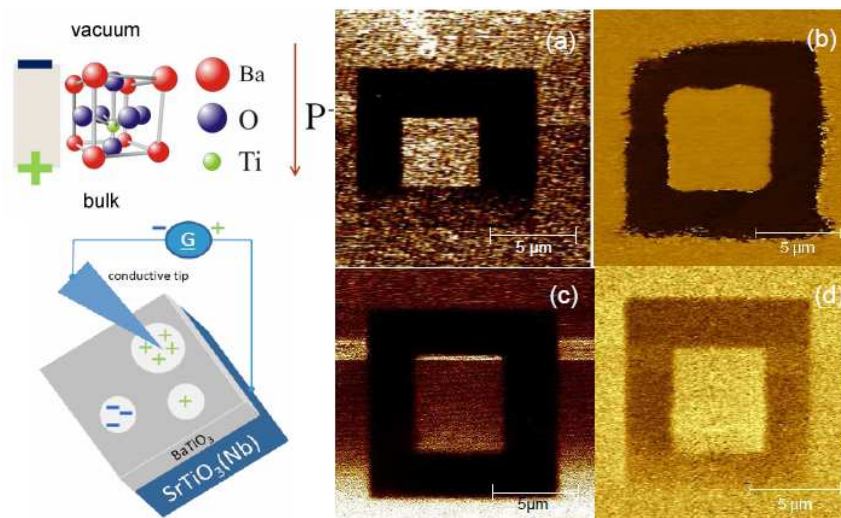

Figure IV. 23 Left panel: Ferroelectric distortion for a BaO-terminated unit cell (upper) and schematic of PFM measurement (lower). Right panel: PFM amplitude contrast images of sample (a), (b), (c) and (d) respectively.

In conclusion, we demonstrate that high quality monocrystalline **c**-axis oriented BTO film can be deposited on STO substrate. The oxygen vacancies in the BTO film play a critical role to influence its electrical property. In order to obtain a ferroelectric BTO film it is necessary to use the atomic oxygen during the growth. Moreover, both of the BTO films ex-situ annealed at P_{O2}=100Pa and fabricated by PLD under P_{O2}=3Pa exhibit good ferroelectric characteristics.

IV.3.2.2) BaTiO$_3$/SrTiO$_3$/Si(001)

The experiences of the growth and characterization of BTO/STO system can be easily transplanted to the BTO/STO/Si heterostructure. A 45nm-thick BTO film is epitaxially grown at 620°C following an annealing at 650°C in atomic oxygen ambience on 5nm-STO/Si(001) template fabricated using "recrystallization" process. Figure IV. 24 displays the RHEED patterns of Si substrate, STO film and annealed BTO film along Si[110] (STO[100]) azimuth. The BTO film shows good crystalline quality with a 2×2 reconstruction indicating a TiO$_2$-terminated surface after the in-stiu annealing. The 1μm×1μm AFM image of the final BTO film with RMS=0.32nm demonstrate a atomic flat BTO surface.
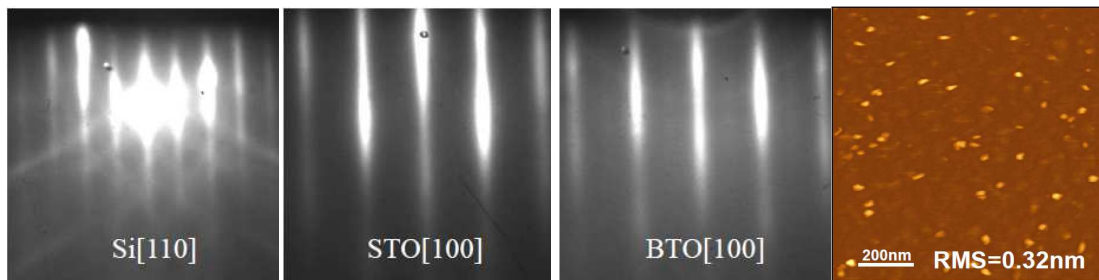
Figure IV. 24 RHEED patterns of Si substrate, STO film and annealed BTO film along Si[110] azimuth and a 1×1μm² AFM image of the BTO film with RMS=0.32nm.

The crystallinity of the BTO layer is explored by HRXRD. Figure IV. 25 shows a typical 2θ/ω scan around BTO (002) Bragg condition for the BTO/STO/Si(001) sample. The epitaxial relationship between BTO, STO and Si substrate is as expected: [100]BTO(001) // [100]STO(001) // [110]Si(001). The BTO epi-layer exhibits good crystalline quality. The FWHM of the rocking curve in ω of BTO (002) peak is only 0.7°.
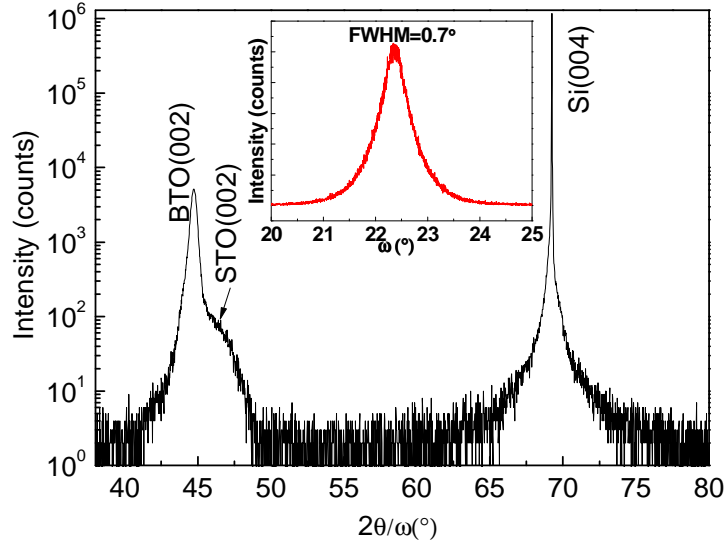
Figure IV. 25 Typical 2θ/ω scans around BTO (002) reflection for a 45nm-BTO/ 5nm-STO/Si (001) sample. Inset shows rocking curve in ω around BTO (002) Bragg condition with a FWHM=0.7°.

To further investigate the structural quality of BTO film on STO/Si template, the RSM maps around STO (002) and (103) are performed respectively, as shown in Figure IV. 26. The left panel shows the mapping around STO(002) reflection. Compared to its counterpart of BTO/STO(001) (Figure IV. 21), it can be found that both STO (a=3.905Å) and BTO (a=3.989Å) film are under compressive strain on Si substrate ($a/\sqrt{2}$=3.840Å). From the RSM image around STO 103 reflection, two maxima of the BTO reflection can be distinguished. One part has the same in-plane parameter with STO film and the other is more relaxed on the STO/Si template.
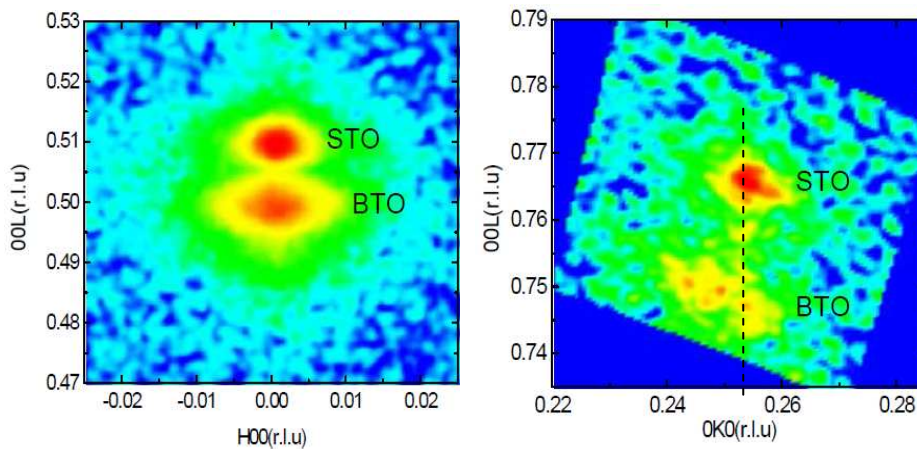
Figure IV. 26 Reciprocal space maps around STO 002 (left panel) and STO 103 (right panel) reflections. Intensities from low to high: blue, green, yellow, red.

180

Figure IV. 27 shows a cross-sectional view of the BTO/STO/Si (001) heterostructure with a 20nm-thick STO grown using the same process. A ~5nm-thick SiO_2 interfacial layer is formed due to the oxidation of the Si surface induced by the oxygen diffusion at 620°C through the growing layer. The STO and BTO films are single crystalline on Si (001). However, different domains exist and are twisted with each other, leading to the mosaicity of the layers.
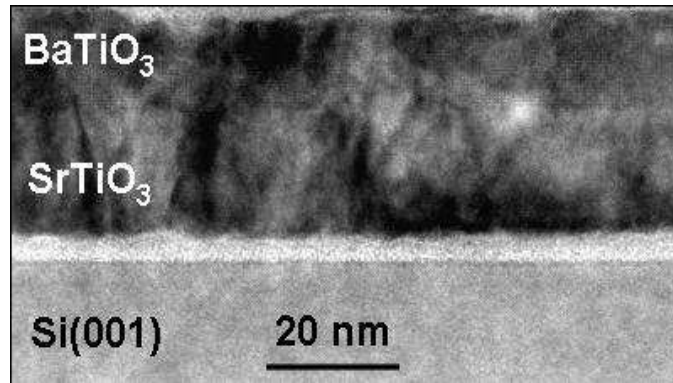
Figure IV. 27 TEM cross-sectional view of a BTO/STO/SiO₂/Si(001) heterostructure.

The electrical properties of the BTO film on STO/Si template is then probed by the fabrication and characterization of Au/Ni/BTO/STO/SiO₂/Si MFIS (Metal Ferroelectric Insulator Semiconductor) capacitor. Ferroelectric memory field effect transistors (FeFET) with a MFIS structure have emerged as promising nonvolatile memory devices due to their attractive properties such as nondestructive readout operation, low power consumption and high switching speed.
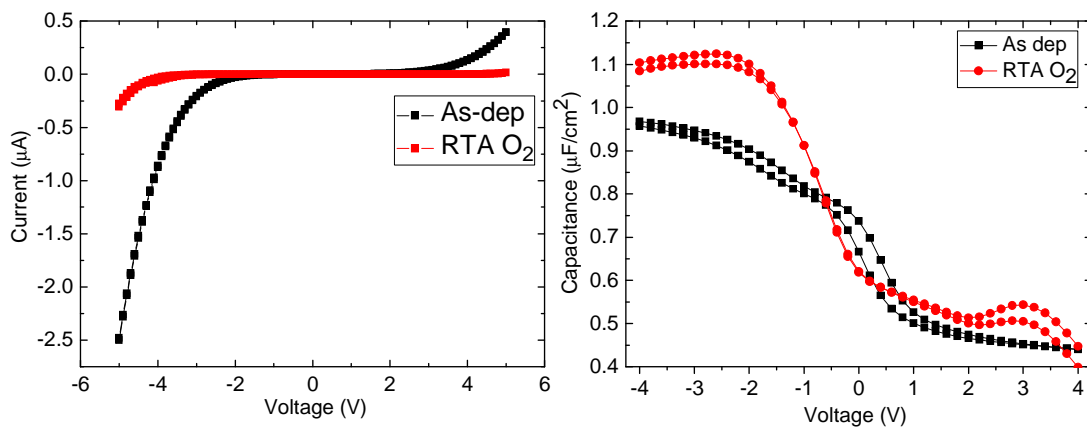
Figure IV. 28 (a) Typical I-V characteristics of the BTO/STO/Si(001) samples of as-deposited one and O₂-RTA annealed one; (b) corresponding C-V characteristic at f=1MHz for the samples. The electrode area is 100μm×100μm.

The Si substrate is *p*-type (B doped) with the doping density 10^{18} cm^{-3}. Both the as-deposited sample and the RTA annealed sample (in O$_2$ atmosphere) show dielectric I-V and C-V properties, as shown in Figure IV. 28 (a) and (b) respectively. The slight hysteresis loop in the C-V curve of the as-deposited sample is related to the charges in the films.

The above-mentioned results demonstrate that the BTO grown in atomic oxygen ambience by MBE is not ferroelectric, although in-situ and ex-situ PDA were also performed. We attribute this phenomenon to the low oxygen partial pressure during the growth. Due to the UHV working environment of MBE, the maximum oxygen partial pressure is ~5×10^{-5} Torr, which is considerably less than that in a PLD chamber (which can reach 100Pa). Hence additional BTO film is deposited on the BTO/STO/Si sample in order to compare its electrical properties with the BTO film deposited by MBE. 50nm-thick BTO epitaxial layer is deposited in PLD chamber at 610°C and 120mTorr O$_2$ partial pressure and cooled under 300Torr O$_2$ ambience. Figure IV. 29 shows I-V and C-V (G-V) characteristics realized at f=1MHz on a 100μm×100μm electrode area of Au/Ni/BTO/STO/SiO$_2$/Si MFIS structure. Evidently, both I-V and C-V curves exhibit hysteresis loops suggesting the ferroelectric behavior. In addition, The C-V curve shows a memory window of 0.75V for the ferroelectric memory application. And the ε_r of BTO/STO/SiO$_2$ heterostructure is roughly estimated as 32, considering that C$_0$ is equal to 5.6×10^{-11}F (at V=7V). This low value of the relative dielectric constant can be explained by the existence of a serie of 3 capacities (BTO, STO, SiO$_2$).
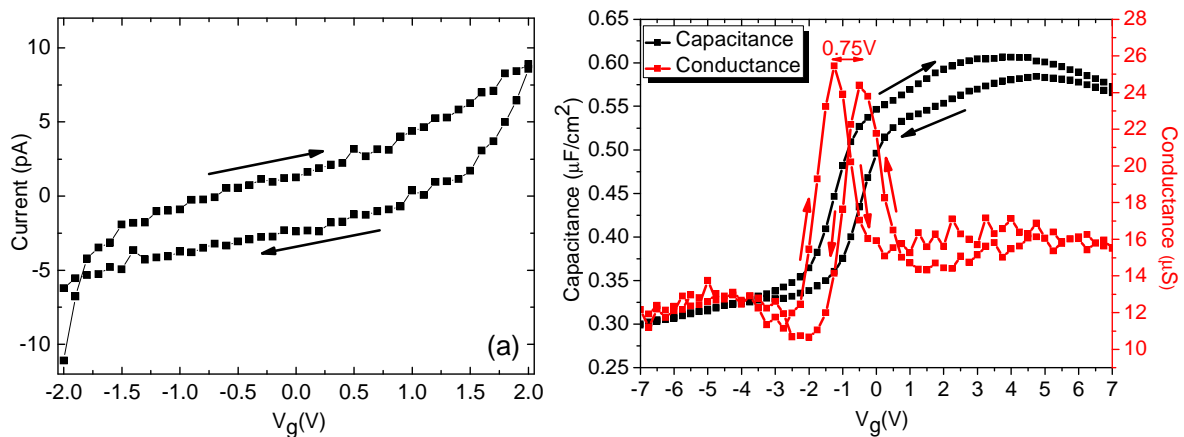
Figure IV. 29 (a) I-V characteristic and (b) C-V (G-V) characteristics (at f=1MHz) on a 100μm×100μm electrode area for the BTO MFIS capacitor.

In conclusion, high quality single crystalline BTO films have been integrated on the STO/Si(001) template using MBE and PLD. The BTO/STO/Si epitaxial film grown by MBE

shows dielectric characteristic, which is probably due to the oxygen vacancy defects existing in the film. Good ferroelectric hysteresis loops can be obtained on the MFIS capacitor of BTO deposited by PLD technique under much higher oxygen partial pressure during the growth.

IV.3.3) Pb(Mg$_{1/3}$ Nb$_{2/3}$)-PbTiO$_3$

Lead Magnesium Niobate-Lead Titanate Pb(Mg$_{1/3}$Nb$_{2/3}$)O$_3$ - PbTiO$_3$ (PMN-PT) attracts numerous studies in recent years as one representative of the relaxor ferroelectrics. Relaxor ferroelectrics is a particular group of ferroelectric materials, the dielectric constant maximum of which does not correspond to transition from non-polar phase to a ferroelectric polar phase. In addition several other particular features make relaxor ferroelectrics distinct from others: frequency dispersion of the dielectric maximum, slim-loop hysteresis behavior near T$_{max}$ and the optical isotropy at the temperatures below the dielectric maximum when there is no external field[33]. The relaxor ferroelectrics exhibit very high-dielectric permittivity[34] and a large piezoelectric response[35] when correctly biased. There are potential applications such as capacitors[36] and in MEMS-type devices[37].

The major difficulties currently limiting PMN-PT are related to the processing of the material itself instead of the aspects of integration. The results shown here focus on issues related to silicon integration and the ferroelectric properties.

26nm-thick PMN-PT film was epitaxially grown on a 1.5nm-STO/Si(001) template using PLD at Orsay, Paris-Sud University (thanks to Valérie Pillard and Philippe Lecoeur). We performed the deposition using a KrF excimer laser (λ = 248 nm) at 600°C and P$_{O2}$=170mTorr. Laser energy was set up to 240mJ. During the post-growth cooling down process, the oxygen pressure was increased to 300Torr. It should be noted that the growth conditions are too aggressive to maintain the integrity of the abrupt SrTiO$_3$/silicon interface. However, they are below the threshold required to disturb the quality of the SrTiO$_3$ layer (which has been shown to occur at temperatures over 800°C)[38].

The crystallography of the PMN-PT film was checked by HRXRD. The left panel of Figure IV. 30 shows the typical 2θ/ω scan around Si(004) Bragg condition, in which intense sharp PMN-PT 00L peaks appear together with the Si(004) reflection, which reveals the good crystallinity of the PMN-PT epitaxial film and a PMN-PT(001)/STO(001) /Si(001) epitaxy relationship. A combination of phi scans under Si (404) and PMN-PT (202) Bragg conditions

is shown in the right panel of figure IV. 30. Thus the epitaxial relationship between the epitaxial films and Si substrate can be described as: [110] PMN-PT (001) // [110] STO (001) // [100] Si (001).
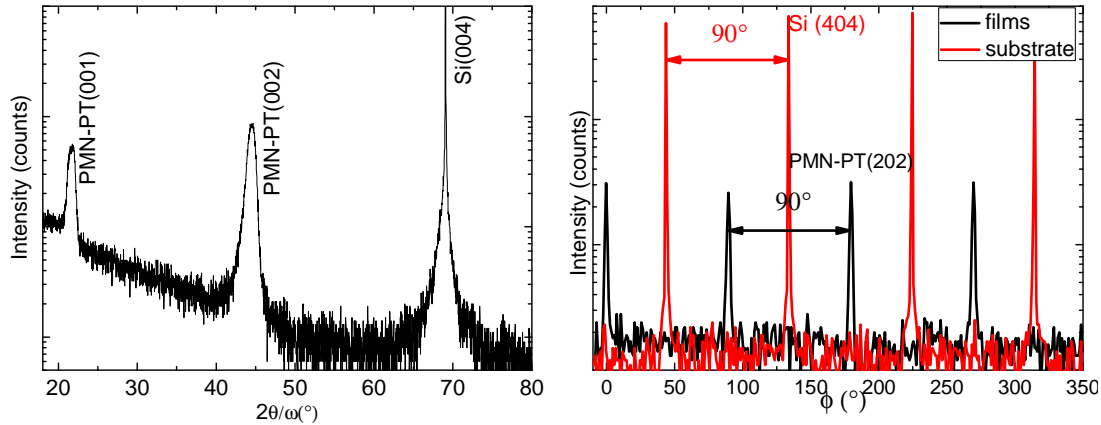
Figure IV. 30 (Left) Typical 2θ/ω scan around Si(004) Bragg condition; (right) phi scans with the Si(404) and PMN-PT (202) Bragg conditions, which reveals the epitaxy relationship between PMN-PT and Si substrate: [110] PMN-PT (001) // [100] Si (001)

The MFIS capacitor of Au/Ni/PMN-PT/STO/Si is fabricated and characterized, as demonstrated in figure IV. 31. The C-V curve show hysteresis loops indicating the ferroelectric behavior. The measurement is performed at f=1MHz on a 100μm×100μm electrode area. The C-V curve shows a memory window of 1.0V. And the ε_r of PMN-PT film is roughly estimated as 48.0, considering that C_0 is equal to 8.5×10^{-11}F (at V=5V)
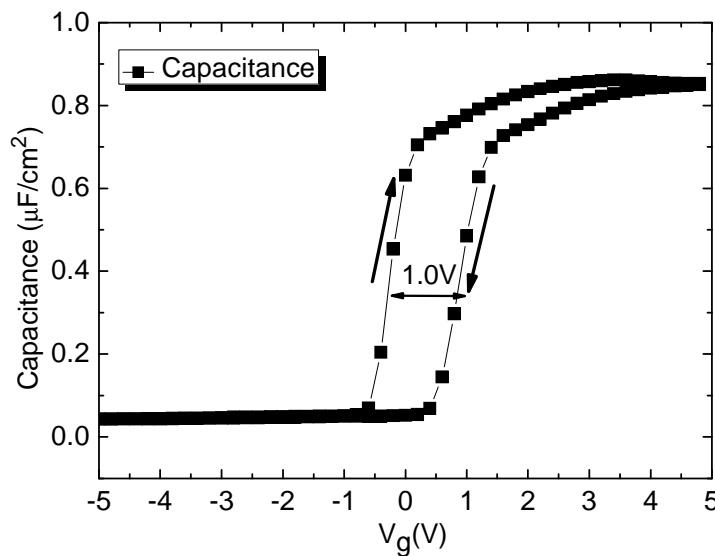
Figure IV. 31 C-V characteristics at f=1MHz on a 100μm×100μm electrode area for the PMN-PT MFIS capacitor.

Due the bad conductivity of silicon in comparison of a metal, it was not possible to determine the d_{33} piezoelectric coefficient using PFM method. New heterostructure will be prepared by introducing a $SrRuO_3$ conductive bottom electrode between the STO buffer layer and the PMN-PT in order to obtain a perfect electrode for ground.

IV.3.4) Pb $(Zr_{0.52}Ti_{0.48})O_3$/SrTiO$_3$/Si(001)

Lead zirconate titanate, $PbZr_{1-x}Ti_xO_3$ (PZT), is a solid solution of $PbTiO_3$ and $PbZrO_3$ compounds. $PbTiO_3$ has a Curie temperature of 490 °C, at which it undergoes a first-order phase transition from cubic paraelectric phase to tetragonal ferroelectric. $PbZr_{1-x}Ti_xO_3$ ceramics with composition (x=0.45~0.5) close to the morphotrophic phase boundary (MPB) are the most commonly used piezoelectric material for various sensors and actuators[39] due to the exaltation of physical properties around the MPB. The motivation of investigating the heterostructure described in this section stem from integrating ferroelectric thin films with CMOS technology to make high density nonvolatile memories.

80nm-thick Pb $(Zr_{0.52}Ti_{0.48})O_3$ film is deposited on 20nm-STO/Si(001) template by sol-gel method (at LETI, Grenoble, thanks to Gwenaël LE RHUN). The process is listed in detail as in Figure IV. 32.

STO/Si 50 mm wafer
Spin coating sol gel 1000 rpm, 1500 rpm/s, 20 s Spin coater
Drying 120°C / 5 min Hotplate
Calcination **350°C**/150 s Hotplate
Cristallisation on ¼ wafer **650°C** / 60 s / O$_2$ RTA furnace
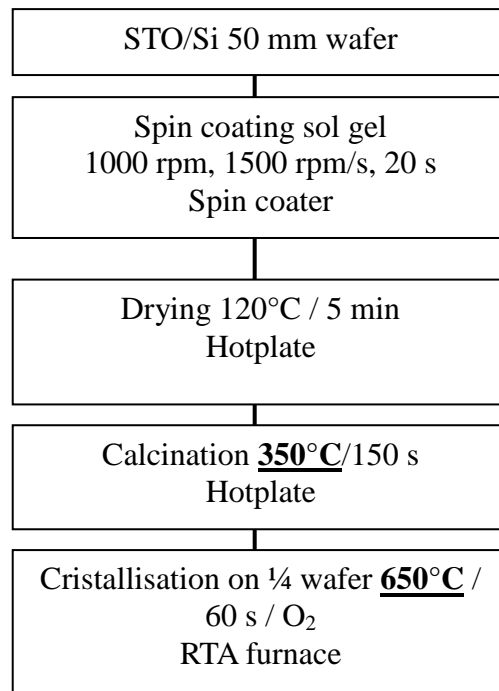
Figure IV. 32 Sol-gel process of PZT deposition on STO/Si (001)

The PZT shows high quality, c-axis oriented single crystallinity on Si substrate. Figure IV. 33 exhibits the typical 2θ/ω scan around Si (004) Bragg condition on the PZT/STO/Si (001) sample (left panel). It can be seen obviously that PZT 00L peaks appear at the right side of STO *00l* peaks. In addition, the φ scans around the Si (404) and PZT (202) Bragg conditions reveal the epitaxial relationship between PZT and Si substrate: [110] PZT (001) // [100] Si (001). The FWHM of the rocking curve in ω of PZT (002) peak (not shown here) is ~0.9°.
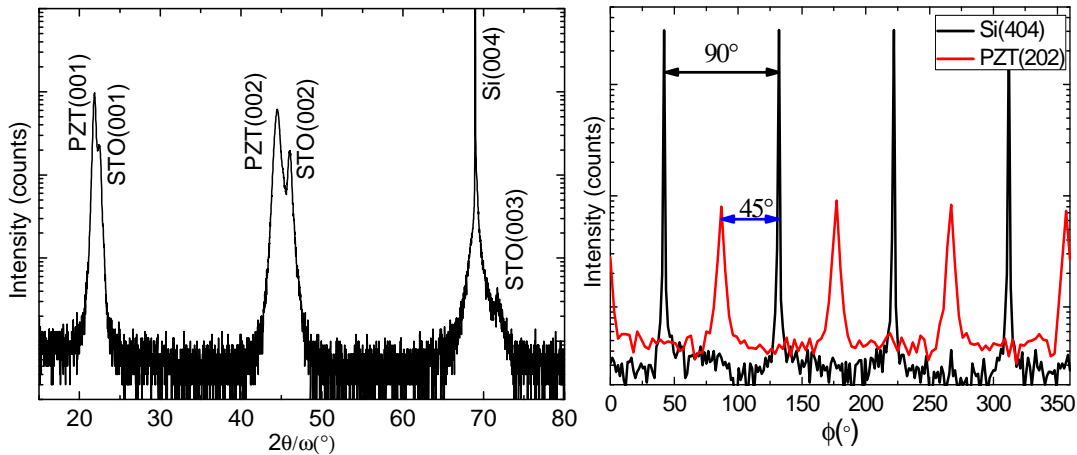
Figure IV. 33 (Left) Typical 2θ/ω scan around Si(004) Bragg condition; (right) phi scans with the Si(404) and PZT (202) Bragg conditions, which reveals the epitaxial relationship between PZT and Si substrate: [110] PZT (001) // [100] Si (001)

The reciprocal space maps around STO 002 and 103 reflections are carried out in order to further investigate the crystallinity of the PZT film on STO/Si(001) template, as shown in figure IV. 34. It can be observed that PZT is partially relaxed on the template.
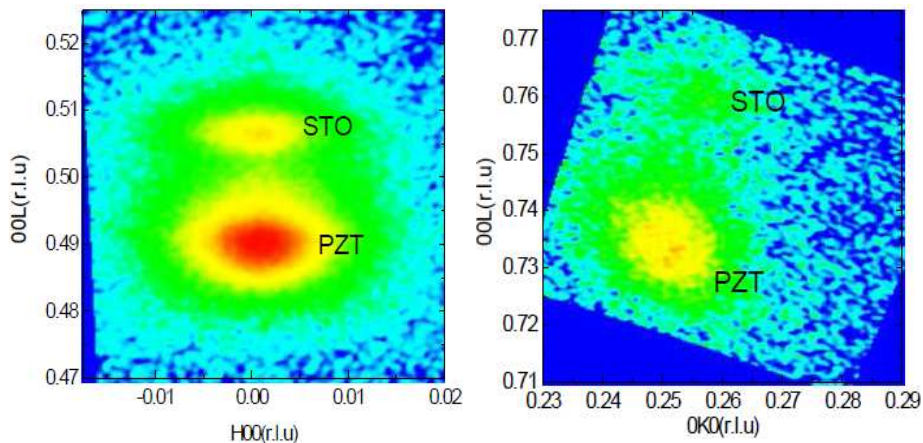
Figure IV. 34 Reciprocal space maps around STO 002 (left panel) and STO 103 (right panel) Bragg conditions. Intensities from low to high: blue, green, yellow, red.

186

The MFIS capacitor of Au/Ni/PZT/STO/Si is then fabricated and characterized, as demonstrated in figure IV. 35. Both the I-V and C-V curves show hysteresis loops indicating the ferroelectric property. The measurement is performed at f=1MHz on a 100μm×100μm electrode area. The C-V curve shows a memory window of 2.6V. And the ε_r of PZT film is roughly estimated as 27.1, considering that C_0 is equal to 8.5×10^{-11}F (at V=-7V)
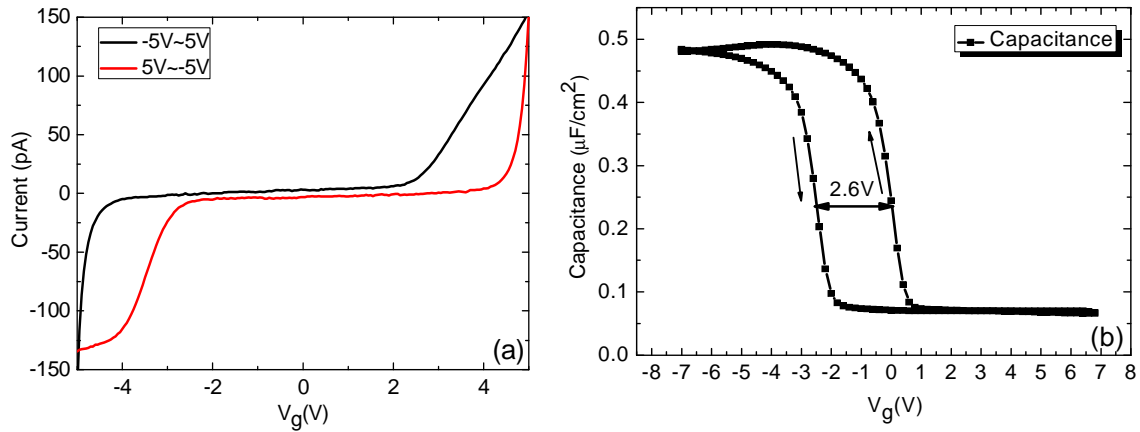
Figure IV. 35 (a) Typical I-V characteristics of the PZT/STO/Si(001) sample; (b) corresponding C-V characteristic at f=1MHz for the sample grown in atomic oxygen ambience. The electrode area is 100μm×100μm.

IV.4) Ferromagnetism: La$_{2/3}$Sr$_{1/3}$MnO$_3$/SrTiO$_3$/Si(001)

Perovskite manganites [(RE)$_{1-x}$(AE)$_x$MnO$_3$, where RE and AE are rare earth and alkaline earth respectively] form an interesting class of compounds where the interplay between metal-insulator and ferromagnetic transitions results in a variety of fascinating properties such as colossal magnetoresistance (CMR)[40,41]. The origin of ferromagnetism in these materials is the double exchange interaction[42] which leads to a strong correlation between magnetization and charge transport properties. Recent years they have received considerable research interests[43,44,45,46] owing to their unique properties leading to potential applications in magnetic, magnetoelectronic, photonic devices, infrared detector, as well as spintronic technology. La$_{2/3}$Sr$_{1/3}$MnO$_3$ (LSMO) is one of the perovskite manganites which show a colossal magnetoresistance and is expected to have a spin polarization close to 100% half metal. In addition, its Curie Temperature (T$_C$) is above 300K (namely 360 K), thus potentially leading to devices operated at room temperature.

The integration of CMR manganites on the semiconducting materials (such as on Si) can lead to potential device applications that utilize both information processing and data storage

in the same device. However, the direct integration of such materials remains a challenging work due to large substrate (a_{Si}=5.431Å) and film lattice mismatch (a_{LSMO}=3.8~3.9 Å), mechanical and chemical disaccords arising from the structural dissimilarities. The STO epitaxial film could serve as a good buffer layer to integrate LSMO film on Si substrate.

30nm-thick $La_{2/3}Sr_{1/3}MnO_3$ film is epitaxially grown on a 1.6nm-STO/Si(001) template by PLD at 600°C and 120mTorr O_2 partial pressure following with a cooling process in O_2 atmosphere of 300mTorr. The 2θ/ω scan around Si 004 reflection exhibits that intense sharp LSMO *00l* peaks appear along with Si (004) peak (Figure IV. 36), suggesting a high quality single crystalline LSMO film on the substrate. The phi scans reveals the epitaxial relationship between the heterostructure: [110] LSMO (001) // [110] STO (001) // [100] Si (001).
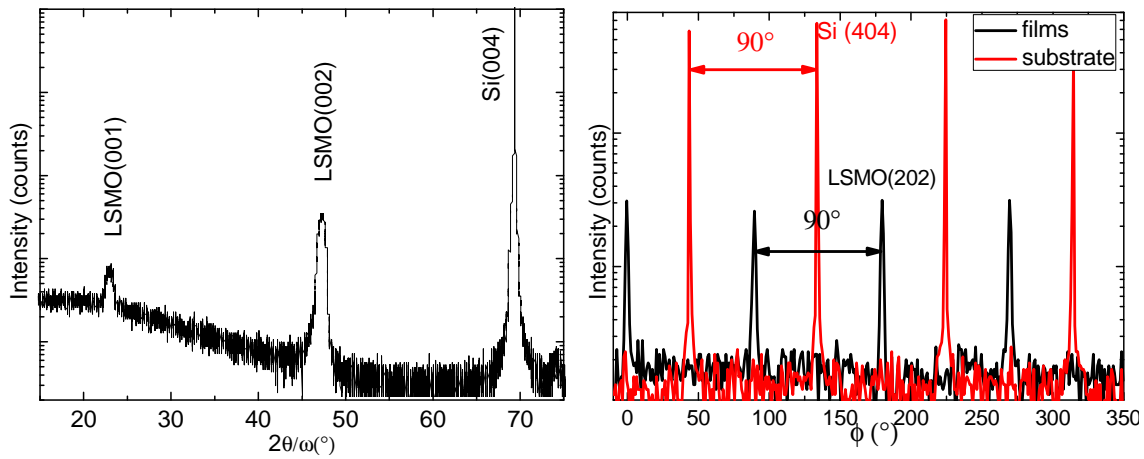
Figure IV. 36 (Left) Typical 2θ/ω scan around Si(004) Bragg condition; (right) phi scans with the Si(404) and LSMO (202) Bragg conditions.

Figure IV. 37 shows a 500nm×500nm AFM image of the LSMO film on the STO/Si pseudo-substrate, which indicates its atomic flat surface with RMS=1.15nm. Despite the difference of thermal dilatation coefficients between silicon and LSMO, the film has no crack after cooling, which confirms the good crystalline quality of the CMR layer.

Rocking curve measurements give information on the spread of the c-axis distribution relatively to the substrate normal. A FWHM of about 0.5° is obtained (not shown here). This value is significantly lower than the one measured for LSMO films deposited on complex buffer stacks such as $Bi_4Ti_3O_{12}/CeO_2$/yttria-stabilised-zirconia buffered Si(001) substrates (FWHM of 1.2°)[47].

Figure IV. 38 displays a Conductive AFM (C-AFM) measurement for the LSMO/STO/Si structure. The hysteresis characteristic of the I-V curve between Si and LSMO electrode (left panel) apparently shows a the directional resistance switching according to the polarity of the applied voltage, which is a Resistance Random Access Memory (ReRAM) behavior. Figure IV 38 right panel shows the current map (500nm×500nm) of the LSMO film. Further investigations are needed to understand the origin of such behavior, charge trapping effect at interface, or ReRAM effect in (La,Ca)MnO$_3$ CMR film[48].
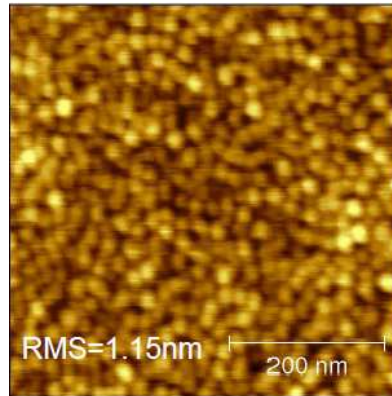
Figure IV. 37 AFM image (500nm×500nm) of 30nm LSMO epitaxial film on STO/Si(001) template.
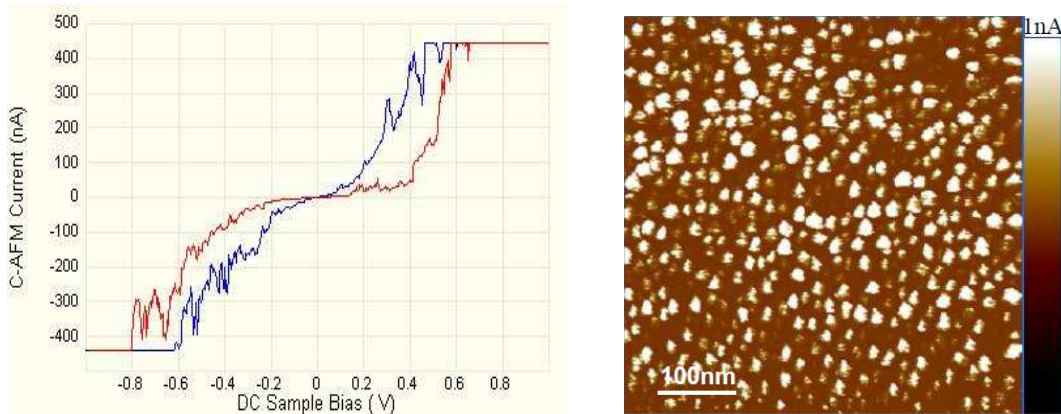
Figure IV. 38 (Left) I-V curve of the LSMO/STO/Si heterostructure and (right) 500nm×500nm current map of the LSMO film.

The resistance variation as a function of the temperature (R-T) is also investigated, as shown in Figure IV. 39. The R-T measurements show a metal-insulator transition temperature higher than room temperature, with a resistivity of 1 mΩ.cm at room temperature. The resistivity at 0K, 0.3 mΩ.cm, is similar to the one measured for LSMO films grown on bulk SrTiO$_3$ substrate[49], which means that the density of bulk defects within the 2 films are close. The LSMO film frown on STO/Si template has same crystallographic and electrical properties

than a film deposited on STO bulk substrate.
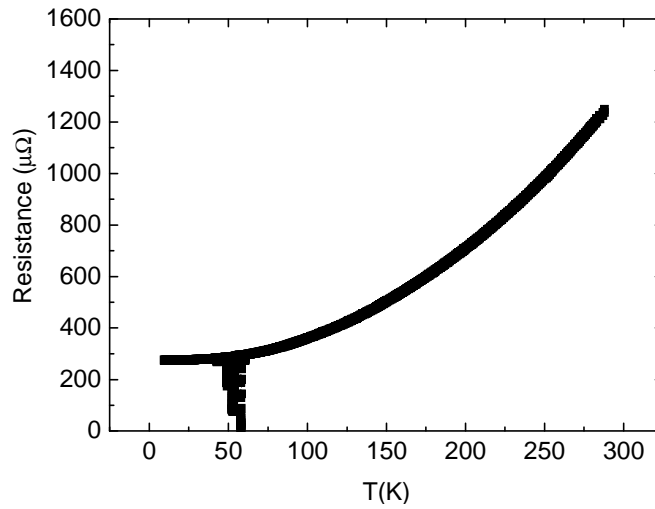
Figure IV. 39 Resistance variation of the LSMO film as a function of the temperature.

The Magneto-Optic Kerr Effet (MOKE) at room temperature (figure IV. 40, left panel) exhibits the ferromagnetic characteristic of LSMO film on Si substrate. Furthermore, a LSMO-STO auto-supported structure that free from the silicon substrate can be realized using the classic silicon etching technique, as shown in the right panel of Figure IV. 40.
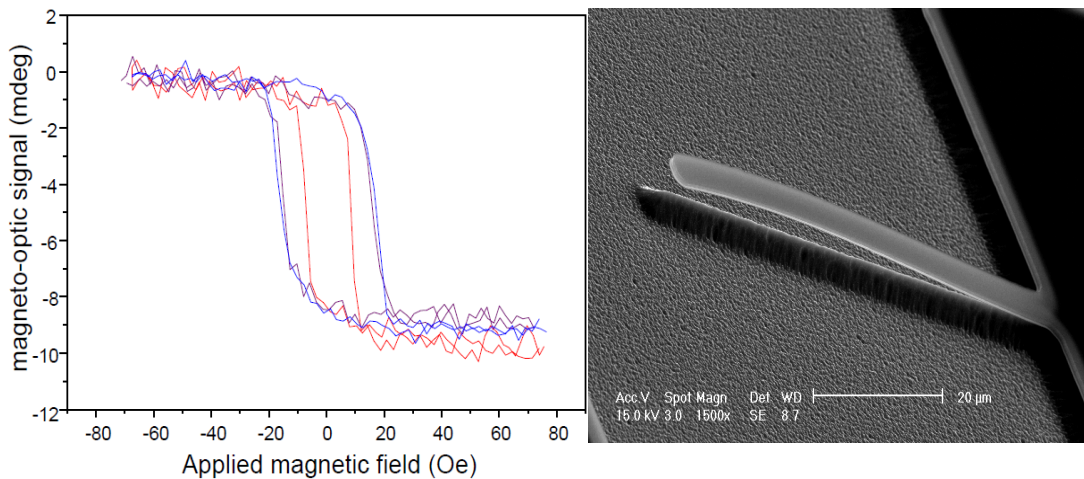
Figure IV. 40 (Left) MOKE measurement of LSMO film and (right) fabrication of the LSMO-STO auto-supported structure.

IV.5) Optoelectronics: Germanium

Due to its high hole mobility, Ge appears as an interesting channel material alternative to Si for high-frequency *p*-MOSFETs. Ge/Si crystalline templates could also be used as templates for the integration of III-V based heterostructures on standard industrial Si wafer thanks to the negligible lattice mismatch between Ge and GaAs (~0.12%). Fabricating such

heterostructures could allow combining high-performance micro- and optoelectronic functionalities on the same silicon basewafer. The direct epitaxy of Ge on Si is challenging: the lattice mismatch between these two materials is about 4.1%, so that threading dislocations are generated in the growing material once the deposited thickness exceeds a critical thickness[50] of a few monolayers. Many strategies have been developed to overcome this difficulty, and the crystalline oxides could serve as a buffer layer for the integration of Ge epitaxial film on Si substrate. In this section, we study the integration of Ge on silicon using the crystalline oxides/Si templates.

IV.5.1) Ge/BaTiO₃/SrTiO₃/Si(001)

Due to the quasi-zero lattice mismatch between Ge ($a_{Ge}/\sqrt{2}$=4.00Å) and BaTiO₃ (3.99 Å) 0.2%, the BTO becomes an interesting buffer layer to for the Ge integration on Si (001).

IV.5.1.1) Growth temperature impact

70ML Ge was grown at a rate of 0.03ML/s in a temperature range between 300°C to 600°C on the BTO film which demonstrates a 2×2 reconstruction after a post growth annealing at 650°C for 30min. The RHEED patterns of Ge layer grown at 300°C , 400°C and 600°C along BTO [100] azimuth are displayed in Figure IV. 41 (a), (b) and (c). It can be seen evidently that the growth of Ge on epitaxial BTO film is indeed of three-dimensional Volmer-Weber-type, suggesting that Ge can not wet the BTO surface, i.e. $\gamma_{Ge}>\gamma_{BTO}+\gamma_{interface}$. A prior TEM study (Figure IV. 41 (d)) of INL on the Ge nanocrystal (NC) on BTO/STO/Si indicates that Ge NC presents large contact angles (sometimes higher than 90°C) and round profile, attesting a large interfacial energy[51]. The Ge growth also presents strong temperature dependence: at temperature less than 300°C the Ge is always polycrystalline and at higher temperatures it is predominantly 100 and 211 oriented, as noted in Figure IV. 41 (b). It should be noted that at the very beginning of the growth at all the temperatures, Ge nanodots shows multi-oriented and 100 and 211 quickly (after 5~10 minutes) become the dominated orientations suggesting they are more favorable than other orientations. However, further deposition of Ge did not change the three-dimensional growth mode but only enhance the augmentation of the Ge crystal size.
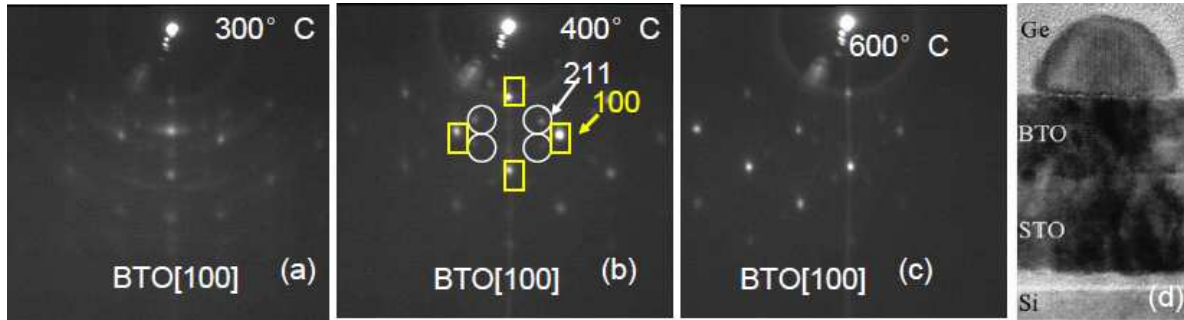
Figure IV. 41   RHEED patterns along BTO[100] azimuth of Ge layers on BTO epitaxial film grown at (a) 300°C, (b) 400°C and (c) 600°C; And (d) a TEM cross-sectional view of the Ge/BTO/STO/Si heterostructure[46].

IV.5.1.2) Surface impact

The crystalline orientation of Ge layer grown on a BTO surface results from a compromise between a minimization of the lattice mismatch (and hence of the interface energy) and a minimization of the surface energy of Ge platelets that are formed before the formation of round-shaped NC[51]. Considering the quite small lattice mismatch between BTO [100] and Ge [100], the surface energy has the determinant influence in the growth of Ge on BTO. Indeed, it has already been widely reported that surface energy plays an important role for the Stranski-Krastanov growth of strained islands for II-VI semiconductors[52] and for nitrides[53].

We deposited 70ML Ge layers at 400°C on different reconstructed BTO surface in order to investigate their impact on the Ge orientations. Figure IV. 42 exhibits the RHEED patterns along BTO[100] azimuth of the Ge layers on Ba-rich, Ti-rich and mixed BTO surfaces. On the Ba-rich BTO surface (left panel) corresponding to a ×2 reconstruction along [110] azimuth and ×1 along [100], the Ge appears to be polycrystalline. Oppositely, on the Ti-rich (corresponding to a ×2 reconstruction along [100] azimuth and ×1 along [110]) and mixed (both are ×1 along [100] and [110]) surfaces, the Ge layers turn out to be predominantly 100 and 211 oriented. The similar behavior is observed for other semiconductors growth on oxides, such as InP/STO system[54].
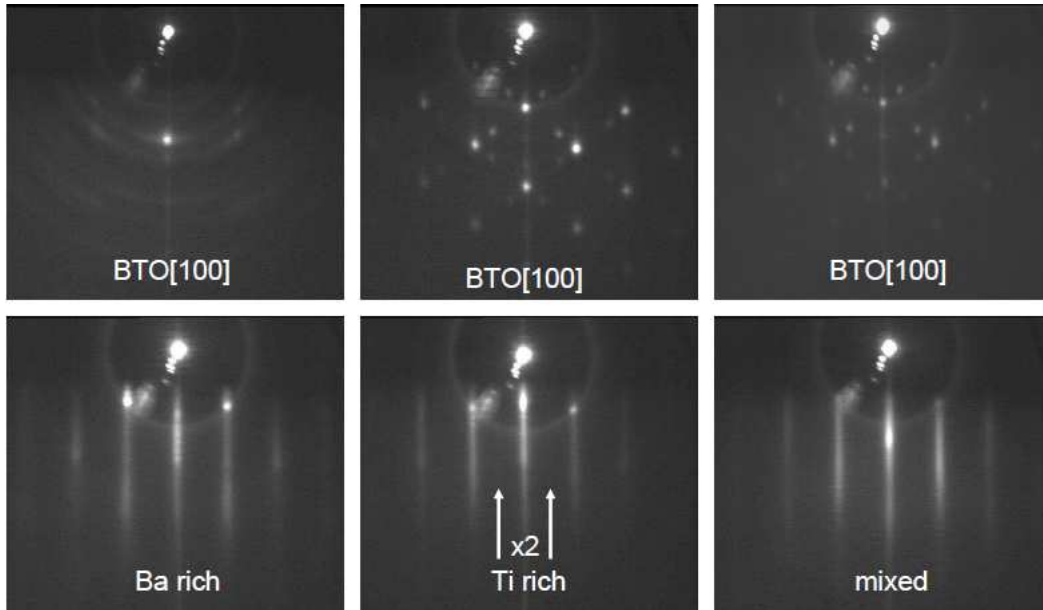
Figure IV. 42 RHEED patterns along BTO [100] azimuth of Ge layers on different reconstructed BTO surfaces.

The objective of this work is to grow a Ge epitaxial layer on the BTO/STO/Si(001) template. However, no complete Ge epi-layer is obtained on the BTO film. For the InP epi-layers realized on STO/Si template (thesis of Jun Cheng, INL 2010), a two-step growth step was employed: high temperature (~500°C), high growth rate (1μm/min) to form single oriented islands (seeds) and low temperature, low growth rate to promote homogeneous coverage of the oxide. Compared with InP/STO system, the Ge epitaxial film deposition on BTO is limited by our Ge growth rate. Due to the too low Ge growth rate (1.2nm/min) we could attain using our MBE Knudsen cell, the single oriented (100 oriented) islands cannot be realized in a short time thus subsequent growth leads to the simultaneously size augmentation of both oriented islands (100 and 211).

IV.5.2) Ge/Gd$_2$O$_3$/Si(111)

IV.5.2.1) Accommodation and growth mode

Figure IV. 43 shows the evolution of the RHEED pattern (recorded along one of the Gd$_2$O$_3$ <110> azimuths) during Ge growth. Before Ge growth starts, the Gd$_2$O$_3$ surface (Figure IV. 43 (a)) presents well-defined streaky lines and a clear ×4 reconstruction, indicating the good crystal and surface quality of the oxide template. Once Ge growth begins, the pattern turns spotty (Figure IV. 43 (b)) indicating an initial three-dimensional growth in the Volmer-Weber mode. At this stage of the growth, the RHEED pattern is very similar to that

observed in Ref.[55] during the growth of Ge on PrO_2/Si (111) templates, or even to that observed during the growth of InP on Gd_2O_3/Si (111) templates[7]. As explained in Ref.55, this pattern results from the superimposition of the (111)-oriented Ge Bragg peaks and of the diffraction of uncovered oxide regions. After the deposition of 40 nm of Ge, the RHEED pattern starts exhibiting diffraction lines, indicating that the initially formed Ge islands coalesce to form a two-dimensional layer. In Figure IV. 43 (c), a clear ×2 reconstruction of the Ge surface can be observed. At the end of the growth (Figure IV. 43 (d)), the RHEED pattern presents bright streaky lines resulting from the diffraction of a flat and well crystallized Ge epilayer. The Ge surface presents a (3×3) reconstruction, already observed for Ge(111) surfaces, possibly with the impurity of carbon or gadolinium[56].
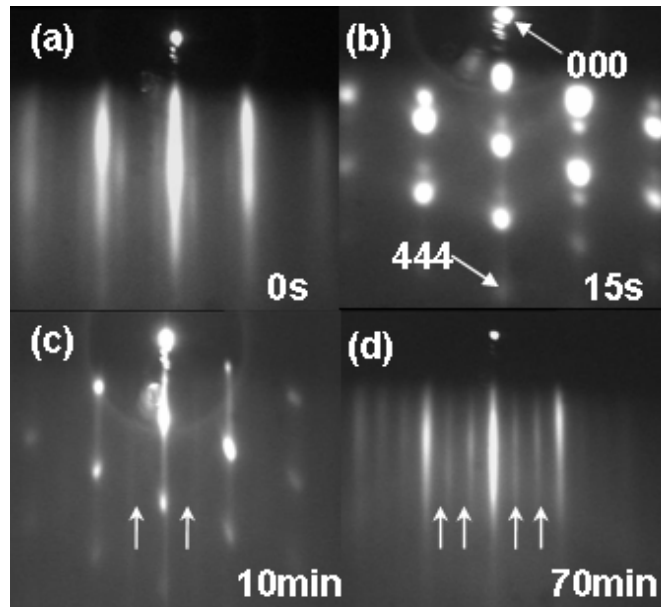
Figure IV. 43 Evolution of the RHEED patterns as a function of Ge thickness. The arrows in (c), (d) highlight the Ge surface reconstructions.

The evolution of the out-of-plane Ge 444 interatomic distance during the early stages of the growth was measured by recording the evolution of distance between the 000 transmitted spot and the 444 Ge reflection spot on the RHEED pattern (as indicated in Figure IV. 43(b)). The result is displayed in Figure IV. 44. The RHEED camera length was calibrated assuming that the Si substrate presents the bulk Si lattice parameter. The Ge 444 interatomic distance remains constant and equals to its value in bulk Ge (≈0.82 Å) during Ge growth. In particular, Ge takes its bulk lattice parameter as soon as it can be measured by RHEED. This behavior has already been observed for several semiconductor/oxide systems[57,58]. For standard mismatched IV-IV or III-V systems, the growing material takes the in-plane lattice parameter

of the substrate at the early stages of the growth, and undergoes a plastic relaxation process during which it progressively recovers its bulk lattice parameter at the expense of the formation of threading dislocations. In contrast here, Ge takes its bulk lattice parameter as soon as growth begins. The lattice mismatch between Ge and Gd_2O_3 is fully accommodated by forming interface dislocations confined at the heterointerface, as described in Ref. 57 for the InP/Gd_2O_3 system or in Ref. 58 for the $InP/SrTiO_3$ system.
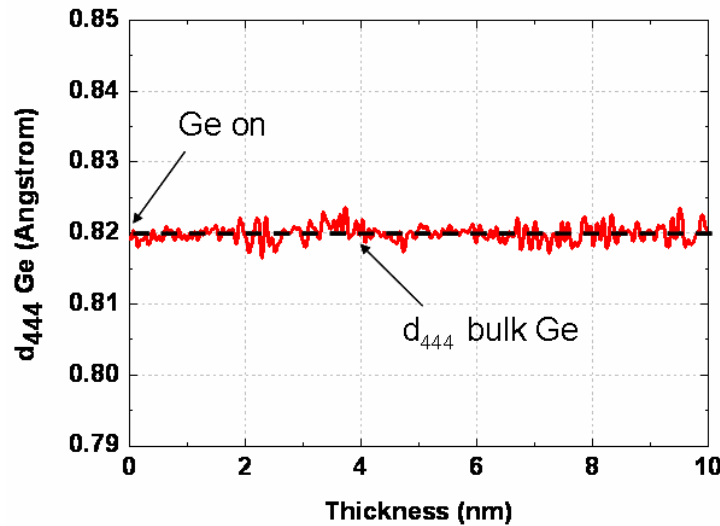
Figure IV. 44 Evolution of the 444 interatomic distance during the early stages of the Ge growth. d_{444} remains constant (~0.82Å) and equals to its value of bulk Ge.

IV.5.2.2) Epitaxial relationship and evidence for twin formation in the Ge layer

X-Ray pole figures were recorded on the sample. For that purpose, the X-ray incident beam was point focused onto a $10mm^2$ area using a poly-capillary lens and crossed slits. A Ge 111 pole figure is shown in Figure IV. 45 (a). On this figure, the radial scale corresponds to the polar angle (ψ), while the azimuthal incidence (ϕ) varies along the perimeter. The 2θ angle was fixed at 27.28° which corresponds to the Ge 111 Bragg angle. Thus, all the visible reflections on the pole figure correspond to the diffraction of planes with interplanar distances close to Ge {111} planes. The coordinates of these reflections allow orientating the different Ge variants with respect to each other in the real space. Additionally, for each reflection in the pole figure of Figure IV. 45 (a), defined by its polar and azimuthal angles, rocking curves where recorded in order to scan the reciprocal space, measure the lattice parameters, and thus detect the different layers of the heterostructure, namely the Si substrate, the Gd_2O_3 template and the Ge layer and determine their relative orientations. Some of these rocking curves are plotted in Figure IV. 46. Using these rocking curves, the pole figure of figure IV. 45 (a) has

been fully indexed.
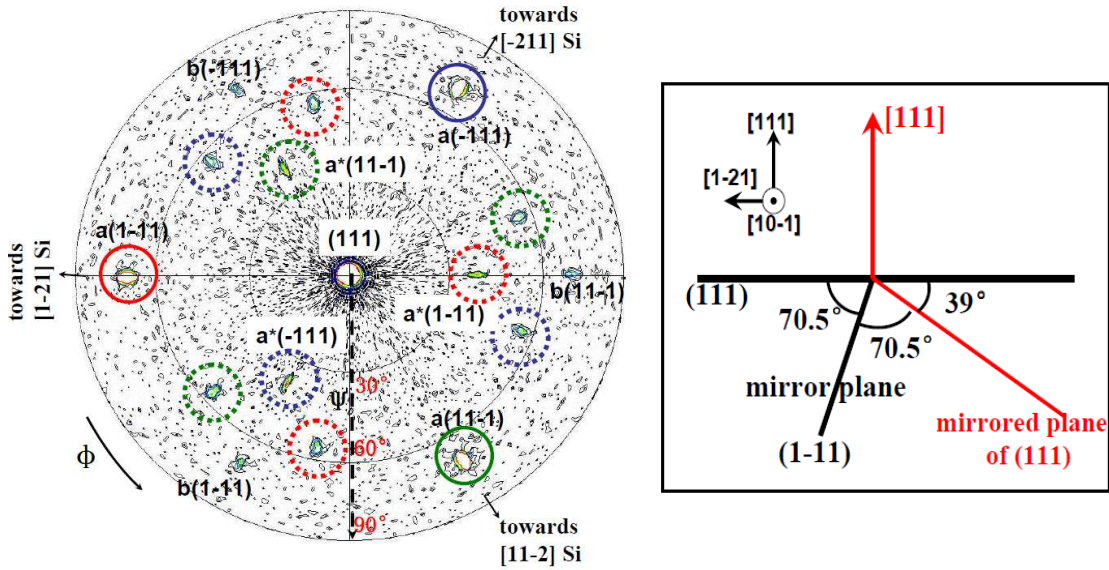
Figure IV. 45 (a) X-ray pole figure recorded near the 111 Si reflections on the sample of Ge/Gd$_2$O$_3$/Si (111). (b) Sketch of the twinning sequence for one of the Ge {111} plane family.

The spot in the center labeled (111) (symmetric conditions) indicates that Ge is (111)-oriented (same out-of-plane orientation as the Si substrate). The three-fold symmetric reflections located at $\psi = 70°$ and $\phi = 60°$, 180° and 300° and labeled a(-111), a(1-11) and a(11-1) correspond to the main variant of the Ge crystal, designated as variant a. The other reflections in the pole figure correspond to the presence of twinned Ge variants in the layer. The set of low-intensity three-fold symmetric reflections at $\psi = 70°$ and $\phi = 0°$, 120° and 240° (labeled b(-111), b(1-11) and b(11-1)) indicate the presence of a second Ge variant in the layer (labeled variant b), twisted of 60° around the Ge (111) vertical direction with respect to variant a. This variant b corresponds to the presence of the twinning with respect to the Ge(111) surface. The mirror planes of these microtwins are the (-111), (1-11) and (11-1) Ge inclined planes respectively. Simple geometric considerations allow concluding that the other reflections in the pole figure result from the presence of twins in the Ge layer. The reflections marked by red, green and blue dotted circles correspond to the twinning of the Ge(111) surface plane relatively to the Ge (1-11), (11-1) and (-111) inclined plane, respectively. This twinning sequence is sketched in the figure IV. 45 (b) for the Ge (1-11) plane. On this figure, the trace of the (111) and (1-11) Ge planes are plotted in the (10-1) Ge plane. In this plane, the symmetric of the Ge (111) plane with respect to the trace of the Ge (1-11) planes (mirror plane) is labeled (1-11)*. It forms an angle of 39° with respect to the Ge

(111) planes. These planes, corresponding to the twin of the Ge (111) planes with respect to the Ge (1-11) planes lead to the observation of a Ge 111 reflection in the pole figure, at ψ = 39° and ϕ = 0°. This reflection is marked with a dotted red circle and labeled a*(1-11) in figure IV. 45 (a). Similarly, a*(11-1) and a*(-111) correspond to the twinning of the Ge(111) surface plane relatively to the (11-1) and (-111) Ge planes. The other secondary reflections located at ψ = 56° correspond to the twinning of the Ge (1-11), (11-1) and (-111) inclined plane relatively to each other. Such twins have already been observed by Schroeder *et al.* during the growth of Ge on Pr_2O_3[59]. Their formation has been interpreted as occurring during the coalescence of the initially formed Ge islands, due to the presence of facets at the surface of these islands.

The ω-2θ rocking curves recorded around the Ge 111, a11-1, b11-1 and a1-11* reflections of the pole figure of Figure IV. 45 (a) are plotted in Figure IV. 46. The rocking curve recorded around the Ge 111 symmetric reflection presents two well resolved peaks centered at ω = 13.65° (Ge 111 reflection) and ω = 14.25° (Si 111 reflection). This confirms that the Ge layer presents the same (111) out of plane orientation as that of the Si substrate. The rocking curves recorded around the Ge a11-1 reflection also present two peaks corresponding to a Ge 111 and a Si 111 reflection, respectively. This indicates that the in-plane orientation of the Ge variant a is the same as that of the Si substrate. The rocking curves recorded around the Ge b11-1 (Ge variant b) presents a significantly different shape: the intensity of the Ge 111 peak is 1700 times smaller than that of variant a. Since all the peaks correspond to reflections with the same 111 structure factor and with the same geometrical angle ψ, the diffracted intensities can be directly compared to quantify the proportion of the two variants. This indicates that 0.06 % of the Ge layer is twisted of 60° around the (111) vertical direction with respect to the Si substrate. The Si 111 reflection is not detected on this rocking curve, as expected for a single crystalline and single domain substrate. The peak centered at ω = 14.38° is a 111 reflection of the Gd_2O_3 layer. The Gd_2O_3 lattice is rotated of 60° around the (111) vertical direction with respect to the Si substrate, as already shown in Ref [60] and [61]. In the end, the rocking curve recorded around the secondary a1-11* Ge reflection s at ψ=36° and 59° only presents a Ge 111 reflection, showing that only the Ge crystal is twinned with respect to {111} asymmetric planes. Since the geometrical angles differ, the quantification of these secondary twinned variants is not possible. Nevertheless, the intensity in these rocking curves is several orders lower than the intensity of the rocking

curves collected at $\psi=70°$ for the main variant a. This qualitatively indicates that only a few part of the Ge material is twinned with respect to {111} asymmetric planes.
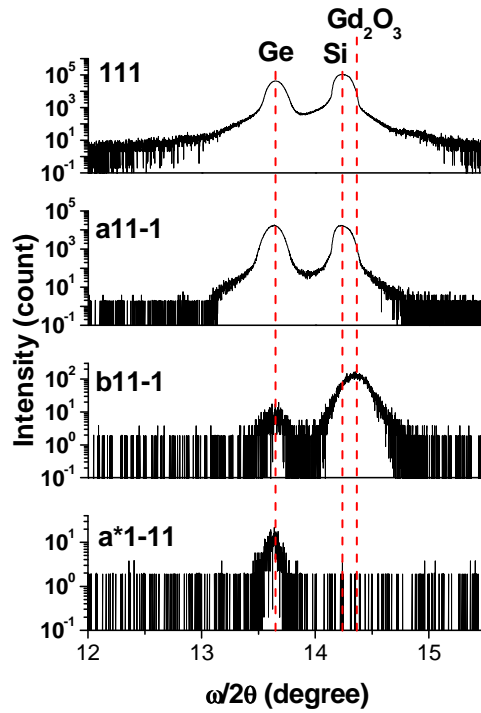
Figure IV. 46 Rocking curves corresponding to the spots in the X-ray pole figure Figure IV. 45(a).

The results discussed in this section allow determining the relative orientations of the layers in Ge/Gd$_2$O$_3$/Si heterostructure (Figure IV. 47). The epitaxial relationship between Ge, Gd$_2$O$_3$ and Si can be defined as [1-10]Ge (111)//[-110]Gd$_2$O$_3$ (111)//[1-10]Si (111). Only 0.06% of the Ge material is twisted around the (111) vertical direction with respect to the main Ge variant, and a very few part of the Ge material is twinned with respect to asymmetric (111) planes.
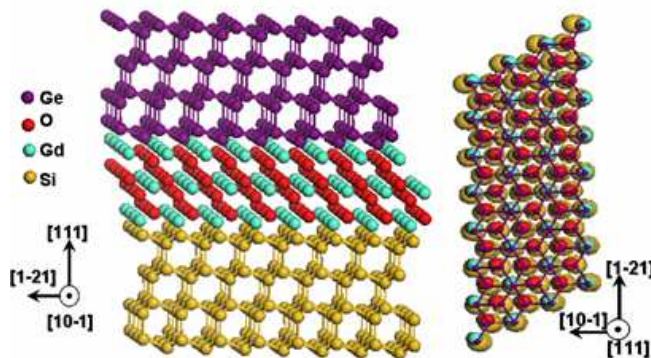
Figure IV. 47 Schematics of the Ge/Gd$_2$O$_3$/Si stack, cross-section view (left) and top view (right).

In conclusion, we have demonstrated that crystalline Gd_2O_3/Si (111) templates could be used for the integration of Ge on silicon. Germanium grows in the Volmer-Weber mode and takes its lattice parameter as soon as growth begins, as already observed for several highly dissimilar semiconductor/oxide systems. 0.06% of the Ge material is twisted of 60° around the vertical (111) direction, and a few part of the Ge material is twinned with respect to the {111} asymmetric planes.

IV.6) Conclusion

Based on the oxides/Si heterostructures, various functionalities have been integrated on the same silicon substrate.

The outstanding dielectric quality of Gd_2O_3 epitaxial film on silicon is in good agreement with the recommendation of the ITRS for the sub-22nm nodes technology, which make Gd_2O_3 as a competitive candidate for the high-κ gate insulator alternative. The PDA treatments can effectively improve the quality of the Gd_2O_3 films.

The STO coherently grown on silicon shows a good rectifying characteristic at room temperature. The STO/Si system can serve as a template to integrate ferroelectric films such as BTO on silicon. The oxygen defects in the BTO films tremendously influence both their structural and electrical properties, due to which the BTO film grown by MBE method does not exhibit ferroelectricity but rectification characteristic. A ferroelectric BTO epitaxial layer is obtained on silicon substrate by combining the MBE and PLD (much higher oxygen partial pressure can be achieved in the chamber) deposition methods.

Using PLD or sol-gel methods, ferroelectric epitaxial films such as PMN-PT and PZT are obtained on STO/Si template. The MFIS structures demonstrate good device quality for the application of the FeRAM application.

Ferromagnetic LSMO layer is also integrated on silicon substrate using STO buffer layer. The MFIS structure based on room temperature superconductive LSMO epitaxial layer shows good I-V characteristic that can be used for ReRAM application. Furthermore, a LSMO-STO auto-supported structure that free from the silicon substrate is realized using the classic silicon etching technique.

Germanium crystalline films are also integrated on silicon using oxides/Si template for the optoelectronic application. Ge shows nonocrystal feature on BTO/STO/Si surface due to the limit growth rate determined by our MBE configuration. A high quality single crystalline Ge epitaxial layer is realized on Gd_2O_3/Si (111) template with quite few twinned parts.

Finally, we have demonstrated that our crystalline oxide/Si templates can be successfully used for the integration of functional materials on silicon.

IV.7) Reference

[1] J. C. Ranuarez, M. J. Deen, C.-H. Chen, "*A review of gate tunneling current in MOS devices*", Microelectronics Reliability **46**, 1939 (2006)

[2] Thesis of L. Becerra, "*Hétérostructures et dispositifs microélectronique à base d'oxydes high-κ préparés sur silicium par EJM*", Ecole Central de Lyon, France, (2008)

[3]. H. D. B. Gottlob, T. Echtermeyer, M. Schmidt, T. Mollenhauer, J. K. Efavi, T. Wahlbrink, M. C. Lemme, M. Czernohorsky, E. Bugiel, A. Fissel, H. J. Osten, H. Kurz, "*0.86-nm CET Gate Stacks With Epitaxial Gd_2O_3 High-κ Dielectrics and FUSI NiSi Metal Electrodes*", IEEE Electron Device Lett. **27**, 814 (2006)

[4]. Y. Li, N. Chen, J. Zhou, S. Song, L. Liu, Z. Yin and C. Cai, "*Effect of the oxygen concentration on the properties of Gd2O3 thin films*", J. Cryst. Growth, **265**, 548 (2004)

[5] International Technology Roadmap for Semiconductors 2008 (ITRS), <http://www.itrs.net/Links/2008ITRS/Home2008.htm>.

[6] Vanessa Capodieci, thesis, "*Molecular Beam Deposition (MBD) and Characterisation of High-κ Material as Alternative Gate Oxides for MOS-Technology*", UNIVERSITÄT DER BUNDESWEHR MÜNCHEN (2005)

[7] S. M. Sze, Physics of Semiconductor Devices, Wiley, New York, (1981)

[8] Thesis of C. Merckling, "*Croissance epitaxiale d'oxydes high k sur silicium pour CMOS avancé : $LaAlO_3$, Gd_2O_3, and γ- Al_2O_3*", France, (2007)

[9] J. H. Haeni, P. Irvin, W. Chang, R. Uecker, P. Reiche, Y. L. Li, S. Choudhury, W. Tian, M. E. Hawley, B. Craigo, A. K. Tagantsev, X. Q. Pan, S. K. Streiffer, L. Q. Chen, S. W. Kirchoefer, J. Levy and D. G. Schlom, "*Room-temperature ferroelectricity in strained $SrTiO_3$*", Nature **430**, 758 (2004).

[10] K. J. Choi, M. Biegalski, Y. L. Li, A. Sharan, J. Schubert, R. Uecker, P. Reiche, Y. B.

Chen, X. Q. Pan, V. Gopalan, L.-Q. Chen, D. G. Schlom, C. B. Eom, "*Enhancement of Ferroelectricity in Strained BaTiO$_3$ Thin Films*", Science **306**, 1005 (2004).

[11] P. M. Warusawithana, C. Cen, C. R. Sleasman, C. J. Woicik, Y. Li, L. F. Kourkoutis, J. A. Klug, H. Li, P. Ryan, L. P. Wang, M. Bedzyk, D. A. Muller, L. Q. Chen, J. Levy and D. G. Schlom, "*A ferroelectric oxide made directly on silicon*", Science, **324**, 367 (2009)

[12] N. Shanthi and D. D. Sarma, "*Electronic structure of electron doped SrTiO$_3$: SrTiO$_{3-\delta}$ and Sr$_{1-x}$La$_x$TiO$_3$*", Phys. Rev. B **57**, 2153 (1998).

[13] D. A. Crandles, B. Nicholas, C. Dreher, C. C. Homes, A. W. McConnell, B. P. Clayman, W. H. Gong, and J. E. Greedan, "*Optical properties of highly reduced SrTiO$_{3-x}$*", Phys. Rev. B **59**, 12842 (1999).

[14] P. Calvani, M. Capizzi, F. Donato, S. Lupi, P. Maselli, and D. Peschiaroli, "*Observation of a midinfrared band in SrTiO$_{3-y}$*", Phys. Rev. B **47**, 8917 (1993).

[15] A. Leitner, C. T. Rougers, J. C. Price, D. A. Herman, and D. R. Herman, "*Pulsed laser deposition of superconducting Nb-doped strontium titanate thin films*", Appl. Phys. Lett. **72**, 3065 (1998).

[16] S. Gopalan, V. Balu, J. H. Lee, J. Hee-han, and J. C. Lee, "*Study of the electronic conduction mechanism in Nb-doped SrTiO$_3$ thin films with Ir and Pt electrodes*", Appl. Phys. Lett. **77**, 1526 (2000).

[17] Z. Luo, J. H. Hao and J. Gao, "*Rectifying characteristics and transport behavior of SrTiO$_{3-\delta}$(110)/p-Si (100) heterojunctions*", Appl. Phys. Lett., **91**, 062105 (2007)

[18] K. Zhao, Y. Huang, Q.Zhou, K. Jin, H. Lu, M. He, B. Cheng, Y. Zhou, Z. Chen, and G. Yang, "*Ultraviolet photovoltage characteristics of SrTiO3−d /Si heterojunction*", Appl. Phys. Lett., **86**, 221917 (2005)

[19] F. Jona and G. Shirane, "Ferrolectric Crystals", Macmillan, New York, (1962)

[20] M. T. Buscaglia, M. Viviani, V. Buscaglia, L. Mitoseriu, A. Testino, P. Nanni, Z. Zhao, M. Nygren, C. Harnagea, D. Piazza, and C. Galassi, "*High dielectric constant and frozen macroscopic polarization in dense nanocrystalline BaTiO$_3$ ceramics*", Phys. Rev. B, **73** 064114 (2006)

[21] K. Ueda, H. Tabata, and T. Kawai, "*Coexistence of ferroelectricity and ferromagnetism in BiFeO$_3$–BaTiO$_3$ thin films at room temperature*", Appl. Phys. Lett. **75,** 555 (1999).

[22] Y. Yano, K. Iijima, Y. Daitoh, T. Terashima, Y. Bando, Y. Watanabe, H. Kasatani, and H. Terauchi, "*Epitaxial growth and dielectric properties of BaTiO$_3$ films on Pt electrodes by*

reactive evaporation", J. Appl. Phys. **76**, 7833 (1994).

[23] Y. Fukuda, H. Haneda, I. Sakaguchi, K. Nuwata, K. Aoki, and A. Nishimura, "*Dielectric Properties of (Ba, Sr)TiO₃ Thin Films and their Correlation with Oxygen Vacancy Density*", Jpn. J. Appl. Phys., Part 2 **36**, L1514 (1997).

[24] T. Tambo, K. Maeda, A. Shimizu, and C. Tatsuyama, "*Improvement of electrical properties of epitaxial SrTiO₃ films on Si(001)-2×1 by in situ annealing*", J. Appl. Phys. **86**, 3213 (1999).

[25] T. Suzuki, Y. Nishi, and M. Fujimoto, "*Analysis of misfit relaxation in heteroepitaxial BaTiO₃ thin films*", Philos. Mag. A **79**, 2461 (1999).

[26] H. P. Sun, W. Tian, X. Q. Pan, J. H. Haaeni, and D. G. Schlom, "*Evolution of dislocation arrays in epitaxial BaTiO3 thin films grown on (100) SrTiO₃*", Appl. Phys. Lett. **84**, 3298 (2004).

[27] G. H. Lee, B. C. Shin, and I. S. Kim, "*Critical thickness of BaTiO₃ film on SrTiO₃ (001)/ evaluated by reflection high-energy electron diffraction*", Mater. Lett. **50**, 134 (2001).

[28] H. Terauchi, Y. Watanabe, H. Kasatani, K. Kamigaki, Y. Yano, T. Terashima, and Y. Bando, "*Structural study of epitaxial BaTiO₃ crystals*", J. Phys. Soc. Jpn. **61**, 2194 (1992).

[29] D. Taylor, "*Thermal Expansion Data. VIII. Complex Oxides, ABO₃, the Perovskites*", Br. Ceram. Trans. J. **84**, 181 (1985)

[30] C. H. Park and D. J. Chadi, "*Microscopic study of oxygen-vacancy defects in ferroelectric perovskites*", Phys. Rev. B **57**, R13961 (1998)

[31] T. Zhao, F. Chen, H. Lu, G. Yang, and Z. Chen, "*Thickness and oxygen pressure dependent structural characteristics of BaTiO₃ thin films grown by laser molecular beam epitaxy*", J. Appl. Phys., **87**, 7442 (2000)

[32] H. Miyazawa, E. Natori, T. Shimoda, H. Kishimoto, F. Ishii and T. Oguchi, "*Relationship between Lattice Deformation and Polarization in BaTiO₃*", Jpn. J. Appl. Phys. **40**, 4809 (2001)

[33] L. E. Cross, "*Ferroelectrics*", **76**, p29, (1987).

[34] A.W. Tavernor, H.-P.S. Li, R. Stevens, "*Production and Characterisation of Composite Relaxor Ferroelectric Multi-layer Structures*", J. Eur. Ceram. Soc. **19**, 1859 (1999).

[35] S.-E. Park, T.R. Shrout, "*Ultrahigh strain and piezoelectric behavior in relaxor based ferroelectric single crystals*", J. Appl. Phys. **82**, 1804 (1997)

[36] E. Fribourrg-Blanc, E. Cattan, D. Remiens, E. Defay, "*PMNT films for integrated capacitors*", Solid State Electron. **47**, 1631 (2003).

[37] M.Detalle,"*Preparation and characterization of ferroelectric films relaxors of PMN-PT*". (2008)

[38] J. Lettieri, thesis, "*Critical issues of complex epitaxial oxide growth and integration with silicon by molecular beam epitaxy*", The Pennsylvania State University, (2002)

[39] B. Jaffe, W. R. Cook, and H. Jaffe, "*Piezoelectric Ceramics*", Academic, London, (1971)

[40] S. Jin, T. H. Tiefel, M. McCormack, R. A. Fastnacht, and R. Ramesh, "*Thousandfold change in resistivity in magnetoresistive La-Ca-Mn-O films*", Science **264**, 413 (1994)

[41] R. von Helmholt, J. Wecker, B. Holszapfel, L. Schultz, and K. Samwer, "*Giant negative magnetoresistance in perovskite-like $La_{2/3}Ba_{1/3}MnO_x$ ferromagnetic films*", Phys. Rev. Lett. **71**, 2331 (1993)

[42] C. Zener, "*Interaction between the d-Shells in the Transition Metals. II. Ferromagnetic Compounds of Manganese with Perovskite Structure*", Phys. Rev. **82**, 403 (1951)

[43] A. Moreo, S. Yunoki, and E. Dagotto, "Phase Separation Scenario for Manganese Oxides and Related Materials", Science **283**, 2034 (1999)

[44] M. Uehara, S. Mori, C. H. Chen, and S.-W. Cheong, "*Percolative phase separation underlies colossal magnetoresistance in mixed-valent manganites*", Nature (London) **399**, 560 (1999)

[45] A. J. Millis, "*Lattice effects in magnetoresistive manganese perovskites*", Nature (London) **392**, 147 (1998)

[46] Y. Tokura and N. Nagosa, "*Orbital Physics in Transition-Metal Oxides*", Science **288**, 462 (2000)

[47] L. Méchin, P. Perna, C. Barone., J.-M. Routoure. and Ch. Simon, "*La0.7Sr0.3MnO3 thin films on Bi4Ti3O12/CeO2/yttria-stabilised-zirconia buffered Si(001) substrates: Electrical, magnetic and 1/f noise properties*', Materials Science and Engineering B **144**,73 (2007)

[48] R. Fors, S. I. Khartsev, and A. M. Grishin., "*Giant resistance switching in metal-insulator-manganite junctions: Evidence for Mott transition*", Phys. Rev. B **71**, 045305 (2005)

[49] A.-M. Haghiri. and J.-P. Renard, 'CMR manganites: physics, thin films and devices', *J. Phys. D : Appl. Phys.* 36,.R127 (2003)

[50] R. People and J. C. Bean, "*Calculation of critical layer thickness versus lattice mismatch for Ge_xSi_{1-x}/Si strained‐layer heterostructures*", Appl. Phys. Lett. **47**, 322 (1985)

[51] L. Largeau, G. Patriarche, G. Saint-Girons, G. Delhaye, and G. Hollinger, "*Self-assembled Ge nanocrystals on $BaTiO_3$ /$SrTiO_3$/Si(001)*", Appl. Phys. Lett. **92**, 031904 (2008)

[52] F. Tinjod, B. Gilles, S. Moehl, K. Kheng, and H. Mariette, "*II–VI quantum dot formation induced by surface energy change of a strained layer*", Appl. Phys. Lett. **82**, 4340 (2003).

[53] B. Damilano, N. Grandjean, F. Semond, J. Massies, and M. Leroux, "*From visible to white light emission by GaN quantum dots on Si(111) substrate*", Appl. Phys. Lett. **75**, 962 (1999).

[54] J. Cheng , P. Regreny, L. Largeau, G. Patriarche, O. Mauguin, K. Naji, G. Hollinger, G. Saint-Girons, "*Influence of the surface reconstruction on the growth of InP on SrTiO₃(001)*", J. Cryst. Growth, **311**, 1042 (2009)

[55] A. Giussani, O. Seifarth, P. Rodenbach, H.-J. Müssig, P. Zaumseil, T. Weisemöller, C. Deiter, J. Wollschläger, P. Storck, and T. Schroeder, "*The influence of lattice oxygen on the initial growth behavior of heteroepitaxial Ge layers on single crystalline PrO₂(111)/Si(111) support systems*", J. Appl. Phys. **103**, 084110 (2008)

[56] G. Profeta and E. Tosatti, "*Novel Electronically Driven Surface Phase Predicted in C/Si(111)*", Phys. Rev. Lett. **95**, 206801 (2005)

[57] G. Saint-Girons and P. Regreny, L. Largeau and G. Patriarche, G. Hollinger, "*Monolithic integration of InP based heterostructures on silicon using crystalline Gd₂O₃ buffers*", Appl. Phys. Lett. **91**, 241912 (2007)

[58] G. Saint-Girons, J. Cheng, P. Regreny, L. Largeau, G. Patriarche and G. Hollinger, "*Accommodation at the interface of highly dissimilar semiconductor/oxide epitaxial systems*", Phys. Rev. B **80**, 155308 (2009)

[59] T. Schroeder, A. Giussani, H. J. Muessig, G. Weidner, I. Costina, Ch. Wenger, M. Lukosius, P. Storck, P. Zaumseil, "*Ge integration on Si via rare earth oxide buffers: From MBE to CVD*", Microelectron. Eng. **86**, 1615 (2009)

[60] T. Schroeder, I. Costina, A. Giussani, G. Weidner, O. Seifarth, C. Wenger, P. Zaumseil, C. Mocuta, T. H. Metzger, D. Geiger, and H. Lichte, "*Self-assembled Ge nanocrystals on high-κ cubic Pr2O₃(111)/Si(111) support systems*", J. Appl. Phys. **102**, 034107 (2007)

[61] A. Fissel, D. Kühne, E. Bugiel and H. J. Osten, "*Cooperative solid-vapor-phase epitaxy: An approach for fabrication of single-crystalline insulator/Si/insulator nanostructures*", Appl. Phys. Lett. **88** 153105 (2006)

General conclusion and perspectives

The oxides materials cover all spectrums of the functional properties: dielectricity, semiconductivity, metallicity superconductivity, non-linear optics, acoustics, piezoelectricity, ferroelectricity, ferromagnetism, etc.

Si-based CMOS technology forms the corner stone of our modern information age. With the continuous scaling of the CMOS feature size, the silica that once was the "standard" oxide in microelectronic industry need imperatively replacing by high-*k* oxides. Crystalline gadolinium oxide turns out to be one of the most promising candidates since it satisfies all the desired requirements for the high-k gate dielectrics selection.

Meanwhile, future "More than Moore" and "Heterogeneous integration" technologies demand more functionalities integrated on the same silicon platform.

In this context, the work completed in this thesis presents the critical aspects towards understanding the growth strategies as well as integration and application issues of heteroepitaxy of crystalline oxides on silicon substrate using Molecular Beam Epitaxy. Substrate-like high quality crystalline $SrTiO_3$ and Gd_2O_3 epitaxial layers were realized on Si and the integration of various functionalinities based on these oxide/Si templates were demonstrated.

The $SrTiO_3$ films growth at different temperatures with a subtle control of oxidant pressure, particularly at the early stages, was investigated by considering both of the kinetic and thermodynamic aspects. The epitaxy "window" exploited for the commensurate growth of $SrTiO_3$ on Si (001) by MBE falls into the regime of the middle temperature and low initial oxidant pressure: ~360°C and initial oxygen partial pressure ~5×10^{-8}Torr. All the structural analysis performed using diverse characterization methods including RHEED, XRD, TEM and T-Hz IR point out that STO films exhibit two-phased structure: a cubic STO phase formed by recrystallization of initially amorphous STO and a tetragonal t-STO phase, which is

already crystalline when the growth begins. The critical thickness for plastic relaxation of strained STO exceeds 24 ML. The origin of the anomalous tetragonality (thus ferroelectricity) in thin STO/Si layers is attributed to O segregation effects (enhanced by the presence of an elevated concentration of O vacancies) at the early stages of the growth.

In order to improve the quality of STO layer grown on silicon substrate, the Si surface passivation engineering has been studied. However, possible alternative passivation strategies such as using Sr_2SiO_4 or $(Ba,Sr)O$ layers turn out not feasible for the coherent growth of high quality STO on Si(001).

The epitaxy of substrate-like STO films has also been explored by comparing several kinetic control deposition processes. In the "2-step" method, the STO film quality shows strong dependence on the buffer STO layer thickness grown in our optimized growth window. As this thickness increases, the STO film demonstrates better crystalline quality. The "recrystallization" method leads to a highly crystallized substrate-like STO/Si layer with a FWHM of 0.14° (for the 50nm-thick film) and an atomic flat surface. The thin SiO_2 interface layer can be attributed to the oxygen diffusion through the buffer layer at the high growth temperature of 550°C.

The electrical properties of the STO layer were also investigated. Our STO films (deposited on *p*-type silicon) shows *n*-type semiconductor behavior due to the oxygen vacancies in the layers and the metal/STO/Si structure thus possesses rectifying current-voltage characteristics.

The second oxide/Si system intensively studied in this thesis was Gd_2O_3/Si(111). The optimal growth conditions (from both structural and electrical points of view) were defined. The Gd_2O_3 epitaxial film thus presents high crystalline quality as well as an abrupt interface with respect to silicon and the growth remains pseudomorphic for a 6.7nm-thick layer. The EOT value of the as-deposited Gd_2O_3 is possible to reach 0.73nm. Various strategies have been used to improve the electrical characteristics of the as-deposited sample. The employment of the atomic oxygen during the growth could effectively decrease the leakage current in the Gd_2O_3 layers. PDA by tubular furnace and RTA can develop the dielectric behavior of the samples. Particularly, the RTA under O_2 atmosphere can effectively reduce the

charge density in the dielectric films while retain almost the same EOT value of the sample.

The ability of STO and Gd_2O_3 to act as a platform for the integration of different functional oxides as well as germanium on silicon has been demonstrated:

• **Piezo-(ferro-)electricity**. The epitaxial growth of high quality monocrystalline **c**-axis oriented BTO on STO/Si (001) using both MBE and PLD methods has been investigated. The oxygen defects in the BTO films play a key role for both the structural and electrical properties. The BTO film grown by MBE (finite oxidant pressure) does not exhibit ferroelectricity but rectification characteristic. A ferroelectric BTO epitaxial layer is obtained on silicon substrate by combining the MBE and PLD deposition methods. Ferroelectric thin films PMN-PT and PZT on STO/Si (001) fabricated by PLD and sol-gel methods respectively were also studied and the corresponding MFIS structures exhibit good memory function for FeRAM application.

• **Ferromagnetism.** The integration of half-metal LSMO on STO/Si (001) template using PLD has been demonstrated. The LSMO layer shows room temperature ferromagnetism and the LSMO-STO-Si heterostructure shows good rectifying current-voltage characteristics that can be used for ReRAM application. A silicon-substrate-free LSMO-STO suspended structure was also realized.

• **Optoelectronics**. The epitaxial growth of germanium on BTO/STO/Si (001) and Gd_2O_3/Si (111) templates were studied. Nanostructures Ge crystallized on BTO/STO/Si surface due to the limit growth rate of our MBE configuration. A high quality single crystalline Ge epitaxial layer was realized on Gd_2O_3/Si (111) template with quite few twin defects by the coalescence of the initial dislocation-free 3D islands.

Based on the results in this thesis, different perspectives can be envisaged in this research field:

• **High-κ gate dielectric CMOS device**

Considering the fabulous electrical characteristics presented by the Gd_2O_3/Si MOS structure, a research on its CMOS process compatibility in MOSFET transistor is envisaged. The possible functional n-MOSFET with epitaxial high-κ Gd_2O_3 gate dielectrics and with Au/Ni electrode is illustrated in figure C. 1.
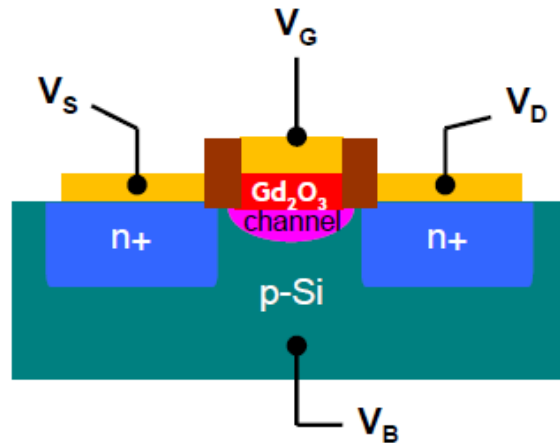
Figure C. 23 Schematic of the p-MOSFET with high-k Gd₂O₃ gate dielectric.

• **Ferroelectric FET device**

The ferroelectric PZT films on STO/Si show good electrical quality. However, complementary studies are needed to further understand the structural (e.g. strain relaxation process) and piezoelectric properties (e.g. the measurement of d_{33}). These studies are onset in the context of the thesis of Shi YIN at INL and LETI (Grenoble). The investigation of PZT on Si is finally towards to the FeFET device application as shown in Figure C. 2
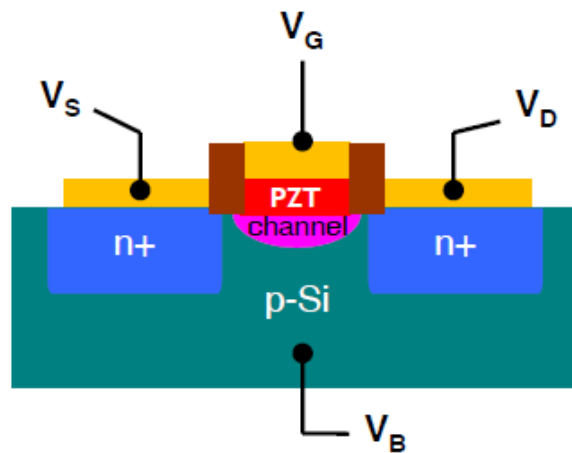

Figure C. 24 Schematic of PZT based FeFET device.

The expertise obtained from the growth of crystalline ferroelectric oxides on silicon substrate can also be extended to other substrate such as germanium. This conception combines the advantages of FeFET and Ge-based high mobility devices and shows promising application for the future monolithic integration technology. We demonstrate our first results (figure C. 3) showing that high quality single crystalline $BaTiO_3$ epitaxial films can be grown on Ge/Si pseudo-substrate, using a Ba-assisted Ge surface passivation and kinetic control "2-step" growth methods.
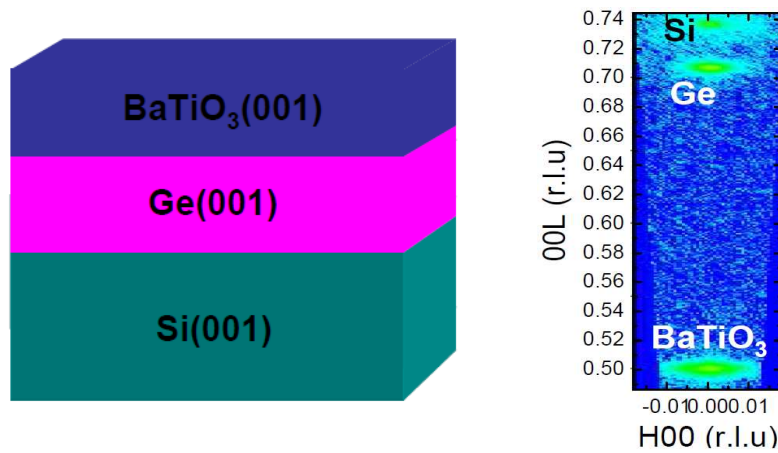
Figure C. 25 Epitaxial growth of crystalline BaTiO₃ layer on Ge/Si pseudo-substrate.

• **Oxide nanoelectronics on silicon**

Based on the STO/Si (001) and Gd_2O_3/Si(111) templates, the integration of new functional oxides on silicon will be an interesting research new area. The investigation of several other functional oxides is ongoing and we demonstrate some interesting first results.

Interfaces between the insulating oxides $SrTiO_3$ and $LaAlO_3$ gained a lot of interest in recent years due to the fact that when LAO is grown on TiO_2-terminated STO, a conductive quasi-two dimensional electron gas (2DEG) exists at the interface. This unique property of LAO/STO can be integrated on Si by growing LAO epitaxial film on STO/Si (001) template, as shown in figure C. 4.

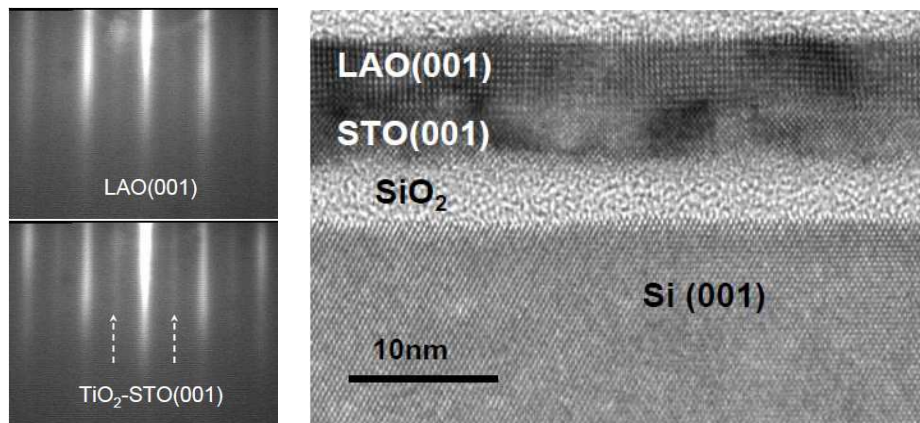*Figure C. 26 RHEED patterns of LAO and TiO_2-terminated STO films along STO(001) azimuth and TEM cross-sectional view of LAO/STO/SiO₂/Si(001) heterostructure.*

Spinel half-metal ferrite $CoFe_2O_4$ (CFO) has been intensively investigated for its wide range of applications such as magnetorestrictive sensors, microwave devices, biomolecular

drug delivery and electronic devices, due to its large magnetocrystalline anisotropy, chemical stability and unique nonlinear spin-wave properties. It has also been considered as an important component for multiferroic multilayers or composites. Figure C. 5 demonstrates the first results of integration of CFO by sputtering on Si substrate (collaboration with ICMAB, Barcelona, Spain) using an oxide buffer layer. It was found that CFO shows polycrystallinity and 3D growth mode on Gd_2O_3/Si(111) and STO/Si (001) templates respectively. However, high quality single crystalline CFO films on Si can be envisaged by optimizing the treatment of the template surface and the growth strategy. As we demonstrated that Metal/STO/Si and Metal/Gd_2O_3/Si junctions show Shottky-type behavior, spin-polarized carries injection in silicon through a tunneling contact can be expected.
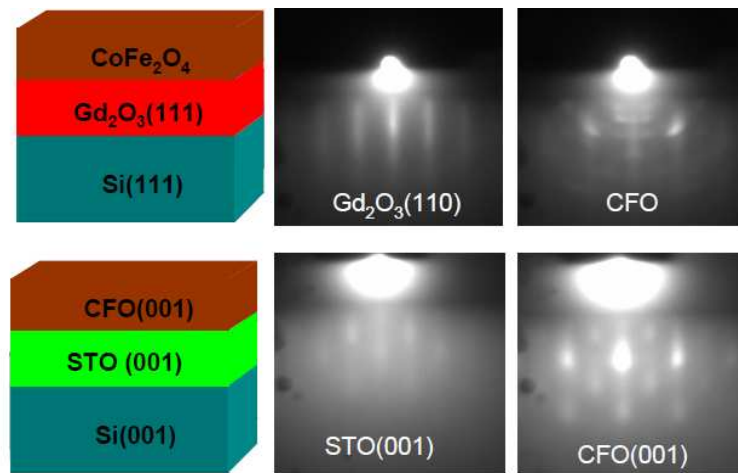

Figure C. 27 Integration of CFO magnetic films on oxide/Si templates.

Vanadium dioxide (VO_2) has a tetragonal *P4/ncc* structure at room temperature. It shows an abrupt and reversible change in its optical and electrical (metal-insulator transition) properties when the temperature is raised beyond a critical point of ~68°C. Films made from this material have a potential to be used in energy efficient "smart" windows with temperature-dependent throughput of solar radiation. We demonstrate the metal-insulator transition by IR spectroscopy (thanks to W. Peng at synchrotron SOLEIL) for VO_2 films grown on our Gd_2O_3/Si(111) template, as shown in Figure C. 6 (collaboration with Prof. Yanagida, Osaka University, Japan).

.

Two characteristic peak (270cm^{-1} and 323 cm^{-1}) disappear (increase of the temperature) or appear (decrease of the temperature) around 65°C, which corresponds to the phase transition of the VO_2 film on Gd_2O_3/Si(111).
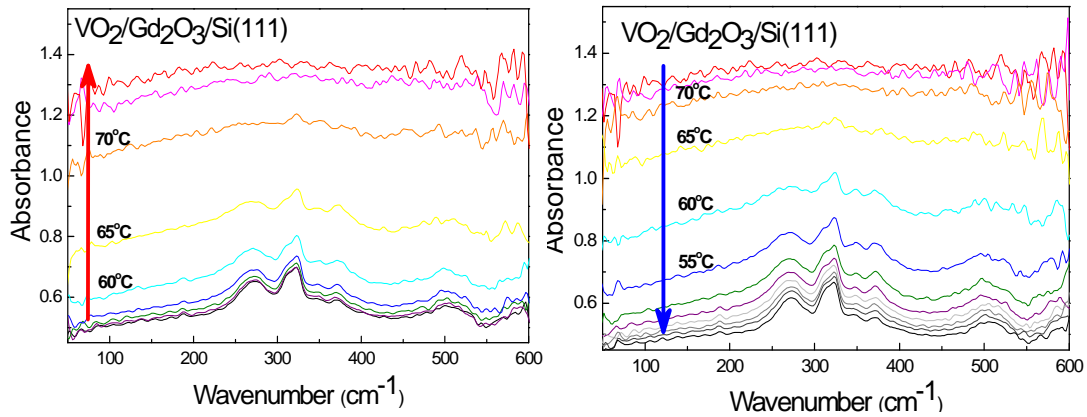
Figure C. 28 IR spectra of VO₂ film on Gd₂O₃/Si(111) of increasing temperature (left) and decreasing (right)respectively.

- **Integration of nanowires on oxide/Si platform**

Since the discovery of the carbon nanotube (CNT), the scientific interests of discovery various nanostructures have been raised. One-dimensional (1D) structures including nanowires, nanobelts and nanowires are supposed to have potential applications to nanoelectronics and optoelectronics, owing to their novel physical properties. The nanowires can also possibly be integration on Si via the oxide buffers.

Magnesium oxide (MgO) is a typical wide-band-gap insulator, having found many applications as catalysis, additives in refractory, paint and superconductor products. We demonstrate first results of the integration of MgO nanowires on Gd₂O₃/Si (111) template, as shown in Figure C. 7 (collaboration with Prof. Yanagida, Osaka University, Japan).
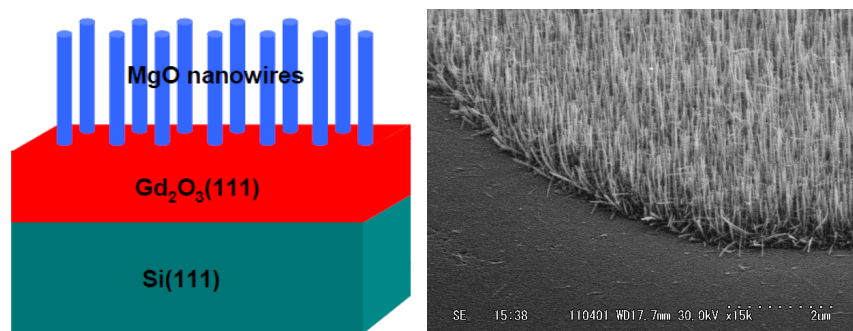
Figure C. 29 Schematic (left) and SEM image (right) of the integration of MgO nanowires on Si (111) substrate via Gd₂O₃ buffer layer.

Khalid NAJI (a parallel thesis at INL) has demonstrated that III-V semiconductor (such as InP) nanowires can be grown on the STO (001) substrate using Vapor-Liquid-Solid (VLS) method. The integration of InP nanowires on Si(001) via STO buffer thus can be expected.

Figure C. 30 The integration of InP nanowires on STO/Si(001) template

Appendix

Appendix A   RHEED

Reflection High-energy Electron Diffraction (RHEED) is a non-destructive technique to check the crystalline structure of the substrate/film surface. This powerf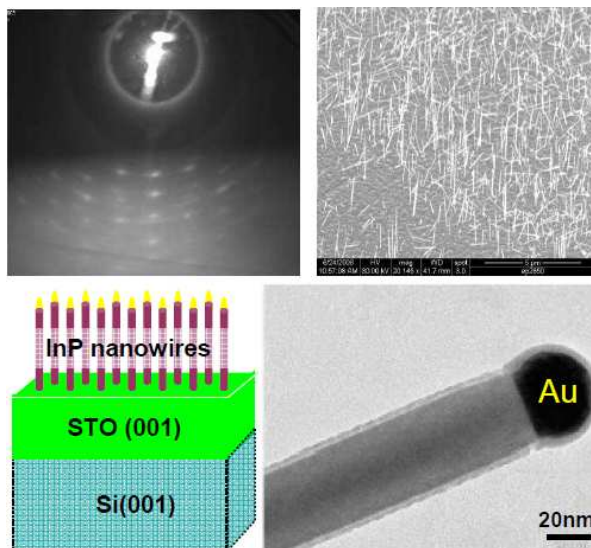ul *in-situ* characterization technique gives important information about the films or surfaces grown with MBE. We will briefly introduce the principle and fundamentals of RHEED as well as the information that can be extracted from this technique.

A. 1 Principle

Figure AA.1 illustrates the typical design for a RHEED experiment. A beam of electrons accelerated by a high tension of 25~30kV is glanced across a surface at low angle (1°~3°). The diffraction pattern then formed on a phosphor screen reflects the surface atomic arrangement. Indeed the component of the electron momentum normal to the surface is very small and the penetration of the beam into the surface is low, being restricted to the outermost few atomic layers, i.e. RHEED gather information only from the surface layer of the sample.
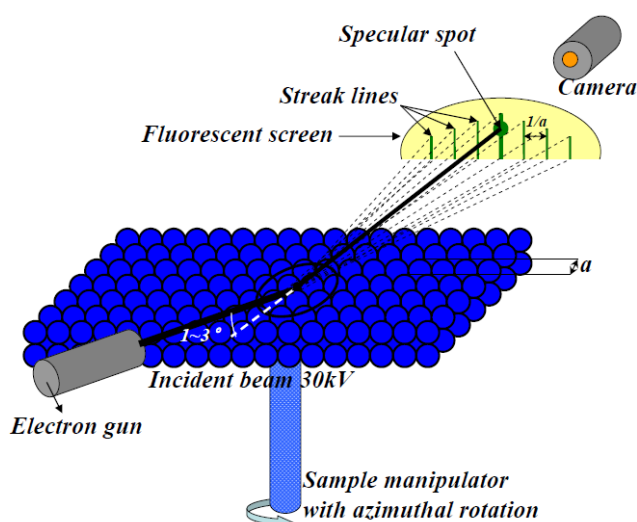

Figure AA.31 Schematic of the experimental principle of RHEED.

A. 2 Fundamentals of Electron Diffraction

To understand the physical origin of the electron diffraction on the screen we firstly recall

the two conceptions: reciprocal lattice and Ewald's sphere.

The crystalline solids are composed a set of identical mesh containing a certain number of atoms called lattice. An infinite three dimensional lattice can be defined by its primitive vectors ($\vec{a_1}, \vec{a_2}, \vec{a_3}$) thus each atom can be represented by a unique vector $\vec{R} = u\vec{a_1} + v\vec{a_2} + w\vec{a_3}$ with u, v and w are integers. The reciprocal lattice is determined by generating the three reciprocal primitive vectors, through the formulas as following:

$$\vec{a_1}^* = 2\pi \frac{\vec{a_2} \times \vec{a_3}}{\vec{a_1} \bullet (\vec{a_2} \times \vec{a_3})} ; \quad \vec{a_2}^* = 2\pi \frac{\vec{a_3} \times \vec{a_1}}{\vec{a_2} \bullet (\vec{a_3} \times \vec{a_1})} ; \quad \vec{a_3}^* = 2\pi \frac{\vec{a_1} \times \vec{a_2}}{\vec{a_3} \bullet (\vec{a_1} \times \vec{a_2})}$$

Therefore the vectors of the reciprocal lattice can be written as: $\vec{G} = h\vec{a_1}^* + k\vec{a_2}^* + l\vec{a_3}^*$ with h, k and l integers. And there exists the relationship between $\vec{G}$ and $\vec{R}$ that belong to the real lattice: $e^{i\vec{G} \bullet \vec{R}} = 1$.

The diffraction condition (Laue condition) is thus defined by:

$(\vec{k'} - \vec{k}) = \vec{G} = h\vec{a_1}^* + k\vec{a_2}^* + l\vec{a_3}^*$.

In a single crystal, the distance between the consecutive parallel and equidistant reticular planes is represented by:

$$d_{hkl} = \frac{2\pi}{\|\vec{G}\|}$$

where h, k, l Miller index designating the orientation of a plane *(h, k, l)* or a direction *[h, k, l]*.

In the case of RHEED diffraction, the penetration of the incident electron beam inside the sample is only several monolayers due to the small grazing angle. The electrons are then diffracted only by the surface atoms. These surface atoms occupy the nodes of a two dimensional network, marked by the translation vectors $\vec{R_{//}} = u\vec{a_1} + v\vec{a_2}$. The Laue condition thereby can be deduced to $(\vec{k'} - \vec{k})_{//} = \vec{G_{//}} = h\vec{a_1}^* + k\vec{a_2}^*$, where h and k are integers. The vectors $\vec{G_{//}}$ form a two dimensional network thereby no restriction exists for the normal component $\vec{G_\perp}$. The vectors $(\vec{k'} - \vec{k})_{//}$ form a group of rods perpendicular to the surface that result from the elongation of the reciprocal lattice spots parallel to the normal direction of the sample. This group of rods is the reciprocal lattice defined by the vectors $\vec{R} = \vec{R_{//}}$.

If no energy is gained or lost in the diffraction process (it is elastic), i.e. $\left\|\vec{k'}\right\| = \left\|\vec{k}\right\| = 2\pi / \lambda$.

The Ewald's sphere with a radius of $2\pi / \lambda$ can be constructed to find the crystallographic properties of the sample surface, the principle of which is illustrated in figure AA.2. The diffraction pattern corresponds to the intersections of the reciprocal rods with the Ewald's sphere.
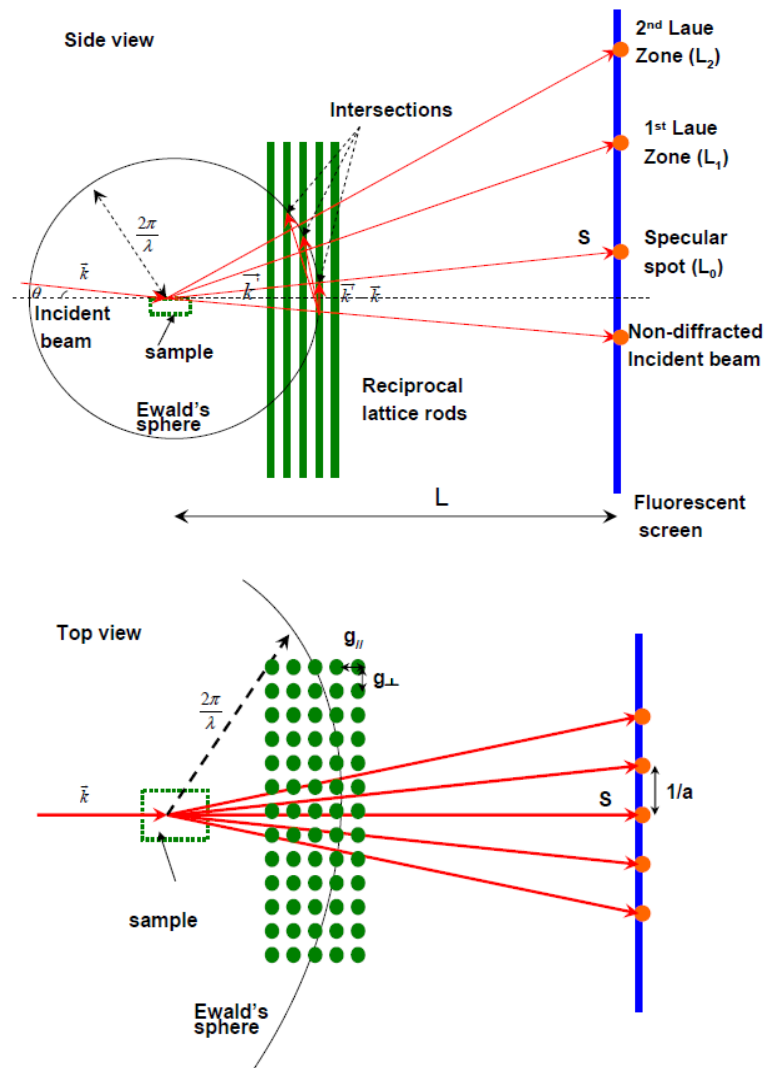

Figure AA.32 Schematic of the principle of RHEED.

A. 3 Information obtained from RHEED

Figure AA.3 shows a RHEED pattern of a Si (111) surface. According to the analysis of this RHEED image, the following information can be obtained:

1) crystallinity;
2) growth mode;
3) surface reconstruction;

4) growth rate;

5) strain relaxation process.
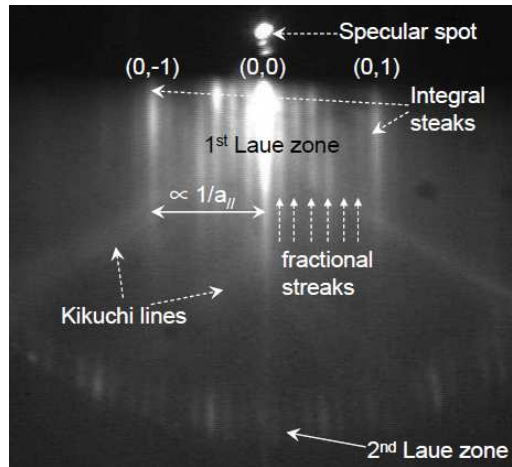
Figure AA.33 An example of RHEED pattern.

A.3.1 Crystallinity

The crystallinity of the growing film can be observed by RHEED, as shown in figure AA.4.
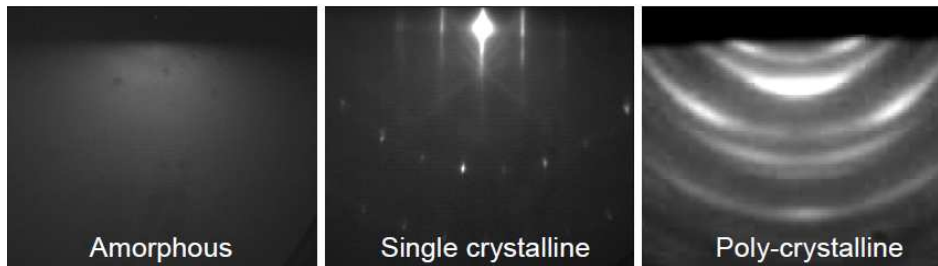
Figure AA.34 The crystallinity of the material observed by RHEED.

For the amorphous materials possessing no order in long distance, RHEED pattern shows a half-circle diffuse halo that is the projection of the Ewald's Sphere. The streak-line feature of the RHEED pattern suggests single crystallinity of the film (or substrate). The streak lines are the projection of the intersection of the reciprocal rods and Ewald's Sphere. The poly-crystalline material, which possesses multi crystalline orientations, displays the Debye-Scherrer rings on the RHEED pattern.

A.3.2 Growth mode

The RHEED pattern can also be used to analyze the growth mode of the crystalline film, as shown in Figure AA.5. When the film is two dimensional with a flat surface, RHEED pattern shows a clear, well-defined steak line feature. The steaks are quite fine accompanied

with some oblique lines - Kikuchi lines - which only appear for a good quality and flat crystalline films. If the surface of the material is rough, RHEED shows the wider steak lines with non-uniformed intensity. For the 3D growth mode, RHEED displays a spotty feature.
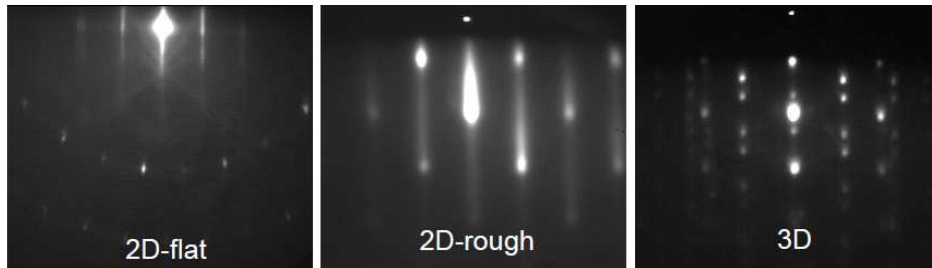
Figure AA.35 The growth mode observed by RHEED pattern.

A.3.3 Surface reconstruction

For a crystal terminated along a given plane, the equilibrium positions of the atoms near the surface will be changed due to the alteration of the force determined by all other atoms in the bulk. Then the surface reconstruction occurs. From the RHEED pattern, we can analyze the surface reconstruction by observe the fractional streaks (Figure AA.3).

A.3.4 Growth rate

In the 2D layer-by-layer growth mode, one can observe the intensity oscillation of the specular spot (Figure AA.6), which is induced by the periodic variation of the surface morphology during the growth of the 2D islands. The intensity of the specular spot displays a dependence of the surface reflectivity which is a function of the inverse of the roughness. The minimum is reached when the surface is half-covered (roughness maximum). Then the roughness decreases again and the reflectivity increases leading to another maximum of the intensity. We thus obtain de growth time for a monolayer film, i.e. the growth rate.
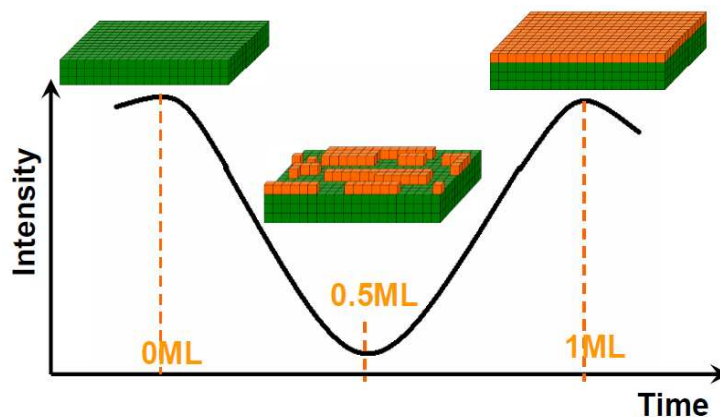
Figure AA.36 Variation of the intensity of the specular spot of RHEED as a function of the coverage of the surface.

A.3.5 Strain relaxation process

The RHEED pattern allows recording the variation of the in-plane lattice parameter $a_{//}$ by measuring the interdistance of the diffraction streak lines, which is inversely proportional to the lattice parameter of the crystalline film lattice. For the 2D layer-by-layer growth, we can study the strain relaxation process by plotting $a_{//}$ as a function of the film thickness. Before the relaxation occurs, the plotting will also oscillate, as shown in Figure AA.7.
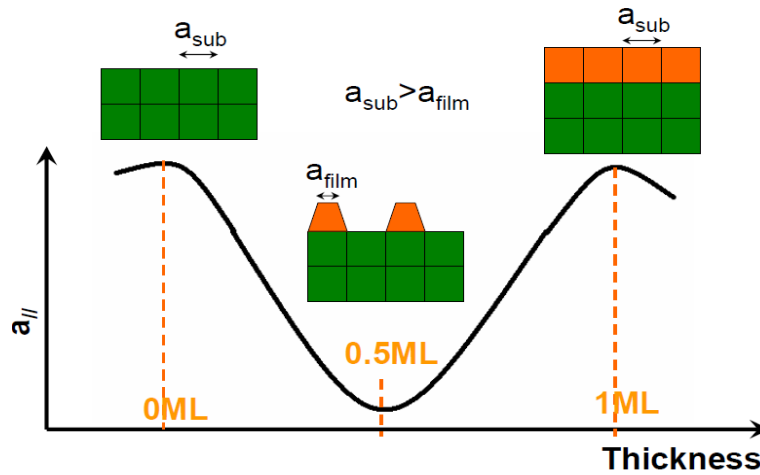
Figure AA.37 Observation of the oscillation of the $a_{//}$ as a function of the film thickness.

In case that $a_{sub} > a_{film}$, the film will tensile strained on the substrate, which imposes clamping effect to the film. When the surface is half-covered, although the lattice parameter of the 2D islands at the bottom will follow that of the substrate, the top of the lattices are free of strain effect, thus a minimum of $a_{//}$ is obtained. Once one monolayer is formed on the substrate, $a_{//}$ increases again to the value of a_{sub}. If the oscillation disappears, the 2D growth mode changes to 3D and the film starts to relax.

Appendix B   AFM

As one of the most widely used Scanning Probing Microscopy (SPM) tools, Atomic Force Microscopy (AFM) technology possesses several unique advantages: (1) no limitation of the sample material (compared to Scanning Tunneling Microscopy); (2) capability to measure a wide range of surface properties including topography, surface potential, electrical and magnetic properties; and (3) it can be performed in diverse environment such in air, water etc. Its resolution in the Z direction is of the order of sub-nanometer, while the lateral is limited by the tip radius of curvature, in the order of few tens of nanometers.

B. 1 Principle

The work principle of AFM is illustrated in Figure AB.1.
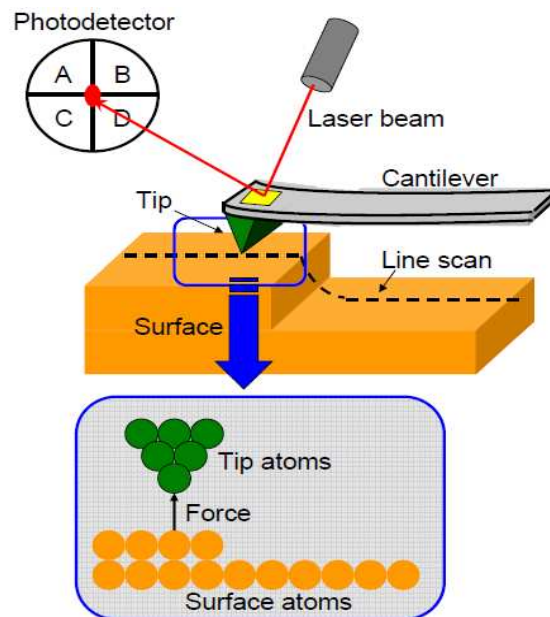
Figure AB.1 Principle of AFM tool

An AFM consists of an extremely sharp tip mounted or integrated on the end of a flexible cantilever. Upon proximity to a surface, the cantilever reacts to the forces between the tip and the investigated surface. Van der Waals force is the dominated atomic force in the interaction. By monitoring the deflection of the cantilever with a feedback loop, the downwards or upwards movement of the probe give the topography of the scanned surface. The deflection of the cantilever is measured by an optical lever mode: a laser light form a solid diode is reflected on the backside of the cantilever and then collected by a photodetector, which

consists of closely spaced photodiodes. Angular displacement of the cantilever leads to one photodiode collecting more light than the other photodiode, producing an output signal. Thus the detector keeps tracking the deflection of the cantilever. The use of a quadrupole photodiode allows separating vertical and lateral contributions of the signal:

Vertical: (A+B)-(C+D)

Lateral: (A+C)-(B+D)

B. 2 Operation modes

B.2.1 Contact mode

In the contact mode, the probe is brought towards the surface by extending the Z scanner. When the tip enters in contact with the surface the cantilever starts bending. The extension of the Z scanner stops when the cantilever deflection reaches the predetermined setpoint, corresponding to a chosen contact force. Scanning over the surface features causes the cantilever deflection to change. The feedback loop regulates the vertical Z scanner position in a way to maintain the deflection constant to the setpoint. The recorded Z scanner movement gives the topography.

The advantages of the contact mode are:
- High scan speed;
- Only AFM technique that can reach atomic resolution;
- More effective on rough surface with extreme changes in vertical topography.

And disadvantages:
- Lateral forces can distort features in the image;
- Forces normal to the tip-sample interaction can be high in air due to capillary forces from the adsorbate layer;
- Lateral forces and high normal forces can result in reduced spatial resolution and damage of soft samples.

B.2.2 Non-contact mode

Non-contact mode is the most widely employed AFM mode. It operates by scanning the probe across the sample surface, while the cantilever is oscillated by a piezo-actuator. Operation can take place in ambient and liquid environments. In the first case the cantilever oscillates at or near its resonance frequency with amplitude ranging typically from 10nm to 100nm. In a liquid, the oscillation need not be at the cantilever resonance. The tip slightly "taps" on the sample surface during scanning, contacting the surface at the bottom of its

swing. Variations in the tip-surface average distance make the oscillation amplitude to change. The feedback loop monitors the RMS of the oscillation, acquired by the photodetector and keeps it constant at the setpoint value by vertical movements of the scanner. Its vertical position at each (x, y) data point is stored to form the topographic image of the sample surface.

With respect to contact mode AFM, non contact-AFM has some advantages:

- Higher lateral resolution on most samples (1nm to 5nm)

- Lower forces and less damage to soft samples imaged in air

- Lateral forces virtually eliminated.

 And one disadvantage:

- A little bit slower scan speed than contact mode.

B. 3 Techniques derived from Contact mode AFM

Some techniques derived from the contact mode AFM are widely used to characterize the electrical properties of the film.

B. 3.1 Conductive AFM

Conductive AFM (C-AFM) allows the characterization of the conductivity variations across conducting and semiconducting materials. The sample is scanned with the tip in contact with the surface at a contact force kept constant by the feedback loop. A DC bias is applied to the tip while the sample is grounded. A linear amplifier senses the current flowing through the sample, with detectable current range of 10pA~1μA. For the current measurements ranging from 100fA to 100pA (adaptable for the measurement of the tunneling current in the oxide thin film), the Tunneling AFM (TUNA) can be employed.

B. 3.2 Piezoresponse Force Microscopy (PFM)

PFM is based on the converse piezoelectric effect. Using the AFM tip as top electrode, an electric field is imposed over the investigated sample, which is usually grown on a bottom electrode. A ferro-(piezo-)electric material changes its sizes in response to the applied field. By changing the vibration orientation of the tip, both in-plane and out-of-plane piezoelectricity of the film surface can be measured.

When the tip is in contact with the surface and the local piezoelectric response of the

sample is detected as the first harmonic component of the tip deflection, the phase φ, of the electromechanical response of the surface yields information on the polarization direction below the tip. For P^- domains (polarization vector oriented normal to the surface and pointing downward), the application of a positive tip bias results in the expansion of the sample, and surface oscillations are in phase with the tip voltage, φ = 0. For P^+ domains, the response is opposite and φ = 180°.

Lateral PFM is a technique where the in-plane component of polarization is detected as lateral motion of the cantilever due to bias-induced surface shearing. The in-plane component of the polarization can be observed by following the lateral deflection of the AFM cantilever, and applying this technique can help to reconstruct the three-dimensional distribution of polarization within domains of ferroelectric single crystals. It is possible to apply this method in order to differentiate 90° and 180° domain switching in $BaTiO_3$ or $PbTiO_3$ thin films.

Provided that the vertical and lateral PFM signals are properly calibrated, the complete electromechanical response vector can be determined, an approach referred to as vector PFM. Finally, electromechanical response can be probed as a function of dc bias of the tip, providing information on polarization switching in ferroelectrics, as well as more complex electrochemical and electrocapillary processes.

Appendix C   XRD

X-Ray Diffraction (XRD) is a technique widely applied for the characterization of crystalline materials. In this technique, interaction of X-rays with the sample creates secondary diffracted beams of X-rays related to interplanar spacings in the crystalline sample according to Bragg's Law.

C. 1 Principle

Figure AC.1 shows the principle of the XRD-Bragg's law. When parallel X-rays strike a pair of parallel lattice planes, every atom within the planes acts as a scattering centre and emits a secondary wave. All of the secondary waves combine to form a reflected wave. The same occurs on the parallel lattice planes for only very little of the X-ray wave is absorbed within the lattice plane distance: *d*. For a certain angle (Bragg angle), the amplification condition (phase difference equals to a whole multiple of wavelengths, $\Delta\lambda = n\lambda$) is satisfied.
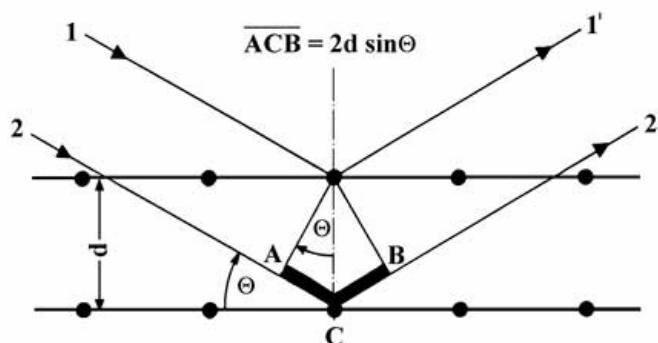
Figure AC.1 Bragg's law

Under amplification conditions, parallel, coherent X-ray light (rays 1, 2) falls on a crystal with a lattice plane distanced d and is scattered below the angle θ (rays 1', 2'). The proportion of the beam that is scattered on the second plane has a phase difference of *|ACB|* to the proportion of the beam that was scattered at the first plane. Following the definition of sine: *|AC|=d sinθ*. The phase difference *|ACB|* is twice of that, so *|ACB| = 2d sinθ*. The amplification condition is fulfilled when the phase difference is a whole multiple of the wavelength *λ*, so *|ACB| = nλ*. Thus we obtain Bragg's law: *2d sinθ= nλ (n=1, 2, 3…)*

Figure AC.2 shows a typical setup of a four-circle diffractometer.

Figure AC. 2 Four-circle diffractometer.

C. 2 X-ray reflectivity measurement
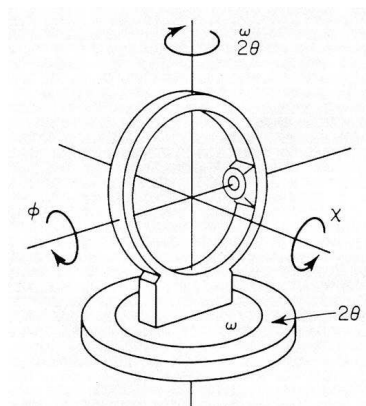
X-ray reflectivity is one of the methods used to analyze thin film thickness, density and roughness. In this method, x-ray beams strike the sample surface at a glancing angle. Reflected x-ray intensity is measured while varying the angle of incidence. Analysis of the resulting profile enables analysis of the structural parameters of the sample thin film. Figure AC.3 shows the relationship between the reflectivity profile and structure parameters (density, film thickness, roughness).
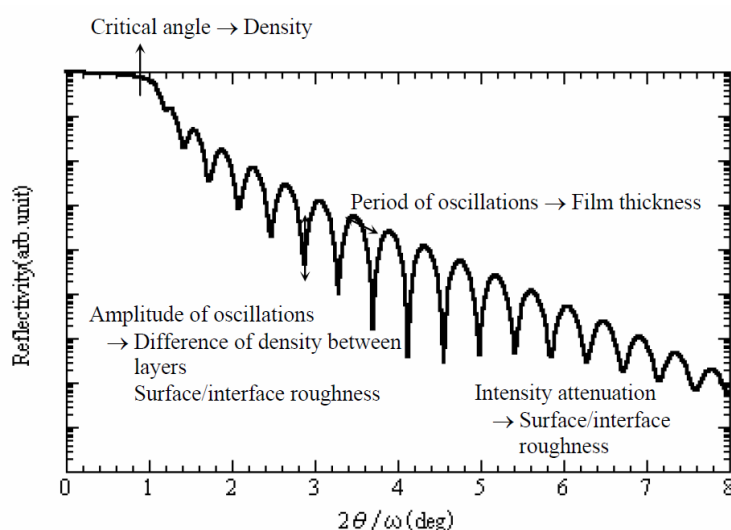
Figure AC.3 Relationship between the reflectivity profile and structure parameters.

C. 3 Rocking curve measurement

Rocking curve measurement is an x-ray technique to analyze the alignment of crystal lattices. It assesses changes in diffracted x-ray intensity when a sample is rocked over a range of omega values. It is based on a given *hkl* reflection from a thin film, and provides the spatial distribution the lattice orientation, called mozaicity. To accomplish a rocking curve measurement, the detector is set to the 2θ value of the targeted reflection. The receiving optics

slits are set comparatively wide in order to measure the changes in intensity when the omega axis is scanned. Figure AC.4 shows the operation principle and the information obtained from the rocking curve scan.
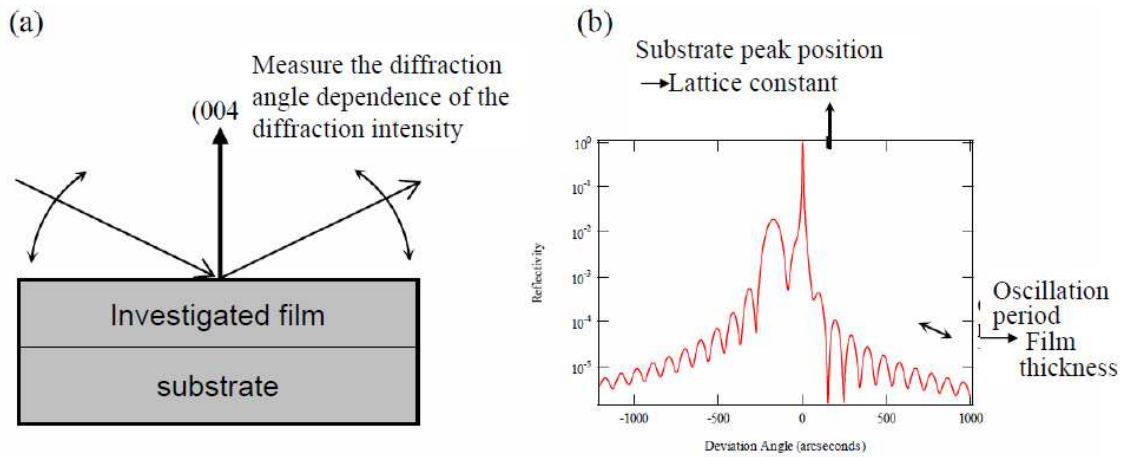
Figure AC. 4 (a) Rocking curve measurement diagram and (b) relationship between measurement results and structural parameters.

C. 4 Reciprocal Space Mapping Measurement (RSM)

The Reciprocal Space Mapping (RSM) measurement is used to analyze the orientation of the substrate crystal phase as it related to the lattice plane of the epitaxial thin film. A RSM measurement acquires a two-dimensional intensity distribution by performing a series of $2\theta/\omega$ scans at stepped values of ω. All diffraction peaks occurring in this scanned area are indicated by increased intensity in the map. Measuring such 2D intensity distributions enables us to analyze peak distributions. We can determine which predominates: peaks spreading in the ω direction (spatial distribution of lattice) or peaks spreading in the $2\theta/\omega$ direction (dispersion of the lattice constant), as shown in Figure AC.5.
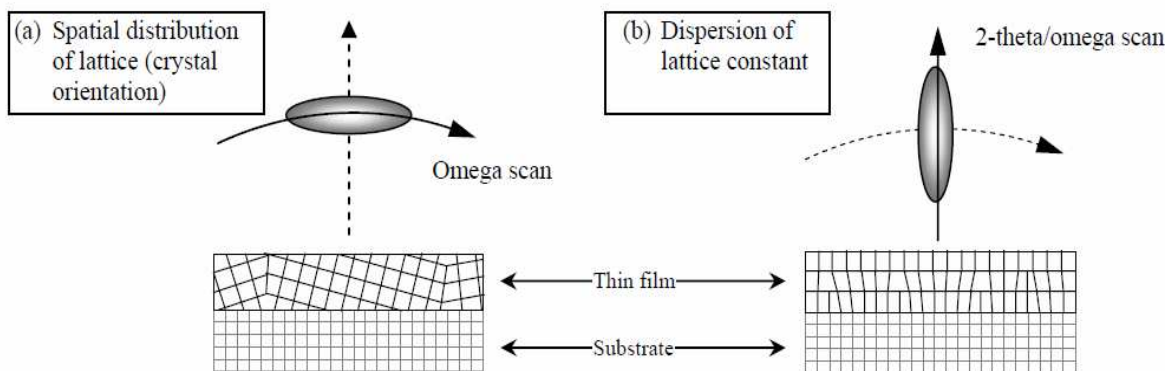
Figure AC.5 Factors causing spread in the peak distribution: (a) Mosaic spread and (b) Spread due to lattice distortion.

C. 5 Pole Figure Measurement

Pole figure measurement is a method to analyze the preferred orientation type, directional relationships and degree of orientation in the sample. It is performed using a constant diffraction angle and the sample is rotated in all directions. A semi-spherical pole figure is scanned by rotating the sample through two preferred orientation axes: alpha (tilt) and beta (in-plane rotation). For a four-axis goniometer, alpha and beta correspond to the chi and phi axes respectively. Figure AC.6 illustrates the pole figure measurement.

Figure AC.6 Pole Figure measurement

Communication list

Publications

1. <u>G. Niu</u>, B. Vilquin, N. Baboux, C. Plossu, L. Becerra, G. Saint-Grions, G. Hollinger, "*Growth temperature dependence of epitaxial Gd_2O_3 films on Si(111)*", Microelectron. Eng., **86**, 1700 (2009)

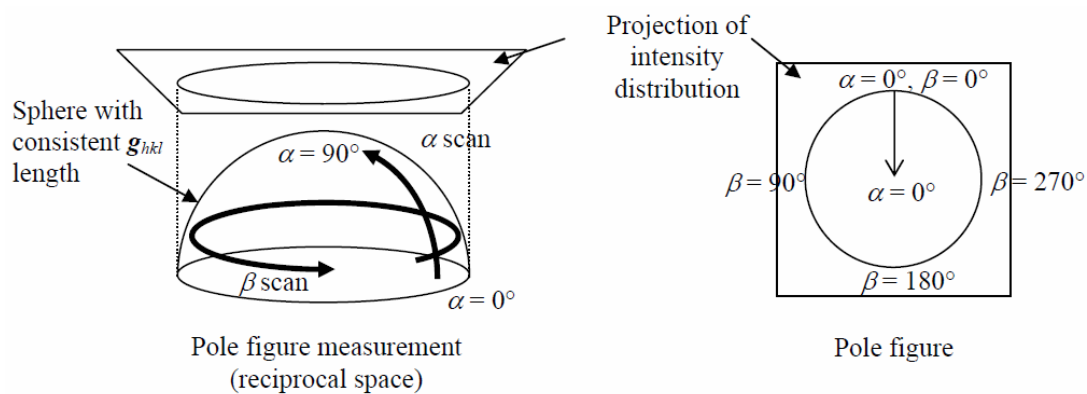2. <u>G. Niu</u>, G. Saint-Girons, B. Vilquin, G. Delhaye, J.-L. Maurice, C. Botella, Y. Robach, and G. Hollinger, "*MBE of $SrTiO_3$ on Si(001): early stages of the growth and strain relaxation*", Appl. Phys. Lett., **95**, 062902 (2009)

3. <u>G. Niu</u>, L. Largeau, G. Saint-Girons, B. Vilquin, J. Cheng, O. Mauguin, G. Hollinger, "*Monolithic integration of Ge on Si using a Gd_2O_3/Si (111) template*", J. Vac. Sci. Tech A, 28 (5), 1187 (2010)

4. <u>G. Niu</u>, B. Vilquin, N. Baboux, G. Saint-Girons, C. Plossu, G. Hollinger, "*Electrical characteristics of crystalline Gd_2O_3 film on Si (111): impacts of growth temperature and post deposition annealing*", Material Research Society proceeding, accepted (2010)

5. G. Saint-Girons, <u>G. Niu</u>; J. Penuelas, L. Largeau, B. Vilquin, J.L. Maurice, C. Botella and G. Hollinger, "*A scenario for the epitaxial growth of $SrTiO_3$ on silicon*", Phys. Rev. Lett., submitted, (2010)

6. N. Barrett, J. Rault, I. Krug, B. Vilquin, <u>G. Niu</u>, B. Gautier, D. Albertini and O. Renault, "*Influence of the ferroelectric polarization on the electronic structure of $BaTiO_3$ thin films*", Surf. Interface Anal., accepted, (2010)

7. D. Esteve, K. Postava, P. Gogol, <u>G. Niu</u>, B. Vilquin, P. Lecoeur, "*In-situ monitoring of La0.67Sr0.33MnO3 monolayers grown by Pulsed Laser Deposition*", Phys. Status Solidi, accepted, (2010)

8. <u>G. Niu</u>, W.W. Peng, G. Saint-Girons, J. Penuelas, P. Roy, J.B. Brubach, J-L. Maurice, G. Hollinger and B. Vilquin, "Direct epitaxial growth of SrTiO3 on Si (001): interface and crystallization", Thin solid film, accepted (2010)

9. <u>G. Niu</u>, J. Penuelas, L. Largeau, B. Vilquin, J.L. Maurice, C. Botella, G. Hollinger and G. Saint-Girons, "*Crystal structure of thin epitaxial $SrTiO_3$ layers grown on silicon*", J. Appl. Phys., submitted (2010)

10. B. Vilquin, Ph. Lecoeur, <u>G. Niu</u>, S. Autier-Laurent, G. Saint-Girons, V. Pillard, Y. Robach, G. Hollinger, "*Epitaxie d'oxydes fonctionnels sur silicium pour la microélectronique avancée*", Journal de la Société des Electroniciens et Electriciens (SEE) dans le cadre de son 125ème anniversaire. (2008)

Communications

1. <u>G. Niu</u>, G. Delhaye, G. Saint-Girons, Y. Robach, G. Hollinger and B. Vilquin, "*Epitaxie directe de SrTiO3 (sans recuit post-dépôt) sur silicium*", Oxydes fonctionnels pour l'intégration en micro- et nano-électronique, Autran (Isère), France, 16-19 March, <u>poster</u> (2008)

2. S. Autier-Laurent, <u>G. Niu</u>, B. Blein, B. Vilquin and Ph. Lecoeur, "*Intégration de manganites sur silicium*", Oxydes fonctionnels pour l'intégration en micro- et nano-électronique, Autran (Isère), France, 16-19 March, <u>poster</u> (2008)

3. <u>G. Niu</u>, G. Delhaye, G. Saint-Girons, Y. Robach, G. Hollinger, B. Vilquin, B. Blein, S. Autier-Laurent and Ph. Lecoeur, "*Epitaxie directe de $SrTiO_3$ sur silicium*", Journées Nano, Micro et Optoelectronique (JNMO'08), Oléron, France, 3-6 June, <u>poster</u> (2008)

4. <u>G. Niu</u>, G. Delhaye, G. Saint-Girons, Y. Robach, G. Hollinger, B. Vilquin, B. Blein, S. Autier-Laurent and Ph. Lecoeur, "*The epitaxy of oxides on Silicon by MBE: $SrTiO_3$, $BaTiO_3$, Gd_2O_3*", Transalp'Nano 2008, Lyon, France, 27-29 October, <u>poster</u> (2008)

5. G. Saint-Girons, J. Cheng, P. Regreny, G. Patriarche, L. Largeau, P. Rojo Romeo, <u>G. Niu</u>, B. Vilquin, G. Hollinger, "*Monolithic integration of III-V and Ge on Si using compliant epitaxial oxide buffers*", Journées Nationales des Technologies Emergentes (JNTE), Toulouse, France 19-21 November, <u>invited talk</u>(2008)

6 <u>G. Niu</u>, G. Saint-Girons, B. Vilquin, "*Epitaxy and characterization of crystalline high k oxides on silicon by MBE*", ECL-Keio workshop, Lyon, France, 1-3 February, <u>oral presentation</u> (2009)

7. <u>G. Niu</u>, B. Vilquin, L. Becerra, S. Pelloquin, G. Saint-Girons, N. Baboux, C. Plossu, "*Growth temperature dependence of epitaxial Gd_2O_3 films on Si (111)*", INFOS 2009 Cambridge, UK, 29 June-1 July, <u>poster</u> (2009)

8. D. Esteve, K. Postava, P. Gogol, <u>G. Niu</u>, B. Vilquin, P. Lecoeur, "*In situ monitoring of $La_{0.67}Sr_{0.33}MnO_3$ monolayers grown by pulsed laser deposition*", Optics of Surface and Interfaces I-VIII, Ischia, Italy, 7-11 September, <u>oral presentation</u> (2009)

9. G. Niu, B. Vilquin, G. Saint-Girons, C. Botella, G. Grenet, P. Regreny, M. Gendry, Y. Robach and G. Hollinger, N. Baboux, C. Plossu, B. Canut, B. Blein, S. Autier-Laurent and P. Lecoeur, J.-L. Maurice, "*Epitaxie d'oxydes cristallins « high k » sur silicium*", JNRDM 2009, Lyon, France, 18-20 May, oral presentation (2009)

10. B. Vilquin, G. Niu, G. Saint-Girons, B. Gautier, Y. Robach, B. Canut and G. Hollinger, "*Integration of functional oxides on silicon: SrTiO₃, BaTiO₃, (La,Sr)MnO₃*", 16th International Workshop on Oxide Electronics (WOE 16), Taragona, Spain, 4-7 October, poster (2009)

10. G. Niu, B. Vilquin, N. Baboux, G. Saint-Girons, C. Plossu, G. Hollinger, "*Electrical characteristics of crystalline Gd₂O₃ film on Si (111)*", MRS 2010 Spring meeting, San Francisco, CA USA, 5-9 April, poster (2010)

11. G. Niu, W.W. Peng, G. Saint-Girons, J. Penuelas, P. Roy, J.B. Brubach, J-L.Maurice, G. Hollinger, and B. Vilquin, "*Direct epitaxial growth of SrTiO₃ on Si (001): interface and crystallization*", E-MRS 2010 Spring Meeting, Strasbourg, France, 8-10 June, oral presentation (2010)

12. G. Saint-Girons, J. Cheng, A. Chettaoui, P. Regreny, G. Niu, J. Penuelas, B. Gobaut L. Largeau, G. Patriarche and G. Hollinger, "*Cristalline oxide/Si templates for the direct epitaxial growth of III-V and Ge on silico*n", E-MRS 2010 Spring Meeting, Strasbourg, France, 8-10 June, oral presentation (2010)

AUTORISATION DE SOUTENANCE

Vu les dispositions de l'arrêté du 7 août 2006,

Vu la demande du Directeur de Thèse

Monsieur G. HOLLINGER

et les rapports de

Monsieur C. BRYLINSKI
Professeur - Directeur adjoint - Laboratoire Multimatériaux et Interfaces (LMI)
Université Claude Bernard Lyon 1 - Bâtiment Claude Berthollet ét. 3 - 22 rue Gaston Berger
69622 VILLEURBANNE cedex

et de

Monsieur E. DEFAY
Chercheur-Ingénieur (hdr) - CEA-LETI Minatec - 17 rue des Martyrs - 38054 GRENOBLE cedex 9

Monsieur NIU Gang

est autorisé à soutenir une thèse pour l'obtention du grade de **DOCTEUR**

Ecole doctorale ELECTRONIQUE, ELECTROTECHNIQUE ET AUTOMATIQUE

Fait à Ecully, le 18 octobre 2010

P/Le Directeur de l'E.C.L.
La Directrice des Etudes

SCOLARITE
3ème Cycle

M-A. GALLAND

Epitaxy of crystalline oxides for functional materials integration on silicon

Abstract

Oxides form a class of material which covers almost all the spectra of functionalities: dielectricity, semiconductivity, metallicity superconductivity, non-linear optics, acoustics, piezoelectricity, ferroelectricity, ferromagnetism…In this thesis, crystalline oxides have been integrated on the workhorse of the semiconductor industry, the silicon, by Molecular Beam Epitaxy (MBE).

The first great interest of the epitaxial growth of crystalline oxides on silicon consists in the application of "high-k" dielectric for future sub-22nm CMOS technology. Gadolinium oxide was explored in detail as a promising candidate of the alternative of SiO_2. The pseudomorphic epitaxial growth of Gd_2O_3 on Si (111) was realized by identifying the optimal growth conditions. The Gd_2O_3 films show good dielectric properties and particularly an EOT of 0.73nm with a leakage current consistent with the requirements of ITRS for the sub-22nm nodes. In addition, the dielectric behavior of Gd_2O_3 thin films was further improved by performing PDA treatments.

The second research interest on crystalline oxide/Si platform results from its potential application for the "More than Moore" and "Heterogeneous integration" technologies. The $SrTiO_3$/Si (001) was intensively studied as a paradigm of the integration of oxides on semiconductors. The crystallinity, interface and surface qualities and relaxation process of the STO films on silicon grown at the optimal conditions were investigated and analyzed. Several optimized growth processes were carried out and compared. Finally a "substrate-like" STO thin film was obtained on the silicon substrate with good crystallinity and atomic flat surface.

Based on the Gd_2O_3/Si and $SrTiO_3$/Si templates, diverse functionalities were integrated on the silicon substrate, such as ferro-(piezo-)electricity ($BaTiO_3$, PZT and PMN-PT), ferromagnetism (LSMO) and optoelectronics (Ge). These functional materials epitaxially grown on Si can be widely used for storage memories, lasers and solar cells, etc.

Key words

Epitaxie d'oxydes cristallins pour l'intégration de matériaux fonctionnels sur silicium

Résumé

Les oxydes forment une classe de matériaux qui couvrent un vaste spectre de fonctionnalités: diélectricité, semiconductivité, métallicité, supraconductivité, optique non linéaire, acoustique, piézoélectricité, ferroélectricité, ferromagnétisme… Dans cette thèse nous avons réalisé l'intégration d'oxydes sous forme de couches minces cristallines sur silicium, en utilisant l'épitaxie par jets moléculaires (EJM).

Le premier objectif de la croissance d'oxydes cristallins sur silicium est de réaliser des isolateurs de grille à forte constante diélectrique pour les technologies CMOS avancées « sub-22nm ». L'utilisation de l'oxyde de gadolinium (Gd_2O_3) a été explorée en détail comme un candidat très prometteur pour remplacer l'oxyde de grille traditionnelle qu'est la silice (SiO_2). La croissance épitaxiale de Gd_2O_3 sur le substrat Si (111) a été réalisée en identifiant les conditions de croissance optimale pour obtenir de bonnes propriétés diélectriques avec notamment l'obtention d'une valeur d'EOT de 0,73nm et des courants de fuite compatibles avec les spécifications de l'ITRS pour les nœuds « sub-22nm ». En outre, les propriétés diélectriques de Gd_2O_3 ont pu être améliorées en effectuant des recuits post-dépôts.

L'autre intérêt d'avoir un empilement d'oxydes cristallins sur silicium repose sur leurs applications potentielles dans les technologies « Plus que Moore » ainsi que pour l' « Intégrations hétérogènes». Le système $SrTiO_3$/Si (001) a été étudié comme un système modèle de l'intégration des oxydes sur semi-conducteur. La cristallinité, la qualité de l'interface oxyde-semiconducteur, l'état de surface et le processus de relaxation de STO déposé sur silicium ont été examinés et analysés, permettant de déterminer des conditions de croissance optimales. Plusieurs processus de croissance ont été réalisés et comparées. Finalement, une couche mince de STO de même qualité qu'un substrat massif a pu être obtenue sur silicium avec une bonne cristallinité et une surface atomiquement lisse.

A partir des empilements de Gd_2O_3/Si et $SrTiO_3$/Si, il a été possible d'intégrer sur silicium des oxydes possédant des fonctionnalités variées comme la ferro-(piézo-)électricité ($BaTiO_3$, PZT et PMN-PT), le ferromagnétisme (LSMO) et l'optoélectronique (Ge). Ces couches minces fonctionnelles sur Si peuvent être alors largement utilisées pour des applications de stockage mémoire, les lasers et les cellules solaires, etc.

Mot clés

Oxydes cristallins; Oxydes "high-*k*"; Oxydes fonctionnels; Germanium; hétéroepitaxie; EOT; Recuit post-dépôt; capacité MOS; cycle d'hystérésis; Epitaxie par jets moléculaires (EJM) ; RHEED; AFM; XRD; XPS; TEM; IR;